

Novel perovskite type oxides as catalysts for generation of synthesis gas with variable H₂ to CO ratio

Thesis Submitted to AcSIR for the Award of
the Degree of
DOCTOR OF PHILOSOPHY
in Chemical Science



By
Dama Srikanth
(Registration Number **10CC11A26040**)

Under the guidance of
Dr. C. V. V. Satyanarayana

Catalysis Division
CSIR-National Chemical Laboratory
Pune-411008, India
October 2017



सीएसआयआर-राष्ट्रीय रासायनिक प्रयोगशाला

(वैज्ञानिक तथा औद्योगिक अनुसंधान परिषद)

डॉ. होमी भाभा मार्ग, पुणे - 411 008. भारत



CSIR-NATIONAL CHEMICAL LABORATORY

(Council of Scientific & Industrial Research)

Dr. Homi Bhabha Road, Pune - 411008. India

Certificate

This is to certify that the work incorporated in the Ph.D thesis entitled “*Novel perovskite type oxides as catalysts for generation of synthesis gas with variable H₂ to CO ratio*” submitted by **Mr. Dama Srikanth**, to the Academy of Scientific and Innovative research (AcSIR), in fulfillment of the requirements for the award of the degree of **Doctor of Philosophy** embodies original research work which was carried out under my supervision at the Catalysis Division, CSIR-National Chemical Laboratory, Pune –411 008, India. I further certify that this work has not been submitted to any other University or Institution in part or full of any degree or diploma. Research material obtained from other sources has been duly acknowledged in the thesis. Any text, illustrations, tables etc used in this thesis from other sources have been duly cited and acknowledged.

Mr. Dama Srikanth
(Research student)

Dr. C.V.V Satyanarayana
(Research supervisor)
CSIR-National chemical laboratory
Pune-411008

Date: 27 October 2017

Place: Pune



Communications
Channels

NCL Level DID : 2590
NCL Board No. : +91-20-25902000
Four PRI Lines : +91-20-25902000

FAX

Director's Office : +91-20-25902601
COA's Office : +91-20-25902660
SPO's Office : +91 20 25902664

WEBSITE

www.ncl-india.org

DECLARATION BY RESEARCH SCHOLAR

I hereby declare that the work described in the thesis entitled “*Novel perovskite type oxides as catalysts for generation of synthesis gas with variable H₂ to CO ratio*” submitted for the degree of *Doctor of Philosophy* in *Chemical Sciences* to the Academy of Scientific and Innovative Research (AcSIR), New Delhi, has been carried out by me at *Catalysis and Inorganic Chemistry Division, CSIR-National Chemical Laboratory, Pune-411008, India*, under the supervision of **Dr. C. V. V. Satyanarayana**. I further declare that the material obtained from other sources has been duly acknowledged in this thesis. The work is original and has not been submitted in part or full by me for any other degree or diploma to this or any other university.

Date: 27 october 2017

Place: Pune



Mr. Dama Srikanth
(Research Student)

ACKNOWLEDGEMENTS...

This thesis has been seen through to completion with the support and encouragement of numerous people including my well wishers, friends and colleagues. At this point of accomplishment I like to thank all those people who made this possible, which is an unforgettable experience for me. First and foremost, I would like to express my heartfelt and sincere gratitude to my research supervisor Dr. Satyanarayana Chilukuri who introduced me to a fascinating realm of chemistry. I am deeply indebted to him for his invaluable guidance and unconditional support. His constant inspiration and constructive criticism helped me a lot to focus my views in proper perspective. His tireless attitude has been an impetus for me throughout the course of study. He gave me the freedom to think, experiment and accomplish. I shall cherish my learning experience under his guidance. I take this opportunity to express my deepest sense of gratitude and reverence towards him for guiding me in the right direction throughout the course of this work.

Words fail me when I intend to express my thanks and gratitude to Dr. T. Raja and Dr Nandini Devi for professional and personal support. I believe the better way of thanking them would be through my future contribution to scientific community by research. I extend my sincere thanks to the Director of CSIR-NCL Prof. Ashwini kumar Nangia and Dr. D. Srinivas (Chair, Catalysis division) for providing me the opportunity to carry out my research work in this prestigious and well-equipped laboratory. My heartfelt thanks are due to Dr. Gopinath Chinnakonda, Dr. Paresh Dhepe, Dr. C.P. Vinod and Ms. Violet Samuel. I also like to thank Mr. Madhu, Mr. Jha, Mr. Purushothaman and all other scientific and non-scientific staff for their help and support during my tenure as a research student. My deepest gratitude to my teachers Prof. Ranga Rao, Prof. B. Viswanathan, Prof. Selvam, Prof. Sivasanker, Prof. Rajanna, Prof. Manohar, Prof. Sayaji Rao, Dr. Shivanageshwar Rao. Mr. Venkateswara Goud, Mr. Venkataramana, Mr. Mahadevayya, Mr. Krishna Reddy, Mr. Gangadhar, Mr. Bechupally, Mr. Balanna, Mr. Shekar, Mr. Satyakumar and Mrs. Vidyulatha for their inspirational teaching, guidance and blessings.

I extend my sincere thanks to Student Academic Office and catalysis division at CSIR-NCL for their help and support at crucial times. I am grateful to UGC, New Delhi, for awarding the research fellowship and Director, CSIR-National Chemical Laboratory for extending all infrastructural facilities.

I have high regard to my seniors Dr. Satyanarayana Reddy, Dr. Narsimha Rao, Dr. Anil Mettu, Dr. Santhosh, Dr. Hanmant, Dr. Ganesh, Dr. Sachin, Dr. Koteswara Rao, Dr. Reji, Dr. Nishita and Dr. Atul for their unconditional support and help during my Ph D. Course. I am indebted to my labmates Richa, Seema, Dr. Lakshmiprasad, Pranjal, Dheerendra, Sivaprasad, Vipul and my previous labmates Aditya, Jay, Mangesh, Lalit, Gajanan, Amlan, Chandan, Anju, Vineetha, Varsha and Venkatesh for their love and encouragement. I sincerely thank all my divisional friends especially Rajesh, Jijil, Edwin, Devadutta, Ashok and my senior colleagues and friends Dr. Rajender, Dr. Sridhar, Dr. Swaroop, Dr. Yadagiri, Dr. Sudhakar, Dr. Suneel, Dr. Bala, Dr. Manoj, Dr. Suresh, Dr. Chandrababu, Dr. Rami Reddy, Dr. Rambabu, Dr. Chaitanya Krishna, Dr. Janaki Ram, Dr. Durga, Dr. Shiva kumar, Dr. Nagendra, Dr. Narendra, Dr. Satish, Dr. Shanthi, Dr. Bhogesh, Dr. Naresh, Dr. Trinadh, Sagar, Swamy, Srikanth Reddy, Nalini, Anand, Viswanath, Srinivas, Tarun, Eswar, Innaiah, Hanuman, Kumar Raja, Pravat. I extend huge thanks to my friends during school, College and Master's days.

I would like to pay high regards to my parents, Shri Nagappa and Smt. Subadramma, my sisters Shirisha and Padmavathi, my brother Jayaprakash and brother-in-law Angali Srikanth for their unconditional love and affection. It gives me great pleasure to thank them for their love, sacrifice, moral support, blessings, care and constant encouragement that they have shown to me. Special thanks and wishes to my cousins Pradeep, Prashant, Suresh, Naresh kumar, Srilatha, Prathyusha, Bheemarayudu, Pooja, Veerasena, Laxminarayana, Devi, Madhusudan and uncles Satyanrayana, Gopal, Krishnamurthy, Bhaskar and my aunts Anasuya, Nirmala, Annapurna for their constant love, support and encouragement. I am very much indebted to all my family members. Above all, I owe it all to Almighty God for giving me the wisdom, health and belief to undertake research work for my thesis and enabling me to its completion.

Dama Srikanth

*.....dedicated to my
beloved parents and
teachers*

“A parent should inspire a child to use success in a way that influences positive change in the world.

A teacher should inspire a student to reach academic success.....”



List of contents

List of titles	i
List of tables	ix
List of figures	x
Abbreviations	xvi

Chapter 1 Introduction

Section No.	Titles	Page No.
1.1.	Introduction to catalysis	2
1.2.	Natural gas	3
1.3.	Current status of CO ₂	4
1.4.	Biogas	4
1.5.	Synthesis gas	5
1.5.1.	Historical review	5
1.5.2.	Syngas production from hydrocarbons	6
1.6.	Steam reforming of methane (SRM)	8
1.6.1.	Thermodynamics of steam reforming reaction	9
1.6.1.1.	Thermodynamic function of SRM	9
1.6.1.2.	Thermodynamic equilibrium of reactant and product distribution	10
1.6.2.	Reaction mechanism and kinetic study of SRM	12
1.6.3.	Advantages of steam reforming of CH ₄	13
1.6.4.	Disadvantages of SRM process	13
1.7.	Dry reforming of CH ₄	13
1.7.1.	Thermodynamics of DRM	14
1.7.1.1.	Effect of temperature on DRM, MD, BR and RWGS reactions	14
1.7.1.2.	Thermodynamic equilibrium of reactant and product distribution	15
1.7.2.	Carbon formation reactions	16
1.7.2.1.	Methane decomposition (MD)	16

1.7.2.2.	Boudouard reaction (BR)	17
1.7.3.	Thermodynamic equilibrium of coke formation in reforming	18
1.7.4.	Advantages of Dry (CO ₂) reforming of CH ₄	19
1.7.5.	Limitations of DRM process	20
1.8.	Partial oxidation of CH ₄	20
1.9.	Auto thermal reforming of CH ₄ (ATR)	21
1.10.	Bi reforming or combined reforming of CH ₄	22
1.11.	Tri reforming of CH ₄	24
1.12.	Sulfur poisoning during reforming	25
1.13.	Reforming catalysts- A literature review	26
1.13.1.	Role of the support in reforming catalysts	26
1.13.2.	Perovskite type structured oxides as catalysts	26
1.14.	Scope and objective of the present thesis	28
1.15.	References	31

Chapter 2 Catalyst preparation and characterization methods

2.1.	Introduction	37
2.2.	Description of chemicals and gases used for this study	37
2.3.	Catalyst preparation	38
2.3.1.	Preparation of perovskite type oxides	39
2.3.1.1.	Preparation of Ni substituted LnAlO ₃ by citrate method	39
2.3.1.2.	Preparation of Ru and Rh substituted CeAlO ₃ perovskites by citric method	40
2.3.1.3.	Preparation of Ni substituted alkaline earth zirconate (MZrO ₃) type perovskite oxides	40
2.4	Catalyst characterisation techniques	41
2.4.1.	X-ray diffraction (XRD)	41
2.4.2.	Brunauer-Emmett-Teller (BET) surface area	43

2.4.3.	Temperature programmed techniques	45
2.4.3.1.	Temperature programmed reduction/oxidation (TPR/TPO)	45
2.4.3.2.	Temperature programmed desorption (TPD)	46
2.4.3.3.	Thermo gravimetric analysis (TGA)	47
2.4.4.	X-ray photoelectron spectroscopy (XPS)	48
2.4.5.	Transmission electron microscopy (TEM)	49
2.4.6.	Infrared Spectroscopy (IR)	50
2.4.7.	Laser Raman spectroscopy (LRS)	51
2.4.8.	Inductively coupled plasma-optical emission spectroscopy (ICP-OES)	52
2.5.	Techniques used for characterization of carbon/coke deposits	53
2.6.	Experimental procedure for catalysts evaluation	54
2.6.1.	Flow controller units	54
2.6.2.	Reactor unit	55
2.6.3.	Product analysis	55
2.7.	References	56

Chapter 3 Steam reforming of methane and simulated biogas over $\text{LnAl}_{1-x}\text{Ni}_x\text{O}_{3-\delta}$ perovskite type catalysts

3.1.	Introduction	60
3.2.	Experimental methods	62
3.2.1.	Synthesis of $\text{LnAl}_{1-x}\text{Ni}_x\text{O}_3$ perovskites	62
3.2.2.	Catalyst evaluation	62
3.3.	Results and discussion	63
3.3.1.	X-ray diffraction investigations of $\text{LnAl}_{1-x}\text{Ni}_x\text{O}_{3-\delta}$ perovskites	63
3.3.2.	Textural and structural characterization of catalysts	67
3.3.3.	Raman analysis of LnAlO_3 perovskites	67
3.3.4.	Temperature programmed reduction of Ni substituted	69

	LnAlO ₃ .	
3.3.5.	Temperature-programmed desorption of oxygen	70
3.3.6.	X- Ray photoelectron spectroscopy (XPS)	71
3.4.	Evaluation of catalysts for steam reforming of methane	72
3.4.1.	Judging the best lanthanide substituted perovskite catalyst for SRM	72
3.4.2.	Time on stream study	74
3.4.3.	Transient pulse experiment of CH ₄ and H ₂ O	75
3.4.4.	Activity of Ni impregnated catalyst versus Ni substituted perovskite catalyst	77
3.4.5.	Time on stream stability of substituted and impregnated catalysts	78
3.4.6.	Kinetic study of SRM reaction over CeAl _{0.8} Ni _{0.2} O _{3-δ} catalysts	78
3.4.7.	Catalytic activity of CeAl _{0.8} Ni _{0.2} O _{3-δ} in simulated biogas reforming	79
3.4.8.	Time on stream study of bi-reforming of methane	81
3.5.	Characterization of spent catalysts	82
3.5.1.	Raman and TGA analysis	82
3.5.2.	XPS of Spent catalysts	83
3.5.3.	TEM analysis of spent catalysts	84
3.6.	Conclusions	85
3.7.	References	87

Chapter 4 Syngas with variable H₂/CO ratios using Ru and Rh substituted perovskites by steam, Bi- and Tri-reforming of methane

Part I. Ru and Ru-Ni substituted CeAlO₃ perovskites for steam, bi- and Tri-reforming of methane		
4.1.	Introduction	92
4.2.	Experimental methods	92

4.2.1.	Preparation of Ru substituted CeAlO ₃ and Ru impregnated CeAlO ₃	92
4.3.	Results and discussion	93
4.3.1.	X-ray diffraction (XRD) studies of CeAl _{1-x} Ru _x O ₃ perovskites	93
4.3.2.	Textural and structural properties	94
4.3.3.	Temperature programmed reduction of CeAl _{1-x} Ru _x O ₃ oxides	97
4.3.4.	Raman spectroscopy of CeAl _{1-x} Ru _x O ₃ perovskite oxides	98
4.3.5.	XPS of CeAl _{1-x} Ru _x O ₃ perovskite oxides	98
4.3.6.	Transmission electron microscopy (TEM)	100
4.4.	Catalytic activity of Ru containing CeAlO ₃ perovskites	100
4.4.1.	SRM activity at different temperatures	100
4.4.2.	Effect of GHSV	101
4.4.3.	Kinetics of SRM reaction over CeAl _{0.85} Ru _{0.15} O _{3-δ} catalyst	102
4.5.	Reforming activity of Ni containing CeAl _{0.9} Ni _{0.1} O _{3-δ} catalysts promoted by Ru	103
4.5.1.	Catalytic activity of CeAl _{0.86} Ni _{0.1} Ru _{0.04} O _{3-δ} in bi- and tri-reforming of CH ₄	104
4.6.	Characterization of spent catalysts	105
4.6.1.	Thermogravimetric analysis of spent catalysts	106
4.6.2.	Transmission Electron Microscopy of spent catalysts	107

Part II. Rhodium substituted CeAlO₃ (CeAl_{1-x}Rh_xO₃) catalysts for SRM, BRM and their sulfur tolerance

4.7.	Introduction	108
4.8.	Experimental methods	108
4.8.1.	Preparation of Rh substituted CeAlO ₃ and Rh/CeAlO ₃ catalysts	108

4.9.	Results and discussion	109
4.9.1.	Structural and textural properties	109
4.9.2.	X-ray diffraction studies of $\text{CeAl}_{1-x}\text{Rh}_x\text{O}_3$ perovskites	109
4.9.3.	Temperature programmed reduction of $\text{CeAl}_{1-x}\text{Rh}_x\text{O}_3$ oxides	112
4.9.4.	XPS of $\text{CeAl}_{1-x}\text{Rh}_x\text{O}_3$ catalysts	112
4.9.5.	Transmission electron microscopy (TEM)	114
4.10.	Catalytic activity of Rh containing CeAlO_3 perovskites	115
4.10.1.	Activity at different reaction temperatures	115
4.10.2.	Time on stream study of $\text{CeAl}_{0.95}\text{Rh}_{0.05}\text{O}_3$ catalysts	116
4.10.3.	Variation of S/C ratio in SRM reaction	116
4.10.4.	Influence of sulfur during SRM over $\text{CeAl}_{0.95}\text{Rh}_{0.05}\text{O}_3$, impregnated Rh/ CeAlO_3 and $\text{CeAl}_{0.8}\text{Ni}_{0.2}\text{O}_{3-\delta}$ catalysts	117
4.10.5.	Effect of sulfur on reforming of simulated biogas over $\text{CeAl}_{0.95}\text{Rh}_{0.05}\text{O}_3$	118
4.11.	Characterization of spent catalysts	119
4.11.1.	Thermogravimetric analysis of spent catalysts	120
4.11.2.	Transmission Electron Microscopy of spent catalysts	121
4.12.	Conclusions	121
4.13.	References	123

Chapter 5 Syngas by Dry reforming of CH_4 and steam reforming of simulated biogas over $\text{MZr}_{1-x}\text{Ni}_x\text{O}_3$ (M= Ca, Sr and Ba) perovskites

5.1.	Introduction	126
5.2.	Experimental methods	127
5.2.1.	Preparation of $\text{MZr}_{1-x}\text{Ni}_x\text{O}_{3-\delta}$ perovskites	127
5.2.2.	Transient pulse study of CH_4 and CO_2 reactions	128
5.2.3.	Evaluation of catalysts for dry reforming	128
5.3.	Results and discussion	129
5.3.1.	Textural and structural characterization of catalysts	129

5.3.2.	X-ray diffraction of $\text{MZr}_{1-x}\text{Ni}_x\text{O}_{3-\delta}$	131
5.3.3.	Raman spectroscopy	132
5.3.4.	Temperature programmed reduction	134
5.3.5.	Temperature programmed desorption of CO_2 and O_2	135
5.4.	Activity of alkaline earth substituted $\text{MZr}_{0.8}\text{Ni}_{0.2}\text{O}_{3-\delta}$ catalysts in DRM	137
5.4.1.	Effect of temperature over $\text{MZr}_{0.8}\text{Ni}_{0.2}\text{O}_{3-\delta}$ (M = Ca, Sr and Ba) catalysts	137
5.4.2.	Durability of $\text{MZr}_{0.8}\text{Ni}_{0.2}\text{O}_{3-\delta}$ (M = Ca, Sr and Ba) catalysts during DRM	138
5.4.3.	Comparison of catalytic activity of Ni substituted $\text{CaZrO}_{3-\delta}$ with Nickel impregnated (Ni/CaZrO ₃) catalyst	139
5.4.4.	Effect of variation in concentration of CH_4 and CO_2 on H_2/CO ratio in product syngas over $\text{CaZr}_{0.8}\text{Ni}_{0.2}\text{O}_{3-\delta}$ catalyst	140
5.4.5.	Long term durability of $\text{CaZr}_{0.8}\text{Ni}_{0.2}\text{O}_{3-\delta}$ catalyst	140
5.4.6.	Transient pulse experiments	141
5.4.7.	In situ FTIR studies	143
5.4.8.	Bi-reforming of methane or steam reforming of simulated biogas	147
5.5.	Characterization of spent catalysts	149
5.5.1.	X-ray diffraction and Thermo gravimetric analysis of spent catalysts	149
5.5.2.	HRTEM of spent catalysts	152
5.5.3.	XPS analysis	153
5.5.4.	Raman analysis of spent catalysts	154
5.6.	Conclusions	156
5.7.	References	158

Chapter 6 Summary of the work

6.1.	Summary and Conclusions	163
6.2.	Recommendations for future work	168

List of Tables

Table No.	Title	Page No.
Chapter 1		
1.1.	Catalytic challenges in the conversion of fossil fuels to usable fuels	3
1.2.	Typical composition of bio-gas.	5
1.3.	Different approaches for kinetics of steam reforming of hydrocarbons	12
1.4.	Feed composition of bi-reforming reaction	24
1.5.	Sulfur adsorption energies and sulfide formation energies	25
Chapter 2		
2.1.	List of chemicals and their specifications used for present study	37
2.2.	Specifications and applications of the gases used	38
2.3.	Different types of carbon species decomposed from Ni catalysts	54
Chapter 3		
3.1.	Textural properties of as-synthesized LnAlO ₃ (Ln = La, Ce, Pr, Nd, Sm, Gd and Dy) phase perovskite catalysts	65
3.2.	Textural properties of LnAl _{0.8} Ni _{0.2} O ₃ (Ln = La, Ce, Pr, Nd, Sm, Gd and Dy) perovskite type oxide catalysts	66
3.3.	Experimental Raman bands of LnAlO ₃ and their respective assignment	68
Chapter 4		
4.1.	Textural and structural properties of CeAl _{1-x} Ru _x O ₃ perovskite type oxide catalysts.	96
4.2.	Textural and structural properties of CeAl _{1-x} Rh _x O ₃ perovskite oxides	111
Chapter 5		
5.1.	Structural and textural properties of MZr _{1-x} Ni _x O _{3-δ} (M= Ca, Sr and Ba; x=0 and 0.2) perovskite oxides	130
5.2.	Raman vibration modes of CaZrO ₃ type perovskite oxides	133
5.3.	C1s and O1s Binding energies of MZr _{0.8} Ni _{0.2} O _{3-δ} catalysts and their assignment	154
5.4.	Crystallite size of graphitic carbon calculated using Raman spectra	156

List of Figures

Figure No.	Title	Page No.
Chapter 1		
1.1.	Interconnectivity between synthesis, characterization and reactivity of a catalyst material	2
1.2.	(a) Increase in CO ₂ concentration over the years and (b) Change in global mean temperature during the period	4
1.3.	Various routes for the production of chemicals from syngas	6
1.4.	Indirect conversion of natural gas to useful products and their relative investment	7
1.5.	Syngas variation in different reforming technology	8
1.6.	Conventional SR reaction scheme	9
1.7.	Variation of thermodynamic parameters against temperature in SRM	10
1.8.	Thermodynamic calculations of SRM at Steam/Carbon=2	11
1.9.	Thermodynamic equilibrium conversions of methane in SRM	11
1.10.	Effect of temperature on DRM, MD, BR and RWGS as predicted by HSC Chemistry software at 1 bar pressure	15
1.11.	Equilibrium concentration of reactants and products at different temperatures as predicted by HSC chemistry software assuming CH ₄ / CO ₂ =1 at 1 bar pressure where (a) without carbon and (b) with carbon deposition	16
1.12.	Thermodynamic equilibrium plots of MD and BR reactions	17
1.13.	Carbon formation at 25.5 bar pressure with variation in H ₂ O/CH ₄ and CO ₂ /CH ₄ ratios	19
1.14.	Effect of operating temperature on reformat equilibrium compositions for ATR predicted by HSC chemistry 5.1 software assuming O/C =0.7; S/C= 1.5 and 1 atm pressure	21
1.15.	Graph represents the thermodynamic equilibrium of H ₂ /CO ratio as function of temperature in 200-700 °C range and 1atm pressure	23

1.16.	Schematic of a ABO_3 perovskite	28
Chapter 2		
2.1.	Flow chart for the preparation of $LnAl_{1-x}Ni_xO_3$ perovskite oxides	40
2.2.	Depiction of X-ray diffraction principle	42
2.3.	Quanta chrome Autosorb IQ instrument used for N_2 physisorption and H_2 chemisorption	44
2.4.	Micromeritics Autochem 2920 instrument used for TPR/TPO	46
2.5.	(a) Mettler Toledo TGA/SDTA 851; (b) Typical TGA and DTG traces	47
2.6.	Principle of photoelectron spectroscopy	48
2.7.	Schematic of a transmission electron microscope	49
2.8.	Energy-level diagram showing the states involved in Raman signal	52
2.9.	Depiction of sample introduction in ICP-OES	53
2.10.	Schematic of the experimental rig used for catalyst evaluation	54
Chapter 3		
3.1.	XRD pattern of (a) $LnAlO_3$ perovskites (b) $LnAl_{0.8}Ni_{0.2}O_{3-\delta}$ perovskite oxides	64
3.2.	Raman spectra of $LnAlO_3$ ($Ln = La, Ce, Pr, Nd, Sm, Gd$ and Dy)	67
3.3.	TPR pattern of $LnAl_{0.8}Ni_{0.2}O_{3-\delta}$ perovskites.	69
3.4.	TPD- O_2 pattern of $LnAl_{0.8}Ni_{0.2}O_3$ ($Ln = Ce, Nd$ and Dy) perovskites.	70
3.5.	XPS of $LnAl_{0.8}Ni_{0.2}O_{3-\delta}$ ($Ln = Ce, Nd$ and Dy) perovskites (a) $O1s$, (b) $Ni 3d$	71
3.6.	SRM reaction over $LnAl_{0.8}Ni_{0.2}O_3$ ($Ln = La, Ce, Pr, Nd, Sm, Gd$ and Dy) at different temperatures	73
3.7.	CH_4 conversion and H_2/CO ratio and as function of Ln in SRM	73
3.8.	TOS study of $LnAl_{0.8}Ni_{0.2}O_{3-\delta}$ ($Ln = Ce, Nd$ and Dy) catalysts in SRM reaction	74
3.9.	Mass spectral signals during the pulse experiment over $LnAl_{1-x}Ni_xO_3$, where $Ln = (a) Ce, (b) Nd$ and $(c) Dy$	76

3.10.	CH ₄ conversion as function of temperature with variation of Ni content and impregnated Ni catalyst in SRM reaction	77
3.11.	Comparison of on stream stability of CeAl _{0.8} Ni _{0.2} O _{3-δ} and CeAl _{0.9} Ni _{0.1} O _{3-δ} catalysts with 5.3 wt% Ni impregnated CeAlO _{3-δ}	78
3.12.	CH ₄ conversion on CeAl _{0.8} Ni _{0.2} O _{3-δ} catalyst at different temperatures and contact time; (b) Arrhenius plot for CeAl _{0.8} Ni _{0.2} O _{3-δ} catalyst	79
3.13.	Steam reforming of a simulated biogas over CeAl _{0.8} Ni _{0.2} O _{3-δ} catalyst	80
3.14.	Variation of H ₂ /CO ratio with H ₂ O/CH ₄ ratio over the CeAl _{0.8} Ni _{0.2} O _{3-δ} for Bi-reforming reaction.	81
3.15.	TOS behaviour of CeAl _{0.8} Ni _{0.2} O _{3-δ} perovskites in bi-reforming of CH ₄ .	82
3.16.	Characterization of coke present on spent catalysts after SRM for 18 hours; (a) Raman spectra, (b) coke content from TGA.	83
3.17.	XPS of spent LnAl _{0.8} Ni _{0.2} O _{3-δ} (Ln = Ce, Nd and Dy) catalysts after SRM	84
3.18.	HRTEM images of spent catalysts for LnAl _{0.8} Ni _{0.2} O _{3-δ} ; where Ln = (a)Dy (b)Nd & (c)Ce.	85

Chapter 4

4.1.	XRD of CeAlO ₃ family of perovskites (a) CeAlO ₃ , (b) CeAl _{0.93} Ru _{0.07} O ₃ , (c) CeAl _{0.9} Ru _{0.1} O ₃ , (d) CeAl _{0.85} Ru _{0.15} O ₃ (e) CeAl _{0.8} Ru _{0.2} O ₃ (f) Ru imp CeAlO ₃	94
4.2.	TPR of CeAl _{1-x} Ru _x O ₃ and Ru impregnated CeAlO ₃ perovskites.	97
4.3.	Raman spectra of Ru perovskite oxides	98
4.4.	XPS spectra of CeAl _{0.85} Ru _{0.15} O ₃ and Ru impregnated perovskites	99
4.5.	TEM images of (a) CeAl _{0.85} Ru _{0.15} O ₃ , (b) CARu-imp; Ru distribution on (c) CeAl _{0.85} Ru _{0.15} O ₃ , (d) CARu-imp	99
4.6.	Effect of temperature on activity of CeAl _{1-x} Ru _x O ₃ (x = 0.07, 0.1, 0.15 and 0.2) and Ru impregnated catalysts	100

4.7.	Effect of space velocity on activity of $\text{CeAl}_{1-x}\text{Ru}_x\text{O}_3$ ($x = 0.07, 0.1, 0.15$ and 0.2) catalysts for SRM reaction	101
4.8.	(a) CH_4 conversion versus reaction temperature at different space velocities; (b) Arrhenius plot for $\text{CeAl}_{0.85}\text{Ru}_{0.15}\text{O}_3$ catalysts for SRM reaction	102
4.9.	Time on stream stability of $\text{CeAl}_{0.86}\text{Ni}_{0.1}\text{Ru}_{0.04}\text{O}_3$ catalyst during SRM	103
4.10.	Time on stream stability of $\text{CeAl}_{0.86}\text{Ni}_{0.1}\text{Ru}_{0.04}\text{O}_3$ catalyst during BRM	104
4.11.	Long term stability of CAN-Ru $_{0.04}$ catalyst during TRM	105
4.12.	Coke estimation after steam, Bi and tri reforming of methane by using TGA	106
4.13.	TEM images of spent catalysts (a) CARu $_{0.15}$ and (b) CANRu $_{0.04}$ for SRM, (c) CANRu $_{0.04}$ for BRM and (d) CANRu $_{0.04}$ for TRM	107
4.14.	XRD patterns of $\text{CeAl}_{1-x}\text{Rh}_x\text{O}_3$ and Rh impregnated catalysts.	110
4.15.	TPR of $\text{CeAl}_{1-x}\text{Rh}_x\text{O}_3$ and Rh impregnated catalysts	112
4.16.	(a) Ce3d (b) O1s XPS analysis of $\text{CeAl}_{1-x}\text{Rh}_x\text{O}_3$ ($x = 0.0, 0.05$ and 0.1)	113
4.17.	Surface ratios of $\text{Ce}^{+4}/\text{Ce}^{+3}$ and O_S/O_L in $\text{CeAl}_{1-x}\text{Rh}_x\text{O}_{3-\delta}$ ($x = 0.0, 0.05, 0.1$) perovskites	114
4.18.	TEM micrographs and analysis; (a) CAO image, (b) SAED of CAO, (c) CARh $_{0.05}$ image, (d) particle size distribution in CARh $_{0.05}$, (e) CARh $_{0.1}$ image and (f) particle size distribution in CARh $_{0.1}$	114
4.19.	CH_4 conversion in SRM as function of temperature with variation of Rh in $\text{CeAl}_{1-x}\text{Rh}_x\text{O}_{3-\delta}$ compared with impregnated Rh catalyst	115
4.20.	Comparison of SRM activity of $\text{CeAl}_{0.95}\text{Rh}_{0.05}\text{O}_{3-\delta}$ with 2.5 wt% Rh impregnated CeAlO_3	116
4.21.	Changes in CH_4 conversion as a function of S/C ratios and temperatures in SRM over $\text{CeAl}_{0.95}\text{Rh}_{0.05}\text{O}_{3-\delta}$ catalyst	117
4.22.	Effect of sulfur on $\text{CeAl}_{0.95}\text{Rh}_{0.05}\text{O}_3$, Rh/ CeAlO_3 and	118

	CeAl _{0.8} Ni _{0.2} O ₃ catalysts during SRM reaction	
4.23.	Steam reforming of simulated biogas containing 11 ppm sulfur over CeAl _{0.95} Rh _{0.05} O ₃ catalyst	119
4.24.	Coke on Ni and various Rh spent catalysts during SRM of sulfur containing methane	120
4.25.	TEM images of spent catalysts (a) CeAl _{0.8} Ni _{0.2} O ₃ (b) Rh impregnated CeAlO ₃ , (c) CeAl _{0.95} Rh _{0.05} O _{3-δ} catalysts	121

Chapter 5

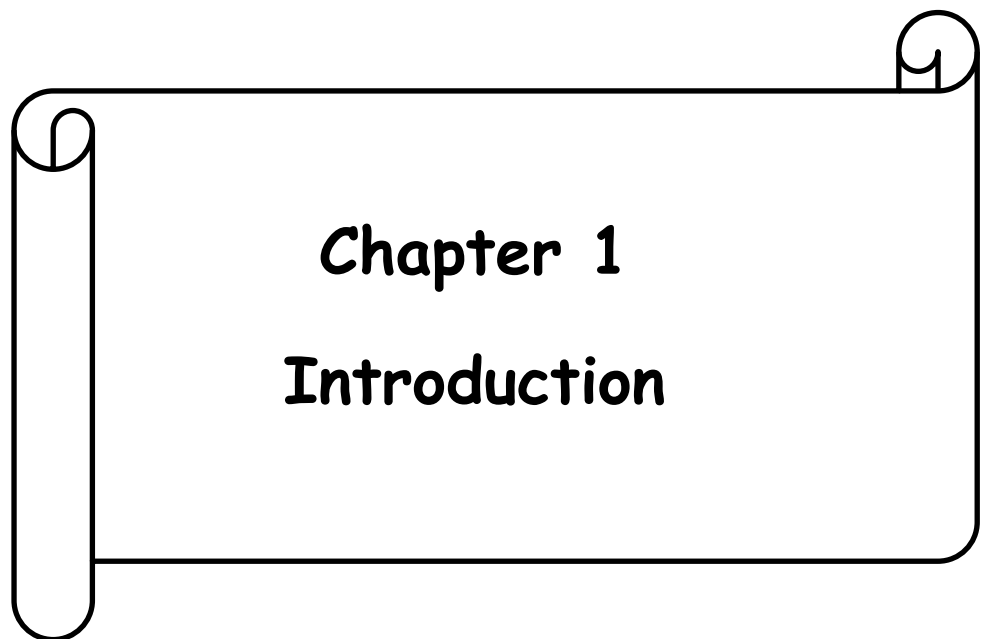
5.1.	XRD pattern of MZr _{1-x} Ni _x O _{3-δ} perovskites; (A) x = 0 and (B) x = 0.2; where M = (a) Ca, (b) Sr and (c) Ba	131
5.2.	Schematic presentation of MZr _{1-x} Ni _x O _{3-δ} perovskites	131
5.3.	Raman spectra of MZrO ₃ ; where M = (a) Ca, (b) Sr and (c) Ba	133
5.4.	Deconvoluted TPR profile of (a) CaZr _{0.8} Ni _{0.2} O _{3-δ} (b) SrZr _{0.8} Ni _{0.2} O _{3-δ} and (c) BaZr _{0.8} Ni _{0.2} O _{3-δ} perovskites	134
5.5.	TPD of (A) CO ₂ and (B) O ₂ profile of MZr _{0.8} Ni _{0.2} O _{3-δ} perovskites, where M= (a) Ca, (b) Sr and (c) Ba	135
5.6.	Influence of temperature over MZr _{0.8} Ni _{0.2} O _{3-δ} catalysts in DRM of methane; (A) CH ₄ conversion and (B) CO ₂ conversion; M= Ca, Sr and Ba	137
5.7.	DRM Catalytic activity with time on stream over MZr _{0.8} Ni _{0.2} O _{3-δ} perovskites; (A) CH ₄ conversion and (B) CO ₂ conversions	138
5.8.	DRM activity of CaZr _{0.8} Ni _{0.2} O _{3-δ} compared with impregnated 6% Ni/CaZrO ₃	139
5.9.	Effect of H ₂ /CO ratio as function of concentration of reactants (a) CH ₄ ; (b) CO ₂ and temperature in DRM reaction over CaZr _{0.8} Ni _{0.2} O _{3-δ} perovskites	140
5.10.	On stream stability study of CaZr _{0.8} Ni _{0.2} O _{3-δ} catalyst in DRM reaction	141
5.11.	MS signals from (A) CaZr _{0.8} Ni _{0.2} O _{3-δ} and (B) BaZr _{0.8} Ni _{0.2} O _{3-δ} catalysts during pulsing of CH ₄ followed by CO ₂	142

5.12.	Insitu FTIR spectra of various species present during the reaction between CH ₄ and CO ₂ over MZr _{0.8} Ni _{0.2} O _{3-δ} catalysts at different temperatures; (A) CaZr _{0.8} Ni _{0.2} O _{3-δ} and (B) BaZr _{0.8} Ni _{0.2} O _{3-δ}	143
5.13.	Deconvoluted FTIR spectra of MZr _{0.8} Ni _{0.2} O _{3-δ} perovskite under DRM conditions at 400 °C	145
5.14.	Bi-reforming reaction over CaZr _{0.8} Ni _{0.2} O _{3-δ} perovskite catalyst	148
5.15.	Variation of H ₂ O/CH ₄ ratio over the CaZr _{1-x} Ni _x O _{3-δ} for Bi-reforming reaction	149
5.16.	Spent XRD of (A) MZr _{0.8} Ni _{0.2} O _{3-δ} (where M = (a) Ca, (b) Sr and (c) Ba) and (B) CaZr _{0.8} Ni _{0.2} O _{3-δ} catalysts before and after DRM reaction for different TOS	150
5.17.	Coke estimated (moles of C.g ⁻¹ .h ⁻¹) after DRM using TGA analysis	151
5.18.	TEM images of spent catalysts (a) CaZr _{0.8} Ni _{0.2} O _{3-δ} , (b) SrZr _{0.8} Ni _{0.2} O _{3-δ} , (c) BaZr _{0.8} Ni _{0.2} O _{3-δ} .	152
5.19.	(A) C1s XPS and (B) O1s XPS spectra of spent MZr _{0.8} Ni _{0.2} O _{3-δ} perovskites after 12 h of TOS study, where M= (a) Ca, (b) Sr and (c) Ba	153
5.20.	Raman spectra of spent (A) MZr _{0.8} Ni _{0.2} O _{3-δ} perovskites after 12 h of TOS study, where M= (a) Ca, (b) Sr and (c) Ba ; (B) spent CaZr _{0.8} Ni _{0.2} O _{3-δ} after different hours of reaction	155

List of Abbreviations

FT	Fischer Tropsch
GHG	Green house gases
SRM	Steam reforming of methane
DRM	Dry reforming of methane
POM	Partial oxidation of methane
ATR	Auto thermal reforming
BRM	Bi-reforming of methane
TRM	Tri-reforming of methane
PSA	Pressure swing absorption
WGS	Water gas shift reaction
MD	Methane decomposition
BD	Boudouard reaction
RWGS	Reverse water gas shift reaction
SPARG	Sulfur-passivated reforming
MWCNT	Multi walled carbon nanotube
Ln	Lanthanides
RE	Rare earth
JCPDS	Joint committee on powder diffraction standards
CH ₄	Methane
CO ₂	Carbon dioxide
CO	Carbon monoxide

H ₂ O	Water
H ₂	Hydrogen
GHSV	Gas hourly space velocity
MFC	Mass flow controller
GC	Gas chromatography
GTL	Gas to liquid
GSAS	General Structure Analysis System
TOS	Time on stream
OSC	Oxygen storage capacity
SMSI	Strong metal support interaction
XRD	X-ray diffraction
TPR	Temperature programmed reduction
TPO	Temperature programmed oxidation
TPD	Temperature programmed desorption
TGA	Thermogravimetric analysis
TCD	Thermal conductivity detector
HRTEM	High resolution transmission electron spectroscopy
FTIR	Fourier transform infrared spectroscopy
XPS	X-ray photo electron spectroscopy
BET	Brunauer -Emmett -Teller
LRS	Laser raman spectroscopy
ICP-OES	Inductively coupled plasma-optical emission spectrometry



1.1. Introduction to catalysis

Catalysis plays an important role in the industrial development of a nation, particularly in the manufacturing of chemicals, pharmaceuticals and motor fuels. Catalysis also helps in environment protection in the form of auto exhaust gas treatment and in the destruction of chemicals that are harmful to the environment. Thus, catalysis not only helps in the economic development of a nation, but also plays vital role in the wellbeing of people. In 21st century, >80% of chemical processes depend on the use of catalysts in one way or the other. In fact, during the last few decades, catalysis has paid immense role in petroleum and petrochemical processes. In recent times, catalysis also started playing an important role in the conversion of renewable biomass to valuable chemicals and fuels. To be able to play a role in all above processes, a catalyst has to be robust and multi-functional. Multi-functional catalysts can transform a given substrate to desired product in few steps.

To design a catalyst for a particular reaction, one should have understanding of the characteristics of chosen catalyst material and its plausible role in the chosen reaction. This exercise will be helpful in understanding the governing principles of the process in order to design an appropriate catalyst.^[1] Figure 1.1 shows the triangular relationship between the reactivity and characteristics of the material synthesized.

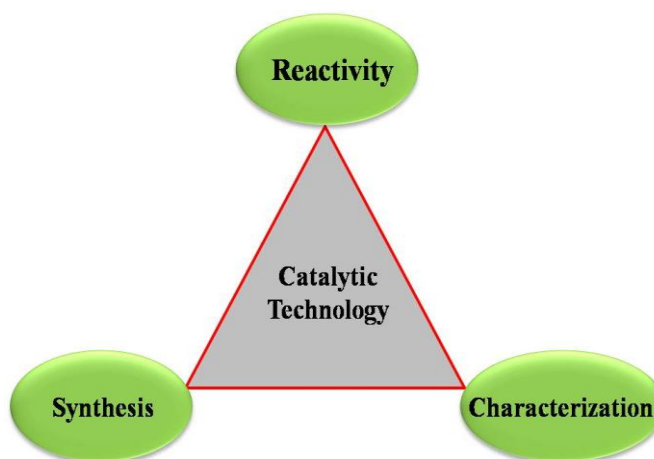


Fig. 1.1 Interconnectivity between synthesis, characterization and reactivity of a catalyst material

The above triangle shows how synthesis is correlated to the characterization of the material and reactivity. It also emphasizes on how reactivity depends on both synthesis route and the characteristic of the material obtained. Above correlation is essential to predict a suitable catalyst for the given catalytic transformation.

Though considerable progress has been achieved in terms of new catalysts and processes, there are still challenges in achieving higher efficiencies and environmental acceptability of certain catalytic processes. Some of the challenges related to the conversion of fossil feedstocks to usable fuels are included in Table. 1.1.

Table. 1.1 Catalytic challenges in the conversion of fossil fuels to usable fuels.

Fossil fuel	Function	Challenges in catalysis	Basic science challenges
Natural gas and Oil	Utilization	FT, Gas to liquid process, Low cost syngas production, Low pressure methanol synthesis	C-H bond activation. Selective production of desired hydrocarbons.
	Environmental clean up	CO ₂ , NO _x reduction	CO ₂ , NO _x reduction chemistry
Coal	Utilization	Gasification	C-C bond activation at low temperatures
	Clean up	CO ₂ , NO _x reduction, S and particulates	CO ₂ , NO _x reduction chemistry

1.2. Natural gas

Natural gas is an important energy source, its utilization is growing at a rapid rate. A two fold increase in its consumption, i.e. 120 to 203 trillion cubic feet (Tcf), is expected by 2040 from 2012 level, as estimated by International energy outlook IEO 2016. Natural gas mostly consists of methane and other lower hydrocarbons, minor percent of CO₂, N₂ and H₂S. This forms below the surface of the earth on decomposition of plant and animal matter, over millions of years. Natural gas is a key fuel in industrial as well as power sector, as it has high energy content and it burns cleaner than coal and petroleum products.

Consumption of natural gas is highest in China and USA followed by India with 5.3% global share in the year 2015. To reduce and cap carbon dioxide (CO₂) emissions, Government of India has started implementing national and regional plans since 2004. The use of natural gas is being encouraged to displace more carbon-intensive coal and liquid fuels.

1.3. Current status of CO₂

In the earth atmosphere, CO₂ is an integral part of the biogenic carbon cycle, in which carbon is exchanged between biosphere, ocean, soil and rocks. Industrial revolution led to 40% rise in CO₂ concentration on earth. It has increased from 280 to nearly 400 ppm by the end of 2017. Present concentration of CO₂ is the highest in the past 20 million years. It is mainly caused due to deforestation, burning of fossil fuels and from anthropogenic sources. The CO₂ level in atmosphere is continuously increasing and has reached dangerous level reportedly causing global warming. Recent estimates show that the accumulation of greenhouse gases (GHG's) has pushed earth's surface temperature by >1.0 °C since 1880. If it reaches 450 ppm level, global temperature is expected to increase by ~2 °C. Therefore, 195 nations have pledged together to reduce the emission of greenhouse gases through Paris agreement; held in December, 2016. Figure 1.2 (a) and (b) represent current CO₂ level and global increase in temperature during 1958 to 2017.

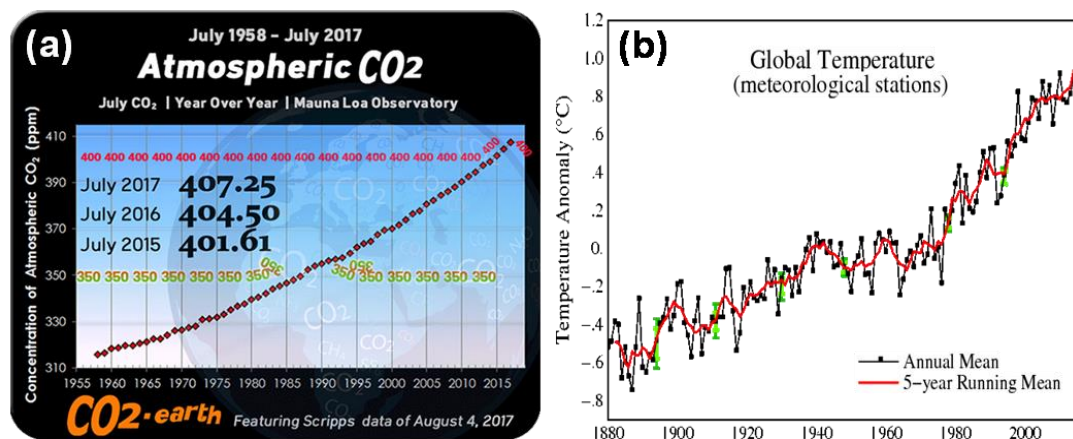


Fig. 1.2 (a) Increase in CO₂ concentration over the years and (b) Change in global mean temperature during the period.^[2]

1.4. Bio gas

Biogas is produced through anaerobic decomposition of organic matter. The organic matter could be agricultural waste, food waste, municipal waste and industrial waste. Biogas mainly consists of CH₄, CO₂ and minor contents of H₂S, NH₃ and water. The composition of biogas released from a digester depends on the type of substrate used and feed rate of the digester (Table. 1.2). As it mostly contains methane, it can be considered as a renewable fuel.

Table. 1.2 Typical composition of bio-gas.

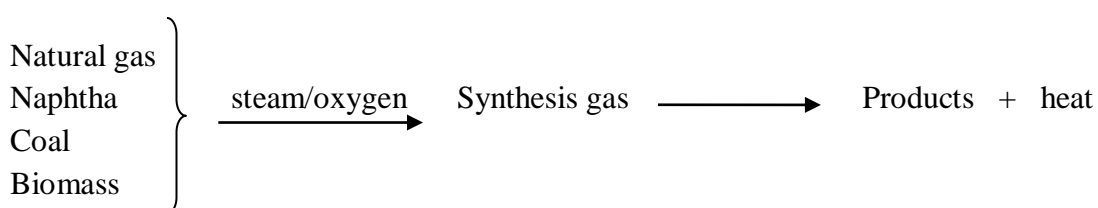
Components in (vol%)	Household waste	Wastewater treatment plants sludge	Agricultural wastes	Waste of agri-food industry
CH ₄	50-60	60-75	60-75	68
CO ₂	34-38	19-33	19-33	26
N ₂	5-0	1-0	1-0	-
O ₂	1-0	< 0,5	< 0,5	-
H ₂ O	0-6	0-6	0-6	0-6
H ₂ S (mg/m ³)	100 – 900	1000 - 4000	3000 – 10 000	400
NH ₃ (mg/m ³)	-	-	50 - 100	-

Biogas can be compressed and used (as compressed natural gas, CNG) in motor vehicles. It can also be used in heat engines, which can convert energy of gas to electricity. Utilization of biogas in the form of energy will help to reduce the utilization of fossil fuels like coal, natural gas and oil.

1.5. Synthesis gas

1.5.1. Historical review

Synthesis gas (syngas) is a mixture of H₂, CO and CO₂. Syngas plays a major role in energy in conversion. It is an input for selective chemical synthesis, fuels and is an important source for H₂ and CO. Syngas can be produced through steam reforming of hydrocarbons like natural gas, coal, oil products and biomass.



The products formed from syngas generate heat which can be utilized for operation of the plant. Production of fuels like Fischer-Tropsch (FT) products and methanol using syngas involve minimal environmental pollutants such as fine air born particles associated with coal, heavy metals and sulphur compounds. In general syngas is produced by standard reforming process like steam reforming of methane, auto thermal reforming, partial oxidation and dry reforming of methane. Mittasch and coworkers filed first patent in 1912 on supported nickel catalysts for steam reforming

of methane.^[3] In 1930 first tubular reformer was installed at Baton Rouge by standard oil of New Jersey.^[4] In 1962 ICI introduced two tubular reformer reactors operating at 15 bar.

1.5.2. Syngas production from hydrocarbons

Current production of syngas from fossil fuels such as coal, oil and natural gas are commercially and technically well developed. Compared to other fossil fuels natural gas is the most environment friendly and clean fuel for this purpose. Though natural gas is a non-renewable fossil resource, its availability, easy storage and transportation makes it a good energy carrier. The composition of natural gas varies from source to source, though its principal component is mostly CH₄. Though CH₄

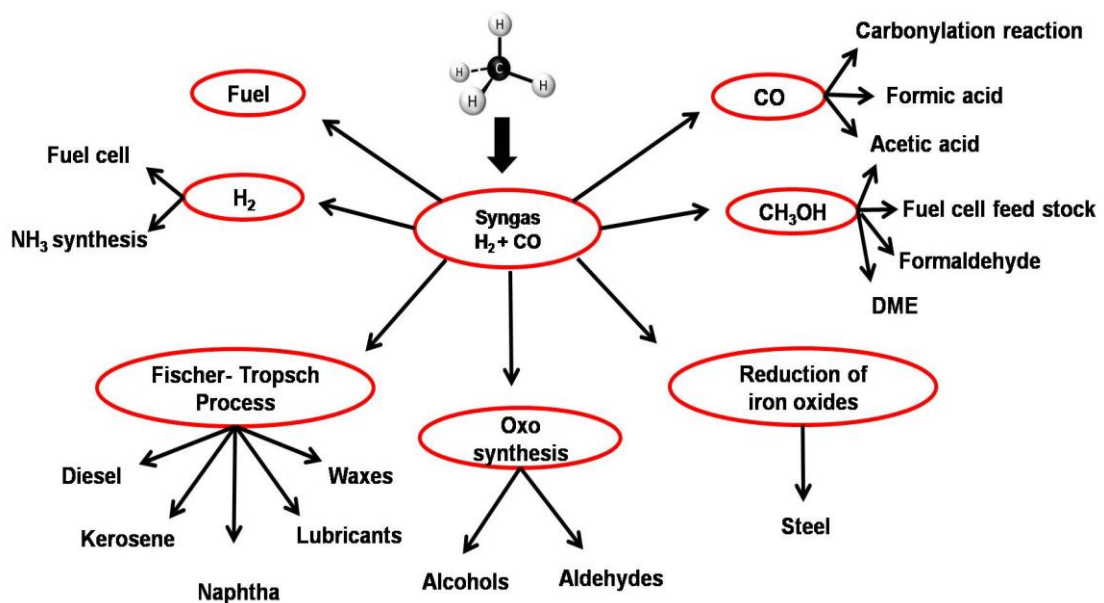


Fig. 1.3 Various routes for the production of chemicals from syngas.^[5]

could play a significant role as a carbon source in the supply of fuels and fuel-based chemicals in this century, it is a major GHG contributor leading to the global warming (~4-9% of GHGs).

It is an academic challenge to avoid the syngas step by direct conversion of CH₄ to useful chemicals. But the yields obtained are very less as compared to the established process and is not economical.^[6,7] In case of methane, C-H bond dissociation energy is 439 kJ/mol, hence it is more stable and resistant to many reactants.



Above reaction is more feasible when Q is oxidizing agent like oxygen. Direct conversion of methane to higher hydrocarbons without assistance of oxygen is not favored by thermodynamics. Indirect conversion route via syngas is more efficient than the direct routes. For example, conversion of natural gas to methanol through syngas is having 99.9% of selectivity and above 95% carbon efficiency. But it requires large energy recovery and exchange units^[8] as illustrated in Fig. 1.4. In fact, the cost of syngas production for converting natural gas to GTL fuels can be more than 60% of the overall cost. Hence, reduction in the cost of production of syngas would play a significant role in the economics of the gas to liquid technology.^[9,10]

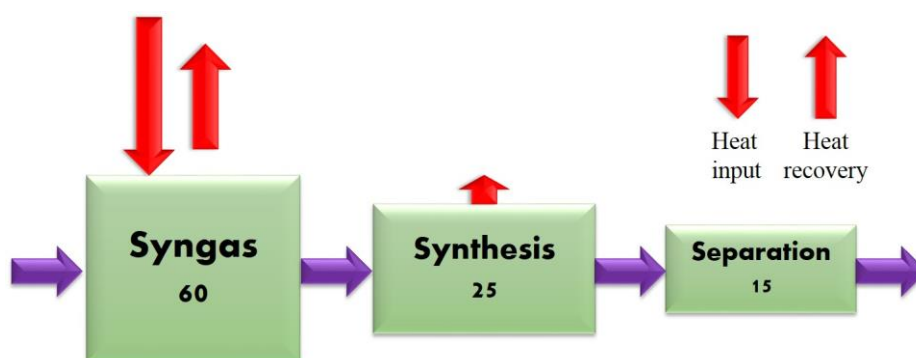


Fig. 1.4 Indirect conversion of natural gas to useful products and their relative investment.

Recently, there has been more focus on optimizing syngas production process and exploring new ideas in production of desired products. The desired product stoichiometry and scale of operation influenced by choice of operation.

- A. Steam reforming of CH₄ (SRM)
- B. CO₂ reforming or Dry reforming of CH₄ (DRM)
- C. Partial oxidation of CH₄ (POM)
- D. Autothermal reforming of CH₄ (ATR)
- E. Bi-reforming or combined reforming of CH₄ (BRM)
- F. Tri-reforming of methane (TRM)

Among all the processes; SRM, POM and ATR process are well established in industrial scale and remaining innovative processes are being improved in terms of energy efficiency and reduction in greenhouse gas emissions. The ratio of H₂/CO in syngas can be varied by employing different processes. The ratios of H₂/CO obtained by various reforming processes are shown in below Fig. 1.5.^[11]

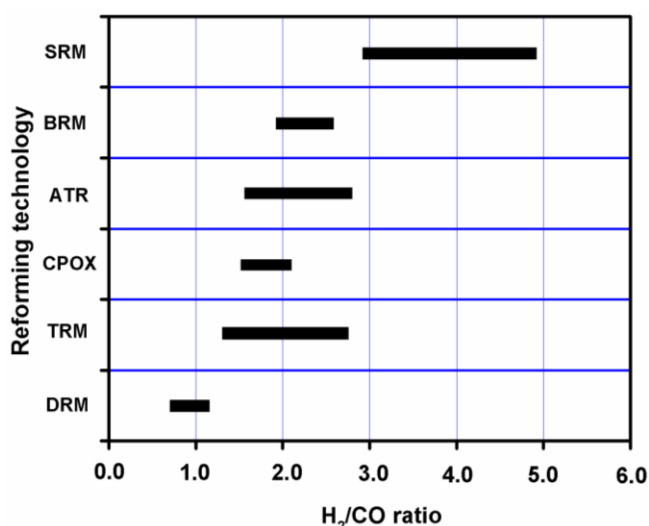
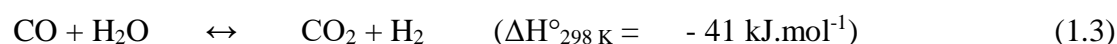
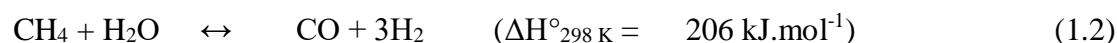


Fig. 1.5 Syngas variation in different reforming technology.

1.6. Steam reforming of CH₄

Steam reforming is the reaction between steam and methane converted to a mixture of H₂, CO and CO₂. It is an important industrial process to produce syngas or hydrogen. In this reaction, product reformat contains H₂ to CO in the ratio of 3, which is more suitable for H₂ production. Along with SRM (eq. 1.2) reaction several other reactions also occur like WGS reaction (eq. 1.3).



Steam reforming reaction is an endothermic process and there is an increase in product molecules compared to reactants; hence as per Le Chatelier principle, higher CH₄ conversion can be achieved at high temperature, low pressure and high steam to carbon ratios. Meeting these parameters require high capital cost, thus making the process quite expensive. The steam reforming term should not be confused with catalytic reforming which is used for paraffinic hydrocarbons like iso-alkanes and aromatics converted to higher octane hydrocarbons.

Conventional steam reforming process for production of H₂ or syngas consists of several reaction units such as pretreatment unit, high temperature reformer unit, high and low temperature water gas shift reactors followed by separation units like pressure swing adsorption (PSA) as shown in Fig. 1.6. This process is implemented in a multi-tubular fixed bed reactor in the presence of metal/metal oxide catalyst.^[12]

Though the SRM is having high efficiency and H₂ concentration, start up time is typically long. It is also limited by several factors: (a) Heat transfer ^[13] (b) Thermodynamic equilibrium ^[14,15] (c) Environmental pollution like CO₂ and NO_x emissions ^[16] (d) Catalyst deactivation due to carbon formation and sintering. ^[17,18] In recent years, to overcome thermodynamic limitations, research has been devoted to use catalytic membrane reactors.

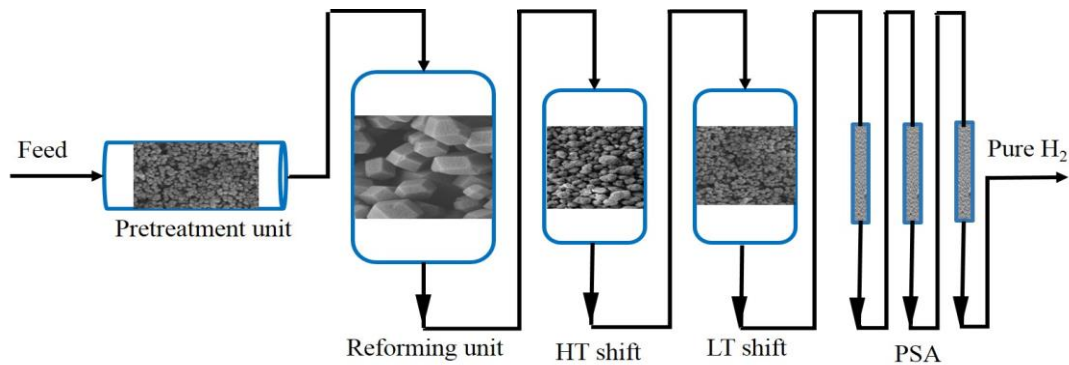


Fig. 1.6 Conventional SR reaction scheme

1.6.1. Thermodynamics of steam reforming reaction

1.6.1.1. Thermodynamic function of SRM

The steam reforming reaction involves two stable molecules methane and water, yielding H₂ and CO, while being highly endothermic. Figure 1.7 shows variation of thermodynamic parameters as a function of temperature in SRM reaction. It shows that enthalpy and entropy are positive and increase as a function of temperature. It implies that high external heat is necessary for the conversion of reactants to desired products. Above graph indicates that SRM is entropy driven.

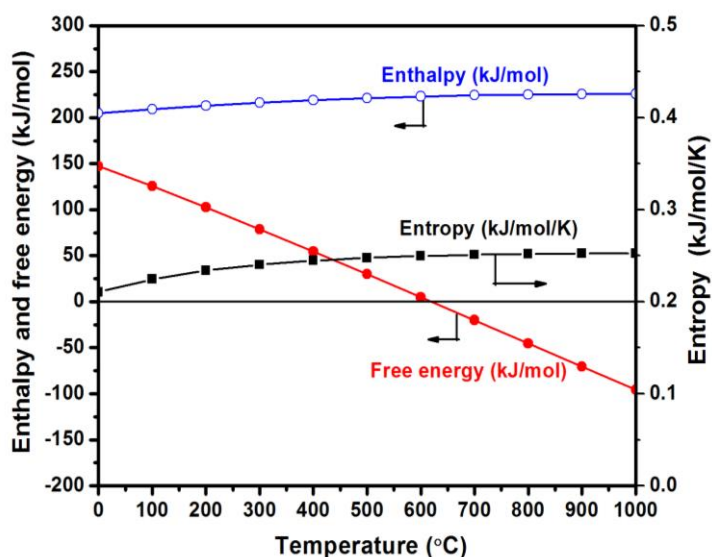


Fig.1.7 Variation of thermodynamic parameters against temperature in SRM.

Free energy of reaction decreases with temperature due to increase in $T\Delta S$ leading to more favorable equilibrium.

$$\Delta S^\circ > 0 ; \Delta H^\circ > 0 ; T\Delta S^\circ > \Delta H^\circ$$

$$\Delta G^\circ = \Delta H^\circ - T\Delta S^\circ < 0$$

1.6.1.2. Thermodynamic equilibrium of reactant and product distribution

In steam reforming, combination of two reactions, i.e., equations 1.2 and 1.3, being endothermic is favoured at high temperatures.



These reactions are reversible and after reaction, volume expansion occurs, hence low pressure is favored for high conversion of methane. Additionally, equation 1.3 is favored at low temperature and is not affected by pressure. Reforming reaction is normally carried out on nickel supported catalyst at high temperatures above 550 °C. Methane molecule dissociates on nickel surface forming CH_x species. The resulting CH_x species reacts with OH, which is present on the support/metal. ^[19]

The product gas composition is governed by the temperature and pressure of the reactor, reactant feed composition, particularly steam/carbon ratio. The product gas contains H_2 , CO_2 , CO, un-reacted CH_4 and steam as shown in Fig. 1.8.

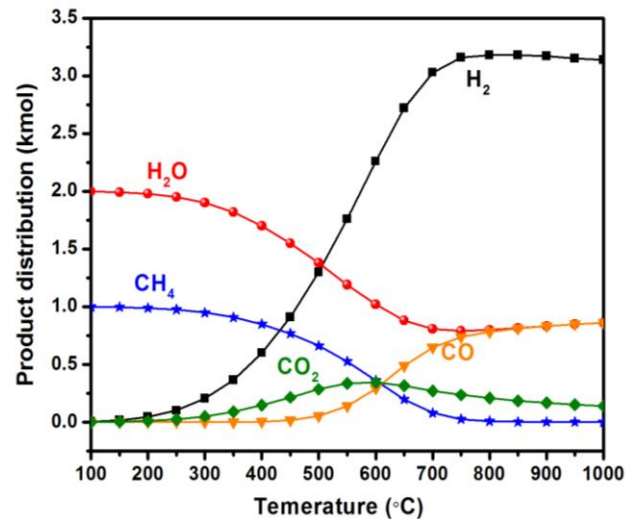


Fig. 1.8 Thermodynamic calculations of SRM at Steam/Carbon=2

Increase in temperature leads to higher CO in reformat, due to prevalence of reverse water gas shift reaction (RWGS). Kinetics and thermodynamic studies can predict the amount of CO in the steam reformat. From thermodynamic point of view, WGS is favoured at low temperature (100-300 °C) and equilibrium drops at high temperatures. In SRM, at higher steam to carbon ratio, complete CH₄ conversion can be achieved. In general steam to carbon ratio is 3, to obtain high CH₄ conversion and CO, CO₂ selectivity. Figure 1.9 shows typical CH₄ conversion with variation of temperature, pressure and steam to carbon ratio. The theoretical results are in conjunction with the studies of Joensen and Rostrup-Nielsen. [20]

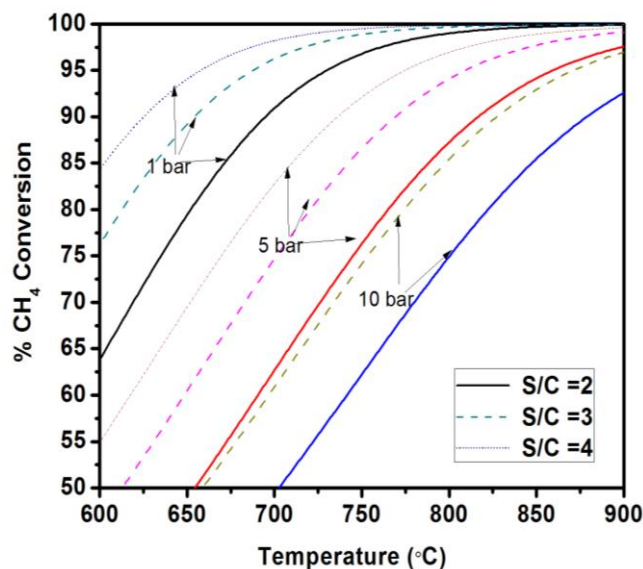


Fig. 1.9 Thermodynamic equilibrium conversions of methane in SRM.

From the graph it is observed that for high CH₄ conversions, SRM has to be operated at high T, lower P and relatively higher steam to carbon ratio.

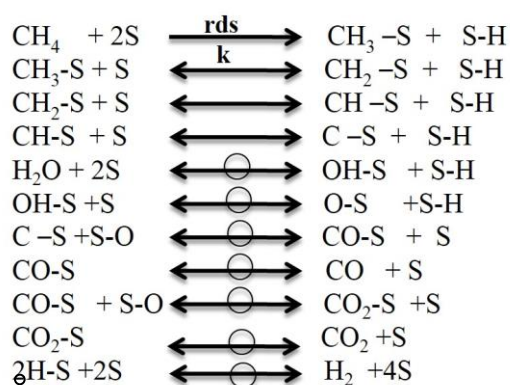
1.6.2. Reaction mechanism and kinetic study of SRM

Mechanism of steam reforming reaction mostly depends on the nature of active metal and the catalyst support. Many reports describe the kinetics of steam reforming of methane reaction (Table. 1.3).

Table 1.3. Different approaches for kinetics of steam reforming of hydrocarbons

Authors	Form of kinetics
Bodrov et al. [21]	Langmuir Hinshelwood
Rostrup-Nielsen [30]	Two-step kinetics power law
Khomenko et al. [25]	Temkin identity
Tøttrup [26]	Pellet kinetics
Aparicio [27]	Microkinetic analysis
Chen et al. [28,29]	Microkinetic model
Xu and Froment [24]	Langmuir Hinshelwood

Xu and Froment [24] have extensively studied the intrinsic kinetics of SMR and water gas shift (WGS) on Ni/MgAl₂O₄ spinel catalyst. Their model was based on Langmuir Hinshelwood reaction mechanism. It did not explain methane dissociation as it does not explain adsorbed precursor. [22] Wei and Iglesia [23] investigated the steam and dry reforming reaction mechanism over the Rh clusters. According to them, the rate of the reaction is proportional to the CH₄ partial pressure and independent of CO₂ and H₂O pressures. Their data indicates the kinetic relevance of C-H activation step which is a rate determining step. All other steps like activation of co-reactants (CO₂ and H₂O) and their coupling with chemisorbed carbon intermediates is fast. They found that reaction between H atoms and OH is quasi equilibrated steps (\leftrightarrow). The WGS is also at equilibrium. The CH₄ activation in reforming reaction is described below:



Scheme. 1.1 Reaction pathways for CH₄ activation in reforming reaction.

where 'S' is the most abundant surface intermediate. From above mechanism in the rate expression only $\text{CH}_4 + 2\text{S} \rightarrow \text{CH}_3\text{-S} + \text{H-S}$ reaction rate constant is involved. The overall rate of the reaction depends on the CH_4 concentration and is independent of the $\text{H}_2\text{O}/\text{CO}_2$ concentration.

$$\text{Rate} = k P_{\text{CH}_4} \quad (1.5)$$

Most of the experimentalists and theoreticians have accepted this model. The reaction mechanism of SR reaction also depends on the nature of the catalyst including active support. Section 1.13 addresses the role of active support and active metal of the research interest for reforming type catalyst in general.

1.6.3. Advantages of steam reforming of CH_4

1. Higher H_2 production due to better selectivity
2. No air separation unit for oxygen is required.
3. Heat required for reforming reaction can be externally supplied by combustion of low quality fuel.
4. Excess steam can be easily recovered and it doesn't change volumetric flow to downstream units.
5. Most extensively used by industry.

1.6.4. Disadvantages of SRM process

1. Carbon or coke formation during SRM reaction is more.
2. It is more costly to build a SRM reactor in addition to its complexity.
3. Heat need to be transferred externally.
3. Methane concentration should be high in the reactant; presence of higher alkanes is detrimental to catalyst life.
4. Due to operation at high temperatures, active metal sintering is widespread.

Economic constraints of SRM led to development of alternative process like dry reforming of methane (DRM), partial oxidation (POX) and auto thermal reforming of methane (ATR) for conversion of CH_4 to syngas.

1.7. Dry reforming of CH_4

In recent years, much attention is devoted to global warming attributed to greenhouse gas emissions like CO_2 and CH_4 . Replacing steam with CO_2 during

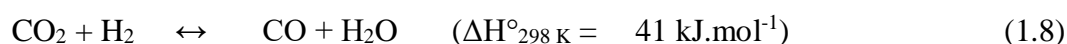
reforming reaction is called CO₂ or dry reforming of methane (DRM). This reaction was first reported by Fischer and Tropsch over Ni/Co catalysts. They observed high carbon formation on the catalyst surface leading to its deactivation.^[31] Reitmeier et al. analyzed relationship between reactant composition and carbon formation which helped in the identification of deactivation mechanism in steam/CO₂ reforming of hydrocarbons.^[32] Rostrup-Nielsen studied reforming of methane and higher hydrocarbons over Al and Mg spinel catalysts in 1964. They have identified Mg as a promoter for activation of CO₂, which was effective in the removal of carbon from active metal surface.^[33] In DRM reaction, for every CO₂ to CH₄ ratio there is optimum temperature range where carbon formation occurs as reported by Gadalla et al. in 1988. They used Ni/Al₂O₃ catalyst for DRM reaction and described the relationship between CO₂ to CH₄ ratio and carbon formation.^[34,35] After 1990, there were extensive reports on utilization of these two major greenhouse gases responsible for global warming. The DRM reaction requires slightly more energy than SRM as may be seen from equation 1.3. In DRM the syngas obtained has H₂/CO ratio close to 1 and requires an active and durable catalyst. The FT process requires H₂ : CO ratio close to 2, while syngas with H₂ to CO ratio nearly 1 is more suitable for synthesis of long chain hydrocarbons.^[36-43]



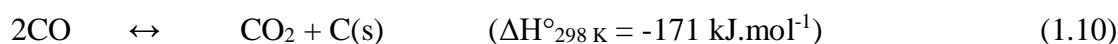
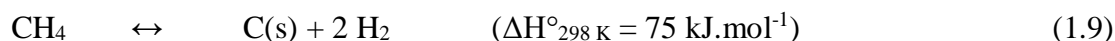
1.7.1. Thermodynamics of DRM

1.7.1.1. Effect of temperature on DRM, MD, BR and RWGS reactions

Thermodynamic analysis helps to develop suitable strategies and obtain desired product from chemical reaction. Thermodynamics relates the macroscopic variables such as temperature, pressure, enthalpy, entropy and heat. Equation 1.6 shows that dry reforming reaction is extremely endothermic and operates in 1000-1273 K temperature range at 1 bar pressure to achieve high equilibrium conversion, while product syngas contains H₂ and CO in the ratio of 1:1. But along with this reaction there is simultaneous occurrence of reverse water gas shift reaction (RWGS), leading to a reduction in H₂ to CO ratio to < 1.^[37, 44]



Apart from RWGS, other possible side reactions are; (i) methane decomposition (MD, eq. 9), where CH_4 dissociates to form solid carbon and H_2 , (ii) Boudouard reaction (BR, where CO disproportionates to form CO_2 and carbon (eq. 10). These later two reactions are responsible for coke formation leading to catalyst deactivation.



Using Gibbs free energy minimization method, lower carbon formation conditions during DRM reaction can be determined. [45]

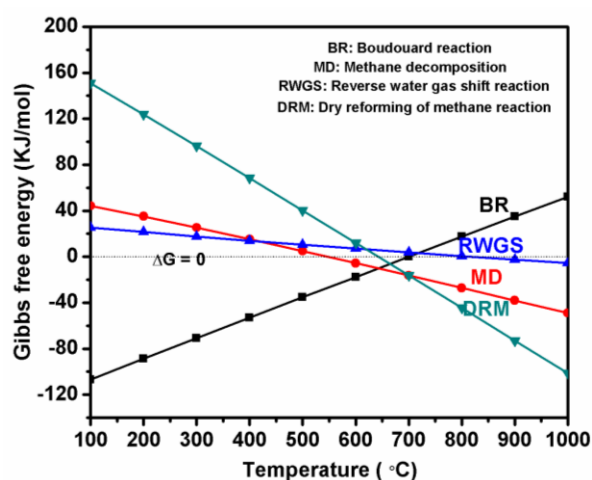


Fig. 1.10 Effect of temperature on DRM, MD, BR and RWGS as predicted by HSC Chemistry software at 1 bar pressure.

Figure 1.10 shows that at higher temperatures, DRM and CH_4 decomposition reactions are more favorable. However RWGS also increases slowly with raising temperature, while Boudouard reaction is favored at lower temperatures. Increasing CO_2 content in the reactant feed suppress the carbon deposition. [46] It has been observed that water and CO are formed through the RWGS reaction. Therefore, as the amount of CO in the system increases, the tendency of coke deposition by CO disproportionation becomes more favorable.

1.7.1.2. Thermodynamic equilibrium of reactant and product distribution

The thermodynamic equilibrium plots of DRM product distribution as a function of temperature at 1 atm pressure is shown in Fig. 1.11a. These plots are generated by Gibbs free energy minimization algorithm using HSC chemistry 5.11

programme. The results show that gaseous CH₄ and CO₂ conversions increase with raise in temperature to form H₂, CO and H₂O as products. After 400 °C, the H₂/CO ratio is in between 0.8-1 and formation of H₂O was observed through RWGS reaction.^[46]

Similar kind of thermodynamic calculations were done in the presence of solid phase carbon to accommodate for methane decomposition and Boudouard reaction. It is shown entirely different equilibrium composition. It is seen from Fig. 11b that below 900 °C the H₂/CO ratio is greater than unity because of lower CO formation as well as high amount of carbon formation. These equilibrium calculations show that formation of C(s) is unavoidable below 900 °C. Above 900 °C the H₂/CO ratio approaches unity.^[47]

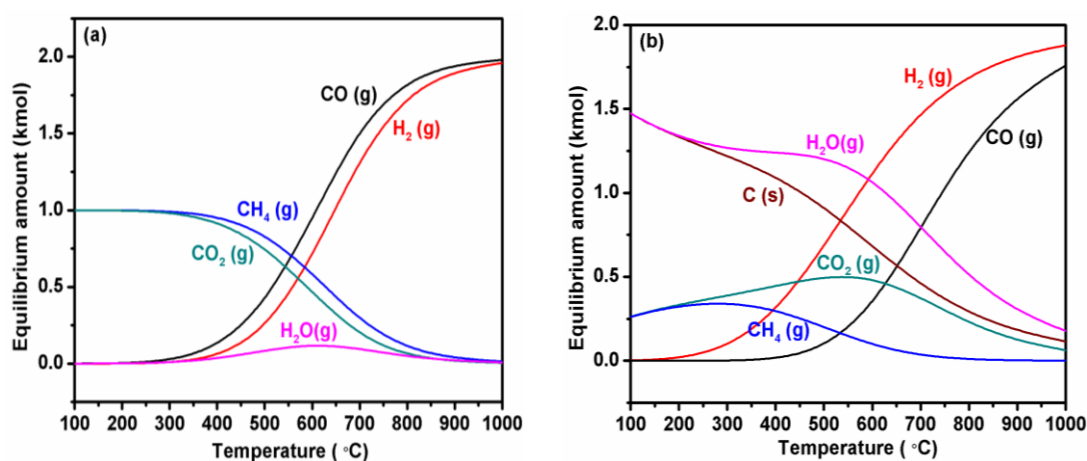
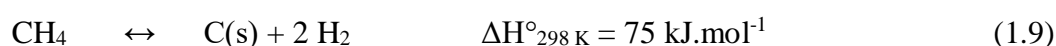


Fig. 1.11 Equilibrium concentration of reactants and products at different temperatures as predicted by HSC chemistry software assuming CH₄ / CO₂ = 1 at 1 bar pressure where (a) without carbon and (b) with carbon deposition.

1.7.2. Carbon formation reactions

During reforming reactions, some side reactions are mostly responsible for coke formation. Carbon formation may result in breaking down of the catalyst, leading to pressure drop across the catalyst. This can lead to hot spots as a result of uneven flow distribution. In reforming, mainly two reactions, (i) methane decomposition and (ii) Boudouard reaction are responsible for carbon formation.

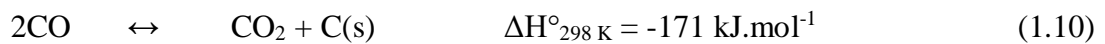
1.7.2.1. Methane decomposition (MD)



The direct decomposition of CH₄ to produce H₂ and solid carbon is called CH₄ cracking. Depending on the operating conditions, carbon is formed in various forms such as amorphous, filamentous, graphitic and as carbon nanotubes. These reactions are endothermic; hence CH₄ decomposition can occur, on supplying external heat even in the absence of any catalysts with a reasonable yield at high temperatures. However, in the presence of catalysts, CH₄ cracking can occur at lower temperatures. Rostrup-Nielsen and Bartholomew et al. have suggested up to five types of carbon formation during CH₄ cracking, viz., vermicular filament, fibres and/or whiskers (C_v), adsorbed atomic (C_α), amorphous or polymeric (C_β), crystalline or graphitic (C_c) and bulk metal carbide (C_γ).^[17, 30]

1.7.2.2. Boudouard reaction (BR)

The CO disproportionation that produces solid carbon and CO₂ is called Boudouard reaction.



It is an exothermic reaction, hence preferably takes place at temperatures lower than 650 °C. DRM reaction operates at high temperature, hence in this case CO disproportionation reaction mostly limited under thermodynamic equilibrium. Moreover, the presence of high CO₂ concentrations is expected to retard its influence to negligible amounts. Also, quick removal of CO from the system should assist in reducing the effect of this side reaction.

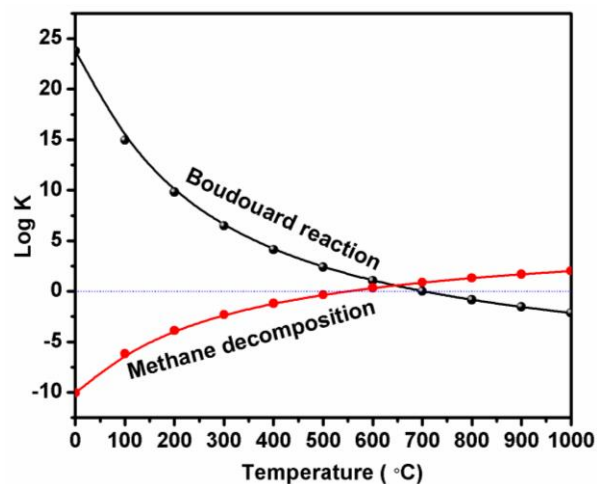


Fig. 1.12 Thermodynamic equilibrium plots of MD and BR reactions.

Figure 1.12 shows variation of equilibrium constant of CH₄ decomposition and CO disproportionation as a function of temperature. It shows that increase in reaction temperature increases CH₄ decomposition, while CO disproportionation reaction decreases. The adsorbed hydrocarbon dissociation or CO disproportionation on the metal yields formation of carbon atoms which dissolve within the metal particle and migrate through the particle to nucleate into the whiskers or filament at metal to support interfaces. Investigation for the type of carbon deposited on the Ni catalyst indicated the presence of α -carbon at about 200 °C, β -carbon or carbon film at about 400 °C and filamentous (δ) carbon at about 580 °C.^[52] Alternatively, it may dissolve into the bulk to create fibre and/or whisker-like or vermicular carbon (C_v).

1.7.3. Thermodynamic equilibrium of coke formation in reforming

From thermodynamic point of view, coke deposition is an important factor along with conversion and H₂/CO ratio for performing coke free reaction for long duration. At high temperatures and pressures, CH₄ cracking leads to coke formation is most likely to occur, while at low temperatures, Boudouard reaction is dominant leading to the formation of carbon and CO₂.^[17] Along with temperature and pressure, feed composition also influences the carbon formation. At higher H₂O/CH₄ and CO₂/CH₄ ratios of reaction feed, coke deposition can be suppressed to achieve steady and high equilibrium conversion. But in practice this leads to cost escalation as a result of loss of steam and re-cycling of unconverted CO₂.^[48]

Coke formation is expected to occur at values lower than minimum threshold ratios of H₂O/CH₄ and CO₂/CH₄ required at a given temperature. Rostrup-Nielsen et al.^[22,49,50] defined thermodynamic limits of carbon formation on various catalysts as given in Fig. 1.13. Based on this model, it is possible to predict coke formation for given operating conditions. The plot clearly shows that CO₂ reforming of methane (DRM) is more critical than SRM. Higher steam/carbon ratio in steam reforming reduces the risk of carbon deposition. For example, on Ni based catalysts A and B, coke formation is expected under certain operating conditions. Noble metal catalyst (catalyst C) and sulfur passivated (SPARG) catalyst (catalyst D)^[51,9] exist on left side of the carbon formation boundary showing lower carbon formation compared to Ni based (A and B) catalysts. This is because noble metals have smaller equilibrium constant for CH₄ cracking and Boudouard reactions. This model has been generated

on 250 nm Ni particle size supported catalyst, at around 25.5 bar pressure with simulation at various H_2O/CH_4 and CO_2/CH_4 ratios.

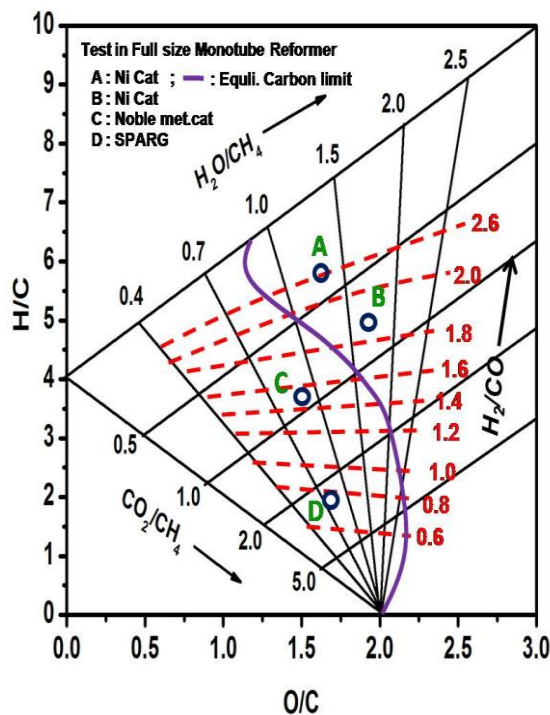


Fig. 1.13 Carbon formation at 25.5 bar pressure with variation in H_2O/CH_4 and CO_2/CH_4 ratios.^[22]

In general, catalyst deactivation occurs through coke formation, sintering and poisoning. Deactivation process that affects catalyst life will increase the cost of operation due to frequent catalyst regeneration, low productivity and loss of time.

1.7.4. Advantages of Dry (CO_2) reforming of CH_4

In DRM process, CO_2 is one of the feed. Since, some gas streams may contain high (~30%) volume of CO_2 , DRM could be a useful process.^[53-54] Biogas is an attractive renewable source as it may consist of 50–75% CH_4 , 25–50% CO_2 with rest being nitrogen, H_2S and moisture. Hence, it is more economical to utilize it for syngas production instead of using expensive separation methods for the recovery of CH_4 .^[55] In addition the DRM has the following advantages:

- ❖ Syngas from DRM reaction will have H_2/CO ratio close to 1, which is suitable for GTL process.^[56-58]
- ❖ CO_2 is inexpensive. Hence slightly lower operating cost as compared to the other reforming processes.^[59]

- ❖ DRM reaction utilizes two important greenhouse gases while yielding useful syngas.^[60]

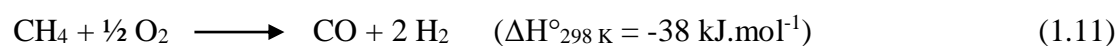
Based on the above considerations, DRM is a better alternative process compared to conventional SRM process for the production of synthesis gas.^[61]

1.7.5. Limitations of DRM process

In spite of many advantages of DRM, so far no durable catalyst and a process are available for commercial application of dry reforming, as a result of severe carbon formation on catalyst surface during the reaction. Hence, the main challenge is to develop a catalyst that shows high durability with less carbon formation along with high activity. Moreover, the given catalysts should have high mechanical strength and thermal stability, to withstand the severe conditions used during the DRM reaction. Catalysts also should be cheaper, like Ni based catalysts used in steam reforming, in addition to easy and inexpensive availability of reactant gases.

1.8. Partial oxidation of CH₄

Partial oxidation (POX) of natural gas is an alternate approach for steam reforming reaction to produce syngas to be utilized for ammonia synthesis. That is instead of steam, oxygen is added to the feed at high space velocities over solid catalyst. Catalytic partial oxidation of methane was first reported by Liander et al. in the year 1929.^[62] This process is more flexible and capable of handling many hydrocarbons like asphalt, waste plastic, in addition to natural gas. There are two types of partial oxidation processes; (i) catalytic partial oxidation and (ii) non-catalytic partial oxidation processes. The catalytic partial oxidation process can take place in presence of a catalyst at lower temperatures, wherein CH₄ reacts directly with oxygen to produce syngas with H₂/CO = 2 as given in eq.1.11.^[63]



The POX of methane is an exothermic process and thus appears to be more economically viable than SRM process. But, the reaction of CH₄ with oxygen is highly exothermic and it needs special precautions and care to avoid explosions.^[64] Hence, it is not popular considering various safety issues involved.

1.9. Auto thermal reforming of CH₄ (ATR)

In auto thermal reforming, natural gas reacts with steam and oxygen to give syngas. It is a combination of endothermic SR and exothermic POX. In general ATR operates at low steam to carbon ratios in the temperature range of 900-1150 °C and pressure in the range of 1-30 bar. Depending on downstream purification process, the oxidant can be air, enriched air or oxygen. Compared to steam reformer, ATR reactor is more compact, but larger than partial oxidation unit. Advantage of this reaction is it produces syngas with H₂/CO ratio 2, which is more suitable for downstream chemical synthesis like FT and methanol synthesis.^[65] At a particular composition of fuel, air and steam, no external heat is required. That is POX reaction supplies all the heat to drive the endothermic SR reaction.

The equilibrium composition of ATR reformat as a function of temperature is shown in Fig. 1.14. The graph is generated for S/C -1.5 and O/C- 0.7 at 1 bar pressure. It shows that CH₄ participation starts in steam reforming reaction at 400 °C onwards and reaches complete conversion above 700 °C. The H₂ concentration reaches maximum at 700 °C. Beyond this temperature, H₂/CO ratio decreases due to domination of reverse water gas shift reaction. Carbon formation is not expected in this reaction above 700 °C. Hence, in this reaction minimum carbon and soot formation occurs. Farrauto and Giroux et al. introduced auto thermal reforming based fuel processor for fuel cell applications.^[66,67]

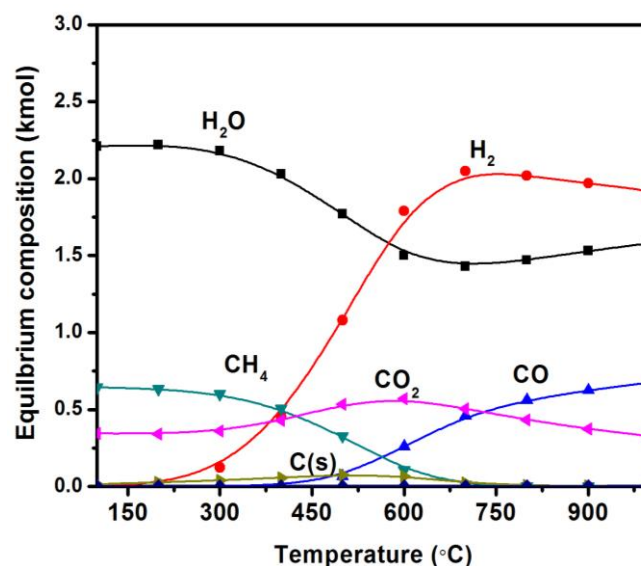
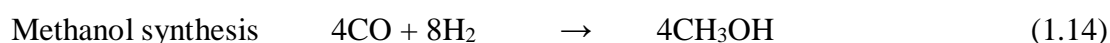
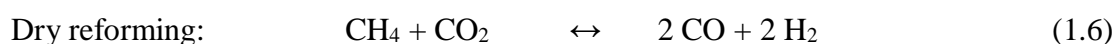
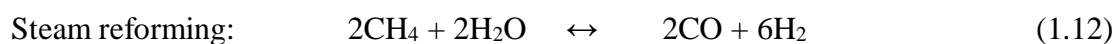


Fig. 1.14 Effect of operating temperature on reformat equilibrium compositions for ATR predicted by HSC chemistry 5.1 software assuming O/C = 0.7; S/C = 1.5 and 1 atm pressure.

Industrially syngas (H₂) production processes includes SR, POX and ATR of natural gas. Recently, bi- and tri-reforming processes have drawn major attention of researcher worldwide.^[68-70] These reactions are mostly proposed for syngas generation by utilizing flue gas which is coming from fossil fuel fired thermal power plants, bio gas from anaerobic digestion of biomass and land fill gas. Advantage of this process is that there is no need for costly CO₂ separation unit and the syngas composition can be tuned to suit various chemical synthesis (ammonia, methanol, dimethyl ether, FT) processes.^[71,72]

1.10. Bi-reforming or combined reforming of CH₄

Commercially, steam reforming of natural gas is well established for syngas/hydrogen production. On the otherhand, dry reforming process is not well developed, because of severe coking of catalysts resulting in their rapid deactivation. To avoid carbon formation, addition of steam or oxygen to the feed is a solution. Combining steam and CO₂ reforming reactions, which is called bi-reforming, is interesting to get syngas with desired H₂/CO ratio. In bi-reforming; CH₄, H₂O and CO₂ are fed in a desired ratio (3:2:1) to yield syngas with H₂/CO ratio 2, which is called ‘metgas.’ This gas mixture is suitable for the preparation of methanol, which subsequently can be used to derive hydrocarbons.^[73,74]



In bi-reforming, DRM operates simultaneously with SR leading to minimization of the carbon formation on the catalyst. The relative contribution of carbon formation reactions like CH₄ decomposition and CO disproportionation depends on reaction conditions and nature of the catalyst used. If carbon is formed, it is removed by steam.

In recent times, utilization of renewable sources like bio-gas is attracting attention of many researchers. Steam reforming of bio-gas is also one kind of bi-reforming reaction. Bio-gas is produced from anaerobic degradation of organic material such as agricultural wastage, municipal wastage, sewage waste, food waste and plant material. The composition of bio-gas depends on nature of raw material and anaerobic digestion process. Typically, the composition of bio gas is 50-75% CH₄,

25-50 % of CO₂ and 0-10 % N₂ and small amount of H₂S, moisture and siloxanes. Synthesis of met gas from bi-reforming of methane is also adaptable for reforming of shale gas. Dry shale gas mostly contains methane (>98%) and wet shale gas may have ethane, propane and higher hydrocarbons.



From thermodynamic point of view, combined steam and dry reforming reaction has a more complex reaction network where various reactions occur simultaneously such as SRM, DRM, WGS and Boudouard reactions. The reaction rate depends on feed composition and temperature range. The composition of resulting syngas can be tuned by adjusting CH₄/H₂O or CO₂/H₂O ratios (Fig. 1.15) in the reaction feed.^[75,76]

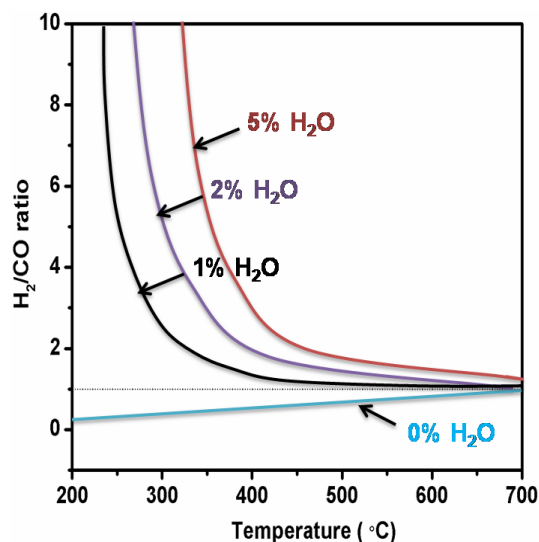


Fig. 1.15 Graph represents the thermodynamic equilibrium of H₂/CO ratio as function of temperature in 200-700 °C range and 1 atm pressure.

Feed compositions used for thermodynamic analysis is given in Table 1.4.^[77] Increased steam content in the bi-reforming favours more SRM and WGS reactions, which will influence H₂/CO ratio. With increasing steam content, H₂ yield increases with simultaneous decrease in CO yield, also helping in lowering the carbon formation on the catalyst surface. As a result, H₂/CO ratio increases as the SRM and WGS reactions are dominant. However, with increasing reaction temperature, DRM reaction also becomes dominant and H₂/CO ratio moves closer to one. On the other hand, the thermodynamic equilibrium can be altered by preferential removal of one of the product component (H₂) using selective membrane during the reaction.^[78]

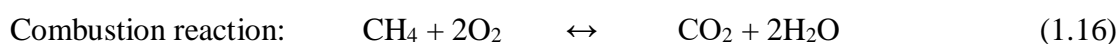
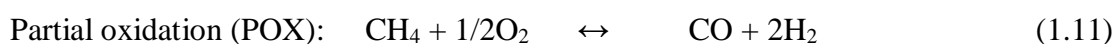
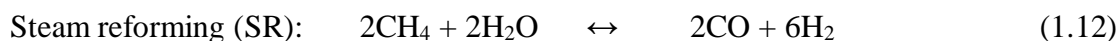
Table 1.4 Feed composition of bi-reforming reaction. ^[77]

CH ₄ (vol %)	CO ₂ (vol %)	H ₂ O (vol %)	He (vol %)
10	10	0	80
10	10	1	79
10	10	2	78
10	10	5	70

1.11. Tri-reforming of CH₄

Recently, concept of tri-reforming of CH₄ has been reported by Song and coworkers.^[71,79] It is a synergetic combination of endothermic SR (eq. 12), DR (eq. 6) and exothermic oxidation of methane (eq. 16). Hence, it is more important in terms of industrial and environmental perspective.^[80]

Tri-reforming of methane (equation, 1, 4 and 9) involves SR, DRM, POX and also CH₄ combustion to some extent;



Along with these reactions coke formation reaction also occur over the catalyst such as:



Combination of steam reforming, partial oxidation and dry reforming could dramatically minimize the carbon formation and enhance the catalyst life, in addition to increasing the efficiency of reforming process. Usually, fall in the activity of Ni-based catalysts is as a result of carbon formation, which can be overcome by adding an oxidizing agent (oxygen) to the reaction mixture (CH₄ + CO₂). Addition of oxygen removes the coke, thus slowing down its accumulation. However, in presence of O₂, steam and CO₂, the oxidation of metallic Ni can occur and lead to a decrease in

catalytic activity. This problem can be solved to some extent by modification of Ni catalysts by rare earth oxides CeO₂, La₂O₃ etc.^[81]

1.12. Sulfur poisoning during reforming

Poisoning of a catalyst can occur due to strong chemisorption of reactants, products or impurities present in the feed, on the active sites. It depends on the adsorption strength of the poison on the active site of the metal.^[82,83] Many poisons originate from feed streams in a catalytic process. For example crude oil has sulfur and some metals like V and Ni, which act as poison in a refinery process. These poisons may induce changes in the electronic and geometric structure of the catalyst, leading to its deactivation. Sulfur is a major poison in the conventional steam reforming reaction. Even if 5 ppm of sulfur is present in the feed, nickel catalysts are poisoned in steam reforming reaction conducted at 800 °C. At lower temperatures, this poisoning is severe, even the sulfur is only 0.01 ppm at 500 °C. Poisoning process, as given below is an exothermic adsorption process.



Somarjai et al. reported that under reforming conditions, sulfur changes surface structure of the Ni catalyst.^[84] The sulfur atoms strongly bind with fourfold and two fold Ni active sites with a maximum coverage. As a result, the methane conversion in steam reforming reaction is reduced. Noble metals such as Pt, Rh and Ir have less sulfur adsorption energy compared to Ni as given in Table. 1.5. Nickel has high sulfur adsorption energy, hence having strong interaction with poison compared to all noble metals. For reforming, developing sulfur tolerant catalysts is an important challenge. There are many literature reports that use precious metals for sulfur tolerance.

Table 1.5 Sulfur adsorption energies and sulfide formation energies.^[85-90]

Metal	Sulfur adsorption energy [kJ/mol ⁻¹]	Sulfide formation energy [kJ/mol ⁻¹]
Ni	-247	-173
Ru	-215	-168
Rh	-166	-148
Ir	-219	-135
Pt	-177	-147

1.13. Reforming catalysts- A literature review

Several types of catalysts are reported in literature for reforming of methane. The most important properties of a reforming catalyst are: (i) it should be highly active, (ii) resistant to carbon formation, (iii) sulfur tolerant and (iv) least susceptible to metal sintering. Moreover, under reforming conditions, catalyst should have good thermal stability and maintain its structural integrity for long (thousands of) hours on stream. Generally, for reforming, different transition metals are used, though Ni is most widely used catalyst. Nickel is cheaper and shows high activity towards methane cracking in reforming reaction. Several catalyst supports are used for reforming reaction. Among them, common support is α -Al₂O₃, it is relatively inexpensive and has good thermal stability.

1.13.1. Role of the support in reforming catalysts

The role of catalytic support in methane reforming reaction can hardly be overrated. It not only contributes towards active metal dispersion and resistance to sintering, but also contributes for effective removal of carbon on active metal surface. It also participates in catalytic reaction by supplying labile 'O' in the oxidation of carbon or CO. Hence, it forms part of a catalytic system. The most widely used supports are ZrO₂, La₂O₃, Al₂O₃, MgO, SiO₂, TiO₂, NiAl₂O₄ and MgAl₂O₄.^[91-95] Catalytic supports that are basic in nature, such as MgO, CaO play important role in minimizing carbon deposition. On the otherhand, acidic supports facilitate decomposition of methane by promoting cracking of hydrocarbons and polymerize the carbon formed over the active surface. Combinations of the above metal oxides help to enhance strong interaction between metal and the support, making the catalyst more resistant to sintering and carbon formation, thus improving the durability of the catalyst.^[96, 97] Similarly, reforming catalysts that have reducible oxides like ceria (CeO₂), active metals like Ru, Ir and Rh, metal substituted perovskites (La_{1-x}Ce_xNiO₃)^[98] and cobalt supported catalysts^[99] have less tendency for carbon formation.

1.13.2. Perovskite type of structured oxides as catalysts

Compared to conventional supported metal catalysts, perovskite type oxides are widely studied during the last decade. Since, the active metals are strongly held in a perovskite lattice, they are expected to show greater thermal stability as reforming catalysts. Additionally, some of perovskites have inherent oxygen conduction which

is increased by the substitution of active metal in to the perovskite lattice. This labile oxygen will help to oxidize the coke and minimize carbon deposition on the active metal.

Perovskite name was derived from the name of a Russian mineralogist L.A. von Perovski (192-1856). The mineral was discovered by Gustav Rose in 1839 and found at Ural Mountains. A general formula of perovskite is ABO_3 , where A is larger cation like lanthanide and/or alkaline earth metal and B is the smaller cation, mostly consist of transition metals. In its unit cell, A cation is 12 co-ordinated while B is 6 co-ordinated, mostly to oxygen anions. Figure 1.16 shows corner sharing octahedra of B cation and center position occupied by A cation. The perovskite structure is built like ReO_3 type frame work of super structure and incorporation of A cation in to the BO_6 octahedra.^[100] In case of ideal cubic structure of perovskite, the atoms are attached with one another. The A-O distance is 1.414 times higher than B-O distance, i.e $(r_A + r_O) = \sqrt{2} (r_B + r_O)$. However, some of the synthesized perovskites deviate from the ideal perovskite structure. The stability and measure of deviation from the ideal structure is defined as tolerance factor (t) and is derived using the following relation developed by Goldschmidt:^[101]

$$t = (r_A + r_O) / \sqrt{2} (r_B + r_O) \quad (1.19)$$

where $t=1$ for ideal cubic perovskites. The t value varies in the range of 0.75 to 1.0.

The simple perovskite structure can be modified by incorporating different types of A and/or B ions with small size in variation and cationic charge. Generally equi-atomic substitution of two ions at A- site and/or B-site in the ABO_3 perovskite with general formula $A_{1-x}A'_x B_{1-y}B'_y O_3$ can be done. The resulting perovskites are of more interest in many catalytic applications, in which oxygen atoms are slightly shifted towards more charged cations and leads to formation of distorted perovskites.

In general, in ABO_3 perovskite, A site is responsible for the thermal stability of the catalyst and B site is for catalytic activity. Different environments around B cation can impart different reactivity to the active center. The non-stoichiometric substitution of A or B site cations generate defects in lattice, which are mostly responsible for catalytic activity and also contribute towards the oxygen mobility within the perovskite structure.

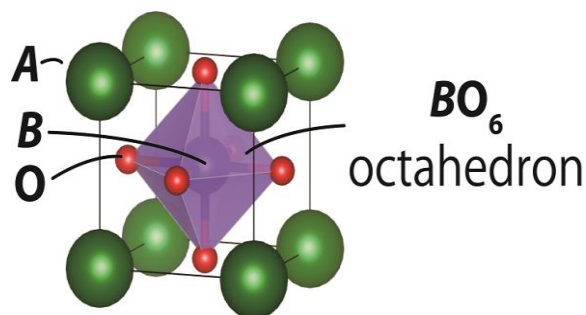


Fig. 1.16. Schematic of a ABO_3 perovskite.^[102]

The lattice oxygen conduction in the perovskite structure could facilitate the rate of oxidation of carbon species on metallic surface. Urasaki et al. have studied a series of Ni supported perovskite catalysts including $SrTiO_3$, $BaTiO_3$, $LaFeO_3$, $LaAlO_3$ and $La_{0.4}Ba_{0.6}Co_{0.2}Fe_{0.8}O_3$. They identified that $LaAlO_3$ and $SrTiO_3$ catalyst shows higher activity and stability in steam reforming methane.^[103] In case of Ce substituted perovskites like $La_{1-x}Ce_xFe_{0.7}Ni_{0.3}O_3$ and $La_{0.23}Ce_{0.1}Sr_{0.67}TiO_{3-\delta}$, significant resistance to coke deposition and higher methane conversion were observed. Introducing Ce into the perovskite lattice enhanced the Ni dispersion and improved oxygen mobility during the reaction.^[104-106]

Batiot-Dupeyrat et al. reported that the catalytic activity of La_2NiO_4 perovskite catalyst was higher than that of Ni/La_2O_3 or $LaNiO_3$ because of the formation of smaller Ni particles in the former after reduction.^[107] Nickel based perovskites were also evaluated for DRM reaction.^[108] The DRM activity varied for the set of catalysts of $La_{1-x}Sr_xNiO_3$ ($x=0-0.1$) and $La_{2-x}Sr_xNiO_4$ ($x=0.0-1.0$) perovskites.^[109] Metal and the support interface gives rise to synergetic active site at the Ni/La_2O_3 interface, offering high activity and stability during DRM reaction. Most of the studies in this thesis are based on the screening of different metals doped in B-site of the perovskites for syngas generation through DRM reaction.

1.14. Scope and objective of the present thesis

With the emerging reforming technology, the catalyst wrestles with number of challenges such as, (i) *Activity*: Catalyst should have sufficient activity for longer duration. (ii) *Sulfur poisoning*: feedstock may have ppm level of sulfur containing compounds that deactivate the catalyst by depositing sulfur species on the active site of metal. The major challenge is to develop catalyst with sulfur tolerance. (iii) *Carbon*

formation: During the reaction carbon formation is major drawback causing deactivation of the catalyst by developing pressure drop, breakage of the catalyst pellets and blockage of the active sites. (iv) *Sintering:* Due to high temperature operating condition and high amount of steam, size of active metal particles may easily grow on the catalyst surfaces. If the above factors are eliminated then carrying out reforming reaction would help to reduce the syngas manufacturing cost. Reforming reaction is not possible to conduct at low temperatures as thermodynamic considerations do not permit. Since, the steam reforming of methane is carried out in industrial scale at very high temperatures, it should be possible to adopt or use the same infrastructure for syngas generation through dry, Bi and Tri reforming reaction. Based on these observations, the main objective of this study is to develop novel catalyst compositions that are stable for few thousand hours. It is possible to develop active metal sintering and carbon formation can be avoided by promoting metal to support interaction by locking the active metal into the perovskite lattice, which can enhance the red-ox property at reforming condition. We have chosen Ni, Ru, Ni-Ru and Rh due to their high activity for DRM, BRM and TRM reaction as well as low cost of the former. To pursue this goal, the scope and objectives of this study are defined as:

- (i) Synthesis of Lanthanide substituted nickel alumina perovskite catalysts using citrate gel method. Characterization of these materials and their evaluation for steam and Bi reforming of methane. Among all the perovskites that were synthesized $\text{CeAl}_{(1-x)}\text{Ni}_x\text{O}_3$ had superior activity as compared to other perovskites, hence this was tested upto 100 h on steam. The results clearly showed that high metal dispersion, good reducibility and active role of the support in the red-ox mechanism through surface oxygen mobility play important roles in activity and stability of these Ce substituted perovskites.
- (ii) After selection of best catalyst $\text{CeAl}_{(1-x)}\text{Ni}_x\text{O}_3$ in reforming reaction, Ru, Ni-Ru and Rh substituted catalyst were synthesized instead of Ni. These structured oxides are thermally stable even in harsh thermal environments. Hence, different families of perovskites, including $\text{CeAl}_{1-x}\text{Ru}_x\text{O}_3$, $\text{CeAl}_{1-x}\text{Ni}_x\text{Ru}_y\text{O}_3$ and $\text{CeAl}_{1-x}\text{Rh}_x\text{O}_3$ type structures were synthesized. The stability of these perovskite structures in the presence of sulfur containing feed stock can be enhanced by

substitution of the B site cations of these structures, with different transition metal ions. Characterization of these materials for Ni and precious metal substitution and testing them for their steam, bi and tri reforming activity was done.

- (iii) Basic promoters like Ca, Sr and Ba were substituted in the perovskites and tested for dry and Bi reforming activity. Amongst the three alkaline earth substituted catalysts, $\text{CaZr}_{1-x}\text{Ni}_x\text{O}_3$ shows superior activity in the temperature range of 600-800 °C. More oxygen storage capacity and strong metal to support interaction improved DRM activity as well as the life of catalysts by reducing the coke formation. A relation between structure and catalytic activity was successfully established.

1.15. References

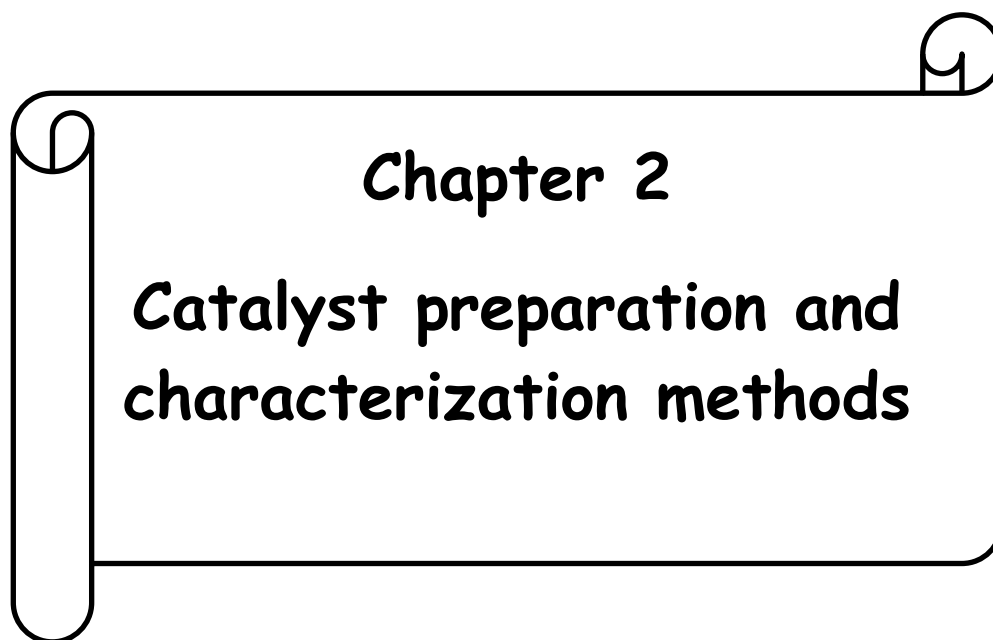
1. J.A. Kokal, B.V. Vora, T. Imai, *Appl. Catal. A: General*, 2001, **221**, 295.
2. Ed Hawkins, P. D. Jones, Q. J. Roy, *Meteorol. Soc.*, 2013, **139**, 1961.
3. A. Mittasch, C. Schneider, DRP 296866, BASF, 1912.
4. J. P. J. Byrne, R. J. Gohr, R. T. Haslam, *Ind. Eng. Chem.* 1932, **24**, 1129.
5. D. J. Wilhelm, D. R. Simbeck, A. D. Karp, R. L. Dickenson, *Fuel Process. Technol.*, 2001, **71**, 139.
6. A. Holemen, *Catal Today*, 2009, **142** 2.
7. J.H. Lunsford, *Catal Today* 2000, **63**, 165.
8. J. R. Rostrup-Nielsen, *Catal Today*. 2002, **71**, 243.
9. J. R. Rostrup-Nielsen, J. H. Bak Hansen, *J. Catal.*, 1993, **144**, 38.
10. J. R. H. Ross, A. N. J. Van Keulen, *Catal. Today*, 1996, **30**, 193.
11. S. A. Ghoneim, R. A. El-Salamony, S. A. El-Temtamy, *World Journal of Engineering and Technology*, 2016, **4**, 116.
12. F. Gallucci, *Ind. Eng. Chem. Res.* 2004, **43**, 928.
13. J. N. Armor, *Appl. Catal. A Gen.*, 1999, **176**, 159.
14. A. M. Adris, B. B. Pruden, C. J. Lim, J. R. Grace, *J. Chem. Eng.*, 1996, **74**, 2, 177.
15. A. M. Adris, C. J. Lim, J. R. Grace, *Chem. Eng. Sci.*, 1994, **49**, 24, 5833.
16. O. Davidson, H. Gitay, D. Griggs, K. Halsnaes, J. Houghton, J. House, Z. Kundzewicz, I. Noble, R. Pachauri, B. Pittock, M. Prather, R. G. Richels, J. B. Robinson, *Climate Change 2001: Synthesis Report*, 24.
17. C. H. Bartholomew, *Appl. Catal. A Gen.*, 2001, **212**, 1, 17.
18. X. H. Ren, M. Bertmer, S. Stapf, D. E. Demco, B. Blümich, C. Kern, A. Jess, *Appl. Catal. A Gen.*, 2002, **228**, 1, 39.
19. J.R. Rostrup-Nielsen, *Physical Chemistry Chemical Physics*, 2001, **3**, 283.
20. F. Joensen, J.R. Rostrup-Nielsen, *J. Power Sources*, 2002, **105**, 2, 195.
21. I. M. Bodrov, L. O. Apelbaum, M. I. Temkin, *Kinetika i Kataliz*, 1968, **9**, 1065.
22. J.R. Rostrup-Nielsen, J. Sehested, J.K. Nørskov, *Advances in Catalysis*, 2002, **47**, 65.
23. J. Wei, E. Iglesia, *J. Catal*, 2004, **225**, 116.
24. Xu, G.F. Froment, *AIChE Journal* 1989, **35**,1, 88.

25. A. A. Khomenko, L. O. Apelbaum, F. S. Shub, Y. S. Snagovskii, M. I. Temkin, *Kinetika i Kataliz*, 1971, **12**, 423.
26. P. B. Toettrup, *Appl. Catal.*, 1982, **4**, 377.
27. L. M. Aparicio, *J. Catal.*, 1997, **165**, 262.
28. D. Chen, R. Lødeng, K. Omdahl, A. Anundskas, O. Olsvik, A. Holmen, *Stud. Surf. Sci. Catal.*, 2001, **139**, 93.
29. D. Chen, R. Lødeng, A. Anundskas, O. Olsvik and A. Holmen, *Chem. Eng. Sci* 2001, **56**, 1371.
30. J. R. Rostrup-Nielsen, Catalytic steam reforming, in *Catalysis - Science and Technology*. J.R. Anderson and M. Boudart. New York: Springer-Verlag, Berlin, 1984, **5**, 1.
31. F. Fischer, H. Tropsch, *Brennst. Chem.*, 1928, **9**, 39.
32. R. E. Reitmeier, K. Atwood, H. A. Bennett, H. M. Baugh, *Ind. Eng. Chem.*, 1948, **40**, 620.
33. J. Rostrup-Nielsen, U.S. Pat., 3,791,993, 1974.
34. A. M. Gadalla, M. E. Sommer, *Chem. Eng. Sci.*, 1989, **44**, 2825.
35. A. M. Gadalla, B. Bower, *Chem. Eng. Sci.*, 1988, **43**, 3049.
36. J. R. H. Ross, *Catal. Today*, 2005, **100**, 151.
37. G. C. de Arauj, S. M. de Lima, J. M. Assaf, M. A. Pena, J. L. Garcia Fierro, M. d. C. Rangel, *Catal. Today*, 2008, **133**, 129.
38. G. S. Gallego, C. Batiot-Dupeyrat, J. Barrault, E. Florez, F. Mondragon, *Appl. Catal., A*, 2008, **334**, 251.
39. O. R. Inderwildi, S. J. Jenkins, D. A. King, *Angew. Chem., Int. Ed.*, 2008, **47**, 5253.
40. L. Kapokova, S. Pavlova, R. Bunina, G. Alikina, T. Krieger, A. Ishchenko, V. Rogov, V. Sadykov, *Catal. Today*, 2011, **164**, 227.
41. Z. L. Zhang, V. A. Tsipouriari, A. M. Efstathiou, X. E. Verykios, *J. Catal.*, 1996, **158**, 51.
42. Z. L. Zhang, X. E. Verykios, *Catal. Lett.*, 1996, **38**, 175.
43. H. Y. Wang, C. T. Au, *Catal. Lett.*, 1996, **38**, 77.
44. J. Kehres, J. G. Jakobsen, J. W. Andreasen, J. B. Wagner, H. H. Liu, A. Molenbroek, J. Sehested, I. Chorkendorff, T. Vegge, *J. Phys. Chem. C*, 2012, **116**, 21407.

45. Fan, M.-S, A.Z. Abdullah, S. Bhatia, *Chem Cat Chem*, 2009, **1**, 2, 192.
46. S. B. Wang, G. Q. Lu, G.J. Millar, *Energy Fuels*, 1996, **10**, 896.
47. D. Pakhare, C. Shaw, D. Haynes, D. Shekhawat, J. Spivey, *J CO₂ Util*, 2013, **1**, 37.
48. L. Basini, L. Piovesan, *Ind. Eng Chem Res*, 1998, **37**, 258.
49. H. C. Dibbern, P. Olesen, J. R. Rostrup-Nielsen, P. B. Tottrup, N. R. Udengaard, *Hydro Process*, 1986, **65**, 71.
50. J.R. Rostrup-Nielsen, J.H. Bak Hansen, L.M. Aparicio, *J Japan Petrol Inst*, 1997, **40**, 366.
51. J.R. Rostrup-Nielsen, *J. Catal.*, 1984, **85**, 31.
52. J. G. McCarty, H. Wise, *J. Catal.*, 1979, **57**, 406.
53. F. Alenazey, C. G. Cooper, C. B. Dave, S. S. E. H. Elnashaie, A. A. Susu, A. A. Adesina, *Catal. Commun.*, 2009, **10**, 406.
54. A. Olafsen, C. Daniel, Y. Schuurman, L. B. Raberg, U. Olsbye, C. Mirodatos, *Catal. Today*, 2006, **115**, 179.
55. D. San-José-Alonso, J. Juan-Juan, M. J. Illán-Gómez, M. C. Román-Martínez, *Appl. Catal. A: Gen.*, 2009, **371**, 54.
56. J. H. Edwards, K. T. Do, A. M. Maitra, S. Schuck, W. Fok, W. Stein, *Energ. Convers. Manage.*, 1996, **37**, 1339.
57. M. C. J Bradford, M. A. Vannice, *Catal. Rev.*, 1999, **41**, 1.
58. E. Ruckenstein, H. Y. Wang, *Appl. Catal. A: Gen.*, 2000, **204**, 257.
59. G. L. Farina, E. Supp, *Hydrocarbon Proc. Int. ed.*, 1992, **71**, 77.
60. L. Qian, Z. Yan, *J. Nat. Gas Chem.*, 2002, **11**, 151.
61. M. M. Halmann and M. Steinberg, *Greenhouse Gas Carbon Dioxide Mitigation: Science and Technology*. Lewis Publishers, Boca Raton, FL, 1999, 568.
62. H. Liander., *Trans. Faraday Soc.*, 1929, **25**, 462.
63. M. Fathi, E. Bjorgum, T. Viig, O. A. Rokstad, *Catal. Today*, 2000, **63**, 489.
64. M. A. Pena, J. P. Gómez, J. L. G. Fierro, *Appl. Catal. A: Gen.*, 1996, **144**, 7.
65. K. Aasberg-Petersen, T.S. Christensen, C.S. Nielsen, I. Dybkjaer, *Fuel Process. Technol.*, 2003, **83**, 253.
66. R. Farrauto, S.Hwang, L. Shore, W. Ruettinger, J. Lampert, T. Giroux, Y. Liu, O. Ilinich, *Annu rev mater res*, 2003, **33**, 1.

67. T. Giroux, S. Hwang, Y. Liu, W. Ruettinger, L. Shore, *Appl. catal. B, Envi*, 2005, **56**, 185.
68. L. Maciel, A. Souza, V. Cavalcanti-Filho, A. Knoechelmann, C. Abreu *React. Kinet. Mech. Catal.*, 2010, **101**, 407.
69. M. Garcia-Vargas, J.L. Valverde, A. de Lucas-Consuegra, B. Gomez-Monedero, P. Sánchez, F. Dorado., *Appl. Catal. A*, 2012, **439**, 49.
70. B. Hernandez, M. Martin., *Ind. Eng. Chem. Res.* 2016, **55**, 6677.
71. C. Song, W. Pan., *Catal. Today*, 2004, **98**, 463.
72. M. Halmann, A. Steinfeld., *Catal. Today*, 2006, **115**, 170.
73. G. A. Olah, G. K. S. Prakash and A. Goepfert, *J. Am. Chem. Soc.*, 2011, **133**, 12881.
74. G. A. Olah, A. Goepfert, M. Czaun and G. K. S. Prakash, *J. Am. Chem. Soc.*, 2013, **135**, 648.
75. V. R. Choudhary, K. C. Mondal, *Appl. Energy*, 2006, **83**,9, 1024.
76. S. Ozkara-AydInoglu, *Int J Hydrogen Energy*, 2010, **35**, 23, 12821.
77. M.A. Soria, C. Mateos-Pedrero, A. Guerrero-Ruiz, I. Rodriguez-Ramos, *Int. J. hydrogen energy*, 2011, **36**, 15212.
78. J. N. Armor, *Appl Catal A Gen.*, 2001, **222**, 91.
79. C. Song, *Chem. Innov.*, 2001, **31**, 21.
80. W. Cho, Y. Baek, S.K. Moon, Y.C. Kim, *Catal. Today*, 2002, **74**, 207.
81. S. A. Solovev, Ye. V. Gubareni, Ya. P. Kurilets and S. N. Orlik, *Theor. Exp. Chem.*, **48**, 2012, 3.
82. C.H. Bartholomew, Elsevier 1987, 34, 81.
83. J.R. Rostrup-Nielsen, Promotion, Elsevier 1991, 68, 85.
84. G.A. Somorjai, *J. Catal.*, 1972, **27**, 453.
85. J.G. McCarty and H. Wise, *J. Catal.* 1985, **94**, 543.
86. J.G. McCarty, K.M. Sancier, H. Wise, *J. Catal.*, 1983, **82**, 92.
87. J.G. McCarty. H. Wise, *J. Chem. Phys.* 1981, **74**, 5877.
88. J.G. McCarty. H. Wise, *J. Chem. Phys.* 1980, 72, 6332.
89. J. Bénard, J. Oudar, N. Barbouth, E. Margot, Y. Berthier, *Surf. Sci.* 1979, **88**, 35.
90. R.I. Hegde, J.M. White, *J. Phys. Chem.* 1986, **90**, 296.
91. T. Wu, Q. Yan, H. Wan, *J. Molecular Catal., A: Chemical*, 2005, **226**, 41.

92. R. Takahashi, S. Sato, T. Sodesawa, M. Yoshida, S. Tomiyama, *Appl. Catal., A: General*, 2004, **273**, 211.
93. V. R. Choudhary, S. Banerjee, A. M. Rajput, *Appl. Catal., A: General*, 2002, **234**, 259.
94. N. Sahli, C. Petit, A. C. Roger, A. Kiennemann, S. Libs, M. M. Bettahar; *Catal. Today*, 2006, **113**, 187.
95. M. V. Twigg, "Catalyst Handbook Mansson," 2nd Edition, Manson Publishing, London, 1994.
96. C.J. Michael, M. Bradford, V. Albert, *Appl. Catal., A: General*, 1996, **142**, 73.
97. S. Wang, G. Q. Lu, *Appl. Catal., B: Environmental*, 1998, **16**, 269.
98. S.M. de Lima, A.M. da Silva, L.O.O. da Costa, J.M. Assaf, L.V. Mattos, R. Sarkari, A. Venugopal, F.B. Noronha, *Appl. Catal. B*, 2012, **1**, 121.
99. H. Song, U.S. Ozkan, *J. Catal.* 2009, **261**, 66.
100. B. Raveau, *Proc. Indian Natl. Sci. Acad.*, 1986, **52**, 67.
101. V. M. Goldschmidt, *Skr. Nor. Viedenk Akad, Kl, Mater. Naturvidensk. Kl.*, **1926**, No. 8.
102. P. D. F. Vernon, M. L. H. Green, A. K. Cheetham, A. T. Ashcroft, *Catal. Today*, 1992, **13**, 417.
103. K. Urasaki, Y. Sekine, S. Kawabe, E. Kikuchi, M. Matsukata, *Appl Catal. A* 2005, **183**, 23.
104. S. O. Choi, S. H. Moon, *Catal. Today*, 2009, **146**, 148.
105. C. Perillat-Merceroz, G. Gauthier, P. Roussel, M. Huve, P. Gelin, R. N. Vannier, *Chem. Mater.* 2011, **23**, 1539.
106. S. M. Lima, J. M. Assaf, M. A. Pena, J. L. G. Fierro, *Appl. Catal. A* 2006, **311**, 94.
107. C. Batiot-Dupeyrat, G. Valderrama, A. Meneses, F. Martinez, J. Barrault and J. M. Tatiboue, *Appl. Catal. A: Gen.* 2003, **248**, 143.
108. A. Erdöhelyi, K. Fodor, F. Solymosi, *Stud. Surf. Sci. Catal.*, 1997, **107**, 525.
109. H. Chen, C. Wang, C. Yu, L. Teng, P. Liao, *Catal. Today*, 2004, **97**, 173.



Chapter 2
**Catalyst preparation and
characterization methods**

2.1. Introduction

Method of catalyst preparation plays an important role in obtaining desired activity and selectivity in heterogeneous catalysis. Characterization of the prepared materials and correlation of activity with physico-chemical properties of the catalyst helps in its better understanding, leading to development of tailor made catalysts. This chapter describes various catalyst materials used in this dissertation, their preparation and characterization using different physico-chemical techniques. Preparation methods used to obtain Ni substituted LnAlO_3 ($\text{Ln} = \text{La}, \text{Ce}, \text{Pr}, \text{Nd}, \text{Sm}, \text{Gd}, \text{Dy}$) oxides; Ru and Rh substituted CeAlO_3 perovskites and Ni substituted MZrO_3 ($\text{M} = \text{Ca}, \text{Sr}$ and Ba) type perovskite oxides is given in the next few sections. Detailed structural characterization of these materials was carried out using powder XRD, FT-IR, Raman spectroscopy, transmission electron microscopy (TEM), N_2 –sorption for textural characterization, thermogravimetry (TGA), X- ray photo electron spectroscopy (XPS), temperature programmed reduction (TPR), temperature programmed desorption (TPD) and ICP-OES for bulk chemical analysis.

2.2. Description of chemicals and gases used for this study

The following chemicals, listed in Table. 2.1 were used for the synthesis of various catalyst materials.

Table 2.1 List of chemicals and their specifications used for present study.

Chemical	Formula	Purity and Make
Nickel nitrate, Aluminium nitrate	$\text{Ni}(\text{NO}_3)_2 \cdot 6\text{H}_2\text{O}$ $\text{Al}(\text{NO}_3)_3 \cdot 9\text{H}_2\text{O}$	99.9%, Merck, India
Rare earth nitrates, and oxides	$\text{La}(\text{NO}_3)_3 \cdot 6\text{H}_2\text{O}$, $\text{Ce}(\text{NO}_3)_3 \cdot 6\text{H}_2\text{O}$, $\text{Pr}(\text{NO}_3)_3 \cdot 6\text{H}_2\text{O}$, $\text{Sm}(\text{NO}_3)_3 \cdot 6\text{H}_2\text{O}$, $\text{Dy}(\text{NO}_3)_3 \cdot 6\text{H}_2\text{O}$, Nd_2O_3 , Gd_2O_3	99.9%, Indian Rare Earths Limited, Mumbai, India
Alkaline earth nitrates	$\text{Ca}(\text{NO}_3)_2$, $\text{Sr}(\text{NO}_3)_2$, $\text{Ba}(\text{NO}_3)_2$	99.9%, Sigma- Aldrich
Zirconyl nitrate	$\text{Zr}(\text{NO}_3)_2 \cdot x\text{H}_2\text{O}$	99.9%, Sigma- Aldrich
Ruthenium (III) nitrosyl nitrate, Rhodium nitrate	$\text{Ru}(\text{NO})(\text{NO}_3)_2$ $\text{Rh}(\text{NO}_3)_3$	99.9%, Sigma- Aldrich
Citric acid, Nitric acid	$\text{C}_6\text{H}_8\text{O}_7$, HNO_3	99.9%, Merck, India

Chapter 2: Catalyst preparation and characterization techniques

Gas mixtures and gases used in the investigations, including reforming reactions are given in Table 2.2. All gases were supplied by M/s. Vadilal chemicals Ltd, Vadodara, India.

Table 2.2 Specifications and applications of the gases used.

Gas	Purity	Application
Carbon Dioxide (CO ₂)	99.9 %	Reactant gas
Methane (CH ₄)	99.9%	Reactant gas
Methane + 11 ppm H ₂ S	99.9%	Reactant gas
Nitrogen (N ₂) Argon (Ar) Hydrogen (H ₂)	99.9% 99.9% 99.9%	Carrier gas in reaction GC Carrier gas Catalyst reduction
Gas mixtures containing H ₂ , CH ₄ , CO ₂ , CO, N ₂	99.9%	For GC calibration
5% H ₂ /Ar	99.9%	For TPR
5% O ₂ /He and 5% CO ₂ /He	99.9%	For TPD

2.3. Catalyst preparation

Catalyst preparation is an important aspect in the development of novel catalysts for a particular process. The scientific basis of catalyst preparation has received much attention in recent years. Usually, for catalyst preparation, various parameters like temperature, pH, active phase content and method of preparation are optimized. Catalyst performance and its durability depend on physico-chemical properties of the catalyst. ^[1, 2] Hence, a minor modification in the preparation conditions or method of preparation influence the characteristics of a catalyst and thereby its activity. ^[3]

The active metal in a catalyst can sinter under severe treatment conditions, for example at high temperatures (600-900°C). Hence, it is challenging to prepare catalysts that have good thermal stability, chemical and mechanical strength during the entire time of reaction. There were several reports in this regard. ^[4-7] Most of the literature deals with catalysts based on transition metals like Pt, Ru, Rh and Ni

deposited on a variety of supports.^[8-12] Noble metals are less sensitive to coke deposition compared to nickel. However, considering cost and availability, Ni based catalyst are more attractive for industrial applications. Developing industrially viable catalysts that are resistant to coke and sintering is usually the motivation in the synthesis of metal supported catalysts.

Recently ABO_3/AB_2O_4 type of structured metal oxides have received huge attention for steam reforming of methane ^[13,14,15], dry reforming of methane ^[16-21], partial oxidation of methane ^[22-24] and for control of automotive emissions. ^[25-26] Efforts have been made to introduce active metals like Ni, Ru and Rh into well-defined ABO_3 structures, to get catalysts that are coke and sintering resistant. These structures have high thermal stability and strong metal to support interaction when subjected to reduction. ^[27-28] Addition of rare earth metals or alkaline earth metals to the perovskite increases its basicity, which can suppress carbon formation on catalyst surface. The basic nature of catalyst can promote the rate of adsorption of steam and oxidation of CH_x on the metallic surface.

2.3.1. Preparation of perovskite type oxides

2.3.1.1. Preparation of Ni substituted $LnAlO_3$ by citric method

All the $LnAl_{1-x}Ni_xO_3$ type perovskite oxides were prepared through citrate gel method. Nitrate salts of lanthanides, $Al(NO_3)_3 \cdot 9H_2O$ and $Ni(NO_3)_2 \cdot 9H_2O$ were used as starting materials. For a nominal composition of $LnAl_{1-x}Ni_xO_3$ ($x=0$ and 0.2), required quantities of metal nitrates were dissolved in distilled water. These nitrate solutions were added to the aqueous citric acid ($C_6H_8O_7 \cdot H_2O$) at room temperature. The resulting solution was stirred vigorously at $80^\circ C$ till a viscous gel is formed. This gel was further heated at $180^\circ C$ till a brown colored foamy gel of $LnAlNi-(C_6H_8O_7 \cdot H_2O)$ was obtained. This dry gel was calcined in air at $750^\circ C$ for 6 h (except for Ce containing oxide), while ramping the temperature at $2^\circ C/min$, to get corresponding perovskite type oxide. In case of Ce containing perovskite oxide ($CeAl_{1-x}Ni_xO_3$), since Ce has to be in +3 oxidation state, it was obtained on reduction at $750^\circ C$ in the flow of reducing gas containing 20% H_2 in N_2 . The synthesis procedure is shown systematically in the form of a flow chart in Fig. 2.1.

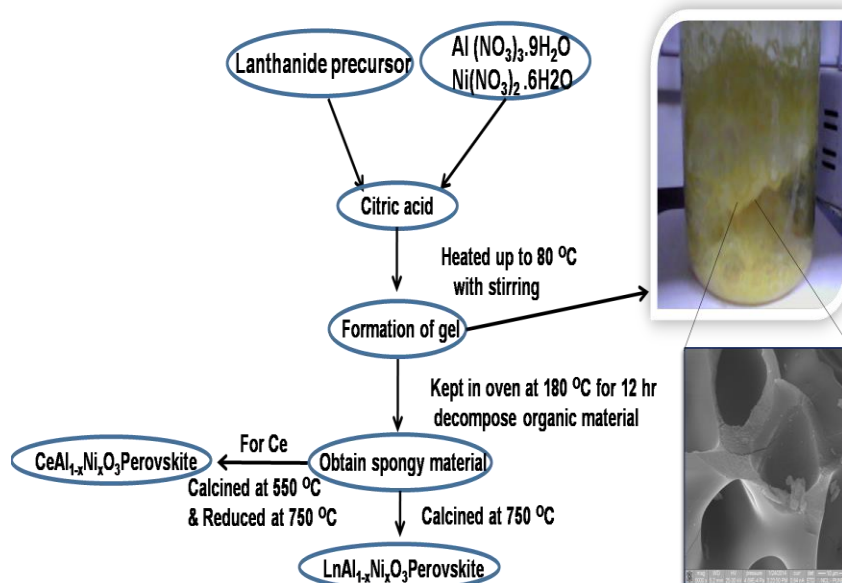


Fig. 2.1 Flow chart for the preparation of $\text{LnAl}_{1-x}\text{Ni}_x\text{O}_3$ perovskite oxides.

Since, the activity of $\text{CeAl}_{1-x}\text{Ni}_x\text{O}_3$ was found to be good, its Ni impregnated version was also prepared by using CeAlO_3 as support. For Ni wet impregnation, aqueous solution of $\text{Ni}(\text{NO}_3)_2 \cdot 6\text{H}_2\text{O}$ was used. Following impregnation with Ni precursor, the material was dried at $100\text{ }^\circ\text{C}$ for 12 h, calcined at $550\text{ }^\circ\text{C}$ and subsequently reduced at $750\text{ }^\circ\text{C}$ in presence 20% H_2 containing N_2 gas.

2.3.1.2. Preparation of Ru and Rh substituted CeAlO_3 by citric method

Ru and Rh substituted CeAlO_3 perovskite materials were prepared by citrate gel method using a similar procedure described above. For this purpose, $\text{Ru}(\text{NO})(\text{NO}_3)_3$ and $\text{Rh}(\text{NO}_3)_3$ were used as Ru and Rh precursors. The mixed oxides obtained on drying followed by calcination at $550\text{ }^\circ\text{C}$ were reduced at $750\text{ }^\circ\text{C}$ in the flow of 20% H_2 in N_2 gas mixture resulting in the formation of perovskite structure. Following this method, Ru containing compositions with $x = 0, 0.04, 0.07, 0.1$ and 0.15 , Rh containing compositions $x = 0.0, 0.02, 0.035, 0.05$ and 0.1 were prepared.

2.3.1.3. Preparation of Ni substituted alkaline earth zirconate (MZrO_3) type perovskite oxides

The $\text{MZr}_{1-x}\text{Ni}_x\text{O}_{3-\delta}$ ($M = \text{Ca}, \text{Sr}$ and Ba) perovskite type oxides with and without Ni were prepared by conventional citrate gel method. For this, stoichiometric amounts of nitrates of the corresponding metals were dissolved in minimum required

distilled water. This solution was added drop wise to the citric acid solution under constant stirring at 353 K. After complexation, water was evaporated at 453 K for 12 hours to obtain spongy amorphous citrate dry gel. This fluffy material was crushed and calcined at 1023 K for 6 h in air flow to get the corresponding $MZr_{1-x}Ni_xO_{3-\delta}$ (M= Ca, Sr and Ba; x = 0, 0.2) perovskite type oxides.

Since, the activity of $CaZr_{1-x}Ni_xO_3$ perovskite type catalyst was good, this material was prepared with different Ni content. The objective of choosing this perovskite catalyst was to take advantage of its redox property, as lattice oxygen is expected to help in the removal of coke formed during the reaction.

For the preparation of Ni impregnated catalyst, $CaZrO_3$ support was used. For this purpose, aqueous solution of $Ni(NO_3)_2 \cdot 6H_2O$ was wet impregnated to achieve 6.4 wt% of Ni loading, which is equivalent to Ni content in $CaZr_{0.8}Ni_{0.2}O_{3-\delta}$. After wet impregnation, the material was dried at room temperature for 12 h, followed by 8 hours drying at 100 °C. This material was calcined at 700 °C in presence of air to get Ni/ $CaZrO_3$ catalyst.

2.4. Catalyst characterization techniques

Above synthesized catalysts were characterized by various physico-chemical technique such as XRD, Raman spectroscopy, N_2 – sorption, H_2/CO chemisorption, temperature programmed techniques (TPD, TPR and TPO), X-ray photoelectron spectroscopy, insitu FTIR and transmission electron microscopy (TEM) to obtain structural, textural and chemical properties of the given samples. The coke on the catalysts used for catalytic evaluation (spent catalysts) was characterized using thermogravimetric analysis and Raman spectroscopy. A brief description of the basic concepts of each these characterization techniques used in this study is given below.

2.4.1. X-ray diffraction (XRD)

X-Ray diffraction is a frequently used technique for catalyst characterization. X- Ray wave lengths are in 0.04 Å to 1000 Å range, hence they can penetrate into the solids and provide structural information, particularly about the long range order of its constituent atoms/ions.^[29] X-Rays are ideal to study the structural arrangement of atoms in different materials and to estimate the particle sizes. X-rays are generated

from metal targets on bombarding with high energy electrons. In a periodic lattice, X-ray diffraction pattern are generated through constructive interference of elastic scattering of X-ray photons by the atoms. Figure 2.2 illustrates the scattered X-rays by the crystal planes constructively as per Bragg's relation: ^[30]

$$n\lambda = 2d \sin\theta \quad \text{where } n = 1, 2, 3, \dots \quad (2.1)$$

This equation illustrates that by measuring diffraction angle (θ) and by knowing wave length of (λ) X-rays, the lattice spacing between diffraction planes (d) can be determined, which is characteristics of the given material.

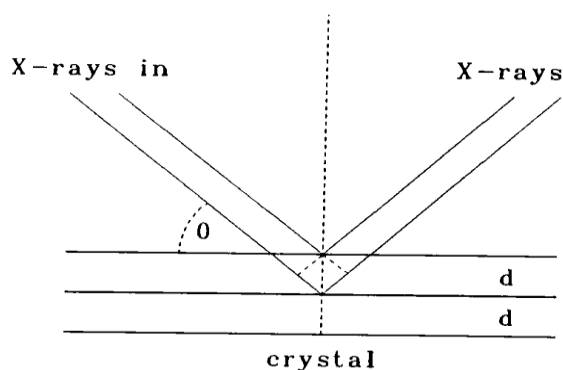


Fig. 2.2 Depiction of X-ray diffraction principle.

The X-ray diffraction can be measured using (Cu $K\alpha$) X-ray source and a movable detector. The detector scans the intensity of diffracted X-rays as function of diffracted angle 2θ . In case of powder samples, diffraction lines appear on constructive interference of crystal planes that are oriented at right angle to the incident beam. These diffraction patterns give information of various phases of the catalyst material. The width of the diffraction peak indicates the dimensions of the reflecting planes. For a perfect crystal, diffraction lines are very narrow. In case of smaller crystallite sizes below 100 nm, the width of the diffraction peak gets broadened. The Scherrer formula correlates the average crystallite size to the diffracted line broadening. ^[31]

$$t = 0.9\lambda/\beta \cos\theta \quad (2.2)$$

Where 't' is the thickness of the crystallites (in Å), λ is the wavelength of X-rays, β is the full width at half maxima of the diffraction peak and θ is the diffraction angle. The XRD pattern of all the samples reported in this thesis were collected using PANalytical X'pert Pro dual goniometer operating at 30 mA and 40 kV. The spectra

were scanned using Cu K α ($\lambda = 1.5406 \text{ \AA}$) radiation using Ni filter. Data was recorded in the 2θ range of $5-90^\circ$ with 0.02° step size using a flat sample holder in Bragg-Brentano geometry.

2.4.2. Brunauer-Emmett-Teller (BET) surface area

The most accepted adsorption model that incorporates multilayer adsorption was developed by Brunauer, Emmett and Teller in 1938, which is known as the BET equation. Langmuir isotherm can be derived for monolayer coverage. The BET assumptions are (i) at zero to full coverage adsorption energy remains constant i.e., heat of adsorption of the gas is equal to the latent heat of condensation in all following layers (ii) no molecular interaction exists between adsorbed gas molecules (iii) except first layer, enthalpy of adsorption is same for any other layer (iv) a new layer will start before another layer is finished. The BET model is: ^[32]

$$P/V (P_0 - P) = 1/ CV_m + [(C-1)/CV_m] (P/P_0) \quad (2.3)$$

Where, P is pressure of gas, V is the volume of gas at STP, V_m is the volume of gas adsorbed equivalent to monolayer coverage at STP, P_0 is the saturated vapour pressure of the liquid at operating temperature and C is a constant correlated to the heat of adsorption and liquefaction. Generally BET equation is used for the estimation of specific surface area. In practical applications, BET is measured at constant temperature and the volume of the adsorbed gas as a function of partial pressure. A linear relationship is arrived between $P/(P_0 - P)V$ and relative pressure P/P_0 . From this, volume of monolayer (V_m) can be calculated from slope and intercept, where theory and practice are reasonably in agreement in the range of relative pressures 0.05 to 0.3. It is often called 'BET region'. The relation in between V_m and surface area (S_{BET}) is

$$S_{BET} = (V_m / 22414) \times 6.023 \times 10^{23} \times A_{N_2} \quad (2.4)$$

Where, S_{BET} is the surface area per gram of sample ($\text{m}^2 \cdot \text{g}^{-1}$), V_m is the volume of the monolayer and the cross sectional area of N_2 molecule (A_{N_2}) is 0.162 nm^2 at 77 K

In this study, multipoint BET surface areas of all the catalyst materials was obtained through N_2 sorption at 77 K on a Quantachrome Autosorb IQ unit. About 300 mg of sample was degassed at 573 K for 3 h and used for N_2 sorption. The adsorbed N_2 was measured at different pressures and the values were then substituted in eq. 2.3 to find V_m . This volume of the monolayer was used in eq. 2.4 to calculate

the surface area of the sample. The N₂ sorption experiments were conducted at Liq N₂ temperature using Quantachrome Autosorb IQ unit (Fig.2.3).



Fig. 2.3 Quanta chrome Autosorb IQ instrument used for N₂ physisorption and H₂ chemisorption.

In supported metal catalysts such as Pt/Al₂O₃, Ru/CeO₂, Ni/CaTiO₃, the active metal is mostly found on the surface. In various reactions, these metal particles are active in their zero oxidation state. The fraction of the active metal exposed on the support is important for such reactions. The location and state of the active metal mainly depends on the catalyst preparation method. In impregnation method, more active metal is located on the surface of support, where as in bulk oxides, active metals may be located across the matrix. The metal dispersion is defined as the fraction of active metal atoms that are exposed on the surface to the total metal atoms present in the sample. The value of D is obtained from the equation

$$D = N_m S M/100L \quad (2.5)$$

Where M and L are the molecular weight and percent loading of the supported metal, S is adsorption stoichiometry, N_m is monolayer uptake of chemisorbed gas in μmol.g⁻¹.

Hydrogen and CO Chemisorption experiments were conducted at 313 K after reduction followed by evacuation at 573 K using Quantachrome Autosorb IQ unit.

2.4.3. Temperature programmed techniques

To study the surface reactions and molecular adsorption on catalyst surface, various temperatures programmed techniques were employed. Compared to many other spectroscopic techniques, it is experimentally simple and less expensive, also applicable to real catalysts and single crystals.

2.4.3.1. Temperature programmed reduction/oxidation (TPR/TPO)

Reduction is an important step in the preparation of metal catalysts. Reduction at improper temperatures prior to reaction can either lead to sintering of the metal or its incomplete reduction. The reduction of oxide species (MO_x) by H_2 is described through below equation.



Above reaction is monitored by raising the temperature linearly with time in argon containing 5% H_2 . Reduction process proceeds via change in the Gibbs free energy. ΔG is negative and its relation to pressure and temperature are given in equation in 2.7.

$$\Delta G = \Delta G^\circ + xRT \ln (P_{\text{H}_2\text{O}}/P_{\text{H}_2}) \quad (2.7)$$

Where

ΔG = Change in the Gibbs free energy in the reduction process

ΔG° = Change in the Gibbs free energy at standard conditions

X = Stoichiometric coefficient of the reaction

R = Gas constant

T = Temperature

P = Partial pressure

A typical TPR/TPO setup has a programmable furnace, thermal conductivity detector (TCD) to measure probe gas (H_2 , O_2 , CO) concentration in the gas stream at the outlet of sample cell. Data of both TPR and TPO experiments were useful in understanding the reducibility and oxidizability of the catalyst sample.

In a typical TPR experiment, freshly calcined sample was loaded in a U shape quartz tube and placed in a programmable furnace. Chromel-alumel (K-type) thermocouple was positioned close to the catalyst material in the U-tube for monitoring the temperature. Prior to TPR, the sample was heated in 5% O_2/He gas

mixture ($30 \text{ mL}\cdot\text{min}^{-1}$) by ramping the temperature to 673 K @ $10 \text{ K}\cdot\text{min}^{-1}$ to remove the adsorbed species on the surface of the sample.

After cooling the catalyst to 323 K , the gas flow was switched over to $5\% \text{ H}_2/\text{Ar}$ ($30 \text{ mL}\cdot\text{min}^{-1}$) and the catalyst was heated to 1273 K at a heating rate of $5 \text{ K}\cdot\text{min}^{-1}$. The change in H_2 concentration at the outlet was monitored by TCD, which was plotted against temperature to get TPR profile. Water produced during the reduction step was condensed and collected in a cold trap. The H_2 consumed for each reduction step was monitored by TCD to assign them to different reduction steps. The TPR/TPO profiles were obtained using a Micromeritics Autochem 2920 catalyst characterization system, equipped with a TCD (Fig. 2.4.)



Fig. 2.4. Micromeritics Autochem 2920 instrument used for TPR/TPO.

2.4.3.2. Temperature programmed desorption (TPD)

Temperature programmed desorption technique is also called as thermal desorption spectroscopy. Through this technique, desorbed molecules from a catalyst surface are monitored while raising its temperature in a programmed way.^[33] The basic set up of a TPD is similar to that of TPR. The desorbed gas concentration is measured through a TCD detector, while a mass probe is coupled with it to identify the desorbed species. TPD of CO_2 is used for characterizing the basic sites and TPD

of NH_3 is used for understanding the acidity of the catalyst. TPD technique can be used for qualitatively monitoring the strength of acid or basic sites of a catalyst and also for their quantification. Additionally, TPD of O_2 is used for the estimation of surface and bulk defect sites in a catalyst. The TPD of CO_2 and O_2 were performed using Micromeritics Autochem-2920 instrument (Fig. 2.4). Before the run, the sample was activated at $400\text{ }^\circ\text{C}$ in He flow (40 mL/min) for 1 h. Subsequently, the sample was cooled to $80\text{ }^\circ\text{C}$ and CO_2/O_2 was sent in the form of 10% CO_2 in He or 5% O_2 in He (30 mL/min) for 30 min. Subsequently, the temperature was increased to $100\text{ }^\circ\text{C}$ and physisorbed CO_2/O_2 was removed by flushing in He stream for 1 h. Desorption of CO_2/O_2 was carried out in He flow (40 mL/min) by ramping the temperature to $1000\text{ }^\circ\text{C}$ @ $10\text{ }^\circ\text{C/min}$. The amount of CO_2/O_2 desorbed was monitored quantitatively by a TCD-MS, which was calibrated before the TPD study.

2.4.3.3. Thermo gravimetric analysis (TGA)

Thermo gravimetric analysis is useful to monitor change in weight of a sample as a function of temperature. TGA is carried out in presence of a carrier gas, which may be inert, oxidative or reductive type. Weight loss can occur due to removal of H_2O or some organic moiety used during synthesis. Similarly, removal of coke can also be studied through TGA.

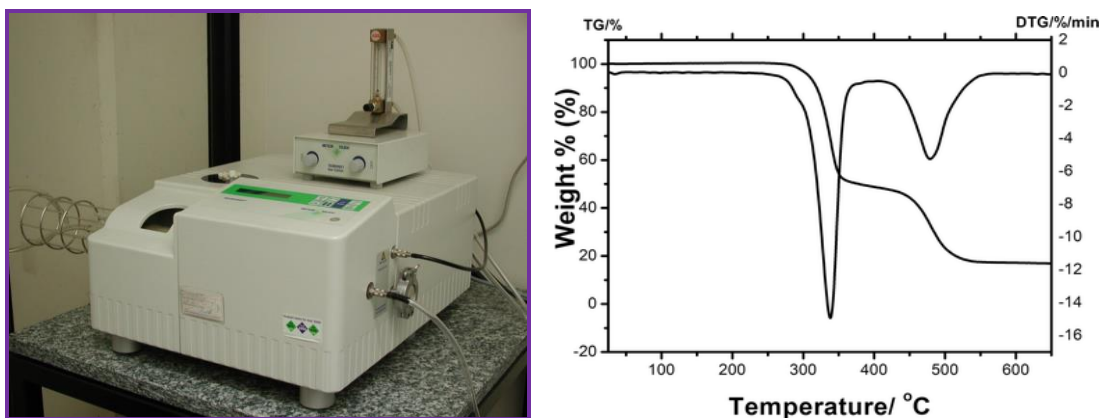


Fig. 2.5. (a) Mettler Toledo TGA/SDTA 851; (b) Typical TGA and DTG traces.

For the present work, TGA measurements were performed with a Mettler Toledo TGA/SDTA 851 apparatus. The analyses were carried out in air ($40\text{ mL}\cdot\text{min}^{-1}$) at a heating rate of $10\text{ K}\cdot\text{min}^{-1}$ using about 10-15 mg samples in a Pt cup. Calcium

oxalate was used to calibrate the instrument. For coke estimation, the studies were carried out in air flow followed by repeat run in 5% H₂ (Fig. 2.5).

2.4.4. X-ray photoelectron spectroscopy (XPS)

X-Ray photoelectron spectroscopy (XPS) technique is based on photo electric effect, discovered by Heinrich Hertz and clarified later by Albert Einstein. [34] It is a very useful technique to identify the oxidation state and composition of elements present on the surface of a catalyst. In this technique, photo electrons emitted during bombardment of a surface with X-rays is analyzed (Fig. 2.6). The emitted photo electrons have distinct kinetic energy, characteristic of the emitted atoms/ions and their bonding state. The relation between the kinetic energy (E_k) and binding energy of emitted photo electron (E_b) is given below

$$E_k = h\nu - E_b \quad (2.8)$$

Where $h\nu$ = Energy of the incident X-ray radiation.

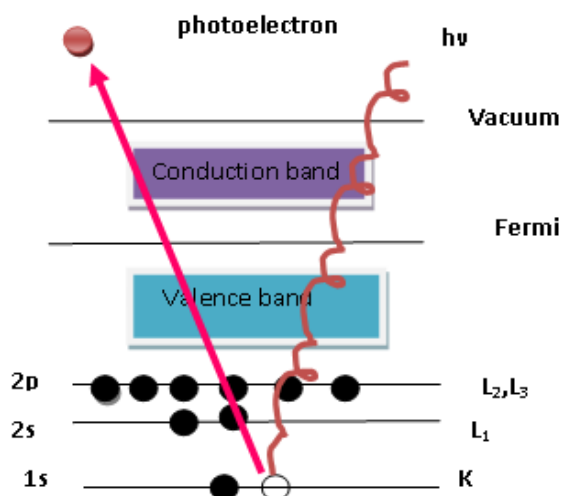


Fig. 2.6 Principle of photoelectron spectroscopy.

The chemical shift of the binding energy (BE) of given photo electron originating from the characteristic element provides qualitative information. In general, BE of an element increases with increasing oxidation state of the element. Intensity of signal gives quantitative information of the elemental present. Being a surface sensitive technique, the depth of the sample analysis is in the range of few

nanometers from the surface. The shape of the peaks and BE is slightly changed based on the chemical state of the element from which the photo electrons are emitted. Thus, XPS can provide information on oxidation state of active species, interaction of the metal with the support and nature of surface impurities.

XPS analyses were performed using VG Micro Tech ESCA 3000 instrument at $\sim 1 \times 10^{-9}$ Torr pressure, (pass energy of 50 eV, electron take-off angle of 60° with overall resolution of ~ 0.1 eV) using monochromatized Mg $K\alpha$ (1253.6 eV) or Al $K\alpha$ radiation (1486.6 eV). The powder sample was pressed into thin discs and mounted on a sample holder to be placed in a surface cleaning/preparation chamber. After the surface cleaning using physical or chemical method, sample was transferred into the analysis chamber, where the XPS spectra were recorded. Charging effects were corrected by adjusting the binding energy of C1s peak to a known position of 285 eV.

2.4.5. Transmission electron microscopy (TEM)

Electron microscopy is a good technique to analyze the topology and morphology of any specimen. Hence, it can be used to determine the size and shape of the supported particles. Figure 2.7 shows the schematic of a TEM instrument.

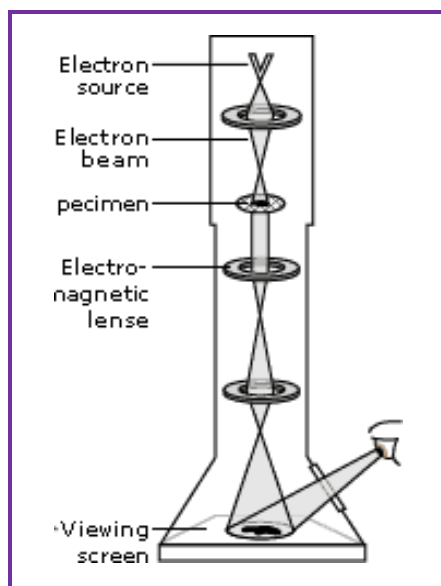


Fig. 2.7 Schematic of transmission electron microscope.

Monochromatic electron stream generated from electron gun are focused on the sample using objective lenses. Some portions of electrons are transmitted through the sample and the number of transmitted electrons depends on the thickness and

density of the corresponding sample. ^[35, 36] Thus transmitted electrons are diffracted from crystalline or semi crystalline material and propagated in different directions. The diffracted electrons are analyzed through angular distribution followed by imaging of the forward scattered electrons based on emitted X- ray energy. These images are magnified using a series of magnetic lenses and detected by charge couple device (CCD) camera and displayed real time on computer. These images provide information about structure of the specimen and position of the atoms within the material. This makes the TEM a very interesting and important tool for the characterization nano materials and heterogeneous catalysis.

The TEM analyses in this study were carried out using a FEI Tecnai TF-30 instrument operating at 30kV. The catalyst specimens were prepared by transferring ultrasonically dispersed fine sample powders in isopropyl alcohol on to a carbon-coated copper grid (mess 200) followed by drying at room temperature. ^[37]

2.4.6. Infrared Spectroscopy (IR)

Infrared spectroscopy is the most important spectroscopic technique that has profound applications in the field of catalysis. This is primarily due to the fact that IR provides information on the structure, geometry and orientation of practically all molecules that are present in a sample, irrespective of the physical state, temperature or pressure. It is therefore a useful tool to identify phases that are present in the catalyst or its precursor stages, the adsorbed species, adsorption sites and the way in which the adsorbed species are chemisorbed on the surface of a catalyst. ^[38,39]

Infrared spectroscopy is the most common form of vibrational spectroscopy and it depends on the vibrations in molecules or in solid lattices by the absorption of photons, which occur if the bonds present have a dipole. A variety of IR techniques have been used to get information on the surface chemistry of different solids. With respect to the characterization of solid catalysts, two techniques largely predominate, namely, the transmission/absorption and the diffuse reflection techniques. In the first case, the sample is prepared by pressing 10-100 mg of catalyst, into a self-supporting disc of approximately less than tenth of a millimeter thickness. In diffuse reflectance mode (DRIFT), samples can be measured simply by depositing powder on a sample holder, avoiding the tedious preparation of wafers. This technique is especially useful

for strongly scattering or absorbing samples. The infrared absorption spectrum is described by Kubelka Munk function ^[40]

$$F(R_{\infty}) = (1-R_{\infty})^2/2R_{\infty} = K/S \quad (2.9)$$

where, K is the absorption coefficient, which is a function of the frequency ν , S is the scattering coefficient and R_{∞} is the reflectivity of a sample of infinite thickness, measured as a function of ν .

The Fourier transform-infrared spectra of the catalysts reported here were recorded using Bruker Tensor 27 FT-IR spectrometer, under ambient conditions. The DRIFT studies were performed after heating the pre-calcined powder samples in-situ from room temperature to 400 °C (the temperature was 175 °C for clay samples) at a heating rate of 5 °C min⁻¹ in N₂ flow (40 ml.min⁻¹). The samples were kept at the activation temperature at 400 °C for 3 h under H₂/N₂ (1/3) flow (30 ml. min⁻¹) and then cooled to 30 °C. Before introduction of dry reforming mixture into the sample cell, it was purged with N₂. The IR spectra were recorded at every 50 °C interval by averaging about 400 scans.

2.4.7. Laser Raman spectroscopy (LRS)

The principal of Raman spectroscopy is based on inelastic scattering of photons that will lose energy by exciting the vibrations in a sample. A vibration is Raman active if there is change in polarizability of the molecule. In general, the molecule should change its shape. For example ellipsoid, cigar shaped and disk shaped molecules are Raman active. Both IR and Raman are complementary techniques in case of highly symmetrical molecules. Raman spectroscopy is more sensitive to the surface phase transition in a metal substituted catalyst. It is also suitable for the characterization of carbon material. The changes in position of the Raman band and its frequency gives information about the orientation of the metal oxide bands. In general, every Raman band has specific vibrational frequency of the bond in the molecule.

Laser Raman spectra were obtained at room temperature using a Horiba JY Lab RAM HR 800 Czerny-Turner spectrograph equipped with an 800 mm focal length and achromatic flat field monochromator along with a mirror-based reflective optics and charge-couple device (CCD) detector. The samples were scanned by using

a He-Ne laser (632.8 nm, 20mW). The scattered light was collected in the back-scattering geometry and detected with a thermoelectrically cooled photomultiplier tube (Fig. 2.8).

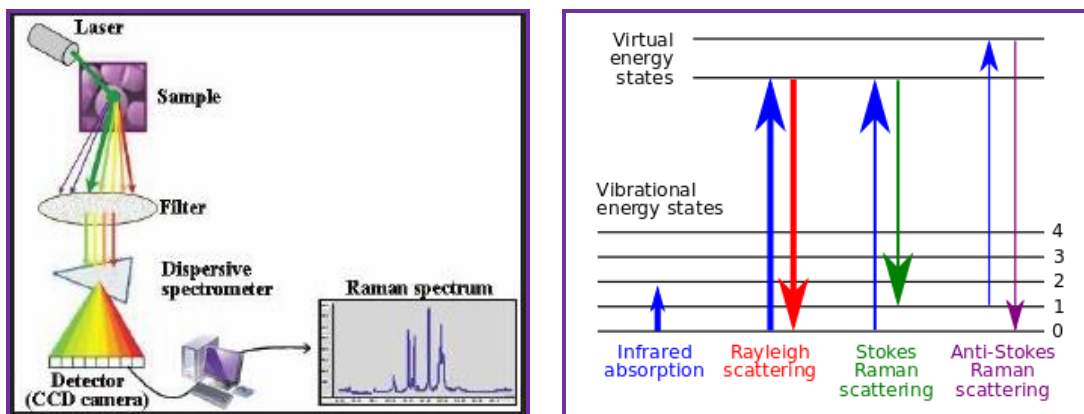


Fig. 2.8 Energy-level diagram showing the states involved in Raman signal.

2.4.8. Inductively coupled plasma-optical emission spectroscopy (ICP-OES)

For estimation of elemental composition of a sample, ICP-OES is a powerful tool. In this technique, atoms and ions are excited by inductively coupled plasma, with emitted radiation being characteristic of the element involved. The intensity of emitted radiation gives concentration of that particular element. Liquid samples, digested in acid are injected into the chamber. Liquid samples are pumped into the nebulizer using a peristaltic pump, where analyte samples are converted into mist and delivered directly in the centre of the plasma flame. The flame temperature is approximately 10000 K, so the mist quickly vaporizes. This energy is sufficient for the collisional excitation within the plasma and gives additional energy to the atoms. The atoms are converted into ions and subsequently ions are transferred to excited states. Excited atoms and ions come back to ground state and emit the photons. Emitted photons have characteristic wave length of specific element. With the increase in the concentration of a particular element, the total number of emitted photons will increase. Sample introduction in ICP-OES instrument is depicted in Fig. 2.9.

Standard solutions containing desired elements were used for the calibration purpose. The catalysts were dissolved in aqua regia and the solutions were analyzed by using Spectro Arcos ICP-OES instrument with the Winlab software (FHS-12).

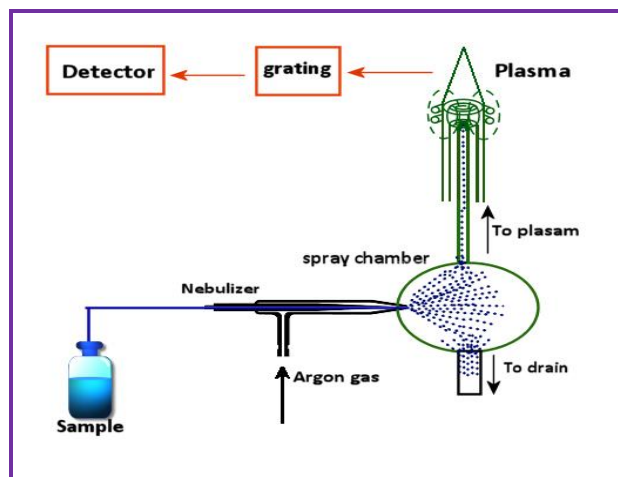


Fig. 2.9 Depiction of sample introduction in ICP-OES.

2.5. Techniques used for characterization of carbon/coke deposits

Several characteristic techniques are used to determine the structure and quantification of deposited carbon on spent (used) catalysts. Among them, spectroscopic (^{13}C -NMR, AES, Laser Raman, SNAS and XPS), microscopic (TEM, HRSTEM, CAEM and AFM), solvent extraction and thermo gravimetric techniques are most useful. Generally, location and amount of carbon deposited depends on the process operating parameters like pressure, temperature, reactant composition and most importantly catalyst properties. Combinations of all these methods help to understand the mechanism of the carbon deposition and its quantification.^[41]

The TGA analysis is predominantly used for investigation of coke, where the weight of a spent catalyst with simultaneous analysis of gaseous components evolved during heating can be studied. Walker and Alenazey et al. independently examined carbon gasification activity using these agents and reported that the rate decreased in the order of: $\text{O}_2 > \text{H}_2\text{O} > \text{CO}_2 > \text{H}_2$ [48, 73]. Also, the type and structure of carbon can be recognized through temperature programmed reduction (TPR) and temperature programmed oxidation (TPO). A study carried out by Bartholomew utilized TPR analysis to classify types and reactivity's of carbon species on Ni catalyst as outlined in Table 2.3.

Table 2.3. Different types of carbon species decomposed from Ni catalysts. ^[42]

Structural type	Designation	Temperature of Formation (K)	Peak temperature during TPR
Adsorbed, atomic (surface carbide)	C _α	200-400	200
Polymeric, amorphous films or filaments	C _β	250-500	400
Vermicular filaments, fibers, and/or whiskers	C _ν	300-1000	400-600
Nickel carbide (bulk)	C _γ	150-250	275
Graphitic (crystalline) platelets or films	C _c	500-550	550-850

Therefore, the above listed forms of carbon may be deposited in various temperature ranges based on the growth mechanism and the operating conditions.

2.6. Experimental procedures for catalyst evaluation

The experimental set up of the fixed bed reactor used in this study is shown in Fig. 2.10. As can be seen, it consists of three modules: flow controller unit, reactor rig and product analysis unit.

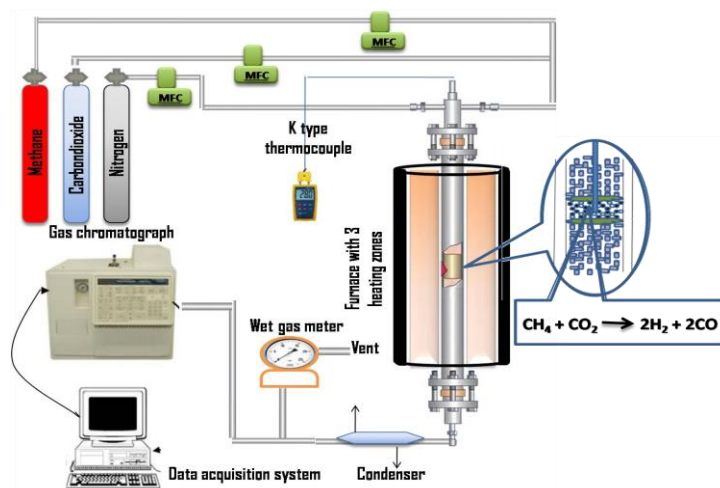


Fig. 2.10 Schematic of the experimental rig used for catalyst evaluation.

2.6.1. Flow controller units

This module is the first part of the set-up where the gas flow rates can be controlled through thermal mass flow controllers (MFC's) and mixed before sending into the reactor. The gas flows were adjusted using Brooks' made MFC's. Each

controller was calibrated for the corresponding gas and their accuracy was checked periodically. Also, a bypass line was connected to an online gas chromatograph (GC) analysis unit, in order to verify the feed composition.

2.6.2. Reactor unit

Dry reforming and steam reforming of methane (DRM and SRM) were carried out in a packed-bed tubular reactor made up of Incolloy HT. The furnace temperature was controlled by programmers with the help of K-type thermocouples positioned at appropriate locations. In a typical experiment, 0.5 cc of catalyst as 0.3-0.5 mm range particles was mixed with 0.5 cc of same size quartz pieces and loaded in reactor, while suspending it between ceramic wool plugs. The catalyst bed temperature was monitored by a K-type thermocouple, centered at the catalyst bed. Prior to reaction, catalyst was calcined at 750 °C for 3 h and reduced 800 °C for 6 h in H₂:N₂ (1:4) gas flow. The product gas was analyzed using GC.

2.6.3. Product analysis

The dry gas product was analyzed using online gas chromatograph (Chemito 6890) equipped with a thermal conductivity detector (TCD). Separation of H₂, CO, CH₄, CO₂ and N₂ components was achieved using Sphero carb packed column and their individual concentrations were estimated using calibration gas mixture of a similar composition. Conversion of CH₄ and CO₂ were calculated as follows:

CH₄ conversion

$$X_{\text{CH}_4} = \frac{F_{\text{CH}_4 \text{ in}} - F_{\text{CH}_4 \text{ out}}}{F_{\text{CH}_4 \text{ in}}} \times 100 \quad (2.10)$$

CO₂ conversion

$$X_{\text{CO}_2} = \frac{F_{\text{CO}_2 \text{ in}} - F_{\text{CO}_2 \text{ out}}}{F_{\text{CO}_2 \text{ in}}} \times 100 \quad (2.11)$$

$$\text{H}_2/\text{CO ratio} = \frac{F_{\text{outH}_2}}{F_{\text{outCO}}} \quad (2.12)$$

2.7. References

1. K. P. De Jong, *Synthesis of Solid Catalysts*. **2009**, Weinheim: WILEY-VCH.
2. J. R. Regalbuto, *Catalyst preparation: Science and Engineering*. **2007**, Boca Raton: CRC Press.
3. J. A. Schwarz, *Chem. Rev.*, 1995, **95**, 477-481.
4. N. Kumar, A. Roy, Z. Wang, E. M. Labbate, D. Haynes, D. Shekhawat, J.J. Spivey, *Appl. Catal. A: Gen.* 2016, **517**, 211–216.
5. J.R. Rostrup Nielsen, *Stud. Surf. Sci. Catal.* 1994, **81**, 25-41.
6. N. Kumar, Z. Wang, S. Kanitkar, J. J. Spivey, *Appl Petrochem Res* 2016, **6** , 201–207.
7. J. Barbero, M.A. Pena, J.M. Campod Martin, J.L.G. Fierro, P.L. Arias, *Catal. Lett.* 2003, **87**, 211-218.
8. M.C.J. Bradford, M.A. Vannice, *J. Catal.* 1999, **183**, 69-75.
9. N. Matsui, K. Anzai, N. Akamatsu, K. Nakagawa, N. Ikenaga, T. Suzuki, *Appl catal A, Gen.* 1999, **179**, 247-256.
10. A. Tsoukalou, Q. Imtiaz, S. M. Kim, P.M. Abdala, S. Yoon, C.R. Müller, *J. Catal.*, 2016, **343**, 208.
11. Y. Schuurman, C. Mirodatos, P. F. Aparicio, I.R. Ramos, A.G. Ruiz, *Catal. Lett.* 2000, **66**, 33.
12. S.M. Gheno, S. Damyanova, B.A. Riguetto, C.M.P. Marques, C.A.P. Leite, J.M.C. Bueno, *J. Mol Catal. A. Chem.* 2003, **198**, 263.
13. J.R. H. Ross, M.C.F. Steel, A. Zeiniifahani, *J. Catal.* 1978, **52**, 280.
14. N. Salhi, C. Petit, A. Kiennemann, *Stud. Surf. Sci. Catal.* 2008, **174**, 1335.
15. A. Alubaid, E.E. Wolf, *Appl. Catal.* 1988, **40**, 73.
16. Z.L. Xu, M. Zhen, Y.L. Bi, K.J. Zhen, *Appl. Catal.*, A 2000, **198**, 267.
17. J. Deng, M. Cai, W. Sun, X. Liao, W. Chu, X. S. Zhao, *ChemSusChem* 2013, **6**, 2061.
18. K. Zhang, G. D. Zhou, J. Li, T.X. Cheng, *Catal. Commun.* 2009, **10**, 1816.
19. N. F. P. Ribeiro, R. C. R. Neto, S. F. Moya, M.M.V. Souza, M. Schmal, *Int. J. Hydrogen Energy* 2010, **35**, 11725.
20. A. R. Gonzalez, Y. J. O. Asencios, E.M. Assaf, J.M. Assaf, *Appl. Surf. Sci.* 2013, **280**, 876.

21. N. Sahli, C. Petit, A.C. Roger, A. Kiennemann, S. Libs, M.M. Bettahar, *Catal. Today* 2006, **113**, 187.
22. W. L. Chu, W.S. Yang, L.W. Lin, *Catal. Lett.* 2001, **74**, 139.
23. K.T.C Roseno, R. Brackmann, M.A. da Silva, M. Schmal, *Int. J. hydrogen energy*, 2016, **41**, 18178.
24. B. Menga, H. Zhanga, Z. Zhaoa, X. Wanga, Y. Jina, S. Liu, *Catal. Today*, 2016, **259**, 388.
25. Y. Nishihata, J. Mizuki, T. Akao, H. Tanaka, M. Uenishi, M. Kimura, T. Okamoto, N. Hamada, *Nature* 2002, **418**, 164.
26. H. Kizaki, K. Kusakabe, S. Nogami, H. Katayama-Yoshida, *Appl. Phys. Express*, 2008, **1**, 104001.
27. E. Pietri, A. Barrios, O. Gonzalez, M. Goldwasser, M. Perez-Zurita, M. Cubeiro, J. Goldwasser, L. Leclercq, G. Leclercq, L. Gingembre, *Stud. Surf. Sci. Catal.* 2001, **136**, 381.
28. G. S. Gallego, F. Mondragon, J. Barrault, J.M. Tatibouet, C. Batiot- Dupeyrat, *Appl. Catal A: Gen.* 2006, **311**,164.
29. J. W. Niemantsverdriet, *Spectroscopic methods in heterogeneous catalysis*, VCH, Weinheim, 1993.
30. B.D. Cullity, S.R. Stock, *Elements of X-ray diffraction*, Prentice Hall, 3rd ed., 2001.
31. N. F. M. Henry, J. Lipson and W. A. Wooster, *The interpretation of X-ray diffraction photographs*, Macmillan and Co Ltd., London, 1951.
32. S. Brunauer, P.H. Emmett, E. Teller, *J. Am. Chem. Soc.*, 1938, **60**, 309.
33. E. Habenschaden, J. Küppers, *Surface Science*, 1984, **138**, 147.
34. (a) T.A. Carlson, *X-ray Photoelectron Spectroscopy*, Dowden, Hutchinson & Ross: Stroudsburg, PA, 1978; (b) D. Briggs, M.P. Seah, *Practical Surface Analysis, Vol. 1: Auger and X-ray Photoelectron Spectroscopy*, 2nd ed., Wiley, New York, 1990.
35. I. Chorkendorff, J.W. Niemantsverdriet, *Concepts of Modern Catalysis and Kinetics*. 2nd ed. 2007: Wiley-VCH.
36. J. R. Fryer, *Chemical Applications of Transmission Electron Microscopy*, Academic Press, San Diego, 1979.

37. J. Freel, *J. Catalysis*, 1972, **25**, 139.
38. J.M. Thomas, O. Terasaki, P.L. Gai, W. Zhou, G. Calbet, *J. Acc. Chem. Res.* 2001, **34**, 583.
39. R.P. Eischens, W.A. Pliskin, *Adv. Catal.* 1958, **10**, 1.
40. P. Kubelka, Z. F. Munk, *Tech. Phys.* 1931, **12**, 593.
41. K. M. Hardiman, C. G. Cooper, A. A. Adesina and R. Lange, *Chem. Eng. Sci.*, 2006, **61**, 2565.
42. C. H. Bartholomew, *Catal. Rev. Sci. Eng.*, 1982, **24**, 67.

Chapter 3

Steam reforming of methane and
simulated biogas over
 $\text{LnAl}_{1-x}\text{Ni}_x\text{O}_{3-\delta}$ perovskite type
catalysts

3.1. Introduction

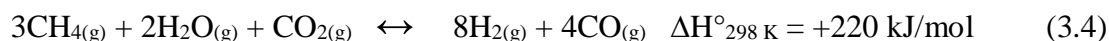
Production of hydrogen and syngas through steam reforming of natural gas is a well established industrial process. Worldwide, there are large scale natural gas reserves, whose consumption leads to relatively low carbon emissions compared to petroleum and coal. ^[1] Hydrogen is important in manufacturing of chemicals, oil refining and it is a fuel for fuel cells. As a result of energy crisis, more emphasis is on finding novel and efficient routes for syngas production, particularly with variable H_2/CO ratios. Steam reforming of methane (SRM) is highly endothermic, hence it is operated at high temperature ($>750\text{ }^\circ\text{C}$). The SRM is also accompanied by the water gas shift (WGS) reaction, a side reaction which is slightly exothermic.



In SRM, excess steam (more than stoichiometric ratio of $\text{H}_2\text{O}/\text{CH}_4 = 1$) is used to prevent coking of catalysts and also to drive the equilibrium towards product formation. But, excess steam and high reaction temperatures increase the cost of H_2 production as a result of high energy consumed. Recently, CO_2 reforming or dry reforming of methane (DRM), which produces syngas with lower H_2/CO ratio (~ 1), is attracting greater attention. Its output is more useful as feed for Fischer-tropsch (FT) synthesis of long chain hydrocarbons.



But, during DRM, catalysts deactivate rapidly due to coke deposition on the catalyst surface. This problem can be somewhat minimized by addition of water to the feed. This process is called Bi-reforming of methane, which also helps to get syngas with desirable H_2/CO ratio by adjusting $\text{CH}_4:\text{CO}_2:\text{H}_2\text{O}$ mole ratios.



The syngas from the above reaction has H_2/CO ratio of 2, which is useful for methanol synthesis. Bi-reforming reaction is more useful when biogas, which has around 25-35 vol% CO_2 is used as feed stock. It saves CO_2 removal cost, to get pure methane from biogas, while giving syngas with appropriate H_2/CO ratio of 2 during

bi-reforming. Methane and CO_2 are major constituents of the biogas, ^[2,3] which is obtained through anaerobic digestion of biomass, molasses, sewage and sludge. Hence, development of active and highly durable catalyst is needed for both bi-reforming (BRM) and DRM are needed.

Noble metal (Pt, Ir, Ru and Rh) and non-noble metal (Ni) based catalysts have been studied for reforming reactions. ^[4] Activity of these metals not only depends on metallic character, but also depends on its particle size, nature of support and reaction conditions. ^[5] Industrial steam reforming is practiced using Ni based catalysts at around 1123-1173 K with steam to carbon (S/C) molar ratio in the range of 2.5-4.0. However, Ni catalysts suffer from deactivation as a result of metal sintering at high temperatures and coke deposition. Coke can deteriorate catalytic activity and lead to destruction of catalyst structure. Coke formation is thermodynamically favored at 910 K at atmospheric pressure, particularly when S/C ratio is less than 1.4. ^[6] The carbon formation happens at the interface of metal to support and separates the active metal from support; resulting in the destruction of catalyst. ^[7] A strategy to control coke formation is to use noble metals, in which carbon dissolution is lower. But, noble metals are expensive, making their commercialization difficult. In order to control sintering and to achieve strong metal to support interaction, hydrotalcite like materials have been studied. ^[8] During the steam reforming, additional drop in activity occurs over Ni/ Al_2O_3 catalysts due to the formation of NiAl_2O_4 spinel. ^[9] Hence, efforts are being made to synthesize Ni catalysts that are resistant to carbon formation and whose structure is stable at high temperatures.

Recently ABO_3 and AB_2O_4 type of structured metal oxides are receiving more attention for SRM,^[10-12] DRM,^[13-18] partial oxidation of methane ^[19-21] and in automotive emission control. ^[22-23] To synthesize Ni catalysts that are carbon resistant under the harsh reaction conditions, efforts are being made to introduce active metal in well-defined perovskite type ABO_3 oxide structure. These structures yield very small particles and possess strong metal to lattice interaction when subjected to reduction.^[24-28] Addition of rare earth metal to the perovskite structure increases basic property of the support by virtue of which carbon formation on the catalyst surface is

suppressed. This modified nature of surface helps to increase the rate of adsorption of steam as well as oxidation of CH_x on the metallic Ni surfaces.

3.2 Experimental methods

3.2.1 Synthesis of $\text{LnAl}_{1-x}\text{Ni}_x\text{O}_3$ perovskites

The rare earth (RE) substituted $\text{LnAl}_{1-x}\text{Ni}_x\text{O}_3$ (Ln = La, Ce, Pr, Nd, Sm, Gd and Dy) perovskite type oxides were prepared by citrate gel method. Lanthanide nitrates, $\text{Al}(\text{NO}_3)_3 \cdot 9\text{H}_2\text{O}$ and $\text{Ni}(\text{NO}_3)_2 \cdot 9\text{H}_2\text{O}$ were used as for the synthesis. Solutions of metal nitrates, required for nominal composition of $\text{LnAl}_{1-x}\text{Ni}_x\text{O}_3$ ($x=0$ and 0.2) were added to the citric acid solution ($\text{C}_6\text{H}_8\text{O}_7 \cdot \text{H}_2\text{O}$) at room temperature. The resulting solution was stirred vigorously at 80°C till viscous gel is formed. This gel was heated at 180°C till a brown colored foamy material was obtained. This was calcined in air at 750°C for 6 h (except for Ce containing oxide), while ramping up the temperature @ $2^\circ\text{C}/\text{min}$, to get corresponding perovskite type oxides. In case of Ce containing perovskite ($\text{CeAl}_{1-x}\text{Ni}_x\text{O}_3$), since Ce has to be stabilized in +3 oxidation state, oxide material obtained after calcination was reduced at 750°C in 20% H_2 containing N_2 .

3.2.2 Catalyst evaluation

Steam (SRM) and dry reforming of methane (DRM) were conducted in a packed-bed tubular reactor made up of Incolloy HT. The reactor was placed in a programmable tubular furnace. All the gases used were regulated using thermal mass flow controllers (Brooks Instruments). The water was charged by a high precision syringe pump (Isco 500D). In a typical experiment, 0.5 cc of catalyst particles in 0.3-0.5 mm range were mixed with 0.5 cc of same size quartz pieces to be loaded in the reactor supported between ceramic wool plugs. The catalyst bed temperature was measured using a K type thermocouple centered in the catalyst bed. Prior to the reaction, catalyst was calcined at 750°C for 3 h and reduced in situ at 750°C for 6 h using $\text{H}_2:\text{N}_2$ (1:4) gas mixture. Steam reforming reactions were performed at $\text{S/C}=3$, GHSV of $20,000\text{ h}^{-1}$ and at atmosphere pressure. Catalyst evaluation was performed in the temperature $600\text{-}750^\circ\text{C}$ zone, while time on stream study was carried out for 1080 min at 750°C at GHSV of $20,000\text{ h}^{-1}$. Bi-reforming of methane was conducted using a simulated biogas composition (CH_4/CO_2 ratio 3/1.5) by mixing with steam in

the ratio $\text{CH}_4:\text{CO}_2:\text{H}_2\text{O} = 3:1.5:2$ at $800\text{ }^\circ\text{C}$ at a GHSV of $22,068\text{ h}^{-1}$ for 100 h. The product gas mixture was analyzed using an online gas chromatograph (GC-TCD; Chemito 1000), equipped with Spherocarb packed column (1/8" OD and 8' length).

3.3 Results and discussion

3.3.1 X-ray diffraction investigations of $\text{LnAl}_{1-x}\text{Ni}_x\text{O}_{3-\delta}$ perovskites

The synthesized perovskite type oxides were investigated for their structural properties using powder XRD. Diffraction patterns shown in Fig.3.1a and 1b show that lanthanide (Ln) substituted oxides have well defined perovskite structure with high crystallinity. All the XRD patterns of these perovskite oxides were obtained on calcination at $750\text{ }^\circ\text{C}$, except for CeAlO_3 . Size of the Ln cation influences the unit cell dimensions of these perovskite oxides. The XRD pattern of La and Ce substituted aluminate perovskites exhibited strong reflections corresponding to the cubic perovskite (JCPDS 39-1471, 28-0260). On the otherhand, perovskites substituted with Pr and Nd shows high 2θ values corresponding to rhombohedral structure (JCPDS 29-0077, 29-0056) with different cell parameter. The diffraction pattern of Sm, Gd and Dy aluminate perovskite samples show well resolved doublet reflection peaks at higher 2θ indicating orthorhombic structure with modified cell parameters (JCPDS 71-1597, 30-0015 and 39-1437).

Partial substitution of Al by Ni at 'B' site in the perovskite lattice also gave perovskite type oxides as may be seen from Fig.3.1b. The peaks of $\text{LnAl}_{0.8}\text{Ni}_{0.2}\text{O}_{3-\delta}$ have shifted to lower angles, on partial substitution of Al by Ni in the lattice. These differences are to be expected considering the ionic radius of Ni^{+2} (0.69 \AA) and Al^{+3} (0.53 \AA) ions. Results also indicate substantial incorporation of Ni in the perovskite lattice.

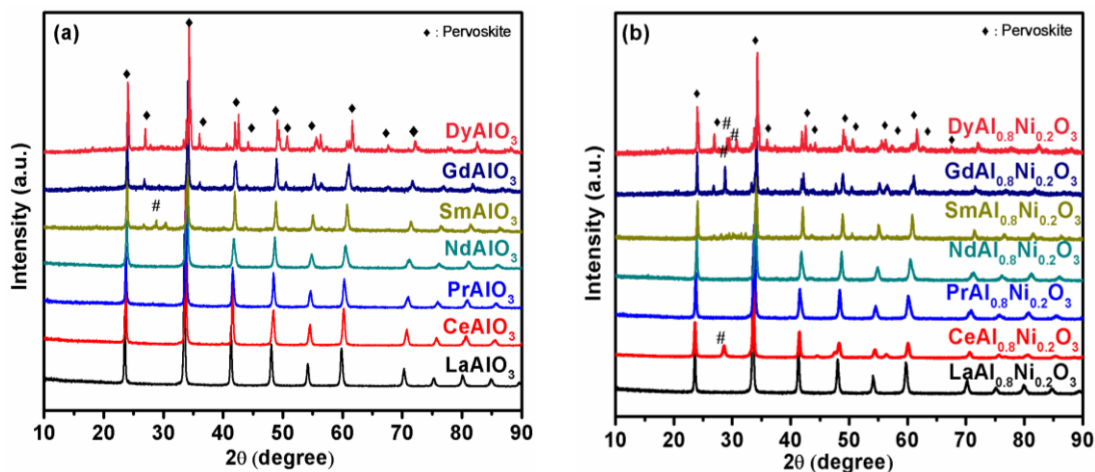


Fig. 3.1 XRD pattern of (a) LnAlO_3 perovskites (b) $\text{LnAl}_{0.8}\text{Ni}_{0.2}\text{O}_{3-\delta}$ perovskite oxides (♦ : perovskite, # : Rare earth oxides).

As a result of lanthanide contraction, the size of lanthanide ion decreases from La to Dy, leading to lattice distortion from cubic to orthorhombic phase passing through rhombohedral phase. In general, this type of distortion depends on the tolerance factor ‘ τ ’, which is defined as:

$$\tau = r_A + r_O / \sqrt{2}(r_B + r_O) \quad (r_A, r_B, r_O \text{ are radius of A, B cations and } \text{O}^{2-}) \quad (3.5)$$

As the tolerance factor is < 1 , there is deviation in perovskite structure from ideal cubic phase. All XRD patterns were refined by using Rietveld method^[29] employing generalized structure and analysis software (GSAS) package and the EXPGUI interface.^[30] Refinement results of all lanthanide substituted aluminate perovskites are shown in Tables 3.1 and 3.2.

Table 3.1 Textural properties of as-synthesized LnAlO_3 (Ln = La, Ce, Pr, Nd, Sm, Gd and Dy) phase perovskite catalysts.

Formulae	LaAlO_3	CeAlO_3	PrAlO_3	NdAlO_3	SmAlO_3	GdAlO_3	DyAlO_3
Space group	Pm-3m	Pm-3m	R-3c (167)	R-3c (167)	Pnam (62)	Pbnm (62)	Pbnm (62)
a/ Å	3.7896(2)	3.7707(3)	5.3134(6)	5.3002(6)	5.2835(4)	5.2499(6)	5.2050(1)
b/ Å	3.7896(2)	3.7707(3)	5.3134(6)	5.3002(6)	5.3083(3)	5.2896(6)	5.2636(1)
c/ Å	3.7896(2)	3.7707(3)	13.0535(7)	12.9397(8)	7.4677(5)	7.4361(9)	7.3932(1)
V/ Å ³	54.42	53.61	368.52	360.51	209.44	206.5	202.55
R _p (%)	8.4	7.4	5.6	7.4	6.8	4.0	4.5
WR _p (%)	9.8	9.3	7.9	9.6	9.3	6.2	6.5
χ^2	1.33	1.89	1.79	1.61	1.73	1.79	1.65
Surface area (m ² /gr) ^a	11.7	9.2	7.9	7.7	6.8	3.3	2.1
Tolerance factor	1.007	1.001	0.986	0.975	0.964	0.956	0.887

^a Calculated from BET Surface area analysis

Chapter 3 – Catalytic application of $\text{LnAl}_{1-x}\text{Ni}_x\text{O}_3$

Table 3.2 Textural properties of $\text{LnAl}_{0.8}\text{Ni}_{0.2}\text{O}_3$ (Ln = La, Ce, Pr, Nd, Sm, Gd and Dy) perovskite type oxide catalysts.

Formulae	$\text{LaAl}_{0.8}\text{Ni}_{0.2}\text{O}_3$	$\text{CeAl}_{0.8}\text{Ni}_{0.2}\text{O}_3$	$\text{PrAl}_{0.8}\text{Ni}_{0.2}\text{O}_3$	$\text{NdAl}_{0.8}\text{Ni}_{0.2}\text{O}_3$	$\text{SmAl}_{0.8}\text{Ni}_{0.2}\text{O}_3$	$\text{GdAl}_{0.8}\text{Ni}_{0.2}\text{O}_3$	$\text{DyAl}_{0.8}\text{Ni}_{0.2}\text{O}_3$
Space group	Pm-3m	Pm-3m	R-3c (167)	R-3c (167)	Pnam (62)	Pbnm (62)	Pbnm (62)
a/ Å	3.7983(3)	3.7899(4)	5.3452(3)	5.3341(3)	5.3043(4)	5.2503(7)	5.2035(3)
b/ Å	3.7983(3)	3.7899(4)	5.3452(3)	5.3341(3)	5.3111(4)	5.3001(5)	5.2912(2)
c/Å	3.7983(3)	3.7899(4)	13.1535(3)	13.0114(4)	7.4788(9)	7.4413(5)	7.4070(7)
V/ Å ³	54.79	54.43	375.81	370.2	210.69	207.06	203.93
Rp (%)	5.2	8.4	7.8	8.1	7.9	5.3	5.3
WRp (%)	7.9	9.5	9.1	9.4	8.6	7.2	7.5
χ^2	1.54	1.57	1.79	1.81	2.03	1.6	2.1
Surface area (m ² /gr) ^a	10.2	7.3	6.4	5.2	3.1	1.5	1.1
Nominal Ni Content (wt%)	5.33	5.3	5.28	5.2	5.06	4.91	4.81
Ni Content (wt%) ^b	5.1	5.0	5.0	5.1	5.2	5.0	4.9
% Ni dispersion ^c	1.5	3.3	0.5	2.3	1.3	0.7	1.8
Tolerance factor	0.992	0.984	0.971	0.959	0.949	0.941	0.873

^a Calculated from BET analysis, ^b Bulk Ni content obtained by chemical (ICP-OES) analysis, ^c Obtained from CO chemisorption

3.3.2 Textural and structural characterization of $\text{LnAl}_{0.8}\text{Ni}_{0.2}\text{O}_3$ catalysts

All perovskite type oxides were subjected to extensive characterization. The results of BET surface area, chemical analysis by ICP-OES and Ni metal dispersion are summarized in Table 3.2. Specific surface areas of these samples were very low as these are prepared at high temperatures. Results also show that after Ni substitution, there was a drop in surface area, though to a minor extent.

3.3.3 Raman analysis of LnAlO_3 perovskites

Perovskite types of structures are often distorted from ideal cubic lattice as a result of BO_6 octahedral tilt. When this tilt is relatively small, it cannot be analyzed by XRD technique due to lower scattering of X-rays by anions. As a result, structural study of such weak scattering oxides is challenging. Raman analysis can help to study octahedral tilt of BO_6 and assist in the identification of such phases in solids, thin films and nano structured oxides. Raman scattering of ABO_3 type perovskite oxides give vibrational modes that provide information about unique signature of crystal structure.

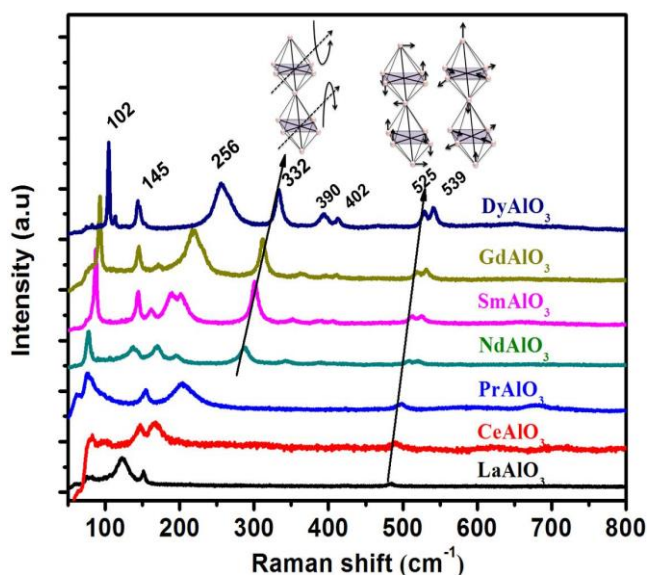


Fig. 3.2 Raman spectra of LnAlO_3 ($\text{Ln} = \text{La}, \text{Ce}, \text{Pr}, \text{Nd}, \text{Sm}, \text{Gd}$ and Dy).

Raman spectra of LnAlO_3 ($\text{Ln} = \text{La}, \text{Ce}, \text{Pr}, \text{Nd}, \text{Sm}, \text{Gd}$ and Dy) perovskites at room temperature are given in Fig. 3.2. At similar scattering, the distortion is enhanced by decreasing the r_{Ln} and most of the bond lengths are shortened. This leads

to shift in Raman frequencies to higher wave numbers and also increased modes of vibrations. In terms of symmetry, perovskite phases transfer from high to lower symmetry. In case of ideal cubic perovskite ABO_3 with space group $\text{Pm}\bar{3}\text{m}$ and $z = 1$; all the atoms are centrosymmetric with fixed coordinates, so Raman modes are inactive.^[31] But in perovskite where $\text{Ln} = \text{La}$ and Ce , three weak peaks are seen at 123-145, 152-165 and 487-495 cm^{-1} . These peaks originate from the rotation of oxygen in octahedral BO_6 around the hexagonal $[001]_h$ direction denoted as A_{1g} mode. Pure La/Ce vibration in the hexagonal $[001]_h$ plane and pure oxygen bending vibration in octahedral is denoted as E_g mode.^[32] Thus minor distortion is observed as a result of deviation from ideal cubic lattice in case of La/Ce substituted aluminates. With further decrease in the size of A cation, phases are converted to rhombohedral lattice. In case of Pr and Nd aluminates, Rhombohedral distortion increased with decreasing size of Ln cation i.e. in NdAlO_3 Raman modes are higher than PrAlO_3 .^[33] The number of modes further increased in the case of Sm, Gd and Dy containing perovskites suggesting transformation of the phases to orthorhombic. The Raman frequencies are given in Table 3.3.

Table 3.3 Experimental Raman bands of LnAlO_3 and their respective assignment.

Catalyst	Raman band (cm^{-1})	Assignment
LaAlO_3	132, 158 487	Rotational Oxygen vibration
CeAlO_3	146, 168 495	Rotational Oxygen vibration
PrAlO_3	53, 151, 202 505	Rotational Oxygen vibration
NdAlO_3	62, 132, 161, 272 506	Rotational Oxygen vibration
SmAlO_3	68, 142, 171, 302 510, 522	Rotational Oxygen vibration
GdAlO_3	82, 162, 183, 312 515, 525	Rotational Oxygen vibration
DyAlO_3	102, 145, 256, 332, 390, 402 525, 539	Rotational Oxygen vibration

In samples containing smaller Ln^{+3} cations at A site, electron-lattice interactions are stronger compared to when larger La^{+3} , Ce^{+3} cations are present, hence they acquire more ionic character. Additionally, the enhanced steric factor leads to increase in global distortion of the perovskite structure. As a result, increasing tilt of the angle is observed while moving from LaAlO_3 to DyAlO_3 .^[34]

3.3.4 Temperature programmed reduction of Ni substituted LnAlO_3 .

The redox nature of Ni substituted LnAlO_3 perovskites was investigated using H_2 -TPR technique; these results are given in Fig. 3.3. Three main reduction peaks are observed. The first reduction peak corresponds to the reduction of Ni^{+3} to Ni^{+2} which is weakly bound to perovskite lattice. The second peak corresponds to the reduction of Ni^{+2} to metallic Ni and the third peak belongs to the reduction of Ni cations present in the bulk of the sample.

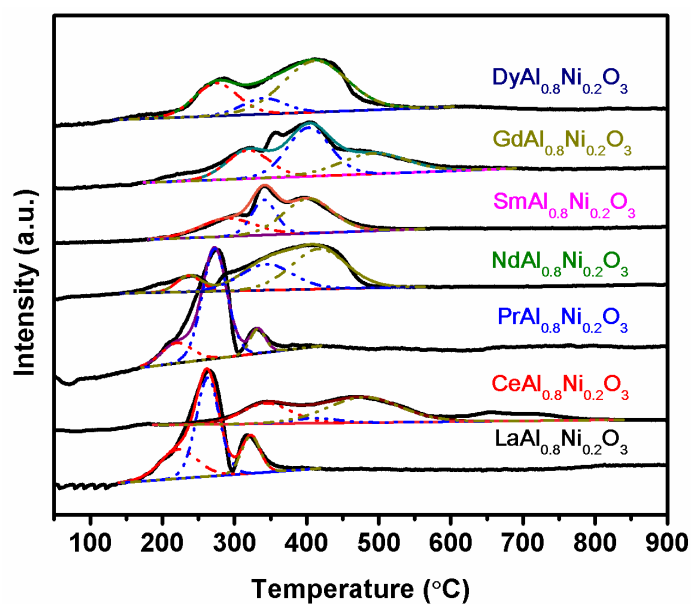


Fig. 3.3 TPR pattern of $\text{LnAl}_{0.8}\text{Ni}_{0.2}\text{O}_{3-\delta}$ perovskites.

Comparison of reduction peak temperatures of $\text{LnAl}_{0.8}\text{Ni}_{0.2}\text{O}_{3-\delta}$ perovskites shows that the concentration of weakly interacting Ni species is more in La and Pr aluminates. While Nd and Dy perovskite have consumed more H_2 compared to Ce implying more amount of Ni is present outside of the perovskite structure and all the peaks observed are at higher temperature. $\text{CeAl}_{0.8}\text{Ni}_{0.2}\text{O}_{3-\delta}$ perovskite has additional reduction peak at 600-750 °C indicating the reduction of surface Ce^{+4} ions, which

facilitates good oxygen storage that can help in the removal of carbon deposited on the catalyst during reforming reaction. The total intensity of the reduction peaks observed follow the order is $\text{Ce} < \text{Nd} < \text{Dy} < \text{Gd} < \text{Sm} < \text{La} \sim \text{Pr}$. The reduction temperatures of Ni in $\text{CeAl}_{0.8}\text{Ni}_{0.2}\text{O}_{3-\delta}$ perovskite catalyst seems to be higher compared to all lanthanide substituted perovskite. An inverse relation seems to be there between the temperature of third TPR peak and the size of the metallic Ni crystallites. During the reduction of Ni substituted perovskite, Ni ions are released in a controlled way from perovskite lattice, thus avoiding sintering.

3.3.5 Temperature-programmed desorption of oxygen

Temperature programmed desorption studies of O_2 help to analyse the type of oxygen vacancies formed in the Ni perovskites. The results of O_2 -TPD studies of Ni substituted LnAlO_3 are shown in Fig. 3.4. The perovskite catalysts that gave reduction peak at higher temperatures were only chosen for this experiment.

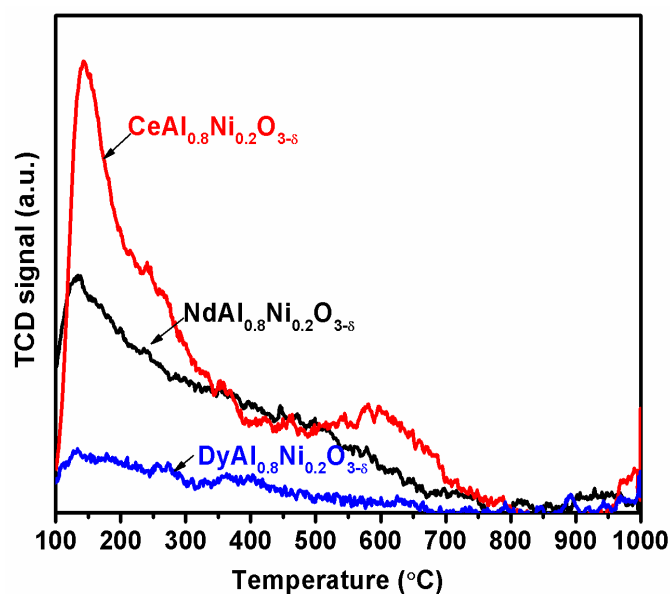


Fig. 3.4 TPD- O_2 pattern of $\text{LnAl}_{0.8}\text{Ni}_{0.2}\text{O}_{3-\delta}$ ($\text{Ln} = \text{Ce}, \text{Nd}$ and Dy) perovskites.

It was observed that when the temperature is raised in a programmed way, oxygen is released from the surface. The O_2 -desorption spectra show two major peaks, with low temperature peak in 100-300 °C temperature zone designated as α peak. This peak originates from weakly bound oxygen to the surface of the perovskite or surface oxygen vacancies.^[34] The second high temperature sharp desorption peak

above 400 °C is designated as β , arises from the bulk of the perovskite. [35-38] From the O_2 -TPD profiles, it was observed that $\text{CeAl}_{0.8}\text{Ni}_{0.2}\text{O}_{3-\delta}$ has more amount of α and β oxygen compared to $\text{NdAl}_{0.8}\text{Ni}_{0.2}\text{O}_{3-\delta}$ and $\text{DyAl}_{0.8}\text{Ni}_{0.2}\text{O}_{3-\delta}$ perovskite catalysts. That is oxygen adsorption and desorption occurs easily and rapidly in the 100-800 °C zone, which falls in the reforming temperature range. Hence, it facilitates delivery of high amount active oxygen to carbon (coke) species, which is effectively removed as CO_x species during the reaction as compared to other perovskite catalysts. Ceria based oxides are known to play a key role in supplying oxygen from its lattice through Mars Van Kraevelen mechanism in reforming reactions. [39] The order of β - oxygen desorption or mobility of lattice oxygen follows the sequence: $\text{CeAl}_{0.8}\text{Ni}_{0.2}\text{O}_{3-\delta} > \text{NdAl}_{0.8}\text{Ni}_{0.2}\text{O}_{3-\delta} > \text{DyAl}_{0.8}\text{Ni}_{0.2}\text{O}_{3-\delta}$, implying the relative ease of oxygen release from $\text{CeAl}_{0.8}\text{Ni}_{0.2}\text{O}_{3-\delta}$ compared to other catalysts.

3.3.6 X- Ray photoelectron spectroscopy (XPS)

X-Ray photoelectron spectroscopy is helpful to understand the surface species present on a solid. Since catalysis is more of a surface phenomenon, XPS helps to unravel the relationship between activity and surface structure.

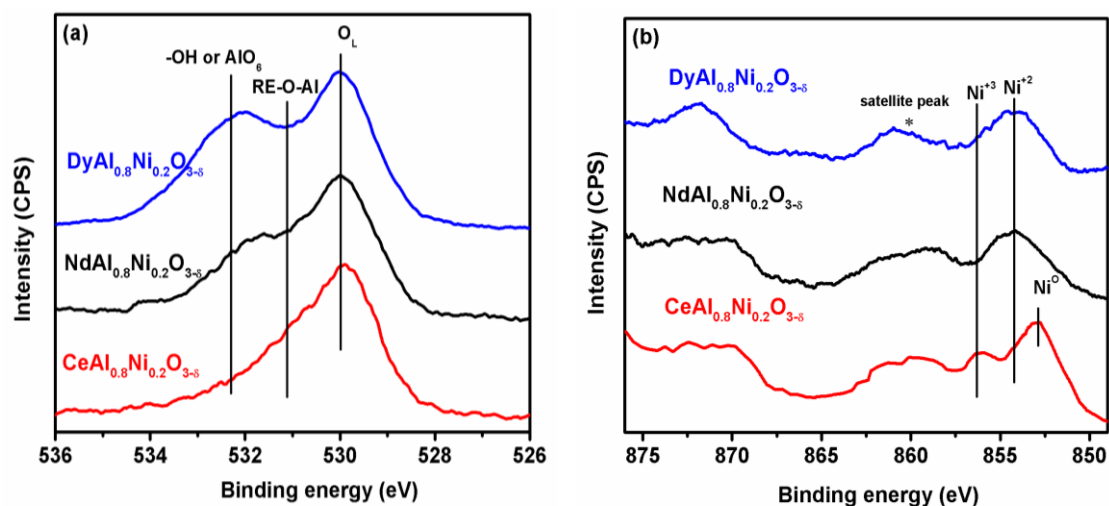


Fig. 3.5 XPS of $\text{LnAl}_{0.8}\text{Ni}_{0.2}\text{O}_{3-\delta}$ ($\text{Ln} = \text{Ce}, \text{Nd}$ and Dy); (a) O 1s, (b) Ni 3d.

Figure 3.5a shows the O 1s core level spectra of $\text{LnAl}_{0.8}\text{Ni}_{0.2}\text{O}_{3-\delta}$ ($\text{Ln} = \text{Ce}, \text{Nd}$ and Dy). The O 1s spectra are more complex and could consist of three components: (i) peak around 529.5-530.0 eV (ii) peak at 531.2 eV and (iii) 532.3 eV. The peak at lower BE is assigned to lattice oxide ion (O^{2-}), while peak at 531.2 eV corresponds to the Ln-O-Al bond and the peak at 532.3 eV may be assigned to hydroxyl/carbonate

groups. ^[40-41] Data show that intensity of high BE peaks increased for $\text{DyAl}_{0.8}\text{Ni}_{0.2}\text{O}_{3-\delta}$ and $\text{NdAl}_{0.8}\text{Ni}_{0.2}\text{O}_{3-\delta}$ perovskite oxides compared to $\text{CeAl}_{0.8}\text{Ni}_{0.2}\text{O}_{3-\delta}$. This high intensity of peaks for $\text{DyAl}_{0.8}\text{Ni}_{0.2}\text{O}_{3-\delta}$ could be attributed to a different kind of oxygen species present in $\text{DyAl}_{0.8}\text{Ni}_{0.2}\text{O}_{3-\delta}$ perovskite, which results from tilting of AlO_6 octahedra.

For the study of Ni chemical state in these catalysts using XPS, exhaustive investigations are required. Limited numbers of models are available in literature for the interpretation of Ni 2P spectra, their multiple splitting and satellite peaks. The XPS spectra of Ni $2P_{3/2}$ and $2P_{1/2}$ for $\text{LnAl}_{0.8}\text{Ni}_{0.2}\text{O}_{3-\delta}$ perovskites (Ln = Ce, Nd and Dy) are shown in Fig. 3.5b. Nickel XPS spectrum of $\text{CeAl}_{0.8}\text{Ni}_{0.2}\text{O}_{3-\delta}$ sample shows that a part of Ni is present on the surface of the perovskite in the form of Ni^0 (852.5 eV) and partly as Ni^{3+} (856.3 eV). On the otherhand, in $\text{NdAl}_{0.8}\text{Ni}_{0.2}\text{O}_{3-\delta}$ and $\text{DyAl}_{0.8}\text{Ni}_{0.2}\text{O}_{3-\delta}$ samples, Ni is mostly in +2 state and a small part of it in +3 oxidation state (854.6 and 856.3 eV respectively). The higher Ni^0 over $\text{CeAl}_{0.8}\text{Ni}_{0.2}\text{O}_{3-\delta}$ can be explained by the fact that it is prepared under H_2 reduction, while the other perovskites are formed under oxidizing atmosphere. ^[42]

3.4 Evaluation of catalysts for steam reforming of methane

All the catalysts described above were evaluated for steam reforming of methane. Out of these, the best catalyst was evaluated more vigorously for its durability and on-stream stability.

3.4.1 Judging the best lanthanide substituted perovskite catalyst for SRM

The catalytic activity of different Ln and Ni substituted perovskite catalysts was tested for SRM by varying the reaction temperature in the 600-750 °C range. Steam to CH_4 ratio of 3 and gas hourly space velocity (GHSV) of 20,000 h^{-1} at 1 atm were used for this comparison. Figure 3.6 shows catalytic activity of different perovskite catalysts as a function of temperature. It can be seen that among the lanthanide substituted perovskites, Ce substituted perovskite catalyst shows relatively better activity in the temperature range explored. The catalytic activity of lanthanide substituted perovskites is in the order $\text{Ce} > \text{Nd} > \text{Dy} > \text{Gd} > \text{La} > \text{Sm} > \text{Pr}$. It can be seen that the activity is closely related to the reducibility and the dispersion of Ni. In addition to these two parameters, SRM activity also depends on the oxygen vacancies,

with the catalyst ($\text{CeAl}_{0.8}\text{Ni}_{0.2}\text{O}_{3-\delta}$) having high oxygen vacancies (see Figure 3.4) being more active.

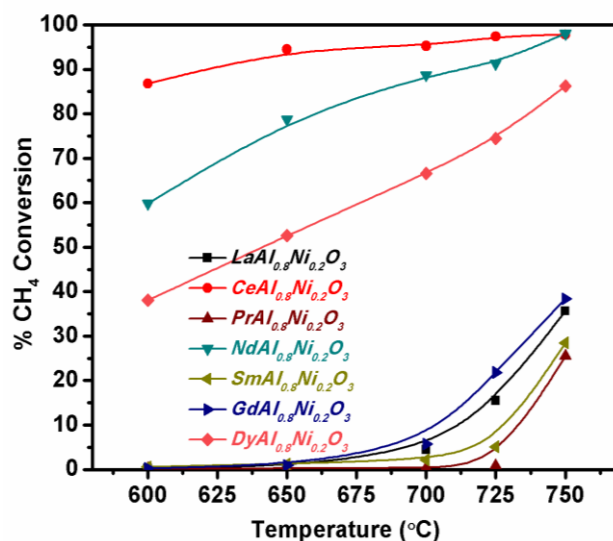


Fig. 3.6 SRM over $\text{LnAl}_{0.8}\text{Ni}_{0.2}\text{O}_3$ (Ln = La, Ce, Pr, Nd, Sm, Gd and Dy) at different temperatures

*Reaction conditions: GHSV- 20,000 h⁻¹; 1atm; CH₄/H₂O = 3

Methane conversion and corresponding H₂/CO ratio at 750 °C as a function of substituted Ln is given in Fig. 3.7. The $\text{CeAl}_{0.8}\text{Ni}_{0.2}\text{O}_{3-\delta}$ catalyst showed highest CH₄ conversion of 86 % at 600 °C, which rose to 98 % at 750 °C. The H₂ to CO ratio of the product stream was 5.4, compared to 5.5 predicted by the thermodynamics.

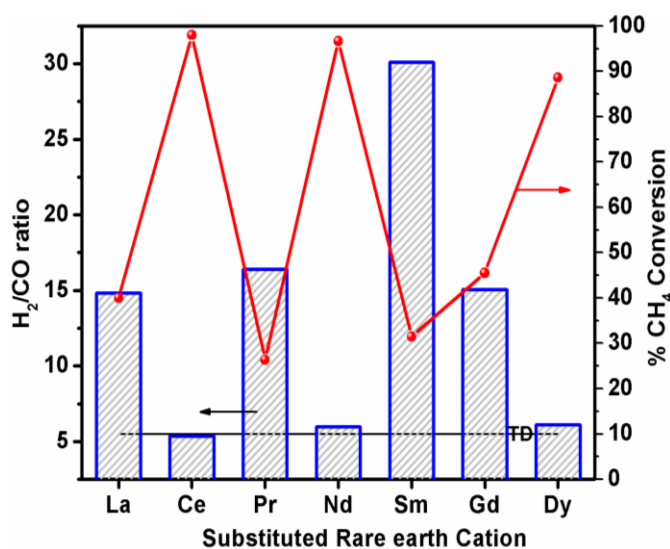


Fig. 3.7 CH₄ conversion and H₂/CO ratio and as function of Ln in SRM.

*Reaction conditions: Temp: 750°C; GHSV- 20,000 h⁻¹; 1atm; CH₄/H₂O = 3

These results show that both steam reforming and RWGS reactions approach to equilibrium in the given reaction conditions. The Ni metal is in close interaction with perovskite lattice in the case of $\text{CeAl}_{0.8}\text{Ni}_{0.2}\text{O}_{3-\delta}$, in addition to its high flexibility of Ce^{+3} to Ce^{+4} transition under varying oxygen lean to rich condition as a result of its high oxygen storage capacity (OSC). Whereas, in the case of other Ln substituted perovskite catalysts, H_2/CO ratios were above thermodynamically calculated values. These results show that the water gas shift reaction is more dominant on these catalysts, leading to the formation of higher H_2 . Overall, the $\text{CeAl}_{0.8}\text{Ni}_{0.2}\text{O}_{3-\delta}$ catalyst shows superior activity and good stability at high reaction temperatures during the screening experiments. [43]

3.4.2 Time on stream study

The on-stream stability of the best three catalysts $\text{CeAl}_{0.8}\text{Ni}_{0.2}\text{O}_{3-\delta}$, $\text{NdAl}_{0.8}\text{Ni}_{0.2}\text{O}_{3-\delta}$ and $\text{DyAl}_{0.8}\text{Ni}_{0.2}\text{O}_{3-\delta}$ were evaluated at 750°C , $\text{S/C} = 3$ and at 1 atm pressure, by changing the GHSV. These results are shown in Fig. 3.8.

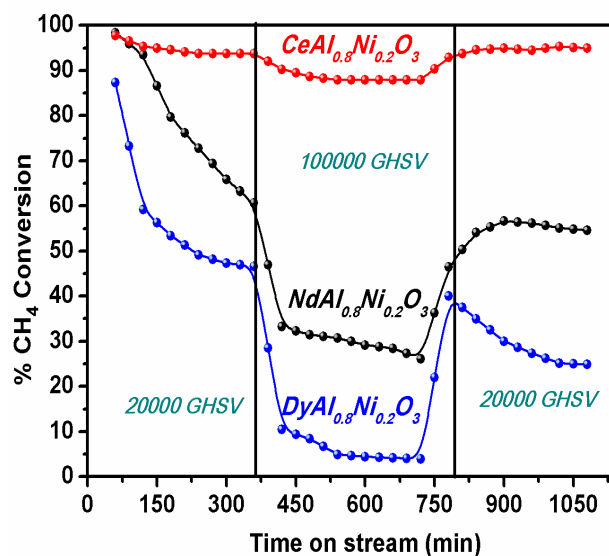


Fig. 3.8 TOS study of $\text{LnAl}_{0.8}\text{Ni}_{0.2}\text{O}_{3-\delta}$ (Ln = Ce, Nd and Dy) catalysts in SRM.
*Reaction conditions: Temp: 750°C ; 1 atm; $\text{CH}_4/\text{H}_2\text{O} = 3$, GHSV varied between 20,000 and 100,000 h^{-1}

The $\text{CeAl}_{0.8}\text{Ni}_{0.2}\text{O}_{3-\delta}$ perovskite catalyst shows better stability during the entire length of the experiment (1080 min). The initial methane conversion on it was 98% at GHSV of 20000 h^{-1} on $\text{CeAl}_{0.8}\text{Ni}_{0.2}\text{O}_{3-\delta}$, which was stabilized over a period of 360 min, after

a slight drop in methane conversion initially. After 360 min, the space velocity was switched to $100,000 \text{ h}^{-1}$, which led to a drop in CH_4 conversion to 88%. But, it was maintained at the same level for next 360 min. Subsequently, when the GHSV was changed back to $20,000 \text{ h}^{-1}$, it regained its initial conversion and was stable thereafter. On the otherhand, in case of $\text{NdAl}_{0.8}\text{Ni}_{0.2}\text{O}_{3-\delta}$ and $\text{DyAl}_{0.8}\text{Ni}_{0.2}\text{O}_{3-\delta}$ catalysts, activity dropped constantly during the same period, while never regaining during the switch over. The spent catalysts on investigation showed coke formation on $\text{NdAl}_{0.8}\text{Ni}_{0.2}\text{O}_{3-\delta}$ and $\text{DyAl}_{0.8}\text{Ni}_{0.2}\text{O}_{3-\delta}$ catalysts. Hence, we may conclude that $\text{CeAl}_{0.8}\text{Ni}_{0.2}\text{O}_{3-\delta}$ catalyst shows superior activity and durability, in addition to its good activity even at high space velocity compared to other lanthanide perovskites.

3.4.3 Transient pulse experiment of CH_4 and H_2O

Mass spectral signals of transient pulse experiments are shown in Fig. 3.9a, 3.9b and 3.9c. The $\text{CeAl}_{0.8}\text{Ni}_{0.2}\text{O}_{3-\delta}$, $\text{NdAl}_{0.8}\text{Ni}_{0.2}\text{O}_{3-\delta}$ and $\text{DyAl}_{0.8}\text{Ni}_{0.2}\text{O}_{3-\delta}$ are chosen for these pulse experiments. Initially, CH_4 was pulsed in to the reaction chamber and immediately followed by it, H_2 species were detected for all the catalysts. The rapid formation of H_2 species implies fast CH_4 decomposition over active Ni species, which has increased with temperature. This can also be seen through the detection of CO and CO_2 species. The carbon species formed during the CH_4 decomposition react with the surface oxygen to give oxygenated carbon products of CO and CO_2 . High intensities of CO and CO_2 in case of $\text{CeAl}_{0.8}\text{Ni}_{0.2}\text{O}_{3-\delta}$ catalyst compared to $\text{NdAl}_{0.8}\text{Ni}_{0.2}\text{O}_{3-\delta}$ and $\text{DyAl}_{0.8}\text{Ni}_{0.2}\text{O}_{3-\delta}$ catalysts may be attributed to its higher active metal dispersion (see Table 3.2). On decomposition of CH_4 over Ni^0 sites, CH_x and adsorbed H atoms are generated, while the later combines and leaves the surface as H_2 . On further decomposition of CH_x carbon species are formed, which are oxidized to produce CO and CO_2 at Ni-perovskite interface following the red-ox process. ^[44-46] The red-ox process is expected to proceed with the formation of surface oxygen vacancies. As these vacant sites are positively charged, they have high affinity towards oxygen. On interaction of H_2O with these positively charged surface vacancies, the H-O-H bond is weakened and subsequently dissociates resulting in the evolution of H_2 .

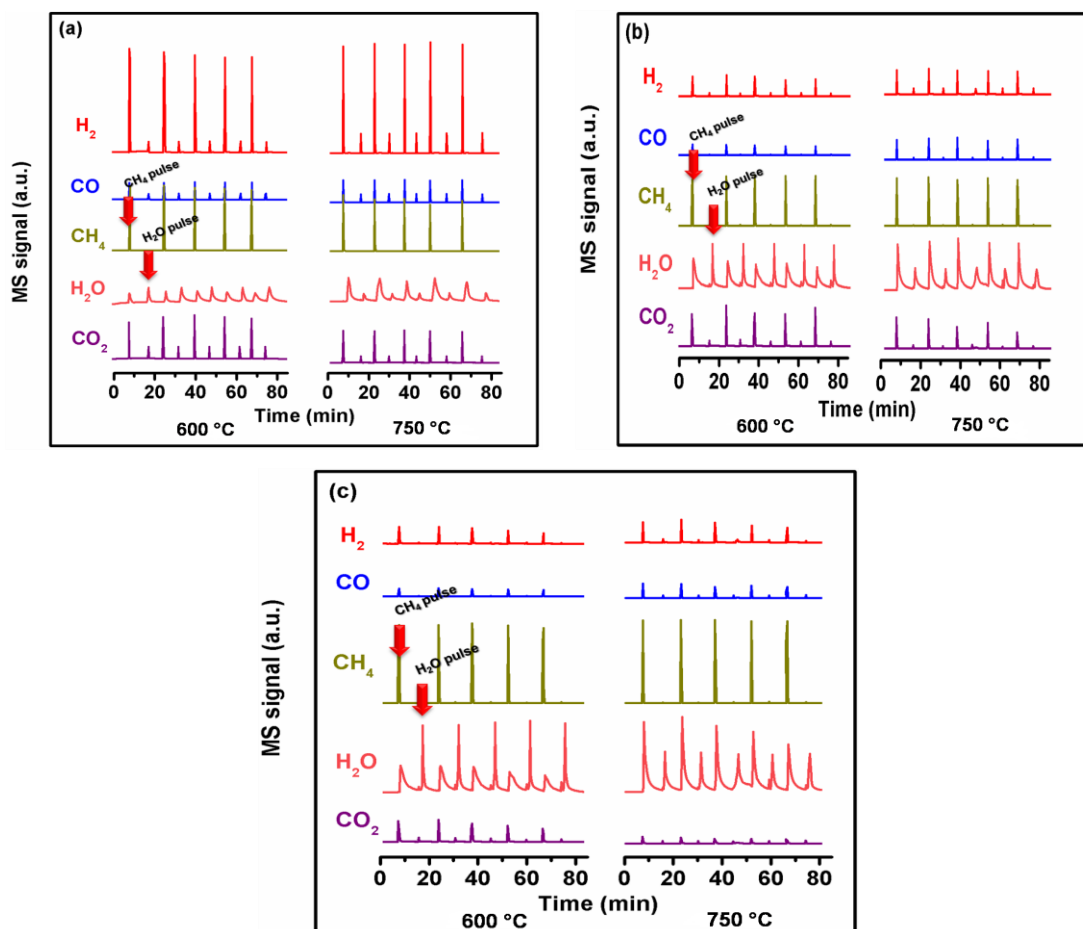


Fig. 3.9 Mass spectral signals during the pulse experiment over $\text{LnAl}_{1-x}\text{Ni}_x\text{O}_3$, where Ln = (a) Ce, (b) Nd and (c) Dy.

The proposed mechanism based on the reaction results and the pulse experiments clearly shows that both highly dispersed Ni and redox properties of $\text{CeAl}_{0.8}\text{Ni}_{0.2}\text{O}_{3-\delta}$ perovskites are important for the superior activity and stability. The intensity of H_2 , CO and CO_2 peaks in case of $\text{NdAl}_{0.8}\text{Ni}_{0.2}\text{O}_{3-\delta}$ and $\text{DyAl}_{0.8}\text{Ni}_{0.2}\text{O}_{3-\delta}$ perovskites are weak, possibly due to the nature of carbon formed over these catalysts, as it might be encapsulating the Ni sites, thereby blocking the reaction path to proceed further. Comparatively, the higher intensity of H_2 , CO and CO_2 signals after the steam pulse over $\text{CeAl}_{0.8}\text{Ni}_{0.2}\text{O}_{3-\delta}$ catalyst indicates the ease of dissociation of water molecules at oxygen vacant sites. The evolved oxygen during this process helps to remove the carbon over the active metal in the form of CO or CO_2 . Apart from this, significant appearance of the H_2 after steam pulse was observed, which may be attributed to the decomposition of formate like intermediates from the perovskite surface. On the

otherhand, this kind of strong signals were absent in the case of $\text{DyAl}_{0.8}\text{Ni}_{0.2}\text{O}_{3-\delta}$ and $\text{NdAl}_{0.8}\text{Ni}_{0.2}\text{O}_{3-\delta}$ perovskite catalysts.

3.4.4 Activity of Ni impregnated catalyst versus Ni substituted perovskite catalyst

Previously discussed results confirm superiority of $\text{CeAl}_{0.8}\text{Ni}_{0.2}\text{O}_{3-\delta}$ catalysts in terms activity and stability during SRM. Hence, Ni content during the synthesis of $\text{CeAl}_{1-x}\text{Ni}_x\text{O}_{3-\delta}$ (where $x= 0$ to 0.25) was varied and they were used for steam reforming of CH_4 . These results are shown in Fig. 3.10. With the increasing Ni content in $\text{CeAl}_{1-x}\text{Ni}_x\text{O}_{3-\delta}$, the CH_4 conversion increased upto $x = 0.2$. This shows that increasing Ni in CeAlO_3 structure creates more defects in addition to availability of more active Ni for steam reforming reaction. Figure 3.10 also compares the activity of Ni impregnated CeAlO_3 catalyst in terms of CH_4 conversion. As may be seen, the CH_4 conversion is much higher on Ni substituted catalyst ($\text{CeAl}_{0.8}\text{Ni}_{0.2}\text{O}_{3-\delta}$) compared to Ni impregnated catalyst (5.3% Ni/ CeAlO_3) that has similar Ni content..

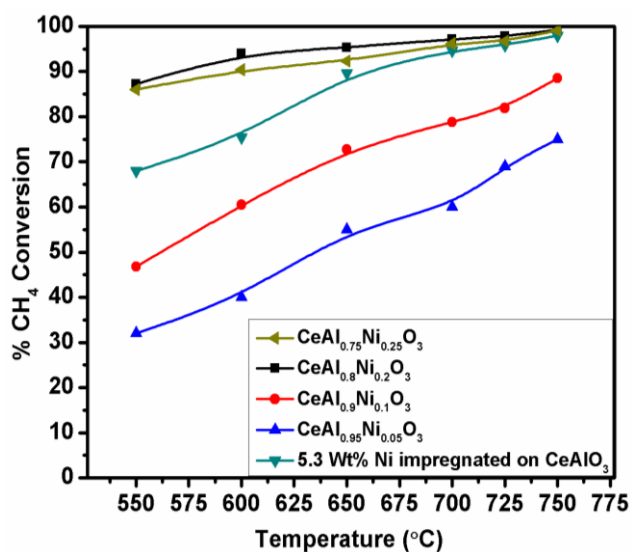


Fig. 3.10 CH_4 conversion as function of temperature with variation of Ni content and impregnated Ni catalyst in SRM reaction.

*Reaction conditions: GHSV- $20,000 \text{ h}^{-1}$; 1atm; $\text{CH}_4/\text{H}_2\text{O} = 3$

Based on the above results, it may be concluded that the following factors play important role in steam reforming reaction. First, substitution of Ni at Al site in the perovskite lattice leads to the generation of defects, i.e., enhanced oxygen storage capacity as observed in O_2 -TPD. Second is the formation of fine well dispersed Ni particles on reduction as observed through CO- chemisorption and the third is

enhanced reducibility of cationic Ni, as observed during H_2 -TPR. The synergy of all the three factors contribute to the superior performance of $\text{CeAl}_{0.8}\text{Ni}_{0.2}\text{O}_{3-\delta}$ catalyst relative to other Ni substituted Ln perovskite catalysts

3.4.5 Time on stream stability of substituted and impregnated catalysts

It is demonstrated that the $\text{CeAl}_{0.8}\text{Ni}_{0.2}\text{O}_{3-\delta}$ perovskite derived oxide is a good catalyst for SRM reaction. Hence, it will be interesting to compare the performance of $\text{CeAl}_{0.8}\text{Ni}_{0.2}\text{O}_{3-\delta}$ catalyst, prepared through citrate gel method, with Ni impregnated (5.3 wt %) catalyst prepared using CeAlO_3 perovskite oxide as support. Figure 3.11 shows that the SRM activity of Ni substituted perovskite ($\text{CeAl}_{0.8}\text{Ni}_{0.2}\text{O}_{3-\delta}$) catalyst is much higher compared to impregnated (Ni/ CeAlO_3) catalyst. The later catalyst was probably coked at a much faster rate owing to side reactions and probably would have completely deactivated if the reaction was continued for longer duration.

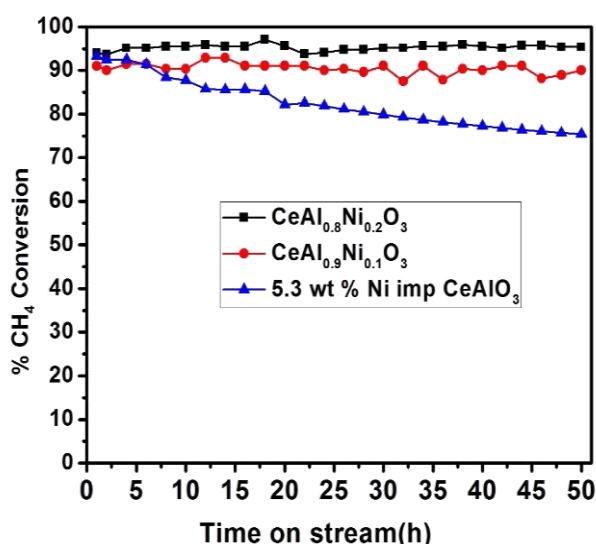


Fig. 3.11 Comparison of on-stream stability of $\text{CeAl}_{0.8}\text{Ni}_{0.2}\text{O}_{3-\delta}$ and $\text{CeAl}_{0.9}\text{Ni}_{0.1}\text{O}_{3-\delta}$ catalysts with 5.3 wt% Ni impregnated CeAlO_3 .

Reaction conditions: S/C = 3, 750 °C, GHSV = 20,000 h⁻¹ at 1 atm.

3.4.6 Kinetic study of SRM reaction over $\text{CeAl}_{0.8}\text{Ni}_{0.2}\text{O}_{3-\delta}$ catalyst

Kinetic data of SRM was collected in 500-600 °C (773 to 873 K) temperature range at 1 atm by maintaining different contact times. Contact time is expressed in terms of physical volume of the catalyst and volumetric flow of feed stream.

$$\text{Contact time} = \frac{\text{Volume of the catalyst (m}^3\text{)}}{\text{Volumetric flow of feed (m}^3\text{/sec)}} \quad (3.6)$$

The methane conversion versus contact time of methane in steam reforming reaction at different temperatures is given in Fig. 3.12.

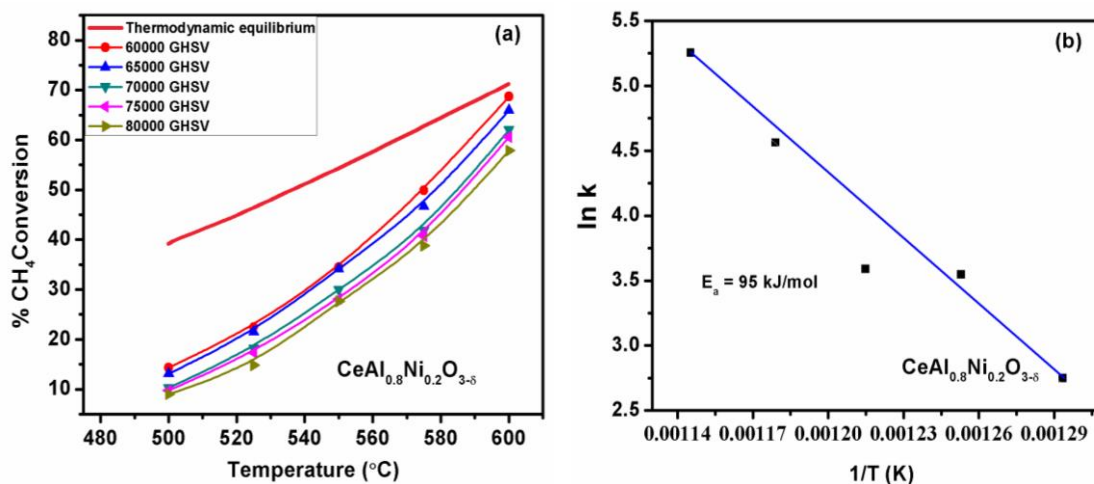


Fig. 3.12 CH₄ conversion on $\text{CeAl}_{0.8}\text{Ni}_{0.2}\text{O}_{3-\delta}$ catalyst at different temperatures and contact time; (b) Arrhenius plot for $\text{CeAl}_{0.8}\text{Ni}_{0.2}\text{O}_{3-\delta}$ catalyst.

*Reaction conditions: Pres- 1atm; H₂O: CH₄ = 3:1

It was observed that in the given temperature range, the CH₄ conversion increased with increasing contact time. As explained in section 1.6.2, based on the Wei and Iglesia mechanism, C-H bond activation is kinetically important step in CH₄ reforming reaction. The forward rate is not influenced by CO or H₂O or H₂ concentration, when they are varied by changing contact time.

$$\text{The rate of forward reaction in SRM} = k P_{\text{CH}_4} \quad (3.7)$$

According to the Arrhenius law, reaction rate SRM is temperature dependant. The plot of lnk versus 1/T provides the true activation energy. Figure 3.11b shows the Arrhenius plot for $\text{CeAl}_{0.8}\text{Ni}_{0.2}\text{O}_3$ perovskite catalyst. The calculated activation energy of 95 kJ/mol and pre exponential factor $2.018\text{E} +06 \text{ min}^{-1}$ are in good agreement with the literature data. [47-49]

3.4.7 Catalytic activity of $\text{CeAl}_{0.8}\text{Ni}_{0.2}\text{O}_{3-\delta}$ in simulated biogas reforming

Steam reforming of biogas was examined over the relatively best $\text{CeAl}_{0.8}\text{Ni}_{0.2}\text{O}_{3-\delta}$ catalyst using CH₄+CO₂ simulated gas mixture that is close to biogas composition. The composition of biogas depends on the specific treatment process, its origin in terms of animal/domestic waste or industrial organic waste.

Variation in Steam to CH_4 ratio in the steam reforming of simulated biogas

For all the reforming reactions involving biogas, a simulated composition consisting 60% CH_4 and 40% CO_2 were used. In real biogas, small concentrations of H_2S and nitrogen compounds are expected to be present even after purification. These can cause deactivation of the catalyst, unless they are removed to sub ppm level. [50-52] However, in these experiments, no external sulfur or nitrogen compounds are added. Conversion of CH_4 and CO_2 as function of time is shown in figure 3.13 at different steam to CH_4 ratios.

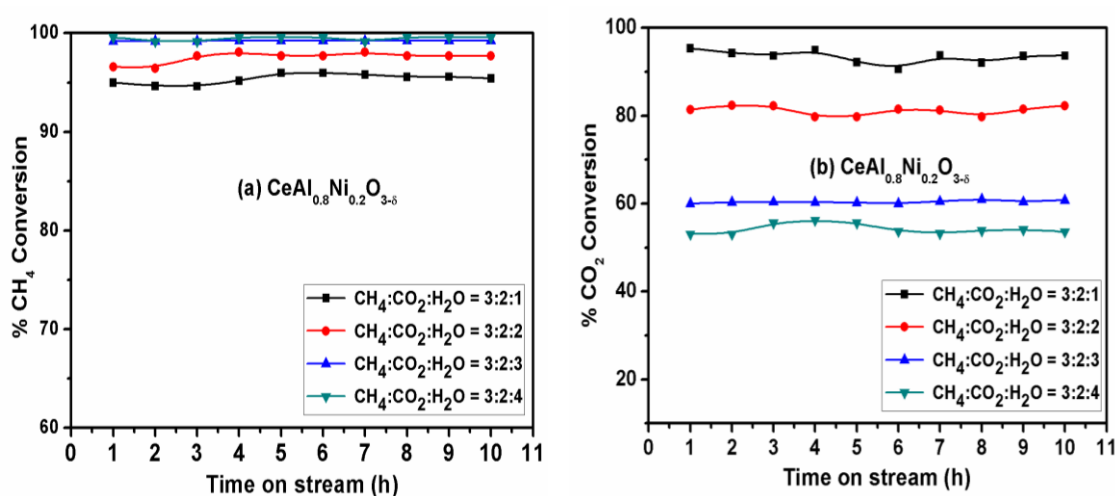


Fig. 3.13 Steam reforming of a simulated biogas over $\text{CeAl}_{0.8}\text{Ni}_{0.2}\text{O}_{3-\delta}$ catalyst.

*Reaction conditions: Temp: 800°C ; GHSV- $19,200\text{ h}^{-1}$; 1atm; $\text{CH}_4/\text{CO}_2 = 3/2$

During steam reforming of simulated biogas, several reactions are possible. Besides main reactions, carbon formation reaction mechanism depends on the process conditions like operating temperature, pressure, reformer design, gas composition and particularly steam content. The carbon formed during the reaction will gasify in the presence of steam or oxygen. [53] Hence, in order to suppress carbon formation, excess steam is added, which will also help to enhance CH_4 conversion. But, excess steam requires more amount of energy, leading to higher process costs. Hence, the steam to carbon ratio needs to be optimized carefully.

As may be seen from Fig. 3.13, CH_4 conversion linearly increased with steam but CO_2 conversion steeply fell, as steam reforming reaction becomes pre-dominant over the dry reforming of methane. At steam to CH_4 ratio 3:4 maximum CH_4 conversion (99%) was achieved. At lower steam to CH_4 ratios, dry reforming reaction

is more prevalent. At increasing $\text{H}_2\text{O}/\text{CH}_4$ ratios, more H_2 is produced leading to higher H_2/CO ratios. This variability in H_2/CO ratio is important, as different ratios are used for synthesis of various chemicals and fuels. When the reaction feed contains CH_4 , CO_2 and H_2O in the ratio of 3:2:4, the syngas produced has H_2/CO ratio of ~ 2 , which is useful for the synthesis of many chemicals, including methanol. Even for FT synthesis, this ratio is quite useful. Variation in H_2/CO ratio with different steam to carbon ratios is shown in Fig. 3.14. This data helps to prepare syngas with a desired composition based on the application. What is remarkable with this catalyst is that for all these feed gas ratios, the catalysts are quite stable.

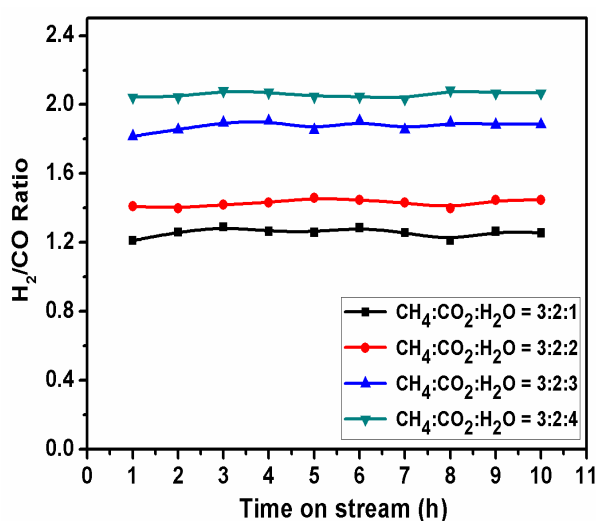


Fig. 3.14 Variation of H_2/CO ratio with $\text{H}_2\text{O}/\text{CH}_4$ ratio over the $\text{CeAl}_{0.8}\text{Ni}_{0.2}\text{O}_{3-\delta}$ for Bi-reforming reaction.

*Reaction conditions: Temp: $800\text{ }^\circ\text{C}$; GHSV- $19,200\text{ h}^{-1}$; 1atm; $\text{CH}_4/\text{CO}_2 = 3/2$

3.4.8 Time on stream study of bi-reforming of methane

Since, $\text{CeAl}_{0.8}\text{Ni}_{0.2}\text{O}_{3-\delta}$ catalyst showed excellent catalytic activity and attained equilibrium CH_4 and CO_2 conversions, its durability was tested for 100 h. Its performance is depicted in Fig. 3.15. It can be seen that both CH_4 and CO_2 conversions remained almost constant at about 95 and 88% respectively upto 100 h. The H_2/CO ratio was close to 1.8. The stable activity of $\text{CeAl}_{0.8}\text{Ni}_{0.2}\text{O}_{3-\delta}$ could be attributed either to the low coke formation on the surface of catalyst or the type of carbon deposited does not block the active sites of the catalysts during the reaction. Probably, the oxygen defects created on Ni substitution might be helping in the

removal of coke formed during the reaction, thus imparting greater durability to the catalyst.

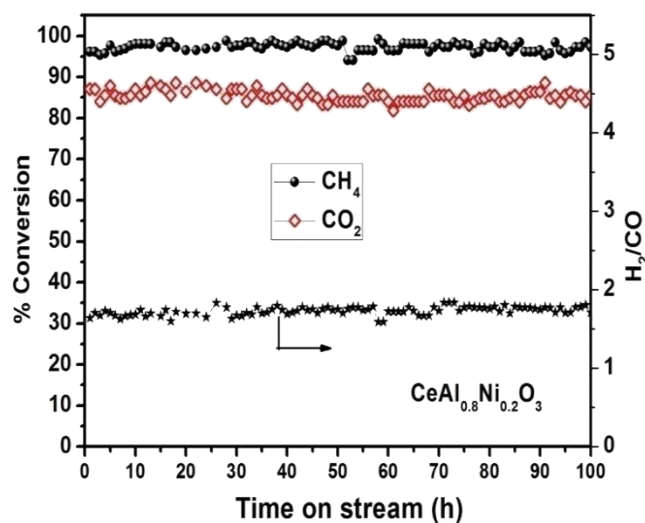
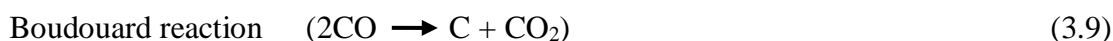
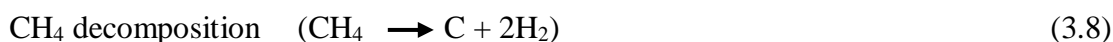


Fig. 3.15 TOS behaviour of $\text{CeAl}_{0.8}\text{Ni}_{0.2}\text{O}_{3-\delta}$ perovskites in bi-reforming of CH_4 .

*Reaction conditions: Temp: 800°C ; GHSV- $22,068\text{ h}^{-1}$; 1atm;
 $\text{CH}_4/\text{CO}_2/\text{H}_2\text{O} = 3/1.5/2$

3.5 Characterization of spent catalysts

Deactivation of the catalysts during SRM due to coking is a serious issue that needs to be addressed to develop a catalyst that is stable for thousands of hours. In this respect, characterization of spent catalysts is important to understand the types of coke precursors deposited on the catalyst, in order to know the potential causes of catalyst deactivation. Generally, there are two main pathways that lead to the carbon formation on catalysts:



The spent catalysts were extensively characterized by Raman spectroscopy, TGA, XPS and HRTEM to understand the coke formed, so that remedial measures can be suggested to suppress its formation.

3.5.1 Raman and TGA analysis

Raman spectroscopy of spent catalyst throws light on various carbon species present on the surface of spent catalyst as shown in Fig. 3.16a.

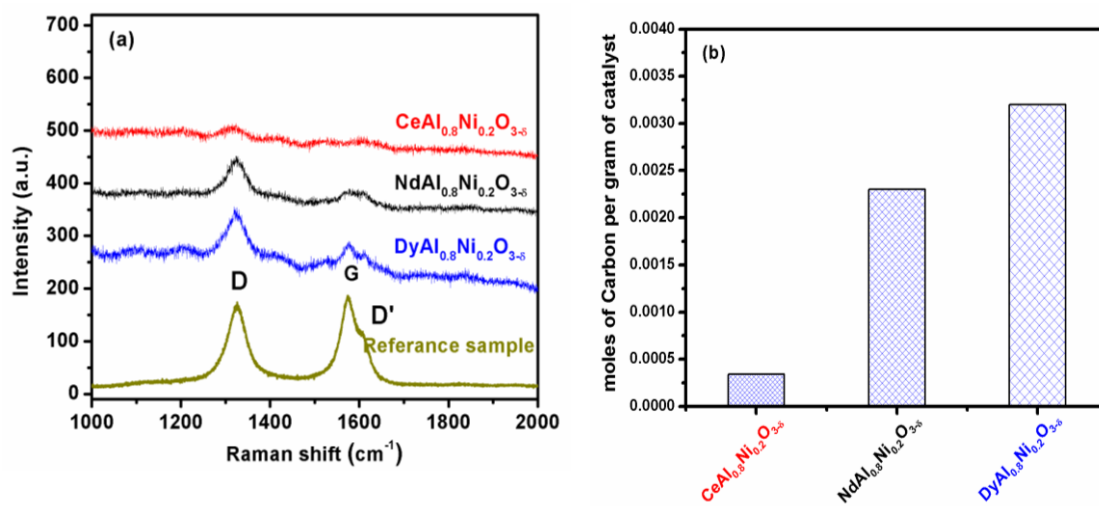


Fig. 3.16 Characterization of coke present on spent catalysts after SRM for 18 h.

(a) Raman spectra, (b) coke content from TGA.

The three catalysts $\text{CeAl}_{0.8}\text{Ni}_{0.2}\text{O}_{3-\delta}$, $\text{NdAl}_{0.8}\text{Ni}_{0.2}\text{O}_{3-\delta}$ and $\text{DyAl}_{0.8}\text{Ni}_{0.2}\text{O}_{3-\delta}$ are compared for the coke formation. Figure 3.16 also contains Raman spectra of coke precursors formed on the catalyst used for dry reforming of methane, to be used as a reference. All spectra show two major bands at 1328 cm^{-1} (D-band) and 1580 cm^{-1} (G-band), with a low intensity peak on the right side to G band. The D-band corresponds to the disordered amorphous carbon formed with structural imperfections [54]. The G- band is attributed to stretching vibrations of sp^2 carbon in graphitic material and was designated as E_{2g} mode. The small band at 1620 cm^{-1} (D'-band) indicates the presence of disordered graphitic material. [55] On all spent catalysts following SRM, the intensity of D- band is higher than that of G- band. The Larger intensity of D- band indicates that during the deactivation abundant defective carbon species are formed which may subsequently convert to graphite. It is seen that relatively more coke was observed over Dy and Nd containing catalysts. In case of Ce substituted perovskite catalysts, minimal coke was observed, which is also confirmed by TGA. Moles of carbon formed per gram of catalyst after 18 h of reaction is shown in Fig. 3.16b. The amount carbon formed over the Ni samples increased in the sequence: $\text{CeAl}_{0.8}\text{Ni}_{0.2}\text{O}_{3-\delta} < \text{NdAl}_{0.8}\text{Ni}_{0.2}\text{O}_{3-\delta} < \text{DyAl}_{0.8}\text{Ni}_{0.2}\text{O}_{3-\delta}$.

3.5.2 XPS of Spent catalysts

Figure 3.17 shows C1s spectra of spent Ce, Nd and Dy doped perovskite catalysts. A broad peak at 284.5 eV corresponds to the graphitic carbon, while the peak at 286.2

eV corresponds to surface carbonates. The intensity of both carbon peaks is very high in the case of $\text{DyAl}_{0.8}\text{Ni}_{0.2}\text{O}_{3-\delta}$ and $\text{NdAl}_{0.8}\text{Ni}_{0.2}\text{O}_{3-\delta}$ perovskite catalysts. Whereas, $\text{CeAl}_{0.8}\text{Ni}_{0.2}\text{O}_{3-\delta}$ spent catalysts has less amount of carbonate carbon. These carbon species are deposited on Ni faces of catalyst and may be responsible for rapid deactivation of $\text{DyAl}_{0.8}\text{Ni}_{0.2}\text{O}_{3-\delta}$ and $\text{NdAl}_{0.8}\text{Ni}_{0.2}\text{O}_{3-\delta}$ catalysts. [56]

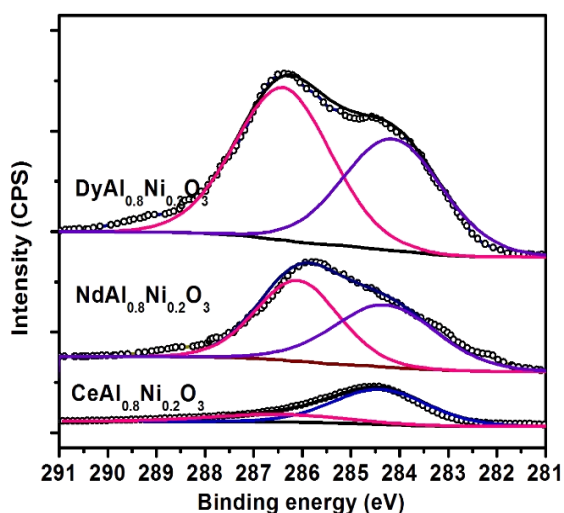


Fig. 3.17 XPS of spent $\text{LnAl}_{0.8}\text{Ni}_{0.2}\text{O}_{3-\delta}$ ($\text{Ln} = \text{Ce}, \text{Nd}$ and Dy) catalysts after SRM.

3.5.3 TEM analysis of spent catalysts

The Raman, TGA and XPS results demonstrate the formation of coke mostly on $\text{DyAl}_{0.8}\text{Ni}_{0.2}\text{O}_{3-\delta}$ and $\text{NdAl}_{0.8}\text{Ni}_{0.2}\text{O}_{3-\delta}$ perovskite catalysts. The type of carbon formed on the spent catalysts was investigated by electron microscopy. The TEM micrographs are expected to reveal the presence of different types of carbon present on the three catalysts depending on the nature of perovskite, oxygen defects and Ni particle size (derived from CO chemisorption). Generally, three types of carbon can be seen, i.e., (i) amorphous carbon, (ii) graphitic carbon and (iii) multi walled carbon nanotubes (MWCNT). Carbon nanotubes can form through diffusion/elimination pathway, which would result in the separation of active Ni species from the support. [57] On the otherhand, some pear shaped Ni particles placed at the tip of carbon nanotubes are expected to be still active for the reaction, while Ni particles that are incorporated into the carbon nanotubes may no longer be available for the reaction.

Figure 3.18 shows TEM micrographs of samples used for 18 h of SRM. The $\text{DyAl}_{0.8}\text{Ni}_{0.2}\text{O}_{3-\delta}$ and $\text{NdAl}_{0.8}\text{Ni}_{0.2}\text{O}_{3-\delta}$ catalysts show different kinds of surface carbon.

These are amorphous carbon, filamentous carbon or carbon nanotubes with Ni at the tip and carbon nanotubes embedded with Ni particles inside. On the otherhand, only amorphous carbon was seen on $\text{CeAl}_{0.8}\text{Ni}_{0.2}\text{O}_{3-\delta}$ catalyst, which is not expected to cause any deactivation of the catalyst during the SRM reaction. Over $\text{DyAl}_{0.8}\text{Ni}_{0.2}\text{O}_{3-\delta}$ catalyst, formation of CNT along with Ni particles in the range of 30-40 nm were seen, which were separated from the perovskite phase. These masked Ni particles may no longer be active for the DRM reaction. Though carbon deposition was noticed in case of $\text{CeAl}_{0.8}\text{Ni}_{0.2}\text{O}_{3-\delta}$ catalyst, this was to a less extent as seen from Fig. 3.18c. Also, the size of Ni particles over $\text{CeAl}_{0.8}\text{Ni}_{0.2}\text{O}_{3-\delta}$ catalyst did not change much (20-25 nm) demonstrating its excellent resistance to sintering.

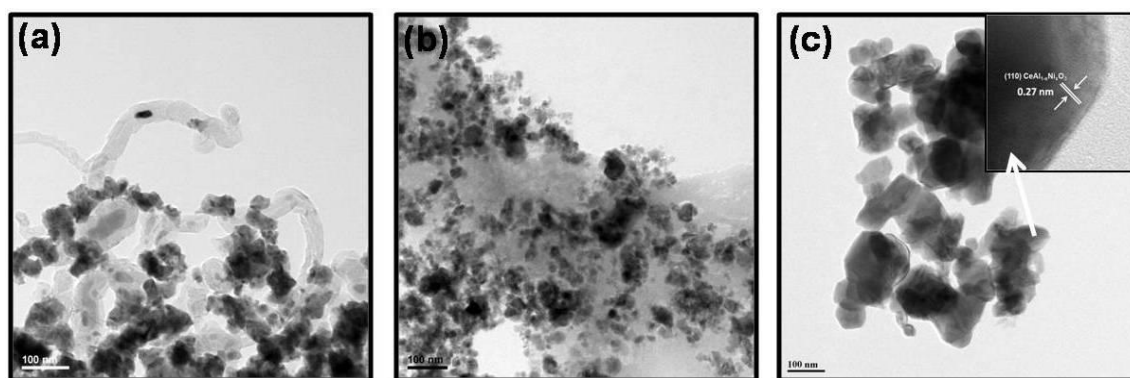


Fig. 3.18 HRTEM images of spent catalysts for $\text{LnAl}_{0.8}\text{Ni}_{0.2}\text{O}_{3-\delta}$; where Ln = (a)Dy (b)Nd & (c)Ce.

3.6 Conclusions

Lanthanide substituted perovskite oxides $\text{LnAlO}_{3-\delta}$ and $\text{LnAl}_{0.8}\text{Ni}_{0.2}\text{O}_{3-\delta}$ (Ln = La, Ce, Pr, Nd, Sm, Gd, Dy; x = 0.0 and 0.2) catalysts were successfully prepared by citrate gel method. These materials were characterized for structural and textural properties by XRD, Raman, BET surface area, CO chemisorption and the Ni substituted oxides were used as catalysts for steam reforming of methane and simulated biogas. Among the catalysts, $\text{CeAl}_{0.8}\text{Ni}_{0.2}\text{O}_{3-\delta}$ was found to be better in terms of active metal dispersion, reducibility and oxygen defects which could be correlated with reforming activity. Similarly, when different Ni containing catalysts were prepared by citrate gel method, $\text{CeAl}_{0.8}\text{Ni}_{0.2}\text{O}_{3-\delta}$ was found to be optimum for good activity. Moreover, when this catalyst was evaluated for 100 h to check its on-stream stability; its activity was found to be stable even after 100 h on stream in bi-

reforming of simulated bio-gas. Transient pulse experiments suggest that carbon species formed on the surface of $\text{CeAl}_{0.8}\text{Ni}_{0.2}\text{O}_{3-\delta}$ perovskite are eliminated through reaction with surface oxygen and hence redox nature of perovskite plays an important role in reforming reactions. However, in case of $\text{NdAl}_{0.8}\text{Ni}_{0.2}\text{O}_{3-\delta}$ and $\text{DyAl}_{0.8}\text{Ni}_{0.2}\text{O}_{3-\delta}$ catalysts, high content of coke was seen on the catalyst, when the catalyst was investigated using thermo gravimetric analysis. It appears from TEM studies that Ni particles on these catalysts are mostly covered with coke as they are present at the tip of the carbon nanotubes formed under steam reforming conditions. However, there is some increase in the size of some Ni particles on prolonged reaction time, which might be responsible for the formation of hard graphitic coke that is responsible for the deactivation of the catalysts. The high activity and stability of $\text{CeAl}_{0.8}\text{Ni}_{0.2}\text{O}_{3-\delta}$ can be correlated to abundant concentration of labile oxygen vacancies and appropriate metal to lattice interaction.

3.7. References

1. P. V. Tuza, M. M. V. M. Souza, *Catal Lett*, 2016, **146**, 47.
2. P. Kolbitsch, C. Pfeifer, H. Hofbauer, *Fuel* 2008, **87**, 701.
3. H.J. Alves, C.J. Bley, R. R. Niklevicz, E.P. Frigo, M.S. Frigo, C.H. Coimbra-Araujo, *Int J Hydrogen Energy*, 2013, **38**, 5215.
4. G. Jones, J.G. Jakobsen, S.S. Shim, J. Kleis, M.P. Andersson, J. Rossmeisl, F. Abild-Pedersen, T. Bligaard, S. Helveg, B. Hinnemann, J.R. Rostrup-Nielsen, I. Chorkendorff, J. Sehested, J.K. Nørskov, *J Catal*, 2008, **259**, 147.
5. D. Mei, V-A. Glezakou, V. Lebarbier, L. Kovarik, H. Wan, K.O. Albrecht, M. Gerber, R. Rousseau, R.A. Dagle, *J Catal*, 2014, **316**, 11.
6. J.P. Van Hook, *Catal. Rev. Sci. Eng.* 1980, **21**, 1.
7. J.R. Rostrup Nielson, D.L. Trimm, *J. Catal.* 1977, **48**, 155.
8. M.A. Nieva, M.M. Villaverde, A. Monzon, T.F. Garetto, A.J. Marchi, *Chem Eng J.* 2014, **235**, 158.
9. A.M. Gadalla, B. Bower, *Chem. Eng. Sci.* 1988, **43**, 11, 3049.
10. J. R. H. Ross, M. C. F. Steel, A. Zeiniifahani, *J. Catal.* 1978, **52**, 280.
11. N. Salhi, C. Petit, A. Kiennemann, *Stud. Surf. Sci. Catal.* 2008, **174**, 1335.
12. A. Alubaid, E. E. Wolf, *Appl. Catal.* 1988, **40**, 73.
13. Z. L. Xu, M. Zhen, Y. L. Bi, K. J. Zhen, *Appl. Catal., A* 2000, **198**, 267.
14. J. Deng, M. Cai, W. Sun, X. Liao, W. Chu, X. S. Zhao, *ChemSusChem* 2013, **6**, 2061.
15. K. Zhang, G. D. Zhou, J. Li, T. X. Cheng, *Catal. Commun.* 2009, **10**, 1816.
16. N. F. P. Ribeiro, R. C. R. Neto, S. F. Moya, M. M. V. M. Souza, M. Schmal, *Int. J. Hydrogen Energy* 2010, **35**, 11725.
17. A. R. Gonzalez, Y. J. O. Asencios, E. M. Assaf, J. M. Assaf, *Appl. Surf. Sci.* 2013, **280**, 876.

18. N. Sahli, C. Petit, A. C. Roger, A. Kiennemann, S. Libs, M. M. Bettahar, *Catal. Today* 2006, **113**, 187.
19. W. L. Chu, W. S. Yang, L. W. Lin, *Catal. Lett.* 2001, **74**, 139.
20. K.T.C. Roseno, R. Brackmann, M.A. da Silva, M. Schmal, *Int. J. hydrogen energy* 2016, **41**, 18178.
21. B. Menga, H. Zhanga, Z. Zhaoa, X. Wanga, Y. Jina, S. Liu, *Catal Today* 2016, **259**, 388.
22. Y. Nishihata, J. Mizuki, T. Akao, H. Tanaka, M. Uenishi, M. Kimura, T. Okamoto, N.Hamada, *Nature* 2002, **418**, 164.
23. H. Kizaki, K. Kusakabe, S. Nogami, H. Katayama-Yoshida, *Appl. Phys. Express* 2008, **1**, 104001.
24. E. Pietri, A. Barrios, O. Gonzalez, M. Goldwasser, M. Pe´rez-Zurita, M. Cubeiro, J. Goldwasser, L. Leclercq, G. Leclercq, L. Gingembre, *Stud. Surf. Sci. Catal.* 2001, **136**, 381.
25. G. S. Gallego, F. Mondragon, J. Barrault, J.M. Tatibouet, C. Batiot- Dupeyrat, *Appl. Catal A: Gen.* 2006, **311**,164.
26. M. C. Weber, J. Kreisel, P. A. Thomas, M. Newton, K. Sardar, R. I. Walton. *Phys rev B* 2012, **85**, 54303.
27. A. M. Abakumov, R. Erni, A. A. Tsirlin, M. D. Rossell, D. Batuk, G. Nenert, G. V. Tendeloo, *Chem. Mater.* 2013, **25**, 2670.
28. M. Shatnawi, E. S. Bozin, J. F. Mitchell, S. J. L. Billinge, *Phys rev B* 2016, **93**, 165138.
29. H. M. Rietveld, *J. Appl. Crystallogr.* 1969, **2**, 65.
30. B. H. Toby, *J. Appl. Crystallogr.* 2001, **34** (2), 210.
31. R. Louden, *Adv. Phys.* 1964, **13**, 42382.
32. M. V. Abrashev, A. P. Litvinchuk, M. N. Iliev, R. L. Meng, V. N. Popov, V. G.

- Ivanov, R. A. Chakalov, C. Thomsen, *Phys rev B* 1999, **59**, 4146.
33. J.F. Scott, *Phys. Rev.* 1969, **183**, 823.
34. J. A. Alonso, M. J. Martinez-Lope, M. T. Casais, M. T. Fernandez-Diaz, *Inorg. Chem.* 2000, **39**, 917.
35. R.J.H. Voorhoeve, J.P. Remeika, P.E. Freeland, B.T. Mattias, *Science* 1972, **177**, 353.
36. M. Alifanti, J. Kirchnerova, B. Delmon, D. Klvana, *Appl. Catal. A Gen.* 2004, **262**, 167.
37. T. Seiyama, N. Yamazoe, K. Eguchi, *Ind. Eng. Chem. Prod. Res. Dev.* 1985, **24**, 19.
38. B. P. Barbero, J. A. Gamboa, L. E. Cadus, *Appl. Catal. B: Envi.* 2006, **65**, 21.
39. F.F. de Sousa, H.S.A. de Sousa, A.C. Oliveira, M.C.C. Junior, A.P. Ayala, E.B. Barros, B.C. Viana, J.M. Filho, A.C. Oliveira, *Int. J. of Hydrogen Energy*, 2012, **37**, 3201.
40. Y.N. Lee, R.M. Lago, J.L.G. Fierro, V. Cortes, F. Sapina, E. Martinez, *Appl. Catal. A* 2001, **207**, 17.
41. G. Pecchia, P. Reyesa, R. Zamoraa, L.E. Cadus, J.L.G. Fierroc, *J Solid State Chem* 2008, **181**, 905.
42. S. Nandy, B. Saha, M. K. Mitra, K. K. Chattopadhyay, *J Mater Sci* 2007, **42**, 5766.
43. M.E.S. Hegarty, A.M. O'Connor, J.R.H. Ross, *Catal Today* 1998, **42**, 225.
44. J.D.A. Bellido, E.M. Assaf, *Appl. Catal. A: Gen.* 2009, **352**, 179.
45. N. Sun, X. Wen, F. Wang, W. Peng, N. Zhao, F. Xiao, W. Wei, Y. Sun, J. Kang, *Appl. Surf. Sci.* 2011, **257**, 9169.
46. J. Gao, Z. Hou, X. Liu, Y. Zeng, M. Luo, X. Zheng, *Int. J. Hydrogen Energy* 2009, **34**, 3734.

47. C.-T. Au, C.-F. Ng, M.-S. Liao, *J. Catal.* 1999, **185**, 12.
48. I. M. Ciobica, F. Frechard, R. A. van Santen, A. W. Kleyn, J. Hafner, *J. Phys. Chem. B* 2000, **104**, 3364.
49. J. P. Liu, P. Hu, *J. Am. Chem. Soc.* 2003, **125**, 1958.
50. M. Ashrafi, T. Proll, C. Pfeifer, H. Hofbauer, *Energy Fuels* 2008, **22**, 4182.
51. J. R. Rostrup-Nielsen, J. Sehested, *Adv. Catal.* 2002, **47**, 65.
52. A. Effendi, K. Hellgardt, Z.-G. Zhang, T. Yoshida, *Fuel* 2005, **84**, 869.
53. A. M. D. Groote, G. F. Froment, *Appl. Catal., A* 1996, **138**, 245.
54. A. Cuesta, P. Dhamelincourt, J. Laureyns,;A. Martinez-Alonso, J.M.D. Tascón, *Carbon*, 1994, **32**, 1523.
55. R. Tsu, J. H. Gonzalez, I. C. Hernandez, *Solid state Commun.* 1978, **27**, 507.
56. J. L. Ewbank, L. Kovarik, C.C. Kenvin, C. Sievers, *Green Chem.* 2014, **16**, 885.
57. C. Wang, N. Sun, N. Zhao, F. Xiao, W. Wei, J. Zhang, T. Zhao, Y. Sun, C. Sun, H. Liu, C.E. Snape, *Chem. Cat. Chem.* 2014, **6**, 640.

Chapter 4

Syngas with variable H₂/CO ratios
using Ru and Rh substituted
perovskites by steam, Bi- and
Tri-reforming of methane

This chapter deals with syngas generation through steam reforming (SRM), bi-reforming (BRM) and tri-reforming (TRM) of methane over Ru and Rh substituted perovskites. It is divided into two parts. Part-I describes the synthesis, characterization and application of Ru substituted CeAlO₃ and CeAl_{1-x}Ni_xO_{3-δ} perovskites for SRM, BRM and TRM of methane, while part-II deals with synthesis and characterization of Rh substituted CeAlO₃ perovskites and their sulfur tolerance in steam reforming of methane and simulated biogas.

Part-I

Ru and Ru-Ni substituted CeAlO₃ perovskites for steam, bi- and tri-reforming of methane

4.1 Introduction

In chapter 3, steam reforming of methane over Ni substituted LnAlO₃ (where Ln = La, Ce, Pr, Nd, Sm, Gd and Dy) perovskite catalysts was discussed. Among them, CeAl_{0.8}Ni_{0.2}O₃ catalyst showed superior activity in steam and bi-reforming reactions. However, these Ni based catalysts are not expected to be tolerant to sulphur in methane even in ppm concentration. It is well known that noble metal based catalysts containing Ru, Rh and Pt are less prone to coke formation and sulfur poisoning compared to Ni based catalysts in reforming reactions.^[1-4] Hence, in this chapter Ru substituted CeAlO₃ catalysts were prepared, characterized and tested for SRM reaction. However, considering higher cost and the limited availability of noble metals, attempt was made to reduce Ru content by using it as second metal in Ni-substituted CeAlO₃, so that it can be translated for commercial applications. This little content of noble metal addition is expected to help promote easy reduction of Ni species and prevent its sintering at higher temperatures. Hence, this part of study was aimed at developing Ru and Ru-Ni metal based catalysts that are resistant to coke formation, while retaining good activity during SRM, BRM and TRM reactions.

4.2 Experimental methods

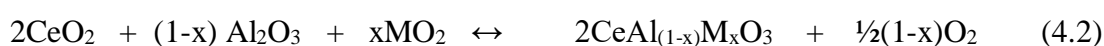
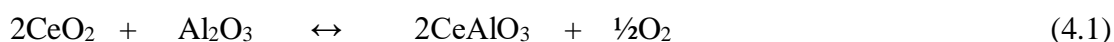
4.2.1 Preparation of Ru substituted CeAlO₃ and Ru impregnated CeAlO₃

The CeAlO₃ perovskite was reported for the first time by Zachariassen in 1949. It was prepared at high temperatures following a solid state reaction method under

vacuum at 1470 K for 48 h. ^[5] In fact, Fu et al. reported its preparation even at higher (1748 K) temperature. ^[6] In the present study, we have carried out CeAlO₃ and CeAl_{1-x}Ru_xO₃ synthesis by following a low temperature synthesis method and substituted transition metals such as Ru and Ni-Ru at its ‘B’ site. For this purpose, citrate gel method was employed to initially get the precursors of the mixed oxides, which were subsequently reduced in 25% H₂ containing nitrogen gas stream at 750 °C for 6 h, to obtain CeAlO₃ and corresponding metal substituted perovskite oxides.

Perovskite type oxides, CeAl_{1-x}Ru_xO₃ (x = 0.07, 0.1, 0.15 and 0.2) with nominal Ru contents of 3.21, 4.54, 6.7 and 9 wt % of Ru were synthesized by the above described method. Required amount of precursors of B site cations Al(NO₃)₃.9H₂O and Ru(NO)(NO₃)₃ and ‘A’ site cation Ce(NO₃)₃.6H₂O were dissolved in minimum amount of de-ionized water. This nitrate solution was added to the citric acid solution at room temperature. The mixture was stirred vigorously at 80 °C till a viscous gel was formed. The gel was further dried at 180 °C for 12 h and crushed to get powder. This was calcined in air at 550 °C for 6 h, to get homogeneous mixed oxides. The mixed oxide was reduced at 750 °C for 6-8h in 25% H₂+75%N₂ gas to yield perovskite.

Samples of CeAlO₃, CeAl_{1-x}Ru_xO₃ and CeAl_(1-x-y)Ru_xNi_yO₃ are obtained on removal of oxygen from oxide precursor according to the following reaction :



Ru impregnated CeAlO₃ catalyst (CARu-imp) was prepared by dry impregnation method. Details of the method of preparation are given in chapter 2 (section 2.3.1). All the prepared catalysts were characterized using various physico-chemical characterization techniques and were evaluated for reforming of methane.

4.3 Results and discussion

4.3.1 X-ray diffraction (XRD) studies of CeAl_{1-x}Ru_xO₃ perovskites

X-ray diffraction pattern of CeAlO₃ (CAO), CeAl_{1-x}Ru_xO₃, with x = 0.07, 0.1, 0.15 and 0.2 denoted as CARu0.07, CARu0.1, CARu0.15 and CARu0.2; and Ru impregnated CeAlO₃ samples are given in Fig. 4.1. The CeAlO₃ diffraction profile shows it has crystallized in cubic phase with space group Pm3m, which is in good

agreement with JCPDS 48-0051. No extraneous phases, particularly CeO₂, are seen in this sample. The peaks are very sharp indicating high degree of crystallinity.

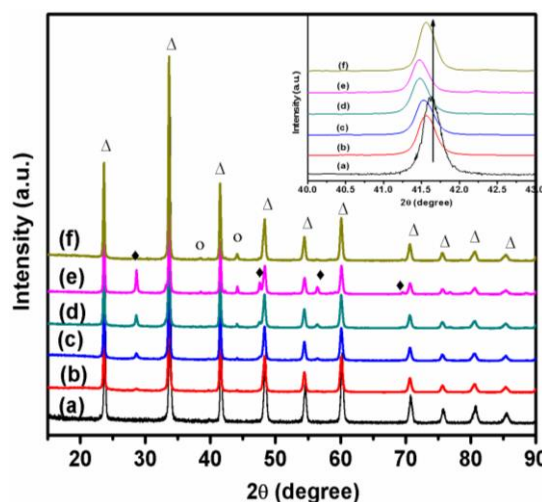


Fig. 4.1 XRD of CeAlO₃ family of perovskites (a) CeAlO₃, (b) CeAl_{0.93}Ru_{0.07}O₃, (c) CeAl_{0.9}Ru_{0.1}O₃, (d) CeAl_{0.85}Ru_{0.15}O₃ (e) CeAl_{0.8}Ru_{0.2}O₃ (f) Ru imp CeAlO₃ (ΔCeAlO₃, ○Ru Metal, ♦CeO₂)

In the case of Ru substituted CeAlO₃ samples, additional peaks were seen at 28.61 and 44.12° assigned to CeO₂ and Ru present in the samples. At higher Ru content, the intensity of these peaks increased, which indicates non substitution of a part of Ce and Ru, used during the synthesis, into perovskite lattice. XRD results reveal that Ru in the perovskite samples exists in two forms: (i) as finely dispersed Ru metal on the surface and (ii) substituted Ru in the bulk of perovskite lattice. When large Ru³⁺ (0.68 nm) cation replaces Al³⁺ at the B site of the CeAlO₃ perovskite lattice, expansion of the host lattice is expected as the Al³⁺ (0.535 nm) is smaller than Ru³⁺. This expansion causes strain in the lattice and changes the lattice plane spacing with the diffraction peak shifting to lower '2θ' positions, thus demonstrating the Ru substitution. The refinement of the diffraction data was carried out using Rietveld methodology [7, 8] to verify the crystal structure. It is observed from Table 4.1 that the cell parameter increased with increasing Ru content.

4.3.2 Textural and structural properties

The BET surface area and metal dispersion were determined by N₂ physisorption and CO chemisorption respectively. Table 4.1 lists specific surface areas and metal dispersion of Ru substituted perovskites. It was observed that with

increasing Ru in the perovskite lattice, surface area has increased as a result of decrease in the crystallite size. However metal dispersion has decreased with increasing Ru content of the sample. In any case, specific surface areas as well as metal dispersion values are low probably as a result of higher calcinations/reduction temperatures used to obtain these structures. The crystallite sizes of the samples were estimated using XRD line-broadening of the peak at $2\theta = 41.4^\circ$ corresponding to the (111) plane using Scherrer equation. The crystallite sizes of CeAlO₃, CARu0.07, CARu0.1, CARu0.15 and CARu0.2 were 42, 37, 35, 31 and 32 nm respectively (Table 4.1), suggesting that the crystallite size decreased with increasing Ru content of the sample. When a dopant is substituted in a lattice, the crystal growth is curtailed, hence their size is reduced. The results indirectly show the substitution of Ru in CeAlO₃ lattice. However, all the textural properties are not much affected above 0.2 substitution of Ru in the CeAlO₃ lattice.

Table 4.1 Textural and structural properties of CeAl_{1-x}Ru_xO₃ perovskite type oxide catalysts.

Formula	CeAlO ₃	CeAl _{0.93} Ru _{0.07} O ₃	CeAl _{0.9} Ru _{0.1} O ₃	CeAl _{0.85} Ru _{0.15} O ₃	CeAl _{0.8} Ru _{0.2} O ₃
Space group	Pm-3m	Pm-3m	Pm-3m	Pm-3m	Pm-3m
a/Å	3.7707(3)	3.7712(2)	3.7716(2)	3.7718(2)	3.7719(3)
b/Å	3.7707(3)	3.7712(2)	3.7716(2)	3.7718(2)	3.7719(3)
c/Å	3.7707(3)	3.7712(2)	3.7716(2)	3.7718(2)	3.7719(3)
V/Å ³	53.612	53.634	53.651	53.659	53.663
R _p (%)	7.4	5.2	8.7	5.3	4.9
wR _p (%)	9.3	6.1	9.5	7.6	6.1
χ ²	1.892	1.495	1.477	1.342	1.791
Crystallite size (nm) ^a	42	37	35	31	32
Ru wt% (From refinement) ^a	0	1.74	2.58	3.20	6.44
Surface area (m ² /g) ^b	5.7	6.3	8.8	10.5	10.8
Tolerance factor ^c	1.00	0.995	0.993	0.989	0.985
Ru wt % from ICP-OES (expected)	-	2.9(3.2)	4.3(4.5)	6.4(6.7)	8.8(9.0)
Ru dispersion (%) ^d	-	10.5	7.8	6.0	4.7
Ru metal surface area (m ² /g) ^d	-	0.71	0.8	0.98	1.14

^a calculated from XRD analysis, ^b calculated from N₂ physisorption studies, ^c $\tau = (r_A + r_O) / \sqrt{2} (r_B + r_O)$, ^d calculated from CO chemisorption studies.

4.3.3 Temperature programmed reduction of CeAl_{1-x}Ru_xO₃ oxides

Reducibility of Ru substituted CeAlO₃ perovskite type oxides was investigated by temperature programmed reduction (TPR). The H₂-TPR profiles of CeAl_{1-x}Ru_xO₃ oxides are given in Fig. 4.2.

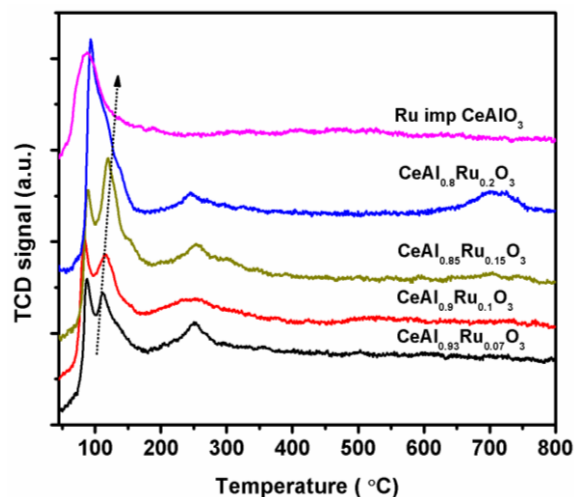


Fig. 4.2 TPR of CeAl_{1-x}Ru_xO₃ and Ru impregnated CeAlO₃ perovskites.

The peaks observed in the 50– 300 °C temperature range correspond to the reduction of ruthenium oxide species. The peak at lower reduction temperature (85-95 °C) may be assigned to reduction of Ru⁺⁴ to Ru⁺³ and peak at 120 °C is assigned to reduction of Ru⁺³ to metallic Ru. It is observed that as the Ru substitution increases to x= 0.15, the peak at around 120 °C is shifted to slightly high temperature and also became broad. This means that smaller Ru particles are formed that are more homogeneously distributed on the surface as a result of strong interaction with the lattice. In case of CARu0.2 catalyst, broad peak at 90 °C indicates weak interaction between the Ru metal and the oxide matrix, resulting in the formation of bigger Ru metallic particles. The peak at 250 °C could be attributed to the reduction of bulk Ru species in the sample. This can be further confirmed by comparing the TPR profiles with that of Ru impregnated CeAlO₃ (CARu-imp), which shows a single reduction peak. The reduction temperatures and peak distribution shows that loading of Ru (below 0.2) has higher degree of interaction between metal and perovskite lattice. The broad reduction peak at around 720 °C is assigned to the reduction of ceria as a result of spill over of hydrogen atoms on to ceria from metallic Ru.

4.3.4 Raman spectroscopy of CeAl_{1-x}Ru_xO₃ perovskite oxides

The XRD results reveal that on formation of CeAl_{1-x}Ru_xO₃ perovskite structures, part of Ru exists inside the perovskite lattice and a fraction of Ru is outside the lattice, distributed on the surface. Further, these results are confirmed by Raman spectroscopy as shown in Fig. 4.3. The Raman spectrum of CARu0.15 (calcined at 400 °C) sample shows three major bands at 540, 630 and 720 cm⁻¹ which are assigned to E_g, A_{1g} and B_{2g} modes respectively of oxidized Ru particles outside the CeAlO₃ frame work. [9,10] This spectrum is compared with reduced CARu0.15 (at 750 °C) and Ru impregnated samples. It reveals that Ru substituted CeAlO₃ catalyst has some percentage of Ru still in the oxidized form which is expected to be present in the lattice of the perovskite phase.

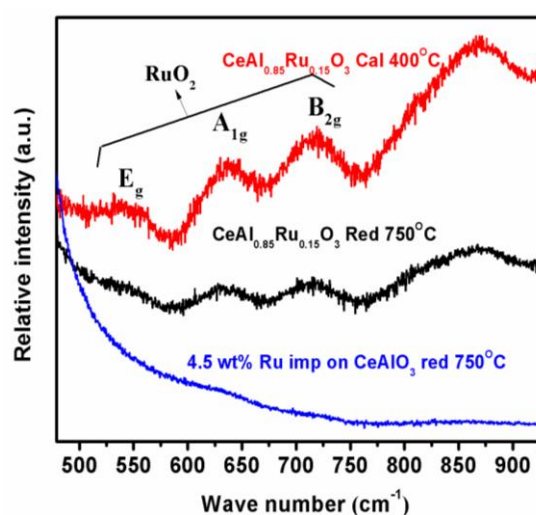


Fig. 4.3 Raman spectra of Ru perovskite oxides.

4.3.5 XPS of CeAl_{1-x}Ru_xO₃ perovskite oxides

The oxidation state of Ru in the substituted and impregnated perovskite oxides was examined by XPS, results are shown in Fig. 4.4. The peaks corresponding to Ru3d_{5/2} and Ru3d_{3/2} core level of spin-orbit components were found to be at 280.5 and 284.6 eV, which are in good agreement with the reported results for Ru⁰ oxidation states. The peak positions at 281.8 and 285.9 eV provide information about the presence of Ru in higher oxidation state (Ru⁺³) which is influenced by the local environment of the perovskite. The concentration of Ru⁰/Ru⁺³ is 2.1 for CARu0.15 perovskite catalysts. These observation show that in CARu0.15 catalyst has most of its Ru in metallic state on the surface, as the sample was reduced in H₂. This is also

confirmed from XRD analysis. However, in case of Ru impregnated (CARu-imp) catalysts XPS spectra reveal the presence of only metallic Ru particles on the perovskite surface. In the CARu0.15 perovskite, part of Ru is present in the bulk of perovskite lattice in the form of Ru⁺³ and remaining Ru must be well dispersed on the perovskite surface after high temperature reduction. Both spectra are has an additional peak at 284.5 eV that belongs to C1s which overlaps with Ru 3d XPS spectra.

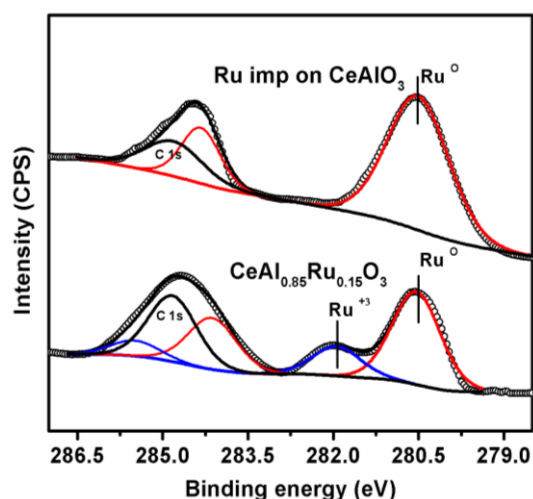


Fig. 4.4 XPS spectra of CeAl_{0.85}Ru_{0.15}O₃ and Ru impregnated perovskites.

4.3.6 Transmission electron microscopy (TEM)

HRTEM analysis results of CeAl_{0.85}Ru_{0.15}O₃ and Ru impregnated (CARu-imp) catalysts is shown in Fig. 4.5a and 4.5b respectively. The analysis was carried out after reduction of the catalysts at 750 °C.

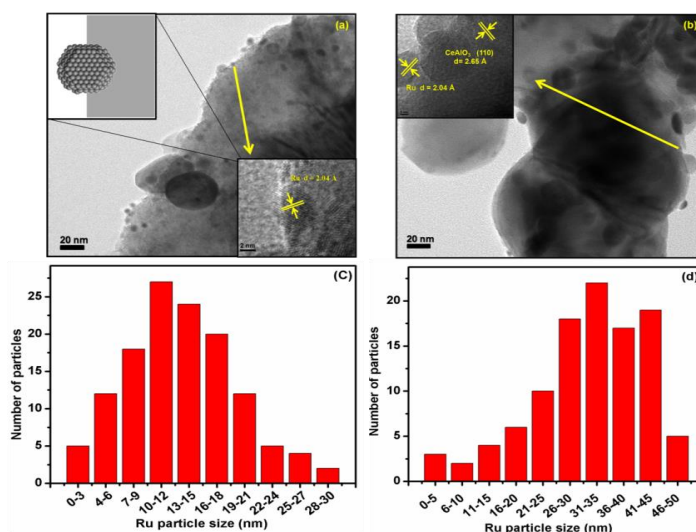


Fig. 4.5 TEM images of (a) CeAl_{0.85}Ru_{0.15}O₃, (b) CARu-imp; Ru distribution on (c) CeAl_{0.85}Ru_{0.15}O₃, (d) CARu-imp.

The TEM micrograph of CeAl_{0.85}Ru_{0.15}O₃ sample shows formation of spherical shape Ru nanoparticles of around 6.5 nm. The inset electron diffraction shows uniform interplaner spacing of 2.04 Å corresponding to 101 plane of the hexagonal closed packed Ru phase. In the case of impregnated sample, TEM image shows formation of bigger and agglomerated Ru clusters on the surface. Ru particle size distribution was derived from TEM analysis, which is presented in Fig. 4.5c and 4.5d for CARu0.15 and Ru impregnated CeAlO₃ respectively. After reduction, the diameter of the particle ranges between 2 to 28 nm and the average size of particles is 12 nm. Infact, the Ru impregnated catalyst has a high proportion of Ru particles in the size range larger than 30 nm.

4.4 Catalytic activity of Ru containing CeAlO₃ perovskites

4.4.1 SRM activity at different temperatures

Ruthenium substituted CeAlO₃ catalysts (CeAl_{1-x}Ru_xO₃) and impregnated catalyst (CARu-imp) were evaluated for SRM activity in the temperature range of 600-750 °C using steam to carbon (S/C) ratio of 3 and GHSV of 20000 h⁻¹ at 1 atm pressure. The results of this study are given in Fig. 4.6.

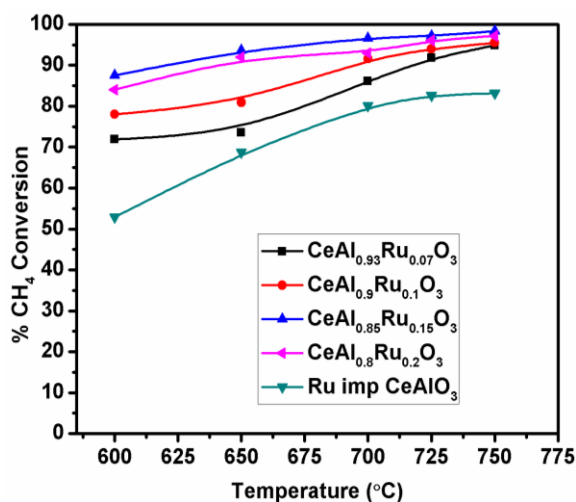


Fig. 4.6 Effect of temperature on activity of CeAl_{1-x}Ru_xO₃ (x = 0.07, 0.1, 0.15 and 0.2) and Ru impregnated catalysts

*Reaction conditions: Pressure 1atm; GHSV- 20,000 h⁻¹; Steam/CH₄ = 3

As may be seen, the CH₄ conversion has increased with temperature over all Ru containing catalyst. In case of Ru impregnated catalyst (CARu-imp), though the Ru content in the catalyst was similar to that of CARu0.15, it has shown much lower

activity. Among all the Ru containing compositions, CARu0.15 showed relatively much higher activity throughout the temperature range compared to other catalysts. Hence, it appears that Ru mole fraction of 0.15 in the (CeAl_{1-x}Ru_xO₃) perovskite oxide appears to be optimum for high SRM activity. This could be attributed to the appropriate Ru metal surface area of the catalyst along its interaction with the perovskite lattice.

4.4.2 Effect of GHSV

Figure 4.7 shows the disparity in the steam reforming activity of all the Ru containing catalysts with increasing gas hourly space velocity (GHSV). At higher GHSV's, the gap in the performance of these catalysts is amplified, as can be seen from Fig. 4.7. In this plot, activity in terms of CH₄ conversion is compared at high GHSV, particularly in 50,000–100,000 h⁻¹ range at 700 °C and 1 atm pressure. The CH₄ conversion dropped continuously with increasing GHSV on all catalysts, but on CARu0.15 catalyst the drop was moderate even upto GHSV of 100,000 h⁻¹. This catalyst showed remarkable activity at high GHSV. The CH₄ conversion was ~98% at a space velocity of 20,000 h⁻¹, which is quite good to translate it for commercial applications. In spite of drop in CH₄ conversion at higher GHSV, this catalyst still showed >90% CH₄ conversion at GHSV of 100,000 h⁻¹.

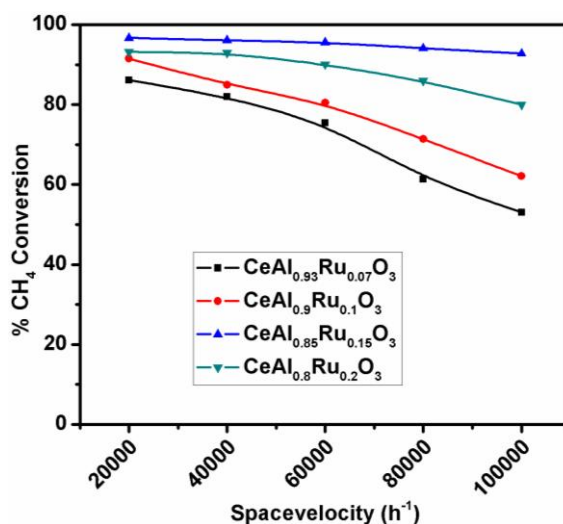


Fig. 4.7 Effect of space velocity on activity of CeAl_{1-x}Ru_xO₃ (x = 0.07, 0.1, 0.15 and 0.2) catalysts for SRM reaction

*Reaction conditions: Pres- 1atm; Temp-700 °C; H₂O:CH₄ = 3:1

Since, CARu0.15perovskite catalyst seems to be promising in terms of high activity (CH₄ conversion), it was investigated further to get kinetic parameters, by conducting reforming experiments to get low conversions.

4.4.3 Kinetics of SRM reaction over CeAl_{0.85}Ru_{0.15}O₃ catalyst

Kinetic experimental data were collected in the 773-873 K (500-600 °C) temperature range at atmospheric pressure by varying contact times in a broad range. Contact /residence time in terms of physical volume of the catalyst and volumetric flow of feed is defined as:

$$\text{Contact time} = (\text{Vol. of the catalyst in m}^3) / (\text{Volumetric flow of feed in m}^3/\text{sec}) \quad (4.3)$$

The methane conversion versus temperature, at different contact times is given in Fig. 4.8a. It was observed that in the given temperature range, CH₄ conversion increased with increasing contact time. As explained in section 1.6.2, on the basis of Wei Iglesia mechanism, C-H bond activation is kinetically important step in CH₄ reforming reaction. The forward rate is not influenced by CO, H₂O or H₂ concentration, when they are varied by changing contact time.

$$\text{Rate of forward reaction in SRM} = k \cdot X_{\text{CH}_4} \quad (4.4)$$

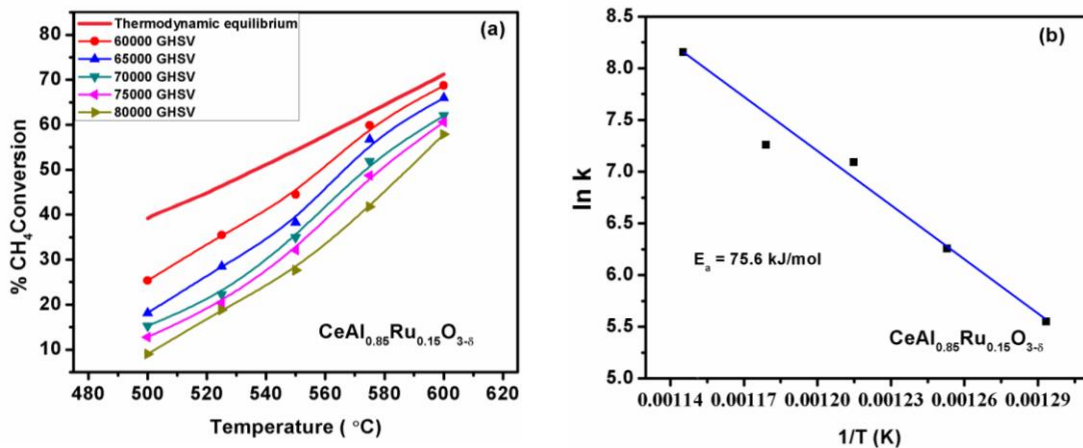


Fig. 4.8 (a) CH₄ conversion versus reaction temperature at different space velocities; (b) Arrhenius plot for CeAl_{0.85}Ru_{0.15}O₃ catalysts for SRM reaction

*Reaction conditions: Pres- 1atm; H₂O: CH₄ = 3:1

According to the Arrhenius law, reaction rate in steam reforming of methane is temperature dependant. The plot between rate of reaction as a function CH₄ concentration (X_{CH₄}) can be used to calculate rate constants (k) in a wide range of temperatures. The plot lnk versus 1/T provides the true activation energy. Figure 4.8b shows the Arrhenius plot for CeAl_{0.85}Ru_{0.15}O₃ perovskite catalyst and thus obtained

activation energy is 75.6 KJ/mol, which is in good agreement with the values given in literature. [11-13]

4.5 Reforming activity of Ni containing CeAl_{0.9}Ni_{0.1}O_{3-δ} catalysts promoted by Ru

All the above studies showed that Ru substituted CeAl_{0.85}Ru_{0.15}O₃ catalyst shows excellent activity even at higher space velocities during SRM. However Ru is expensive compared to base metals like Ni. Hence it is advisable to use Ni catalysts, if the process has to be translated into a commercial one. But, Ni catalysts are prone to carbon deposition and sintering. It may be possible to minimize these short comings by adding minor content of relatively cheaper noble metal such as Ru to Ni substituted (CeAl_{0.9}Ni_{0.1}O_{3-δ}) perovskite that may help to improve the performance and stability of the catalyst. It was reported that the addition of Ru to the Ni supported on Al₂O₃ and MgAl₂O₄ showed superior activity in SRM reaction than non-doped Ni catalyst under pre-reduction conditions by Jeong et al. [14] Hence, these studies have been aimed at developing Ru promoted CeAl_{0.9}Ni_{0.1}O_{3-δ} catalyst by doping it with very lower content of Ru and test them for SRM, BRM and TRM activity.

To study the stability of Ru substituted CeAl_{0.9}Ni_{0.1}O_{3-δ} catalyst (CeAl_{0.86}Ni_{0.1}Ru_{0.04}O_{3-δ}), it was evaluated for SRM under reaction conditions of GHSV: 20,000 h⁻¹; H₂O:CH₄ = 3:1; 800 °C and at 1 atm. The results of this experimental run are given in Fig. 4.9.

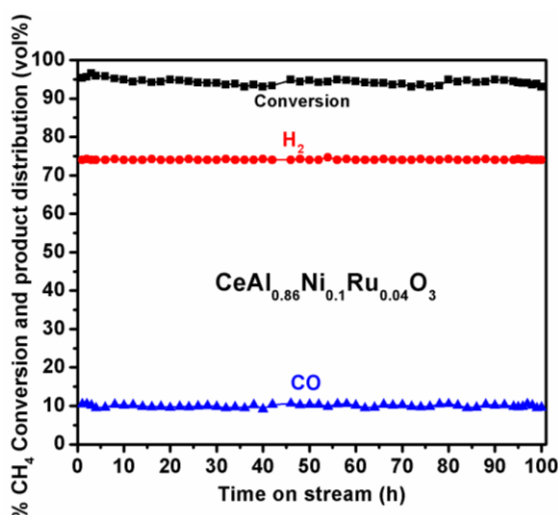


Fig. 4.9 Time on stream stability of CeAl_{0.86}Ni_{0.1}Ru_{0.04}O₃ catalyst during SRM.

*Reaction conditions: Temp.- 800 °C; 1atm; GHSV- 20,000 h⁻¹; S:C = 3:1.

The CH₄ conversion and product distribution in terms of H₂ and CO were remarkably steady at about 95 and 75, 10 % respectively. Even at the end of 100 hours of reaction, CeAl_{0.86}Ni_{0.1}Ru_{0.04}O_{3-δ} catalyst did not show any loss of activity, showing that it is highly stable for SRM reaction.

4.5.1 Catalytic activity of CeAl_{0.86}Ni_{0.1}Ru_{0.04}O_{3-δ} in bi- and tri-reforming of CH₄

During the steam reforming reaction, if an oxidant like CO₂, O₂ and H₂O can be injected along with the reactant feed, in small quantities, the coke formed is likely get oxidized instead of being accumulated on metal surface. In addition, the tri-reforming (CO₂+ CH₄ + O₂ + H₂O) and bi-reforming (CO₂+ CH₄ + H₂O) processes can also help to achieve the desired H₂/CO ratios. Hence, it is aimed to use the best catalyst of this study for tri-reforming and bi-reforming studies. These processes should help to increase the catalyst life to few thousands of hours or even longer.

Figure 4.10 represents the bi-reforming (BRM) or combined steam and dry reforming reaction was carried out on CAN-Ru_{0.04} (CeAl_{0.86}Ni_{0.1}Ru_{0.04}O_{3-δ}) at 1 atm pressure and at 800 °C. The product syngas has a H₂/CO ratio close to 2, which can be used for methanol synthesis, FT and many other applications, without involving additional steps such as WGS for adjusting the H₂/CO ratio. [15-18] For the present investigation of combined reforming, reactant mixture in the ratio CH₄:CO₂: H₂O = 3:1.5: 2 was used. This composition is typical of biogas, after the removal of impurities such as H₂S and nitrogen compounds. [19-22] Conversions of CH₄ and CO₂ as a function of time were investigated and the results are shown in Fig. 4.10.

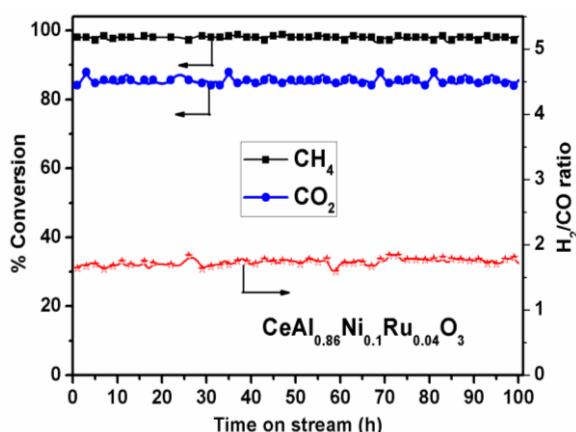


Fig. 4.10 Time on stream stability of CeAl_{0.86}Ni_{0.1}Ru_{0.04}O₃ catalyst during BRM.

*Reaction conditions: Temp., 800 °C; 1atm; GHSV- 22,068 h⁻¹;

CH₄:CO₂: H₂O = 3: 1.5: 2.

The most active catalyst CAN-Ru_{0.04} (CeAl_{0.86}Ni_{0.1}Ru_{0.04}O_{3-δ}) was chosen for this combined reforming study owing to its high activity and stability over extended periods during steam and dry reforming reactions. Stable activity was observed, in the bi-reforming of simulated biogas employing CH₄:CO₂:H₂O in 3:1.5:2 ratio, when it was evaluated for 100 h continuously.

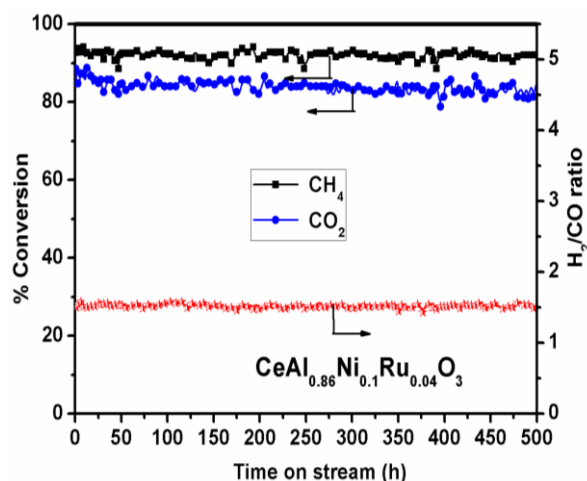


Fig. 4.11 Long term stability of CAN-Ru_{0.04} catalyst during TRM.

*Reaction conditions: Temp., 800 °C; 1atm; GHSV- 23,935 h⁻¹; CH₄:CO₂: H₂O : O₂ = 1: 0.47 : 0.6: 0.03.

Tri reforming of methane (TRM) was carried out on CAN-Ru_{0.04} at 800 °C, 1 atm pressure, GHSV 23,935 h⁻¹ with the reactant mixture composition of CH₄: CO₂: H₂O:O₂ = 1:0.47:0.6:0.03. The results of this study are given in Fig. 4.11. The best catalyst CeAl_{0.86}Ni_{0.1}Ru_{0.04}O_{3-δ} (CAN-Ru_{0.04}) was chosen for tri-reforming study owing to its high activity and stability over extended periods during SRM, DRM and partial oxidation reactions. Stable activity was observed, in typical tri-reforming reaction, when it was evaluated for 500 h continuously. The H₂/CO ratio was ~1.6, but it can be increased further by adding more steam to the input reactant mixture.

4.6 Characterization of spent catalysts

Though reforming activity of most of the catalysts evaluated in this study was stable for long hours on-stream, accumulation of some amount of coke and sintering of metal particles can not be ruled out. Hence, we systematically studied the used (spent) catalysts by employing TGA and HRTEM studies.

4.6.1 Thermogravimetric analysis of spent catalysts

Thermogravimetry (TGA) is a highly useful technique for quantification of coke present on a spent catalyst. Figure 4.12 shows the carbon estimated using TGA. This carbon was deposited during steam, bi- and tri-reforming reactions in terms of moles of carbon per gram per hour. The weight loss of spent catalysts is generally due to oxidation of carbon as CO_x from various types of carbon deposits. The TGA results show the weight losses occurred due to the loss of carbon deposits at 7×10^{-5} mol of C. g⁻¹.h⁻¹ on CARu_{0.15} after 50 h of SRM reaction; 4.8×10^{-5} mol of C. g⁻¹.h⁻¹ on CAN-Ru_{0.04} after 100 h of SRM reaction, 5.1×10^{-5} mol of C. g⁻¹.h⁻¹ from CAN-Ru_{0.04} after BRM for 100 h. The CAN-Ru_{0.04} catalyst shows least amount of carbon deposited (1.5×10^{-5}) in tri-reforming reaction after 500 h on stream. This small coke formed on CAN-Ru_{0.04} catalyst did not affect its activity, as the reaction is carried out under equilibrium conditions at high temperature (800 °C).

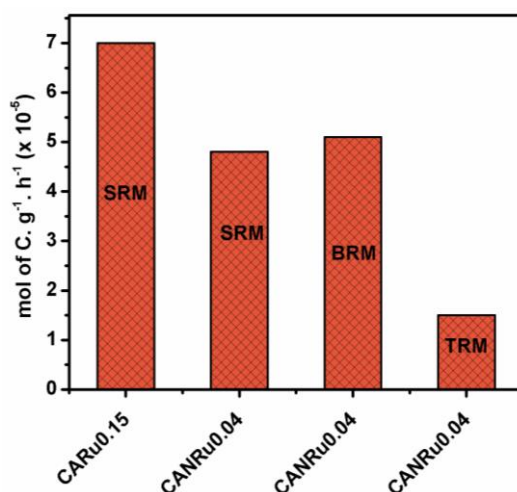


Fig. 4.12 Coke estimation after steam, Bi and tri reforming of methane by using TGA.

Figure 4.12 also shows that relatively lower amount of carbon is deposited on CAN-Ru_{0.04} as compared to CARu_{0.15} catalyst during steam reforming reaction. This may be attributed to the presence of Ru metal as a promoter for CAN catalysts, creating a pool of oxygen for efficient gasification of the carbon formed during SRM reaction. Also, it is well known that noble metals increased the oxidation rate of carbon which results in prolonged performance of the catalyst. This enhanced resistance to deactivation is seen as the coke formation is very low on Ru promoted catalysts.

4.6.2 Transmission Electron Microscopy of spent catalysts

The TEM analysis of spent CARu0.15 and CANRu0.04 catalysts after various reforming reactions is shown in Fig. 4.13. Spent CARu0.15 catalyst (Fig. 4.13a) shows high content of amorphous and graphitic carbon formation on the perovskite. On Ru promoted CeAl_{0.9}Ni_{0.1}O₃ catalyst, i.e., CANRu0.04 no graphitic carbon was seen (Fig. 4.13b, c and d). The CANRu0.04 catalyst (Fig. 4.13d) shows least carbon formation on the catalyst surfaces in tri- reforming reaction. The TEM results clearly show that graphitization of carbon (carbon nanotubes) reduced with the introduction of oxidizing agents like CO₂ and O₂ in the reforming reaction.

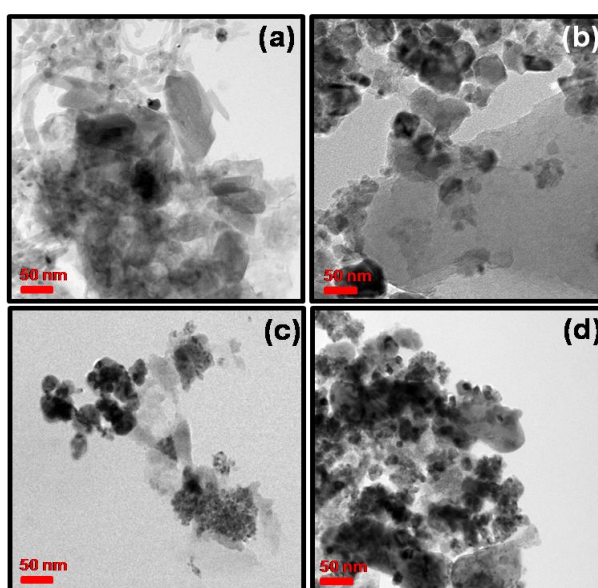


Fig. 4.13 TEM images of spent catalysts (a) CARu0.15 and (b) CANRu0.04 for SRM, (c) CANRu0.04 for BRM and (d) CANRu0.04 for TRM.

The TEM analysis clearly shows that Ru promotion of CeAl_{0.9}Ni_{0.1}O₃ catalysts helps to reduce the carbon formation as compared to unpromoted catalysts.

Part-II: Rhodium substituted CeAlO₃ (CeAl_{1-x}Rh_xO₃) catalysts for SRM, BRM and their sulfur tolerance**4.7 Introduction**

In the earlier sections steam reforming, bi-reforming and tri-reforming activity of Ru substituted CeAlO₃ perovskite catalysts was discussed. Among the Ru substituted catalysts, CeAl_{0.85}Ru_{0.15}O₃ catalyst showed superior activity in SRM. Coke formation and catalytic performance has also been discussed. It is reported that supported Rh catalysts are less prone to coke formation and sulfur poisoning compared to Ni based catalyst in the reforming reaction. [1-3] The Rh substituted perovskite structure is expected to be less reactive with sulfur compared to Ni doped catalysts. [23] Substitution of different metal ions at B site creates vacancy and produce small sized active metal particles which can develop sulfur tolerance. Metal at B site is responsible for the catalytic activity, while metal at A site imparts thermal stability to the catalysts. [24, 25] Part-II of this chapter deals with synthesis, characterization and catalytic activity of novel Rh substituted CeAlO₃ (CeAl_{1-x}Rh_xO₃) perovskite oxides. A comparative investigation of catalytic properties as a function of Rh metal content in the perovskite is discussed in the following sections.

4.8 Experimental methods**4.8.1 Preparation of Rh substituted CeAlO₃ and Rh/CeAlO₃ catalysts**

The CeAl_{1-x}Rh_xO₃ Perovskite oxide catalysts were synthesized using citrate gel method as described in Chapter-2 (section 2.3.3). They were characterized by various physico-chemical techniques for finding their phase purity, crystallinity and textural properties. The CeAl_{1-x}Rh_xO₃ perovskites were prepared with x= 0, 0.01, 0.02, 0.035, 0.05 and 0.1; which are denoted as CAO, CARh0.01, CARh0.02, CARh0.035, CARh0.05 and CARh0.1 respectively. One additional catalyst with 2.3 wt % Rh was prepared by impregnation using CeAlO₃ as support, with Rh content equivalent to that of CeAl_{0.95}Rh_{0.05}O₃ and denoted as Rh imp CAO.

4.9 Results and discussion

4.9.1 Structural and textural properties

The results of BET surface area, crystallite size, active metal dispersion, lattice parameters and bulk chemical analysis of catalysts by ICP-OES are summarized in Table 4.2. The crystallite size of CeAl_{1-x}Rh_xO₃ (where x = 0.0, 0.01, 0.02, 0.035, 0.05 and 0.1) perovskite oxides were calculated from FWHM of prominent XRD peak present in the sample, using Scherrer equation. It is seen from the results (Table 4.2) that the crystallite size of the sample decreased on Rh substitution. The trend observed was: CAO > CARh0.01 > CARh0.02 > CARh0.035 > CARh0.05 > CARh0.1. Consequently, the BET surface areas follow exactly the opposite order, as surface area increases with reduction in crystallite size. Hence, the BET surface areas follow the order: CAO < CARh0.01 < CARh0.02 < CARh0.035 < CARh0.05 < CARh0.1. The results of bulk chemical analysis by ICP-OES show that the Rh metal content of these samples is similar to that of input metal content used in their synthesis.

4.9.2 X-ray diffraction studies of CeAl_{1-x}Rh_xO₃ perovskites

The XRD pattern of CeAl_{1-x}Rh_xO₃ (X= 0.0, 0.01, 0.02, 0.035, 0.05 and 0.1) and Rh impregnated CeAlO₃ perovskite (Rh/ CeAlO₃) calcined at 550 °C followed by reduction at temperature 750 °C are given in Fig. 4.13. The XRD pattern show that CeAl_{1-x}Rh_xO₃ samples mostly contain single phases of cubic perovskite with space group Pm3m, upto Rh fraction x=0.05. These results are in good agreement with the standard JCPDS-28-0260 data. However, additional peak at 28.62° was observed at higher Rh concentration, which is attributed to the CeO₂ phase. No additional peaks corresponding to Rh metal or its oxides were seen in the XRD. The plots also include the XRD of impregnated ‘Rh imp CAO’ catalyst

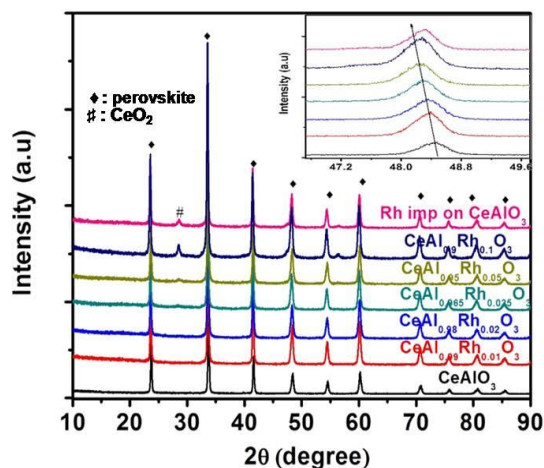


Fig. 4.14 XRD patterns of CeAl_{1-x}Rh_xO₃ and Rh impregnated catalysts.

The refinement of all diffraction data was carried out using Rietveld methodology [7, 8] to verify the crystal structure and cell parameters as shown in Table 4.2. It is observed that cell parameters increased with increasing Rhodium content. This increase is due to unit cell expansion as the smaller Al³⁺ (0.535 Å) ions in the crystal lattice are substituted by the larger Rh³⁺ (0.66 Å) ions. This is seen in terms of shifting of peaks to lower 2θ values, with increasing Rh substitution (see inset Fig. 4.14). Metal dispersion was investigated through CO chemisorption. Dispersion of Rh decreased with increasing Rh metal content in the sample.

Table 4.2 Textural and structural properties of CeAl_{1-x}Rh_xO₃ perovskite oxides

Formula	CeAlO ₃	CeAl _{0.99} Rh _{0.01} O ₃	CeAl _{0.98} Rh _{0.02} O ₃	CeAl _{0.965} Rh _{0.035} O ₃	CeAl _{0.95} Rh _{0.05} O ₃	CeAl _{0.90} Rh _{0.1} O ₃
Space group	Pm-3m	Pm-3m	Pm-3m	Pm-3m	Pm-3m	Pm-3m
a/Å	3.7707(3)	3.7708(2)	3.7710(3)	3.7713(3)	3.7717(4)	3.7718(2)
b/Å	3.7707(3)	3.7708(2)	3.7710(3)	3.7713(3)	3.7717(4)	3.7718(2)
c/Å	3.7707(3)	3.7708(2)	3.7710(3)	3.7713(3)	3.7717(4)	3.7718(2)
V/Å ³	53.61	53.62	53.63	53.64	53.65	53.66
R _p	0.1011	0.0935	0.0931	0.0966	0.1088	0.076
WR _p	0.1390	0.1208	0.1211	0.1242	0.1377	0.099
χ ²	1.892	1.442	1.439	1.624	1.987	1.579
Tolerance factor	1.0006	1.0000	0.9993	0.9983	0.9973	0.9942
Crystallite size (nm)	64.3	70.1	57.2	56.2	55.8	57
Surface area (m ² /g)	5.7	6.2	10.5	11.0	12.3	10.8
Rh wt% (ICP-OES)	-	0.3	0.9	1.6	2.2	4.4
Rh metal dispersion (%)	-	11.9	9.5	8.8	7.3	6.0
Metal surface area	-	0.25	0.4	0.54	0.76	1.33

Rh content determined by ICP-OES, BET Surface area by N₂ sorption, Cell parameters and crystallite sizes were calculated by Rietveld refinement and active Rh metal dispersion obtained from CO chemisorption.

4.9.3 Temperature programmed reduction of CeAl_{1-x}Rh_xO₃ oxides

Reducibility of the CeAl_{1-x}Rh_xO₃ perovskite oxides was investigated by temperature programmed reduction of H₂. The H₂-TPR profiles of CeAl_{1-x}Rh_xO₃ samples are given in Fig. 4.14. All the catalyst gave mainly two reduction peaks; one in 60–160 °C region, attributed to the reduction of Rh₂O₃ species, while the other broad peak in 140–250 °C range was attributed to the reduction of Rh ions that are part of perovskite lattice. Increasing Rh content in the perovskite may have led to higher degree of interaction between metal and the lattice which may cause the shift of the reduction to higher temperature and increasing peak width. This indicates that the catalyst with higher Rh content may have more active metal after reduction, which will play role in C-H bond cleavage of methane.

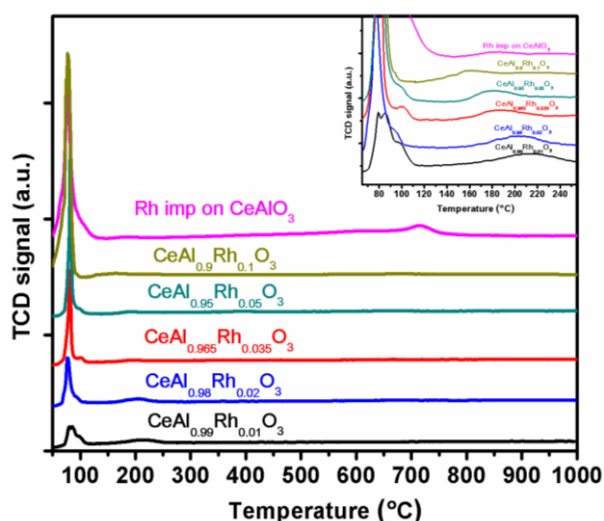


Fig. 4.15 TPR of CeAl_{1-x}Rh_xO₃ and Rh impregnated catalysts.

4.9.4 X-ray photo electron spectroscopy of CeAl_{1-x}Rh_xO₃ catalysts

X-ray photo electron spectroscopy is a useful technique to identify the chemical state of the elements and their surface proportions in CeAl_{1-x}Rh_xO₃ ($x = 0.0, 0.05$ and 0.1) perovskites. Figure 4.15a shows Ce 3d spectra (multiplets of v and u) that arise from spin-orbit coupling which gives $3d_{5/2}$ and $3d_{3/2}$ transitions. These spin orbit splittings are separated by 18.6 eV. The major difference in Ce (III) and Ce (IV) XPS spectra is that, Ce (III) oxides have two pairs of spin orbit doublets [26, 27] i.e. the highest binding energy (BE) peaks u' and v' are located at 905.2 ± 0.4 eV and 886.5 ± 0.4 eV respectively which arise from Ce $3d^9 4f^1 O 2p^6$ state. [28] The lower BE state u_0 and v_0 are observed at 901.2 ± 0.4 eV and 882.5 ± 0.4 eV respectively, which

arise from Ce 3d⁹ 4f² O 2p⁵. In case of Ce (IV) oxides there are three pairs of spin-orbit doublets with highest binding energy peaks u''' and v''' which are located at 917.3±0.4 eV and 898.2±0.4 eV respectively arising from Ce 3d⁹ 4f⁰ O 2p⁶ state. The lowest binding energy peaks are u, v and u'', v'' located at 902.5, 883.2 and 908.1, 889.4±0.4 eV respectively resulting from Ce 3d⁹ 4f² O 2p⁴ and Ce 3d⁹ 4f¹ O 2p⁵. It is clear from the investigation of Ce 3d XPS analysis that Ce⁺⁴/Ce⁺³ ratio increases with substitution of Rh at Al site (see Fig. 4.15).

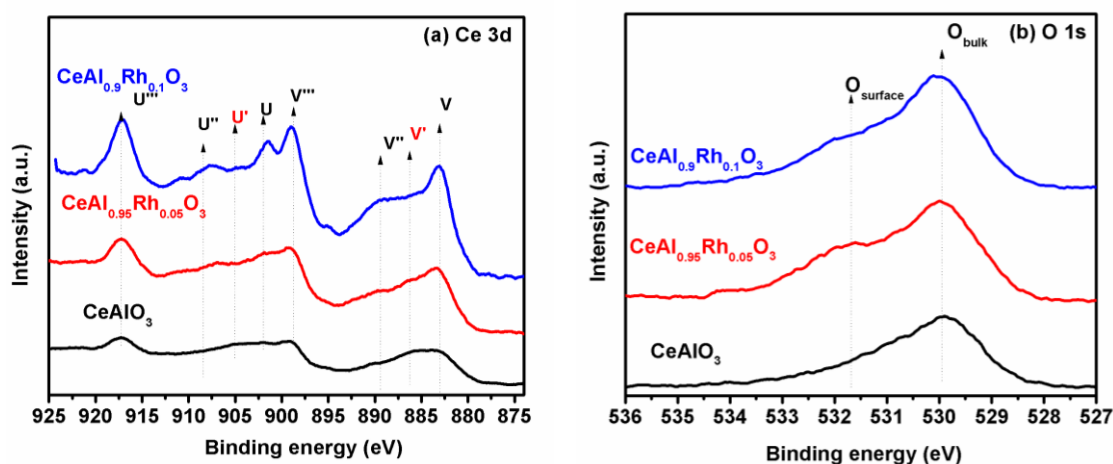


Fig. 4.16 (a) Ce3d (b) O1s XPS analysis of CeAl_{1-x}Rh_xO₃ (x = 0.0, 0.05 and 0.1).

The O 1s core level spectra of CeAl_{1-x}Rh_xO₃ (x= 0.0, 0.05 and 0.1) are given in Fig. 4.16b. Two different peaks of O1s peaks were observed. The first peak close to 530 eV is assigned to lattice oxide in perovskite network and the other peak close to 531.8 eV arises from weakly adsorbed surface oxygen species or defective oxygen species. [29] The comparison of O 1s spectra in CeAl_{0.95}Rh_{0.05}O₃ catalyst shows very high contribution of surface oxygen species at 531.8 eV, which is expected to play an important role in the removal of carbon/coke during the reforming reaction. When CeAlO₃ is compared with CeAl_{0.9}Rh_{0.1}O₃, the later sample has higher contribution of surface oxygen species. The ratios of Ce⁺⁴/Ce⁺³ and O_{surface}/O_{bulk} derived from XPS studies are shown in the Fig. 4.17. As may be seen, the Ce⁺⁴/Ce⁺³ ratios increased with Rh content, which reached maximum at x=0.5, and thereafter the ratio reduced with further increase in Rh content. On the otherhand, O_{surface}/O_{bulk} (O_{surf}/O_{Lattice}) ratio continuously increased with Rh content which is parallel to increase in BET surface areas, except in case of sample CeAl_{0.9}Rh_{0.1}O₃.

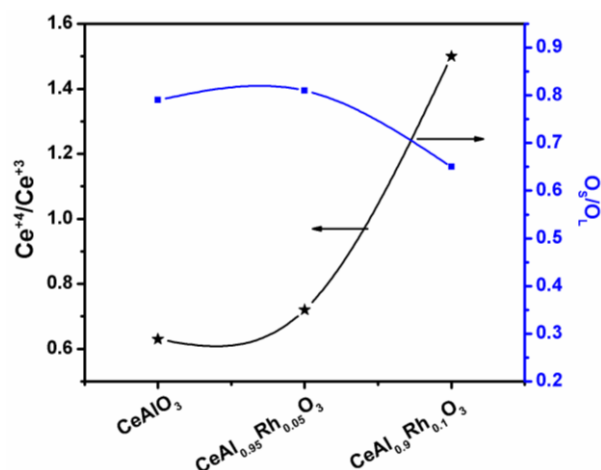


Fig. 4.17 Surface ratios of Ce⁴⁺/Ce³⁺ and O_S/O_L in CeAl_{1-x}Rh_xO₃ (x = 0.0, 0.05, 0.1) perovskites.

4.9.5 Transmission electron microscopy

Electron microscopy (HRTEM) results of CeAl_{1-x}Rh_xO₃ samples where x = 0.0, 0.05, 0.1 are shown in Fig. 4.18a, 4.18c and 4.18e respectively. Figure 4.18b shows selected area electron diffraction (SAED) pattern of CeAlO₃ catalyst, while Fig. 4.18d and Fig. 4.18f show particle size distribution in CARh0.05 and CARh0.1.

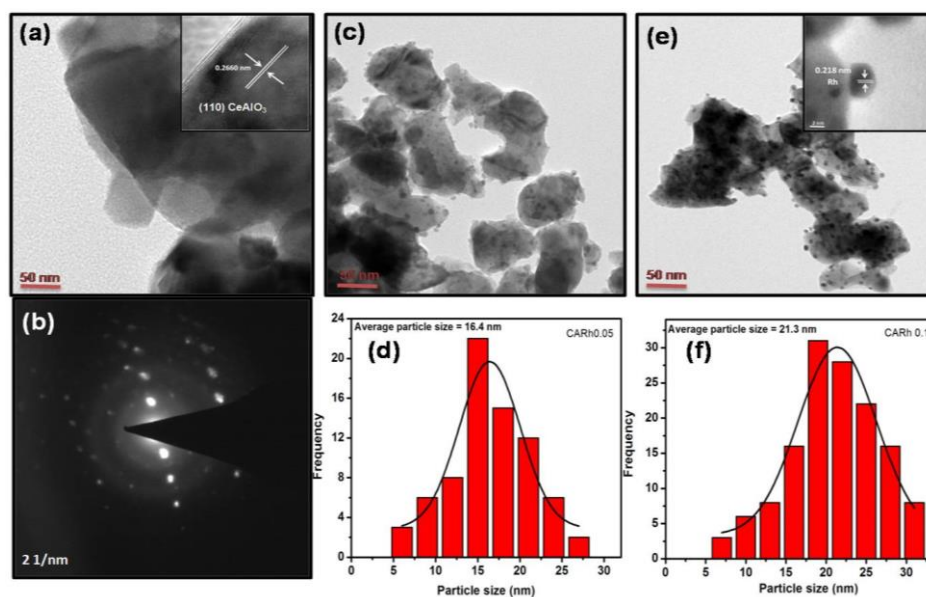


Fig. 4.18 TEM micrographs and analysis; (a) CAO image, (b) SAED of CAO, (c) CARh0.05 image, (d) particle size distribution in CARh0.05, (e) CARh0.1 image and (f) particle size distribution in CARh0.1.

The HRTEM analysis was performed after subjecting the catalysts to 6 h reduction at 750 °C. The TEM micrograph of CeAlO₃ (CAO) sample (Fig. 4.18a)

reveals uniform interplaner spacing of 2.66 Å corresponding to 110 plane of the cubic phase. The SAED image of CAO sample shows formation of perfect crystalline perovskite phase. Rh substituted CAO perovskite after reduction under H₂ at 750 °C clearly shows the presence of spherical particles of Rh (Fig. 4.18c and 4.18e). Rh particle size distribution was derived from TEM analysis and shown in Fig. 4.18d and 4.18f for CARh0.05 and CARh0.1 respectively. After reduction, the size of the Rh is in the range of 5 to 27 nm and most of them are less than 20nm in the case of CARh0.05, while their distribution is more dominant in the higher range in case of CARh0.1 perovskite sample.

4.10 Catalytic activity of Rh containing CeAlO₃ perovskites

Steam reforming activity of various Rh substituted CeAlO₃ perovskite catalysts was evaluated under various reaction conditions.

4.10.1 Activity at different reaction temperatures

The methane steam reforming over CeAl_{1-x}Rh_xO₃ (where x= 0.0 to 0.1) catalysts was studied and the results are given in Fig. 4.19. With increasing Rh content in CeAl_{1-x}Rh_xO₃, methane conversion increased upto x = 0.05, but no improvement was observed on increasing Rh further to x = 0.1. It shows that with increase in Rh substitution in CeAlO₃ structure, more active Rh sites are available for the reaction, in addition to additional defects generated on Rh substitution.

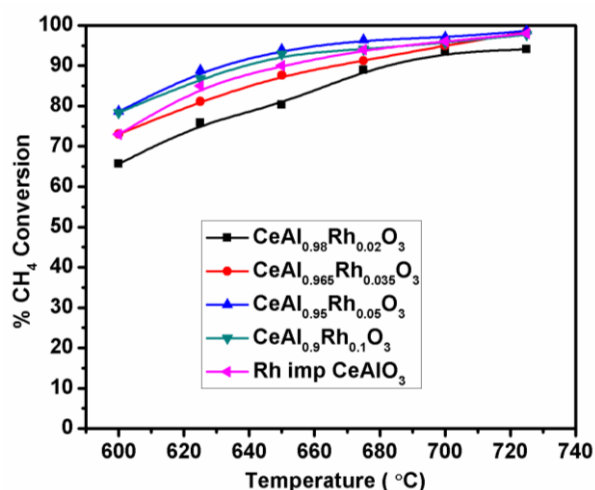


Fig. 4.19 CH₄ conversion in SRM as function of temperature with variation of Rh in CeAl_{1-x}Rh_xO₃ compared with impregnated Rh catalyst.

In Fig. 4.19, the performance of Rh impregnated CeAlO₃ catalyst was compared with Rh substituted perovskites; methane conversion was lower on the former catalyst

compared to CeAl_{0.95}Rh_{0.05}O₃ catalyst, which has Rh content similar to that of impregnated catalyst. From the above experiments, it may be summarized that three factors play important role in steam reforming reaction: (i) substitution of Rh at Al site in perovskite led to increase in defect sites were observed from O 1s in XPS; (ii) on reduction of the oxide, fine active Rh particles are formed as observed by CO-chemisorption and (iii) Reducibility of Rh is enhanced due to strong synergic effect as observed from H₂-TPR. All these three factors led to better activity of CeAl_{0.95}Rh_{0.05}O₃ catalyst.

4.10.2 Time on stream study of CeAl_{0.95}Rh_{0.05}O₃ catalysts

The above described results demonstrate that CeAl_{0.95}Rh_{0.05}O₃ perovskite derived oxide is a good catalyst for SRM. Hence, its performance was compared with Rh impregnated (2.5 wt %) catalyst for their durability. The activity of Rh substituted catalyst (CeAl_{0.95}Rh_{0.05}O₃) was always higher compared to impregnated catalyst throughout its 50 h on stream. But, methane conversion on both the catalysts was stable during the time of observation.

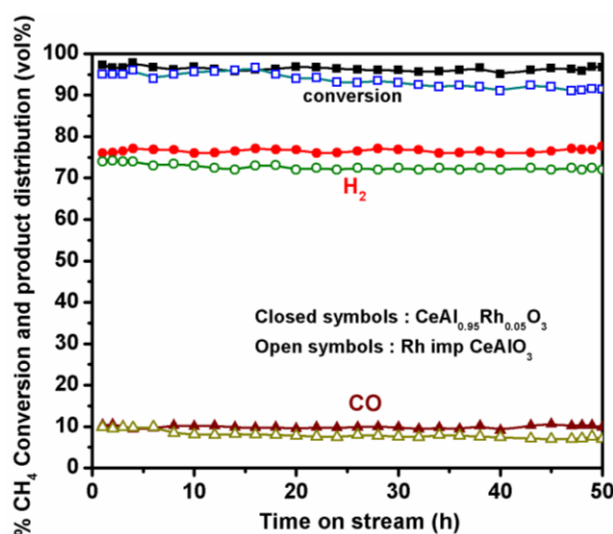


Fig. 4.20 Comparison of SRM activity of CeAl_{0.95}Rh_{0.05}O₃ with 2.5 wt% Rh impregnated CeAlO₃.

Reaction conditions: S/C = 3, Temp. 750 °C, GHSV = 20, 000 h⁻¹ and 1 atm.

4.10.3 Variation of S/C ratio in SRM reaction

Above described results indicate that CeAl_{0.95}Rh_{0.05}O₃ catalyst is highly active, for SRM reaction, in the temperature range studied and also during the period of time on stream. Hence, it will be interesting to understand catalytic activity at various

steam to carbon (S/C) ratios and at different temperatures. Figure 4.21 shows that by increasing S/C ratio, methane conversion has increased. Moreover, at lower S/C ratio (= 1), CeAl_{0.95}Rh_{0.05}O₃ catalyst shows 60% CH₄ conversion at 725 °C. Increasing the temperature enhanced the rate of reaction at all S/C ratios.

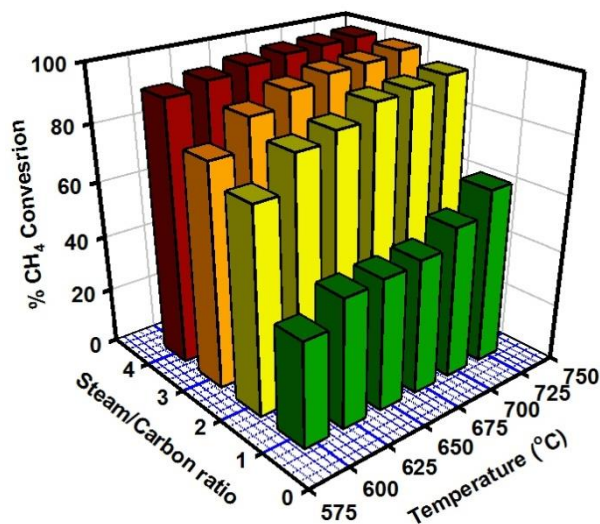


Fig. 4.21 Changes in CH₄ conversion as a function of S/C ratios and temperatures in SRM over CeAl_{0.95}Rh_{0.05}O₃ catalyst
Reaction conditions: GHSV = 20,000 h⁻¹ and 1 atm

4.10.4 Influence of sulfur during SRM over CeAl_{0.95}Rh_{0.05}O₃, impregnated Rh/CeAlO₃ and CeAl_{0.8}Ni_{0.2}O_{3-δ} catalysts

Effect of sulphur on CeAl_{0.95}Rh_{0.05}O₃, impregnated Rh/CeAlO₃ and Ni substituted CeAl_{0.8}Ni_{0.2}O_{3-δ} catalysts was monitored at 700 °C using optimum steam (S/C=3), at GHSV 20,000 h⁻¹ and at 1 atm, by cycling of methane containing 11 ppm of H₂S (Fig. 4.22). The CeAl_{0.95}Rh_{0.05}O₃ perovskite catalyst showed superior activity and stability throughout the duration of the experiment (20 h). When methane was sent without any sulphur, all the three catalysts CeAl_{0.95}Rh_{0.05}O₃, Rh/CeAlO₃ and CeAl_{0.8}Ni_{0.2}O_{3-δ} catalysts performed well with methane conversions close to 99%, till the methane with 11 ppm sulphur is introduced after 7 h on stream. At this point, the methane conversion fell rapidly on Ni substituted CeAl_{0.8}Ni_{0.2}O_{3-δ} catalyst, while the activity dropped slowly with some hysteresis on impregnated Rh/CeAlO₃ catalyst. On the otherhand, only a very small dip in methane conversion (~ 97%) was observed on CeAl_{0.95}Rh_{0.05}O₃ catalyst, which was steady for the next 6 h on stream, till the pure methane is switched back for reforming. On restoring pure methane feed, the initial conversion was restored on CeAl_{0.95}Rh_{0.05}O₃ catalyst, while it was stable thereafter for

next 7 h. On the otherhand, SRM activity was not restored on CeAl_{0.8}Ni_{0.2}O_{3-δ} and Rh/CeAlO₃ catalysts. Infact, activity dropped continuously over CeAl_{0.8}Ni_{0.2}O_{3-δ}, possibly due to irreversible adsorption of sulphur on Ni in this catalyst.

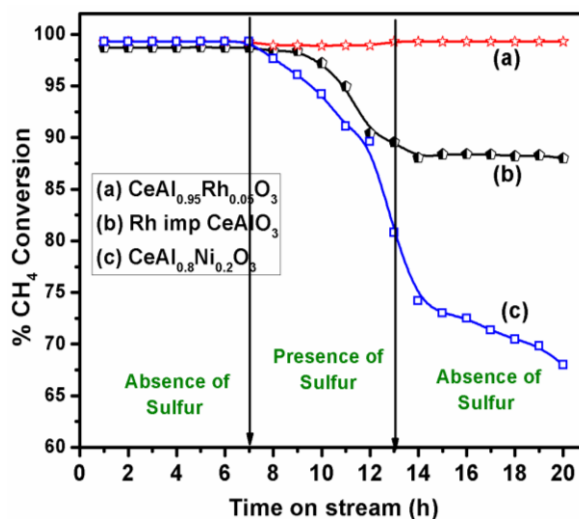


Fig. 4.22 Effect of sulfur on CeAl_{0.95}Rh_{0.05}O₃, Rh/CeAlO₃ and CeAl_{0.8}Ni_{0.2}O_{3-δ} catalysts during SRM reaction.

Reaction conditions: temperature 700 °C; GHSV = 20, 000 h⁻¹ and 1 atm

The spent catalysts after this study showed that the deactivation was due to the carbon formation. Based on this study, it may be concluded that CeAl_{0.95}Rh_{0.05}O₃ catalyst shows superior activity even in the presence of sulphur in the feed.

4.10.5 Effect of sulfur on reforming of simulated biogas over CeAl_{0.95}Rh_{0.05}O₃

It is challenging to develop sulfur tolerant catalysts for reforming reactions (SRM or DRM). Commercial Ni catalysts are highly sensitive to sulfur containing feed stocks. Hence, purification of hydrocarbon, free of sulphur, is a crucial step before the SRM step. Biogas is produced from livestock waste, food and municipal waste; hence it consists of some toxic and odour compounds. Among the impurities present in biogas, H₂S is produced by sulfate reducing bacteria. [30] Commercial processes to achieve low H₂S concentrations in the feed are quite common. But, this sulfur removal (<1ppm) step needs additional investment and operating costs in syngas manufacture. An alternative to overcome this problem is to use sulphur tolerant noble metal containing catalysts like CeAl_{0.95}Rh_{0.05}O₃ perovskites for steam reforming of feeds that contain trace amount (~10ppm) of sulphur. Ceria type of oxides show sulfur tolerance in case of anode ceremets used in SOFC applications. It

is highly active, low cost, effective in sulfur removal and improves coke resistance in many catalytic processes. [31-33]

The above described results demonstrate that CeAl_{0.95}Rh_{0.05}O₃ perovskite derived catalyst is resistant to sulphur poisoning during steam reforming of methane. Hence, it will be interesting to check the SRM activity for longer hours by using simulated biogas (60% CH₄ and 40% CO₂) containing sulphur. Usually, biogas has trace amount of H₂S which can lead to significant deactivation of the catalyst. [17,18,34] All the experiments were conducted using 11 ppm of H₂S in methane at GHSV of 19,200 h⁻¹, temperature at 800 °C and at 1 atm pressure. The CH₄ conversion, CO₂ conversion and H₂/CO ratio are plotted as a function of time as shown in Fig. 4.23. Throughout the 50 h reaction, CeAl_{0.95}Rh_{0.05}O_{3-δ} catalyst shows good activity and time on stream stability, while maintaining H₂/CO ratio in the range of 1.8-2.0. This ratio is desirable for methanol, FT synthesis and in the manufacture of many chemicals.

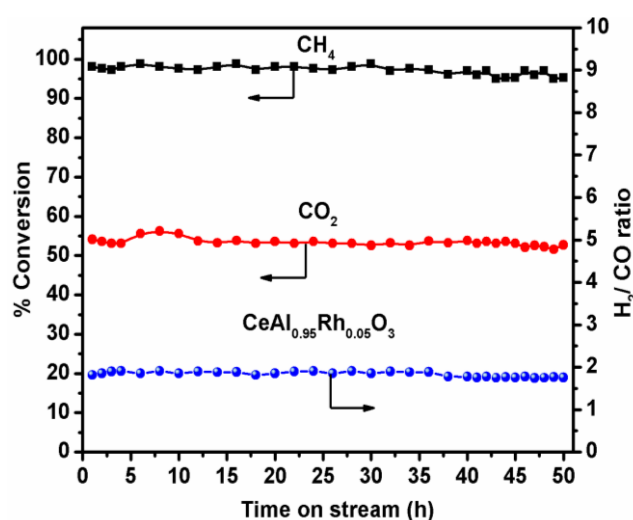


Fig. 4.23 Steam reforming of simulated biogas containing 11 ppm sulphur over CeAl_{0.95}Rh_{0.05}O_{3-δ} catalyst.

Reaction conditions: CH₄:CO₂:H₂O is 3:2:4, Temp. 800 °C, GHSV 19,200 h⁻¹, 1 atm.

4.11 Characterization of spent catalysts

When sulphur containing methane is used to test performance of steam reforming catalysts, several side reactions are possible. Besides, the carbon formation reaction mechanism depends on the steam reforming conditions like operating temperature, pressure and gas composition. A number of methods are available to investigate the coke formed during the reforming reaction.

4.11.1 Thermogravimetric analysis of spent catalysts

Thermogravimetric analysis (TGA) was employed to estimate the coke/carbon deposited on the catalyst during the steam reforming (see Fig. 4.22) of H₂S containing methane. The moles of carbon per gram of catalyst were calculated from the weight loss observed during TGA in air flow. This weight loss from spent catalysts is generally due to combustion of various types of carbon deposits. For the spent catalysts, which were on stream for 20h, the weight losses observed were 0.011 moles C.g⁻¹ for CeAl_{0.8}Ni_{0.2}O_{3-δ}; 0.002 moles C.g⁻¹ per gram for impregnated Rh/CeAlO₃ catalyst and only 0.001 moles C.g⁻¹ in case of CeAl_{0.95}Rh_{0.05}O₃ catalyst respectively. These results clearly demonstrate that Rh substitution in CeAlO₃ perovskite helped to reduce the coke deposition considerably. Further, the reactivity of the carbon also determines the catalytic activity, i.e., whether it is amorphous or graphitic carbon. If active metal is embedded by carbon, accessibility of the active metal to the reactants is restricted. All these factors decide the durability of the catalyst. Hence, from the results, though a small amount of coke is observed on CeAl_{0.95}Rh_{0.05}O_{3-δ} catalyst, hardly any deactivation of the catalyst is observed.

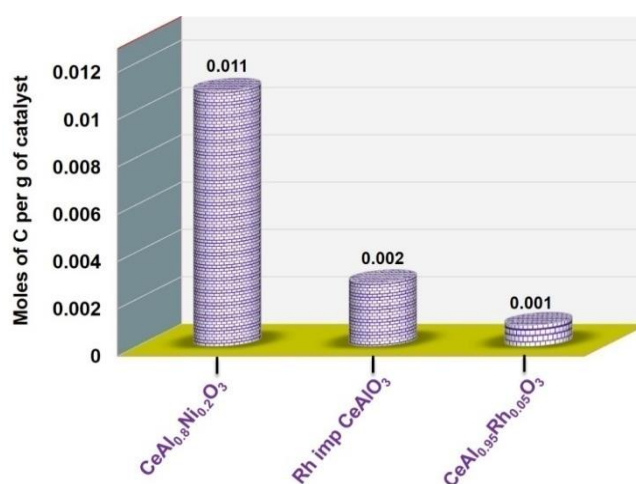


Fig. 4.24 Coke on Ni and various Rh spent catalysts during SRM of sulphur containing CH₄.

TGA data showed that accumulated carbon was lower on catalyst that is prepared by Rh substitution in CeAlO₃ lattice. Further studies were carried out to investigate the type of carbon on these catalysts by using TEM.

4.11.2 Transmission Electron Microscopy of spent catalysts

The TEM analysis of spent catalysts; CeAl_{0.8}Ni_{0.2}O_{3-δ}, Rh/CeAlO₃ and CeAl_{0.95}Rh_{0.05}O₃ catalysts after 20 h on-off cycle run were carried out, these results are shown in Fig. 4.25. The spent catalyst CeAl_{0.8}Ni_{0.2}O_{3-δ} (Fig. 4.25a) has large amounts of amorphous carbon, graphitic carbon and nano tubes with attached metal particles (dark regions) on their surface. Rh impregnated CeAlO₃ catalyst (Fig. 4.25b) shows presence of carbon nanotubes attached with more agglomerated Rh particles. On the otherhand, CeAl_{0.95}Rh_{0.05}O₃ catalyst shows very less carbon formation on its surface (Fig. 4.25c).

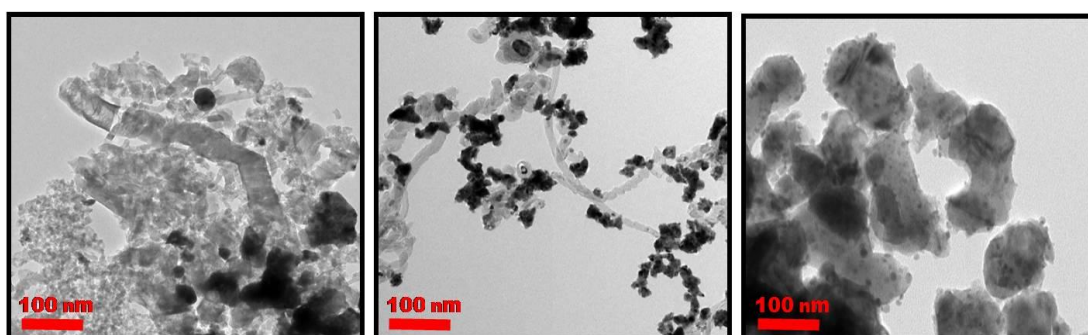


Fig. 4.25 TEM images of spent catalysts (a) CeAl_{0.8}Ni_{0.2}O₃ (b) Rh/CeAlO₃, (c) CeAl_{0.95}Rh_{0.05}O₃ catalysts.

The TEM analysis could explain the reasons for deactivation in case of CeAl_{0.8}Ni_{0.2}O₃ and Rh impregnated CeAlO₃ catalysts. In these catalysts metallic sites are covered with carbon, hence these active sites are not accessible to the reactants.

4.12 Conclusions

This chapter deals with reforming of methane on Ru and Rh containing CeAlO₃ perovskites catalysts, which were prepared through citrate gel and impregnation methods. Their characterization by powder XRD and Rietveld refinement analysis revealed that all perovskites are crystallized in cubic phase. XPS and Raman analysis shows that even after reduction, part of Ru particles is present inside the perovskite lattice. As a result, substituted metal has greater interaction with the support compared to impregnated catalyst. These perovskite type oxides were tested for steam reforming of methane by varying their Ru content. Higher Ru content in perovskite structure enhanced the catalytic activity in steam reforming of methane. Moreover, it was proved that Ru substituted catalyst is better than Ru impregnated

catalyst, as former shows superior activity compared to the later. Kinetic experiments were carried out over CeAl_{0.85}Ru_{0.15}O₃ catalysts following Wei and Iglesia mechanism and the activation energy observed was 75 kJ/mol.

To reduce the Ru content, Ni substituted CeAlO₃ perovskite was promoted by substituting it with Ru. These Ru and Ni substituted CeAlO₃ structures (CeAl_{0.9-x}Ru_xNi_{0.1}O_{3-δ}) were synthesized by citrate gel method. Ru metal helped to reduce Ni in CeAl_{1-x}Ni_xO₃ and helped to improve the dispersion of Ni metal in these samples. This Ru promoted catalyst was tested for bi- and tri reforming methane. It was highly active and durable for 100h and 500 h without deactivation in bi- and tri-reforming reactions respectively. Carbon content was estimated using TGA over these samples and found only 5.1x10⁻⁵ and 1.5x10⁻⁵ moles carbon g⁻¹.h⁻¹ after bi- and tri-reforming reactions respectively. The results show that substitution of a little fraction of a noble metal into the perovskite catalyst stabilizes the catalytic activity for long hours on stream.

It was also the goal of this study to develop highly stable catalysts that are tolerant to sulphur, when it is present in methane gas in ppm levels. Hence, Rh substituted CeAlO₃ (CeAl_{1-x}Rh_xO₃) perovskites were prepared for steam reforming of methane and bi-reforming of simulated biogas. Substitution of Rh in CeAlO₃ lattice was established using powder XRD refinement. The partial substitution of Al by Rh in CeAlO₃ catalyst (CeAl_{1-x}Rh_xO₃, x = 0.0, 0.01, 0.02, 0.035, 0.05 and 0.1) led to changes in cell parameters, BET surface area and Rh particle size. The modification of these properties upon Rh substitution could be directly correlated with the catalytic activity of the perovskite in SRM and bi-reforming of simulated biogas. Based on TPR, reducibility of the Rh and oxygen defects (XPS study) appears to influence the activity in reforming. The CeAl_{0.95}Rh_{0.05}O₃ catalyst showed superior activity and durability for 50 h time on stream. It is stable even when methane contains few ppm of sulphur, compared to Ni catalysts and Rh impregnated catalysts. Characterization of spent catalysts showed that CeAl_{0.95}Rh_{0.05}O₃ has good thermal stability with less carbon deposited on it. The coke content and types of carbon present on these catalysts has been analyzed by TGA and TEM. Similarly, when CeAl_{0.95}Rh_{0.05}O₃ catalyst was studied for its durability during steam reforming of simulated biogas that contains 11 ppm of H₂S, its activity was very good and stable during time on stream for 50 h at 800 °C, as it retained its high activity in terms of CH₄ and CO₂ conversion.

4.13 References

1. A. T. Ashcroft, A. K. Cheetham, M. L. H. Green, P. D. F. Vernon, *Science* 1991, **352**, 225.
2. J. R. Rostrup-Nielsen, J. H. B. Hansen, *J. Catal.* 1993, **144**, 38.
3. D. Qin, J. Lapszewicz, *Catal. Today* 1994, **21**, 551.
4. J. Kehres, J. G. Jakobsen, J. W. Andreasen, J. B. Wagner, H. H. Liu, A. Molenbroek, J. Sehested, I. Chorkendorff, T. Vegge, *J. Phys. Chem. C*, 2012, **116**, 21407.
5. L. Vasylechko, A. Senyshyn, D. Trots, R. Niewa, W. Schnelle, M. Knapp, *J. Solid State Chem.*, 2007, **180**, 1277.
6. W. T. Fu and D. J. W. IJdo, *J. Solid State Chem.*, 2004, **177**, 2973.
7. H. M. Rietveld, *J. Appl. Crystallogr.* 1969, **2**, 65.
8. B. H. Toby, *J. Appl. Crystallogr.* 2001, **34** (2), 210.
9. Y. L. Kim, H-A .Choi, N-S. Lee, B. Son, H. J. Kim, J. M. Baik, Y. Lee, C. Lee, M. H. Kim, *Phys. Chem. Chem. Phys.* 2015, **17**, 7435.
10. J. Lee, H-S. Yang, N-S. Lee, O. Kwon, H-Y. Shin, S. Yoon, J. M. Baik, Y-S. Seo, M. H. Kim, *CrystEngComm*, 2013, **15**, 2367.
11. C.-T. Au, C.-F. Ng, M.-S. Liao, *J. Catal.* 1999, **185**, 12.
12. I. M. Ciobica, F. Frechard, R. A. van Santen, A. W. Kleyn, J. Hafner, *J. Phys. Chem. B* 2000, **104**, 3364.
13. J. P. Liu, P. Hu, *J. Am. Chem. Soc.* 2003, **125**, 1958.
14. J. H. Jeong, J. W. Lee, D.J. Seo, Y. Seo, W.L. Yoon, D.K. Lee, D.H. Kim *Appl. Catal. A: Gen.*, 2006, **302**, 151.
15. H.-S. Roh, K. Y. Koo, J. H. Jeong, Y. T. Seo, D. J. Seo, Y.-S. Seo, W. L. Yoon, S. B. Park, *Catal. Lett.* 2007, **117**, 85.
16. H.-S. Roh, K. Y. Koo, U. D. Joshi, W. L. Yoon, *Catal. Lett.* 2008, **125**, 283.
17. K. Y. Koo, H.-S. Roh, U. H. Jung, W. L. Yoon, *Catal. Lett.* 2009, **130**, 217.

18. K. Y. Koo, H.-S. Roh, Y. T. Seo, D. J. Seo, W. L. Yoon, S. B. Park, *Int. J. Hydrogen Energy* 2008, **33**, 2036.
19. G. A. Olah, A. Goepfert, M. Czaun, G. K. S. Prakash, *J. Am. Chem. Soc.* 2013, **135**, 648.
20. M. Ashrafi, T. Proll, C. Pfeifer, H. Hofbauer, *Energy Fuels* 2008, **22**, 4182.
21. J. R. Rostrup Nielsen, J. Sehested, *Adv. Catal.* 2002, **47**, 65.
22. J. W. Kang, C. M. Jeong, N. J. Kim, M. I. Kim, H. N. Chang, *Biotechnol. Bioproc. Eng.* 2010, **15**, 505.
23. R. Munkundan, E.L. Brosha, F.H. Garzon, *Electrochem. Solid-State Lett.*, 2004, **7** (1), A5.
24. N. Yamazoe, Y. Teraoka, *Catal. Today*, 1990, **8** (2), 175.
25. M.A. Peña, J.L.G. Fierro, *Chem. Rev.*, 2001, **101** (7), 1981.
26. A. Pfau, K.D. Schierbaum, *Surf. Sci.* 1994, **71**, 321.
27. J. Fang, X. Bi, D. Si, Z. Jiang, W. Huang., *Appl. Surf. Sci.* 2007, **253**, 8952.
28. A. Kotani, T. Jo, J.C. Parlebas, *Adv. Phys.* 1988, **37**, 37.
29. S. Kaliaguine, A. Van Neste, V. Szabo, J. E. Gallot, M. Bassir, R. Muzychuk, *Appl. Catal. A: Gen.* 2001, **209**, 345.
30. V. A. Vavilin, V. B. Vasiliev, S. V. Ritow, A. V. Ponomarev, *Bioresour. Technol.* 1994, **48**, 1.
31. M. Flytzani-Stephanopoulos, M. Sakbodin, Z. Wang, *Science*, 2006, **312**, 1508.
32. M. Gong, X. Liu, J. Trembly, C. Johnson, *J. Power Sources* 2007, **168**, 2, 289.
33. H. Devianto, *J. Power Sources*, 2006, **159** (2), 1147.
34. A. Effendi, K. Hellgardt, Z.-G. Zhang, T. Yoshida, *Fuel* 2005, **84**, 869.

Chapter 5

Syngas by Dry reforming of CH₄
and steam reforming of simulated
biogas over MZr_{1-x}Ni_xO₃ (M= Ca,
Sr and Ba) perovskites

5.1 Introduction

World community is grappling with the affects of global warming attributed to green house gas (GHG) emissions. Carbon dioxide (CO₂) is at the top of all the GHG emissions. Currently, the CO₂ in atmosphere is inching towards 400 ppm level ^[1], which is accounted for uncertain weather pattern that may lead to rising sea level, heavier precipitation and flooding etc. This has motivated tremendous interest in the development of CO₂ capture and utilization technologies that can either cap or reduce CO₂ level in the atmosphere. Similarly, CH₄ being a GHG, its emissions are also a cause of concern. Recently, many research programmes are focused on utilization of the green house gases by transforming them into value added chemicals and fuels. In this context, dry reforming of methane (DRM) reaction is an interesting concept to utilize two abundantly available green house gases to produce syngas, which has many applications for obtaining fuels and chemicals. In DRM, the H₂/CO ratio obtained is close to 1, which is useful to produce long chain hydrocarbons through Fischer-Tropsch (FT) synthesis. ^[2-7] Dry reforming reaction is given below:



The H₂/CO ratio obtained from dry reforming reaction also depends on the occurrence of reverse water gas shift (RWGS) reaction,



The DRM could not be translated to an industrial process so far due to two major problems. First problem, it is highly endothermic reaction, hence needs to be conducted at high temperatures; second problem is the lack of catalyst stability as a result of metal sintering and coke formation under the reaction conditions. ^[8]

Numerous studies were reported using supported noble metal catalysts that are suitable for the dry reforming reaction as these are less sensitive to carbon deposition and metal sintering. ^[9-12] However, their utility is limited owing to their low abundance and high cost. Nickel based catalysts are best in this regard, but they are highly prone to deactivation due to sintering as well as coking. ^[13] Hence, understanding coking mechanism of Ni based catalysts and improve their resistance to carbon formation and sintering are worthy challenges to be tackled, if the dry reforming reaction has to be implemented on industrial scale. ^[14,15]

In general, dry reforming reaction proceeds via CH₄ decomposition and oxidation of carbon species. Hence, a bi-functional catalyst is most suitable for sustaining the reaction for a long duration on stream. The bi-functional catalysts should catalyze the CH₄ cracking and effectively remove carbon species from the active metal surface. For this purpose, a catalyst has to be designed to attain high metal dispersion, good redox property and excellent thermal stability. In this connection, hydrotalcites, structural oxides like perovskites and spinels may be useful [16-17]. In addition, if promoters like basic or redox type oxides are added, they will fortify the catalysts further. [18-21] Addition of basic oxides to the support enhances the CO₂ activation and also enables gasification of deposited carbon on the active sites, leading to decrease in the rate of deactivation by coking. [22,23] Considering these aspects, we have synthesized perovskite type oxide catalysts that have active metal Ni incorporated into their lattice. Also, substitution of alkaline earth metals Ca, Sr and Ba into A site of the perovskite lattice is expected to enhance the activity and stability of the catalysts. In heterogeneous catalysis, ZrO₂ is widely used as support because of its higher thermal stability and unique chemical properties like redox and acid –base functions. [24] Several reports suggest that Ni/ZrO₂ catalyst deactivates easily due to coke formation and sintering. The stability of Ni/ZrO₂ catalyst can be improved by adding some basic oxides like CaO, MgO and CeO₂. [25-26] The present chapter describes the successful synthesis of Ni substituted MZrO₃ (M= Ca, Sr and Ba) perovskite oxides by citrate gel method, their characterization and applications DRM reaction. These were studied by CO₂ -temperature programmed desorption (CO₂-TPD) for investigation of basicity and temperature programmed reduction (TPR) for finding reducibility. The results of these studies were used to establish structure-basicity-performance relation of these perovskite type oxides.

5.2. Experimental methods

5.2.1. Preparation of MZr_{1-x}Ni_xO_{3-δ} perovskites

The MZr_{1-x}Ni_xO_{3-δ} (M= Ca, Sr and Ba; x = 0 and 0.2) perovskite type oxides were prepared by conventional citrate gel method. Stoichiometric quantities of the corresponding metal nitrates were dissolved in minimum required water and added drop wise to the citric acid solution under constant stirring at 80 °C. Following the

complexation, the solution was evaporated and dried at 180 °C for 12 h to obtain spongy amorphous citrate gel. This fluffy material was crushed and calcined at 750 °C for 6 h in air to get the corresponding $MZr_{1-x}Ni_xO_{3-\delta}$ (M= Ca, Sr and Ba; x = 0 and 0.2) perovskite type oxides.

5.2.2. Transient pulse study of CH₄ and CO₂ reactions

Transient pulse experiments of methane followed by CO₂ reaction on different catalysts was conducted using a Micromeritics Autochem 2920 system coupled to a mass probe (Pfeiffer QMS 200). Typically, fresh calcined sample (100 mg) was held between quartz wool plugs in a U shaped quartz tube and reduced in 5% H₂ /Ar flow (30 ml/min⁻¹) at 600 °C for 2 h. Following this pre-treatment, the sample was purged in He flow for 1h. Subsequently, 0.5 ml of CH₄ was pulsed into He flow which was followed by CO₂ pulse (0.5 ml) at an interval of 8 minutes. Each experiment was conducted with four consecutive pulses of each gas, at three temperatures, viz., 600, 700 and 800 °C. Signals of m/z = 2, 28, 15, 18 and 44 were monitored corresponding to H₂, CO, CH₄, H₂O and CO₂ respectively. The contribution of CO₂ to the signal at m/z=28 was subtracted to eliminate the errors of CO signal.

5.2.3. Evaluation of catalysts for dry reforming

The dry reforming reactions were carried out in a packed-bed tubular down flow reactor made up of Incolloy HT, after placing it in a programmable tubular furnace. All the gases (CH₄, CO₂ and N₂) used for the reaction were regulated by thermal mass flow controllers (Brooks Instruments). In a typical experiment, 0.5 cc of catalyst particles in 0.3-0.5 mm range were mixed with 0.5 cc of same size quartz pieces and loaded in the reactor supported between ceramic wool plugs. The catalyst bed temperature was monitored by means of a chromel-alumel thermocouple centered in the catalyst bed. Prior to the reaction, catalyst was calcined at 400 °C for 3 h and reduced in situ at 600 °C for 6 h using 20% H₂ in N₂ gas mixture. Subsequently, the DRM reaction was carried using a gas mixture consisting of CH₄, CO₂ and N₂ in the volume ratio of 1:1:1. The catalytic activity was evaluated at different temperatures (600, 650, 700, 750 and 800 °C). The product gas mixture was analyzed using an online gas chromatograph (Chemito 1000) equipped with a spherocarb packed column (1/8" OD and 8 feet length).

Methane and CO₂ conversions and H₂/CO ratio were calculated based on the gas

composition estimated by GC and by using the following formulae:

CH₄ Conversion:

$$X_{\text{CH}_4} \% = [(F_{\text{CH}_4 \text{ in}} - F_{\text{CH}_4 \text{ out}})/F_{\text{CH}_4 \text{ in}}] \times 100 \quad (5.3)$$

CO₂ Conversion:

$$X_{\text{CO}_2} \% = [(F_{\text{CO}_2 \text{ in}} - F_{\text{CO}_2 \text{ out}})/F_{\text{CO}_2 \text{ in}}] \times 100 \quad (5.4)$$

H₂/CO ratio:

$$\text{H}_2/\text{CO} = [F_{\text{out H}_2}/F_{\text{out CO}}] \quad (5.5)$$

Deactivation percent (%)

$$= [(\text{Initial conversion} - \text{Final conversion}) / \text{Initial conversion}] \times 100 \quad (5.6)$$

5.3. Results and discussion

5.3.1. Textural and structural characterization of catalysts

The BET surface areas and active metal (Ni) dispersions obtained through CO chemisorption of MZr_{1-x}Ni_xO_{3-δ} (M= Ca, Sr and Ba; x=0 and 0.2) perovskite type catalysts is listed in Table 5.1. Specific surface area of the MZrO₃ perovskite type oxides has increased with change in alkaline earth cation down the group from Ca to Ba at the A site of perovskite. A similar trend was observed even in the case of Ni substituted samples. Hence, BET surface areas follow the order CaZr_{0.8}Ni_{0.2}O_{3-δ} < SrZr_{0.8}Ni_{0.2}O_{3-δ} < BaZr_{0.8}Ni_{0.2}O_{3-δ}; for x=0 and 0.2. Surface areas of the samples increased to a little extent on Ni substitution, which is attributed to a small reduction in crystallite size. This was clearly seen from crystallite sizes calculated with the help of Debye–Scherrer equation using XRD line widths. The Ni metal dispersion on CaZr_{0.8}Ni_{0.2}O_{3-δ} perovskite type catalyst was higher compared to Sr and Ba perovskite type catalysts, i.e. more active metal (Ni) is present on the surface of CaZr_{0.8}Ni_{0.2}O_{3-δ} perovskite compared to SrZr_{0.8}Ni_{0.2}O_{3-δ} or BaZr_{0.8}Ni_{0.2}O_{3-δ}.

Table 5.1 Structural and textural properties of MZr_{1-x}Ni_xO_{3-δ} (M= Ca, Sr and Ba; x=0 and 0.2) perovskite oxides.

	CaZrO ₃	CaZr _{0.8} Ni _{0.2} O ₃	SrZrO ₃	SrZr _{0.8} Ni _{0.2} O ₃	BaZrO ₃	BaZr _{0.8} Ni _{0.2} O ₃
Space group	Pcmn (62)	Pcmn (62)	Pm-3m	Pm-3m	Pm-3m	Pm-3m
a/Å	5.5920(1)	5.5911(9)	4.1005(2)	4.0920(4)	4.1900(4)	4.1878(6)
b/Å	8.0114(6)	8.0106(1)	4.1005(2)	4.0920(4)	4.1900(4)	4.1878(6)
c/Å	5.7505(1)	5.7502(9)	4.1005(2)	4.0920(4)	4.1900(4)	4.1878(6)
Rp (%)	6.2	5.6	6.3	6.4	6.3	7.6
WRp (%)	8.3	6.4	8.4	8.1	8.4	9.3
Chi ²	2.3	1.6	2.7	2.6	1.6	2.3
Surface area (m ² /g)	9.2	13.2	12.1	14.1	13.4	14.6
Tolerance factor*	0.91	0.92	0.94	0.95	1.00	1.01
Crystallite size (nm)	42	38	40	36	35	34
Ni dispersion (%)	-	13.5	-	4.0	-	3.9
Ni metal surface area (m ² /g)	-	6.2	-	1.5	-	1.4
Average Ni crystallite size (nm)	-	7.2	-	25.0	-	25.6

* calculated using formulae $\tau = (r_A+r_O)/(\sqrt{2}(r_B+r_O))$.

5.3.2. X-ray diffraction of MZr_{1-x}Ni_xO_{3-δ}

Powder XRD pattern of freshly calcined MZr_{1-x}Ni_xO_{3-δ} (M= Ca, Sr and Ba) perovskite oxides and corresponding Ni substituted compositions (x =0 and 0.2) is given in Fig. 5.1A. Spectra show that on varying the alkali earth cation in A site from Ca to Ba, the number of diffraction lines decreased indicating phase transition from orthorhombic to cubic lattice (See Fig. 5.2). Additional peaks belonging to respective alkaline earth carbonate impurities were also seen in the XRD spectra, particularly in the Sr and Ba containing samples. These carbonates were not decomposed even after calcination at 750 °C for 6 h in air. The cell parameters calculated by refinement of

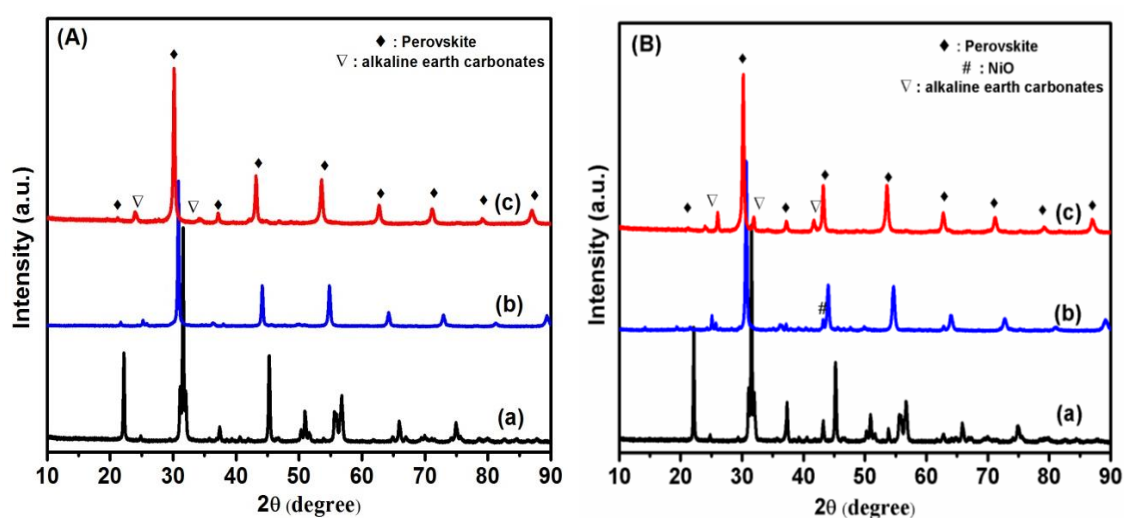


Fig. 5.1 XRD pattern of MZr_{1-x}Ni_xO_{3-δ} perovskites; (A) x = 0 and (B) x = 0.2; where M = (a) Ca, (b) Sr and (c) Ba.

XRD data are in good agreement with reported data (JCPDS –PDF No. 76-2401, 75-0467 and 74-1299). Both Sr and Ba substituted perovskites crystallized in cubic phase, while cell parameter of BaZrO₃ is higher compared to SrZrO₃ sample.

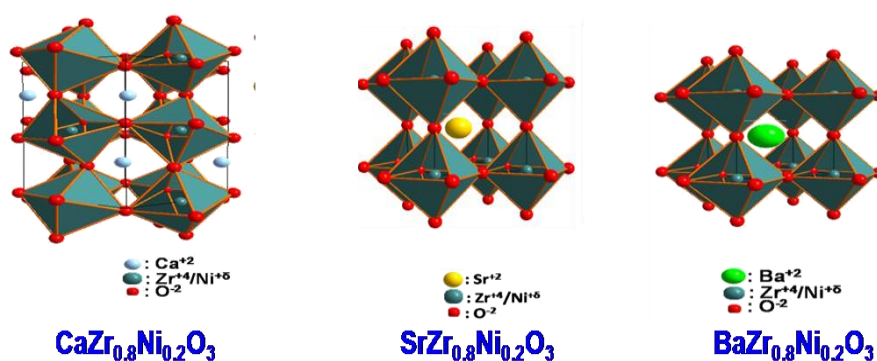


Fig. 5.2 Schematic presentation of MZr_{1-x}Ni_xO_{3-δ} perovskites.

In the case of Ni substituted perovskites (MZr_{0.8}Ni_{0.2}O_{3-δ}), the diffraction pattern clearly shows that the parent perovskite phase is retained on Ni substitution, as shown in Fig. 5.1B. Minor peaks in the 2θ range of 25 to 30° are assigned to the respective alkaline earth carbonate impurities and small impurity of NiO (θ = 43.2°) was also seen in these samples. The intensity of impurity peaks increased on Ni substitution. Moreover, the Rietveld refinement results reveal that on Ni substitution into Zr site, the lattice parameter decreased, indicating the incorporation of Ni into the perovskite lattice. A fraction of NiO also appears to be well dispersed on the surface. The decrease in lattice parameter is explained on the basis of smaller Ni⁺² (69 pm) replacing the larger Zr⁺⁴ (72 pm), with the same coordination number (VI). Thus, it appears that the Ni in these samples is present in two forms; i.e (i) Ni substituted in the bulk of perovskite lattice and (ii) a small fraction of Ni highly dispersed on the surface. The stability and distortion in ideal ABO₃ cubic perovskite structure is determined by tolerance factor (τ). The tolerance factor for Ca substituted sample is somewhat deviated from the ideal value (~1). Hence, this perovskite is crystallized in orthorhombic phase (space group: Pcmn (62)).

$$\tau = (r_A + r_O) / (\sqrt{2}(r_B + r_O)) \quad (5.7)$$

where r_A, r_B and r_O are the ionic radii of A, B and O ions. The cell parameters, surface areas and tolerance factors are given in Table 5.1.

5.3.3. Raman spectroscopy

The Raman spectra of calcined MZrO₃ (M= Ca, Sr and Ba) samples are given in Fig. 5.3. They show that the number of vibration modes decreased during the orthorhombic to cubic phase transition from Ca to Ba substituted perovskites. In case of CaZrO₃, which has orthorhombic Pcmn (62) phase, it is theoretically expected to show 24 Raman active modes. But, some modes may not be detectable due to their low polarizability or some modes could be hidden in highly intense bands.^[27] Hence, we observe only 10 vibrations in the 80-600 cm⁻¹ region (Fig. 5.2). Also, at higher frequencies, the Raman peaks are broad due to second order scattering, resulting in the superposition of different combination modes. The frequencies of the observed Raman bands and their modes are listed in Table 5.2 and all are in agreement with reported data.^[28-31] The shapes of the Raman bands indicate that the CaZrO₃ particles

exist in nano regime as confirmed by XRD. The grain size of the perovskite is inversely proportional to the half width at half height of the Raman bands. [28]

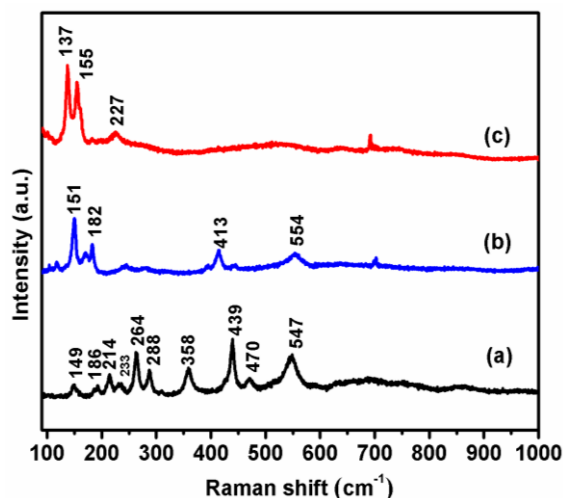


Fig. 5.3 Raman spectra of MZrO₃; where M = (a) Ca, (b) Sr and (c) Ba.

Table 5.2 Raman vibration modes of CaZrO₃ type perovskite oxides.

Our work (Γ cm ⁻¹)	Mode	K. Boobalan et al. [28] (Γ cm ⁻¹)	Martine Tarrida et al. [29] (Γ cm ⁻¹)	Orera et al. [30] (Γ cm ⁻¹)	Perry et al. [31] (Γ cm ⁻¹)
149	A _g	121, 147	145, 151, 172	145	153
186	B _{2g}	183	185		186
214	B _{2g}	212	213, 229	212, 227	
233	B _{2g}		235	234	228
264	A _g	262	263	262	
288	A _g	283	287, 310	286, 305	
358	A _g	356	358, 423	358, 418	340
439	A _g +B _{1g}	437	439	439	377, 418
470	B _{2g}	469	470	469	515
547	B _{1g} or B _{3g}	546	548	543	551

On the otherhand, Raman bands corresponding to carbonate impurities (151,182, 413,554 and 155,227) were seen only for SrZrO₃ and BaZrO₃ perovskite samples. Since, these samples crystallized in cubic phase (Pm3m), they are expected to show 12 vibrations, but all of them are forbidden Raman transitions. [32] The spectra of Ba and Sr based carbonates are similar, but due to the difference in their atomic mass

(137.33 for Ba and 87.62 for Sr) bathochromic shift is expected in the case of Ba carbonate. The Raman bands of carbonates are narrow; revealing covalent bonding of CO₃ vibrational units with no disorder. [33] The presence of these carbonates was also confirmed by XRD.

5.3.4. Temperature programmed reduction

The reduction nature of Ni substituted perovskites was investigated by H₂-TPR. Figure 5.4 shows deconvoluted TPR profiles of three regions of hydrogen consumption observed for CaZr_{0.8}Ni_{0.2}O_{3-δ} and SrZr_{0.8}Ni_{0.2}O_{3-δ} perovskite oxides. In case of BaZr_{0.8}Ni_{0.2}O_{3-δ}, only two peaks were seen. Bai et al. also observed similar TPR peaks in the 230-330 °C temperature range, which were attributed to the reduction of NiO. [34] Rudolfo et al. also reported 300 °C reduction peak belonging to the amorphous NiO on surface. [35] The low temperature peak corresponds to the reduction of weakly interacting NiO species, which are present on the perovskite surface.

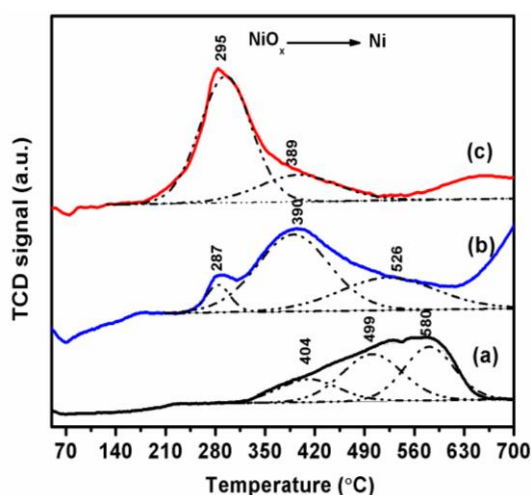


Fig. 5.4 Deconvoluted TPR profile of (a) CaZr_{0.8}Ni_{0.2}O_{3-δ} (b) SrZr_{0.8}Ni_{0.2}O_{3-δ} and (c) BaZr_{0.8}Ni_{0.2}O_{3-δ} perovskites.

In the case of CaZr_{0.8}Ni_{0.2}O_{3-δ} and SrZr_{0.8}Ni_{0.2}O_{3-δ} samples, peaks at 499 °C and 410 °C may be assigned to the reduction of NiO_x species, which are present on surface and sub surface region of the perovskite. The high temperature peaks above 510 °C are assigned to the NiO_x species, which are part of bulk perovskite lattice (Zr⁺⁴-O-Ni⁺²). Above 550 °C, reduction of carbonate impurities of Sr and Ba samples has been observed, whose presence was confirmed by Raman and XRD spectra. On close

observation of TPR profiles of CaZr_{0.8}Ni_{0.2}O_{3-δ}, it is clear that the peaks appear at higher temperatures compared to other two catalysts. The evolution of reduction peak at high temperature could be due to presence of smaller NiO crystallites on the surface. These observation indicate relatively less probability of Ni sintering in CaZr_{0.8}Ni_{0.2}O_{3-δ} at lower temperatures, which is expected to play vital role in retaining dry reforming activity at high reaction temperatures.

5.3.5. Temperature programmed desorption of CO₂ and O₂

The nature of surface basicity and strength were studied using CO₂-TPD, these results are illustrated in Fig. 5.5A. Since CO₂ is an acidic gas, basic support is expected to adsorb and promote its activation. It can be seen that all the samples show CO₂ desorption at high temperatures; therefore carbonate species must have formed on exposing the sample to CO₂. The CO₂-TPD profiles indicate that strength of basicity increased from Ca to Ba substituted perovskite samples. The CaZr_{0.8}Ni_{0.2}O_{3-δ} sample shows sharp desorption peak in the 500-750 °C temperature region. In case of SrZr_{0.8}Ni_{0.2}O_{3-δ} and BaZr_{0.8}Ni_{0.2}O_{3-δ} perovskites, the peaks were seen at higher temperatures (around 800 °C), as the corresponding SrCO₃ and BaCO₃ are decomposed only at high temperatures. [36, 37]

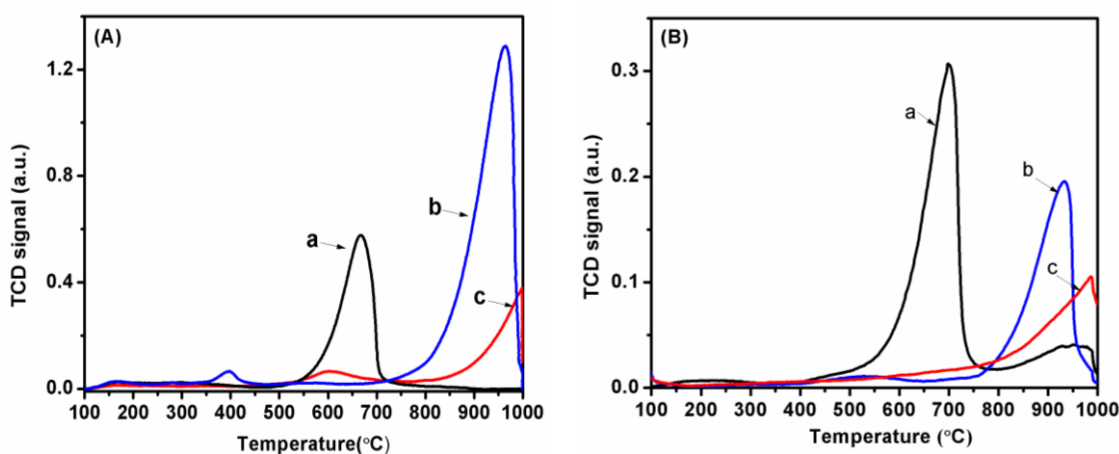


Fig. 5.5 TPD of (A) CO₂ and (B) O₂ profile of MZr_{0.8}Ni_{0.2}O_{3-δ} perovskites, where M= (a) Ca, (b) Sr and (c) Ba

Since the gas-solid reaction occurs over the perovskite surface, the amount of carbonate formation is expected to be related to surface area of the perovskite. The CO₂-TPD spectra of CaZr_{0.8}Ni_{0.2}O_{3-δ} indicate that CO₂ is adsorbed on the surface at lower temperature and is subsequently activated with ease. This activation is expected

to play a key role in the elimination of carbon during dry reforming of methane. Further, on Sr and Ba substituted perovskites, the carbonate desorption peaks are broader and shifted to very high temperatures. Yan et al. [38] also observed similar results in case of Ba_xSr_{1-x}Co_{0.8}Fe_{0.2}O₃ and have observed higher CO₂ adsorption with increased Ba doping. Finally, CO₂-TPD results confirm that CO₂ is adsorbed on the perovskite surface and form carbonate species which are decomposed at high temperatures (>650 °C). The shape of the TPD peak is asymmetric, indicating that desorption rate follows first order kinetics. The CO₂ desorption activation energy can be calculated following the Chan-Aris-Weinberg method. [39]

$$E_d = RT_m \left[-1 + \sqrt{1 + 5.832 \left(\frac{T_m}{W_{1/2}} \right)^2} \right] \quad (5.8)$$

where R is the gas constant, T_m is the maximum temperature of TPD peak and W_{1/2} is the peak width at half maximum and E_d is the activation energy of the desorption (directly proportional to T_m). The calculated activation energy values of CO₂ desorption from different alkaline earth substituted perovskites are in the order:

$$\text{Ca (55.9 kcal.mol}^{-1}\text{)} < \text{Sr (84.2 kcal.mol}^{-1}\text{)} \ll \text{Ba (more than 84.2 kcal.mol}^{-1}\text{)}$$

The O₂ –TPD MS experiments help to identify oxygen defect sites in the perovskite lattice unambiguously. In this experiment, the temperature is raised in a programmed manner leading to the release of the oxygen from the lattice associated with lower valence cations (Ni⁺²/Ni⁺³) that were substituted in place of high valence (Zr⁺⁴) cations, as the perovskite lattice must compensate for the charge imbalance. [40] This charge imbalance creates oxygen defects/vacancies. This charge compensation phenomenon is more important under reducing atmosphere. The O₂-TPD experiments were carried out for all the Ni substituted catalysts and is shown in Fig. 5.5B. For CaZr_{0.8}Ni_{0.2}O_{3-δ} sample, the oxygen desorption peak has been observed in temperature range of 600-800 °C. But in case of SrZr_{0.8}Ni_{0.2}O_{3-δ} and BaZr_{0.8}Ni_{0.2}O_{3-δ} perovskites, O₂ desorption peak shifted to >800 °C, while their intensities were lower compared to Ca substituted perovskite. The loss of lattice oxygen at elevated temperature leads to increase in the volume of the unit cell or decrease in the density of unit cell. [41] Moreover, passing over from Ca to Ba substituted samples, the amount of O₂ adsorption decreases drastically, with the peak areas in the order CaZr_{0.8}Ni_{0.2}O_{3-δ}>

$\text{SrZr}_{0.8}\text{Ni}_{0.2}\text{O}_{3-\delta} > \text{BaZr}_{0.8}\text{Ni}_{0.2}\text{O}_{3-\delta}$. Higher concentration of defect sites in the form of adsorbed O₂ is favourable in terms of resistance to carbon formation during dry reforming reaction. Consequently $\text{CaZr}_{0.8}\text{Ni}_{0.2}\text{O}_{3-\delta}$ perovskite catalyst should have more ability to provide oxygen vacancies and improved donation of lattice oxygen from bulk to surface, which is useful for removal of carbon.

5.4. Activity of alkaline earth substituted $\text{MZr}_{0.8}\text{Ni}_{0.2}\text{O}_{3-\delta}$ catalysts in DRM

The perovskite type oxides containing Ni and different A site cations (Ca, Sr and Ba) were evaluated for their performance in dry reforming of methane (DRM).

5.4.1. Effect of temperature over $\text{MZr}_{0.8}\text{Ni}_{0.2}\text{O}_{3-\delta}$ (M = Ca, Sr and Ba) catalysts

Basicity of the perovskite oxides is expected to be influenced by the presence of the alkaline earth cation substituted at A site, while the catalytic activity depends on factors like active metal dispersion and oxygen defects. The CO₂ reforming of methane was studied over the three $\text{MZr}_{0.8}\text{Ni}_{0.2}\text{O}_{3-\delta}$ (M= Ca, Sr and Ba) perovskite type oxides following their in-situ reduction in H₂ at 600 °C. Conversion of CH₄ and CO₂, as a function of reaction temperature are given in Fig. 5.6A and 5.6B respectively.

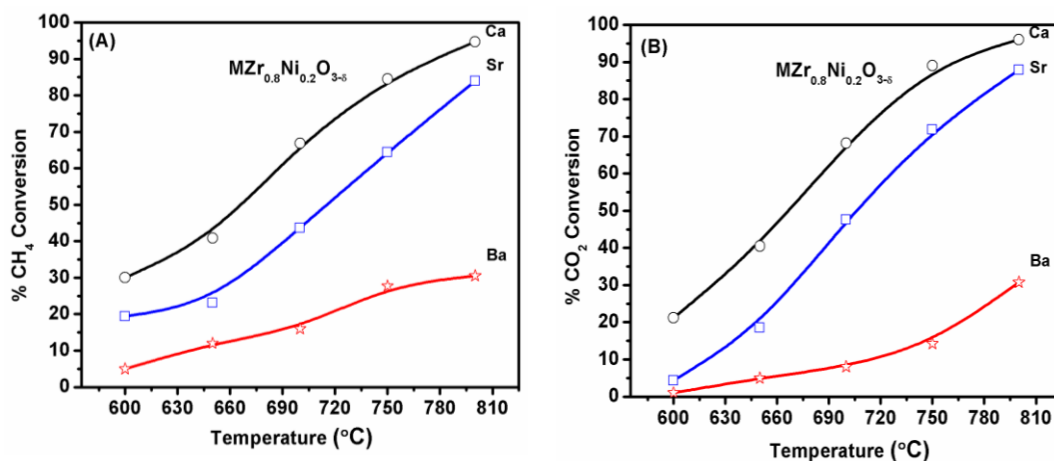


Fig. 5.6 Influence of temperature over $\text{MZr}_{0.8}\text{Ni}_{0.2}\text{O}_{3-\delta}$ catalysts in DRM of methane; (A) CH₄ conversion and (B) CO₂ conversion; M= Ca, Sr and Ba.

Reaction conditions: CH₄:CO₂:N₂ = 1:1:1, GHSV = 28,800 h⁻¹ at 1 atm.

Both CH₄ and CO₂ conversions increased with temperature, with a sharp rise in the 600- 800 °C temperature range. At higher reaction temperatures, the CO₂ conversion was slightly higher than CH₄ conversion, resulting in the lower H₂ to CO ratio (< 1) of syngas produced. If DRM reaction occurred stoichiometrically, the H₂/CO ratio would

have been equal to unity. But, at higher temperatures, the side reactions like reverse water gas shift reaction (RWGS) and reverse Boudouard reaction must be prevalent resulting in H₂/CO ratio < 1. As a result of these side reactions, additional CO is produced, leading to lower H₂/CO ratio. There were several studies that reported such observations during dry reforming reaction. [42]



The CaZr_{0.8}Ni_{0.2}O_{3-δ} catalyst shows relatively higher CH₄ and CO₂ conversions compared to SrZr_{0.8}Ni_{0.2}O_{3-δ} and BaZr_{0.8}Ni_{0.2}O_{3-δ} catalysts. Based on these results, reaction temperature of 800 °C was chosen for further studies.

5.4.2. Durability of MZr_{0.8}Ni_{0.2}O_{3-δ} (M = Ca, Sr and Ba) catalysts during DRM

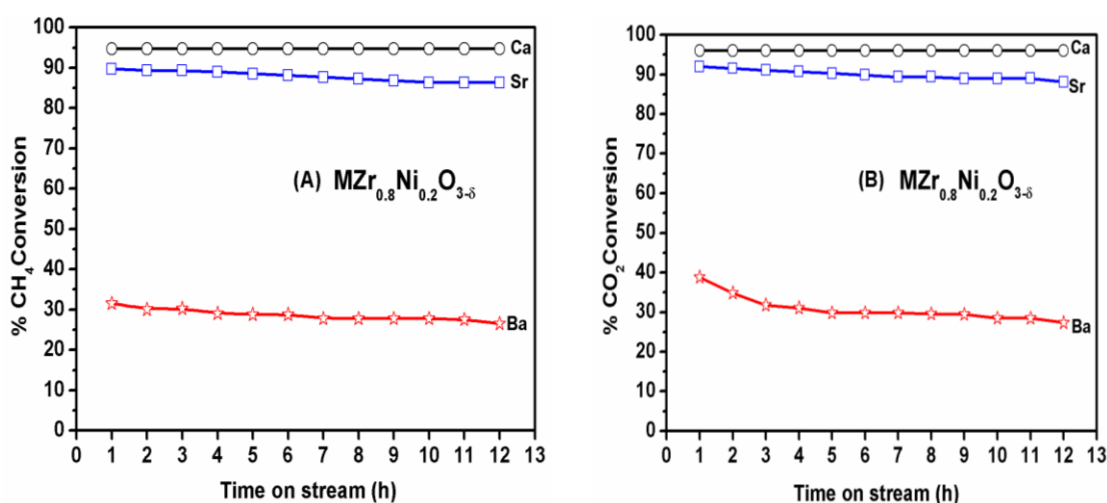


Fig. 5.7 DRM Catalytic activity with time on stream over MZr_{0.8}Ni_{0.2}O_{3-δ} perovskites, (A) CH₄ conversion and (B) CO₂ conversions.

Reaction conditions: CH₄/CO₂/N₂ = 80/80/80, 800 °C, GHSV = 28,800 h⁻¹ at 1 atm.

It is generally reported that DRM catalysts deactivate rapidly due to the formation of coke that blocks the active metal sites. The coke formation occurs as a result of side reactions such as methane cracking and CO disproportionation (Boudouard) reactions. Hence, the durability of the above catalysts was investigated for 12 h on stream, under optimized dry reforming conditions: GHSV 28,800 h⁻¹; CH₄:CO₂:N₂ (1:1:1), temperature, 800 °C; atmosphere pressure. The results of this experiment are given in Fig. 5.7A and 5.7B. The CaZr_{0.8}Ni_{0.2}O_{3-δ} catalyst showed

stable CH₄ and CO₂ conversions of 95 and 96% respectively without any noticeable drop in the activity. On the otherhand, both SrZr_{0.8}Ni_{0.2}O_{3-δ} and BaZr_{0.8}Ni_{0.2}O_{3-δ} catalysts deactivated with time. To understand this deactivation process, spent catalysts were characterized after 12 h of time on stream, using various techniques to analyze the quantity and nature of carbon deposited over them.

5.4.3. Comparison of catalytic activity of Ni substituted CaZrO_{3-δ} with Nickel impregnated (Ni/CaZrO₃) catalyst

The above discussed results demonstrate that CaZr_{0.8}Ni_{0.2}O_{3-δ} perovskite derived oxide is a good catalyst for DRM reaction. Hence, it will be interesting to study the role of substituted Ni in the reaction. Hence, a Ni impregnated (6 wt %) catalyst was prepared by using CaZrO₃ as the support and compared its performance with Ni substituted perovskite oxide catalyst prepared through citrate gel method. Fig. 5.8 shows that the activity of Ni substituted perovskite oxide (CaZr_{0.8}Ni_{0.2}O_{3-δ}) catalyst is much better compared to impregnated (Ni/CaZrO₃) catalyst. Moreover, the CO₂ conversion is relatively higher compared to CH₄ conversion on impregnated catalyst.

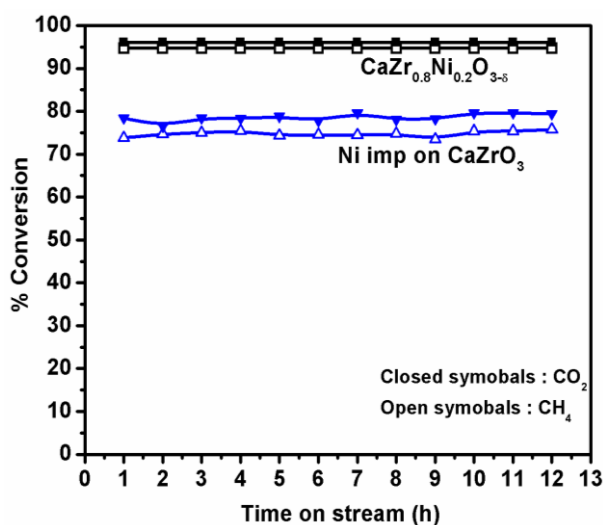


Fig. 5.8 DRM activity of CaZr_{0.8}Ni_{0.2}O_{3-δ} compared with impregnated 6% Ni/CaZrO₃. Reaction conditions: CH₄:CO₂:N₂ = 1:1:1, 800 °C, GHSV = 28,800 h⁻¹ at 1 atm.

This in turn led to lower H₂/CO ratios (< 1). In terms of stable activity of catalysts in the form of CH₄ and CO₂ conversions, both catalysts appear to be similar. But, impregnated catalyst is expected to coke at a faster rate, as a result of side reactions, which would have been seen if the reaction is continued for a longer duration.

5.4.4. Effect of variation in concentration of CH₄ and CO₂ on H₂/CO ratio in product syngas over CaZr_{0.8}Ni_{0.2}O_{3-δ} catalyst

The variation in the feed gas concentrations in dry reforming experiment were carried out by keeping one of reactant concentration constant. The results of product H₂/CO ratio with concentration of one of the feed are shown in the Fig. 5.9a and 5.9b. Two different sets were performed at five different temperatures 650, 675, 700, 725 and 750 °C. As illustrated in Fig. 5.9a, that with increasing the concentration of CH₄ in the feed by keeping CO₂ constant, the H₂/CO ratio in the product gas increased. This indicates increased rate of CH₄ decomposition reaction, during dry reforming reaction. This rate of decomposition reaction is accelerated with increasing the temperature. However, in case of increasing the moles of CO₂ at constant concentration of methane, the H₂/CO ratio decreased (<1). This is due to the lower extent of dry reforming reaction, along with higher contribution of RWGS reaction to the overall process. Keeping these findings in view, equal concentration of feed (CH₄: CO₂ = 1:1) was used for all their studies, where the DRM is of primary interest.

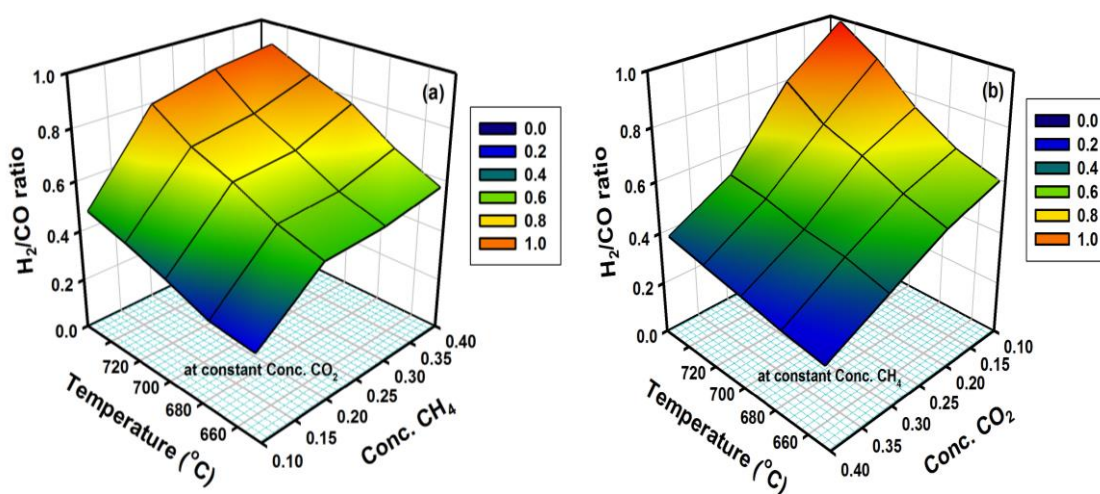


Fig. 5.9 Effect of H₂/CO ratio as function of concentration of reactants (a) CH₄ ; (b) CO₂ and temperature in DRM reaction over CaZr_{0.8}Ni_{0.2}O_{3-δ} perovskites.

5.4.5. Long term durability of CaZr_{0.8}Ni_{0.2}O_{3-δ} catalyst

Since, CaZr_{0.8}Ni_{0.2}O_{3-δ} catalyst showed excellent catalytic activity and attained equilibrium CH₄ and CO₂ conversions, its performance was monitored for 500 hours, which was shown in Fig. 5.10. Both CH₄ and CO₂ conversions remained stable and almost constant at 95 and 96%, respectively upto 500 h. The H₂/CO molar ratio was

also close to unity. The stable activity of CaZr_{0.8}Ni_{0.2}O_{3-δ} could be attributed either to the low amount of carbon formed on the surface of the catalyst or the type of carbon formed does not block the active sites of the catalysts during the reaction, as it must be undergoing gasification continuously. Moreover, the well dispersed active metal may not have sintered significantly to retard the reaction. Probably, the oxygen defects generated on Ni substitution may also have been helpful for the removal of coke formed, thus giving long life to the catalyst.

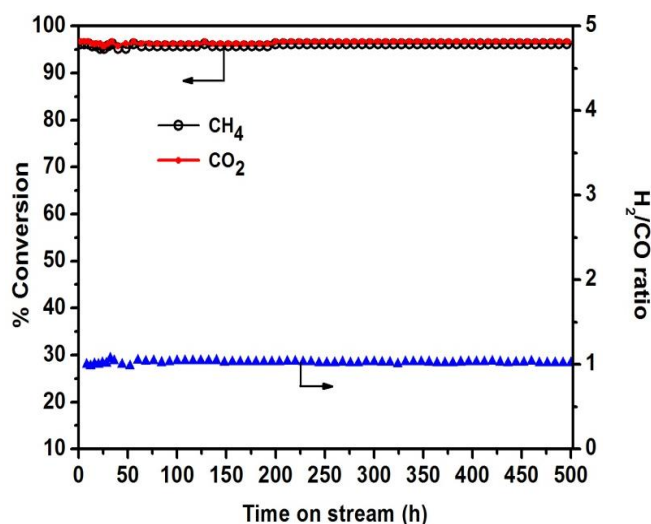


Fig. 5.10 On stream stability study of CaZr_{0.8}Ni_{0.2}O_{3-δ} catalyst in DRM reaction.

Reaction conditions: CH₄:CO₂:N₂ = 1:1:1, GHSV = 28,800 h⁻¹, Temp.800 °C, 1 atm.

5.4.6. Transient pulse experiments

Mass spectral signals of transient pulse experiments are given in Fig. 5.11A and 5.11B. Hydrogen species were detected as soon as CH₄ was pulsed in to the cell containing CaZr_{0.8}Ni_{0.2}O_{3-δ} or BaZr_{0.8}Ni_{0.2}O_{3-δ} perovskite catalysts, which indicate CH₄ decomposition over active Ni sites. More importantly, H₂O signal was observed with some hysteresis as compared to H₂, CO, CO₂ and CH₄ signals. Moreover, the intensity of the H₂O signal increased at higher reaction temperatures. This clearly suggests that CH₄ decomposition increased with temperature and thus formed hydrogen reacts with surface oxygen species to generate hydroxyl species. These hydroxyl species on dehydration give water. The hysteresis could be due to the slower reaction rate of dehydration reaction relative to other reactions. Upon pulsing methane; CO and CO₂ species were also detected, which were probably generated by the reaction between lattice oxygen and the carbon species. The intensities of CO and

CO₂ signals were much stronger in case of CaZr_{0.8}Ni_{0.2}O_{3-δ} perovskite catalyst compared to BaZr_{0.8}Ni_{0.2}O_{3-δ}, which may be interpreted for its higher active metal dispersion (see Table 5.1). CH₄ decomposition over Ni⁰ sites produces adsorbed CH_x and H species; the latter species combine with each other and leave the surface as H₂. Finally, after complete decomposition of CH₄, the carbon species formed is oxidized to CO and CO₂ at the interface of Ni and support oxide [11, 43], leading to the generation of surface oxygen vacancies. These vacant sites are positively charged and must be possessing high affinity to oxygen. When CO₂ interacts with the oxygen vacancies, it results in the rupture of C-O bond leading to the decomposition of CO₂ with simultaneous transfer of oxygen to vacant sites. These processes indicate that both metal and redox sites in CaZr_{0.8}Ni_{0.2}O_{3-δ} perovskite are important for achieving high activity of the catalyst and also to retain it for long hours.

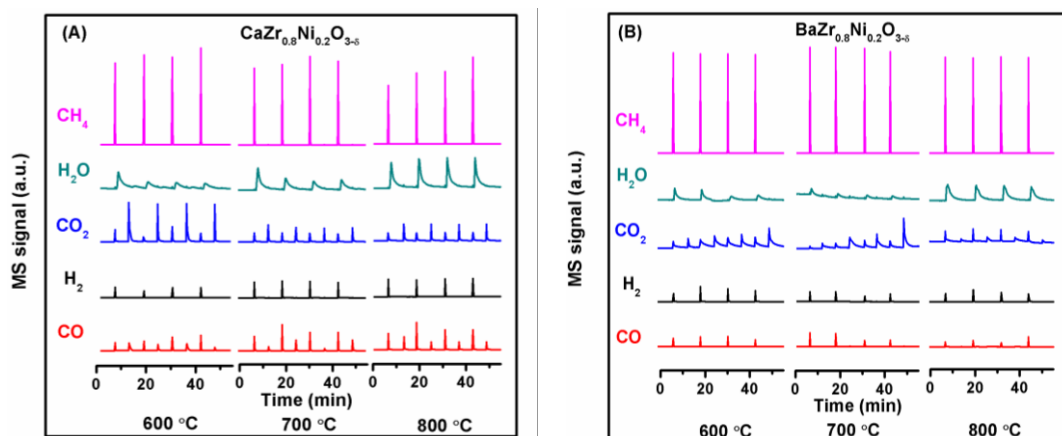


Fig. 5.11 MS signals from (A) CaZr_{0.8}Ni_{0.2}O_{3-δ} and (B) BaZr_{0.8}Ni_{0.2}O_{3-δ} catalysts during pulsing of CH₄ followed by CO₂.

In case of BaZr_{0.8}Ni_{0.2}O_{3-δ} catalyst, CO formation was not observed on pulsing of CO₂ and the intensity of CO₂ signal at the outlet was less intense probably due to its strong adsorption on the catalyst. Higher intensity of CO signals after the CO₂ pulsing over CaZr_{0.8}Ni_{0.2}O_{3-δ} perovskite indicates ease of dissociation of CO₂ at oxygen vacant sites and deposition of inactive carbon over the active metal that can be easily removed by CO₂ via reverse Boudouard reaction. Absence of CO signals during pulsing of CO₂ on BaZr_{0.8}Ni_{0.2}O_{3-δ} catalyst may be attributed to the nature of carbon formed, which must be capping the Ni surface of the catalyst leading to its deactivation.

5.4.7. Insitu FTIR studies

Insitu FTIR experiments were conducted initially in N₂ flow at 25 °C to study various vibrations of the sample that were used as background spectra. Subsequently, the reaction mixture containing CH₄ and CO₂ in 1:1 ratio was passed through the sample and spectra were recorded in the temperature range of 250 to 400 °C, at 50 °C intervals. Figures 5.12A and 5.12B show different species present over the catalysts CaZr_{0.8}Ni_{0.2}O_{3-δ} and BaZr_{0.8}Ni_{0.2}O_{3-δ} at various temperatures.

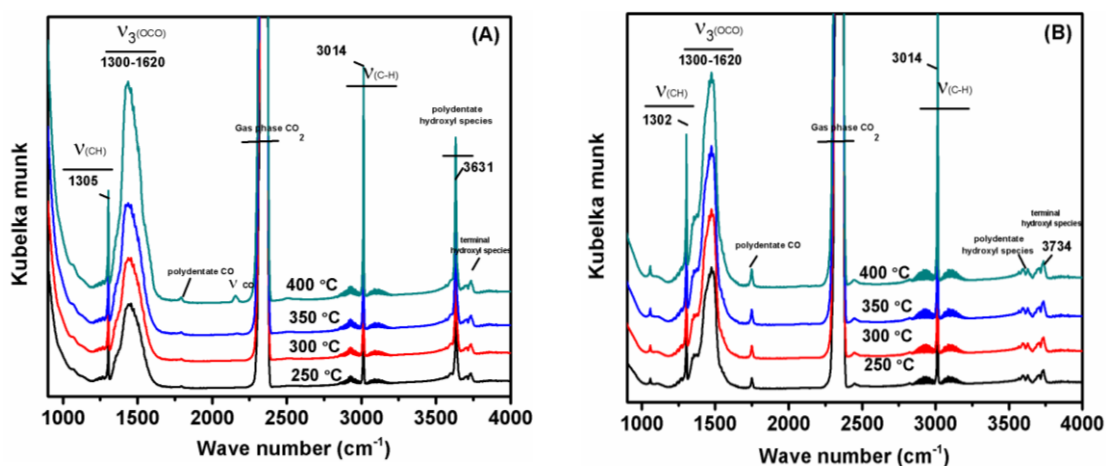
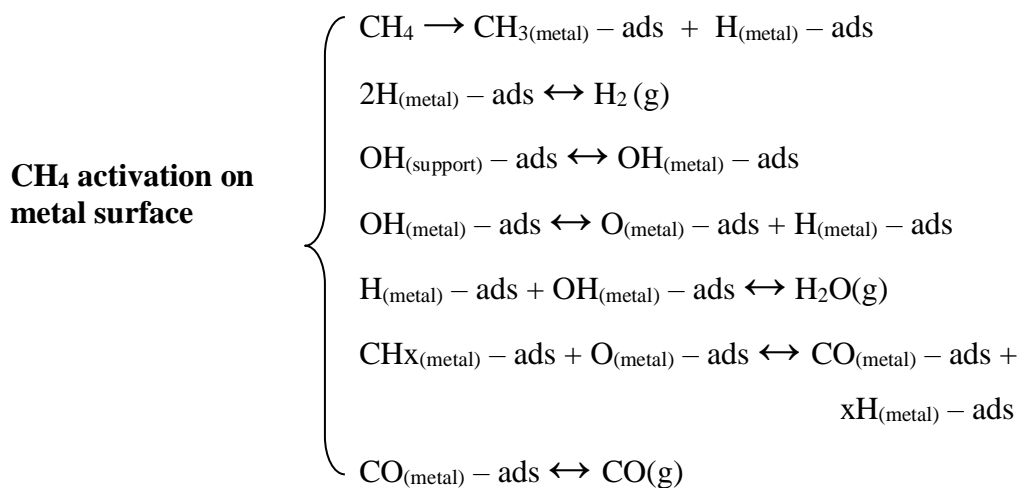


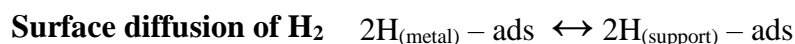
Fig. 5.12 Insitu FTIR spectra of various species present during the reaction between CH₄ and CO₂ over MZr_{0.8}Ni_{0.2}O_{3-δ} catalysts at different temperatures; (A) CaZr_{0.8}Ni_{0.2}O_{3-δ} and (B) BaZr_{0.8}Ni_{0.2}O_{3-δ}.

There are significant differences in the type of species present over CaZr_{0.8}Ni_{0.2}O_{3-δ} and BaZr_{0.8}Ni_{0.2}O_{3-δ} catalysts, which were better evident with increasing temperature. A major difference was observed in the intensities of the hydroxyl species (~3630 cm⁻¹) and formate type intermediates (1590 and 1365cm⁻¹), which were more intense on CaZr_{0.8}Ni_{0.2}O_{3-δ} as compared to BaZr_{0.8}Ni_{0.2}O_{3-δ}. This shows that coke accumulation follows different mechanistic pathways on these catalysts during the DRM depending on the nature of substituted alkaline earth cation at A site. Aparicio et al. reported use of transient techniques by employing isotopically labelled reactants over Ru on silica and alumina supports. According to the authors, the nature of the support influences the reactant residence time. [44] On catalysts that are supported on alumina, a complex reaction network is involved during DRM reaction, in which hydroxyl groups are continuously supplied by the support to the active Ru metal-Al₂O₃ interface, which effectively can remove the carbon species. [16] Similar features were observed in the present investigation over

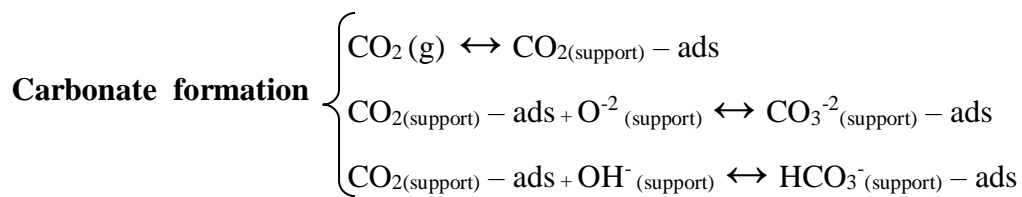
CaZr_{0.8}Ni_{0.2}O_{3-δ} catalyst. On CH₄ decomposition over Ni sites, hydrogen atoms are produced and also consumed by perovskite for the formation of hydroxyl species. Subsequently, reaction takes place between adsorbed H and OH species leading to the formation of H₂O and desorption of CO as illustrated below:



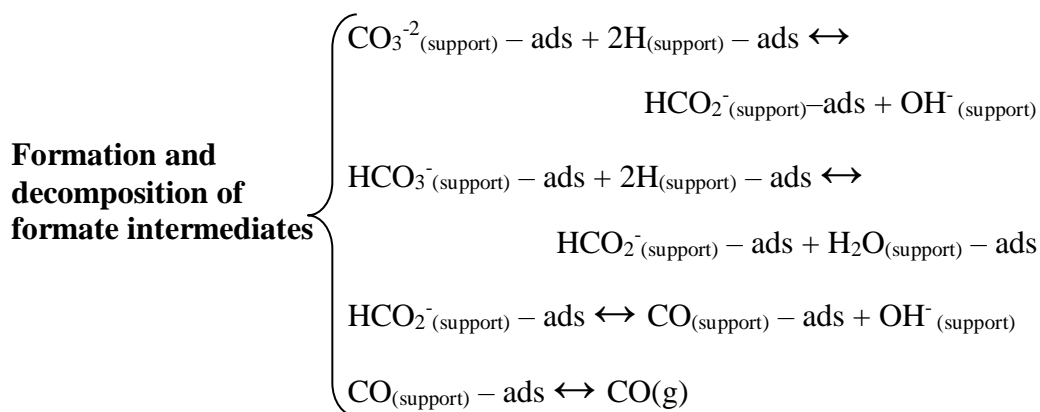
The H atoms upon CH₄ decomposition over metal surface spill over on to the surface of support.



After adsorption of CO₂ on catalyst surface, CO₂ reacts with surface oxide/hydroxyl species to form carbonate/bicarbonate species.



Finally carbon monoxide is released into gas phase from adsorbed intermediate species (formates) which is formed by reaction between CO₂ and hydrogen/hydroxyl species on the perovskite surface. These formate species decompose to release CO.



FTIR studies show that increase in the residence time of carbonaceous intermediates on the surface of active metal leads to its polymerisation and eventually leads to graphitization of carbon over the active Ni metal.

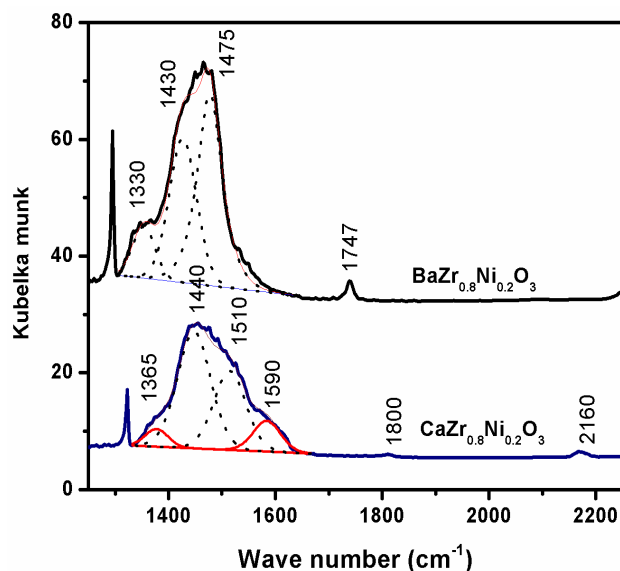


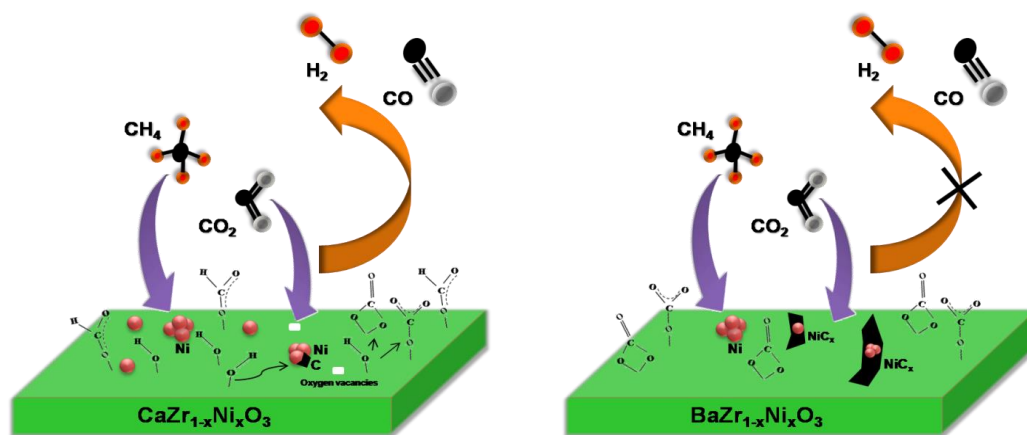
Fig. 5.13 Deconvoluted FTIR spectra of $\text{MZr}_{0.8}\text{Ni}_{0.2}\text{O}_{3-\delta}$ perovskite under DRM conditions at 400 °C.

After collection of spectra using dry reforming reaction mixture, strong intense bands in the 1300-1620 cm^{-1} region were seen for both the Ca and Ba substituted catalysts, which are attributed to carbonate and bicarbonate species (Fig. 5.12). The main bands in the spectra with high intensities may be attributed to the gaseous adsorbed species of (i) C-H vibrations of CH_4 at 3014 cm^{-1} and 1305 cm^{-1} , (ii) CO_2 gaseous rotation-vibrations of P band at 2360 cm^{-1} and R band at 2340 cm^{-1} . On increasing the temperature, additional bands are generated at 1800 cm^{-1} and 1747 cm^{-1} which are

assigned to the CO stretching vibrations of polydentate or bridged carbonate species present on the surface. [45] In case of CaZr_{0.8}Ni_{0.2}O_{3-δ} perovskite, a small peak was seen at 2000-2200 cm⁻¹ assigned to the gaseous CO formation at 400 °C which is also confirmed by online GC analysis.

Figure 13 illustrates the deconvolution of FTIR bands of Ca and Ba perovskite in the 1300-1620 cm⁻¹ region obtained at 400 °C. These deconvoluted peaks of CaZr_{0.8}Ni_{0.2}O_{3-δ} at 1590 and 1365cm⁻¹ are assigned to asymmetric C-O stretching and bending modes of H-C-O of the formate species respectively on the surface. [46] The intensity of the formate species bands change as a function of temperature with the protons for formate species being obtained from surface hydroxyl groups, whose intensity is high in the case of Ca perovskites. Bitter et al. proposed formation of similar kind of formate species at metal – support interface through bifunctional mechanism in DRM reaction over Pt/ZrO₂ catalyst. [47] They found that catalyst is not efficient if the carbonate species are not formed. The bands at 1075, 1440 and 1510 cm⁻¹ were assigned to the formation of mono-dentate and poly-dentate carbonate formation over the perovskite surface respectively. In case of BaZr_{0.8}Ni_{0.2}O_{3-δ} perovskite, bands were observed at lower wave numbers, i.e., 1057, 1430 and 1475 cm⁻¹, which are assigned to strongly bonded mono-dentate and tridentate carbonates on the surface. The free CO₃²⁻ ions have D_{3h} symmetry and hence expected to show single band around 1500 cm⁻¹, but bands are observed at lower than uncoordinated carbonates [16] and they loose trigonal symmetry of free carbonate ions. The main difference in IR spectra is in the intensity of O-H stretching frequencies at 3500-3750 cm⁻¹ attributed to the terminal or polydentate hydroxyl species. The intensity of this band increases with temperature, which is present on the perovskite surface. In case of Ca perovskite the intensity of polydentate O-H band at 3630 cm⁻¹ band is very sharp and highly intense compared to Ba perovskite. This shows that in case of Ca substituted perovskite, more hydroxyl species are produced during the reaction and transported to metal– support interface to form formate intermediates at a very high rate. Hence, CaZr_{0.8}Ni_{0.2}O_{3-δ} catalyst shows stable conversion for longer hours. But, in case of BaZr_{0.8}Ni_{0.2}O_{3-δ} catalyst, CO₂ dissociative adsorption appears to be much lower and there is less formation of hydroxyl species for the DRM reaction to proceed. Eventually, accumulation of dehydrogenated carbon occurs on active Ni site

which undergoes graphitization leading to the deactivation of the catalyst. Based on all the aforementioned results, mechanism of dry reforming reaction over Ca and Ba perovskite surfaces is proposed in scheme 5.1.



Scheme 5.1 Schematic representation of reaction mechanism in the DRM process.

5.4.8. Bi-reforming of methane or steam reforming of simulated biogas

Bio gas contains both CH₄ and CO₂. Hence, its reforming can be termed either as Bi-reforming of methane (BRM) or steam reforming of biogas. The most active catalyst (CaZr_{0.8}Ni_{0.2}O_{3-δ}) in DRM was used for reforming of simulated biogas. The composition of biogas depends on the specific treatment process, its origin like domestic waste or and industrial effluent. In this investigation, simulated biogas with the composition 60% CH₄ and 40% CO₂ was used for reforming.

Variation of steam to CH₄ ratio in simulated biogas steam reforming

Usually, in biogas, H₂S and NH₃ are expected to be present, unless the biogas is subjected to thorough purification. Presence of these impurities can affect the performance of the catalysts and lead to their deactivation. [48-50] Hence, all the reforming experiments were conducted in the absence of sulfur and ammonia. Variation of steam to CH₄ ratio as a function of time is plotted in Fig. 5.14a and 5.14b, with separate plots for CH₄ and CO₂ conversions.

During steam reforming of biogas, several reactions are possible in which carbon formation reaction mechanism depends on the reforming reaction conditions like operating temperature, pressure, gas composition and amount of catalyst loaded in the

reactor. The carbon formed is expected to be gasified by the steam or oxygen. [51] Hence to avoid carbon accumulation, excess steam is required which will also enhance CH₄ conversion. But in a commercial operation, high energy is needed to produce steam which increases size of the plant as well as cost of the equipment. Hence, optimal steam to carbon ratio is maintained based on energy considerations.

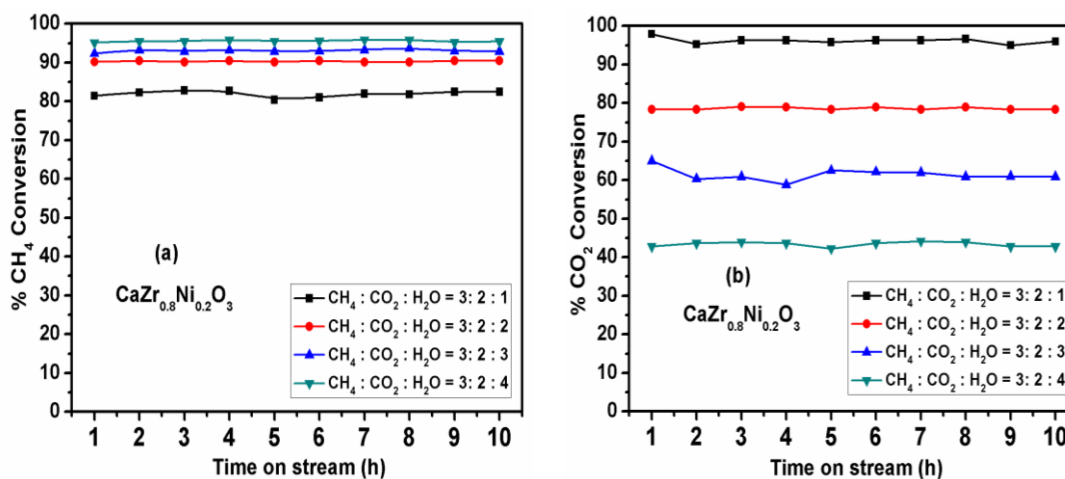


Fig. 5.14 Bi-reforming reaction over CaZr_{0.8}Ni_{0.2}O_{3-δ} perovskite catalyst. Reaction condition: GHSV = 19,200 h⁻¹ temperature = 800 °C and 1 atm.

Figure 5.14 shows that with increasing steam to carbon ratio, CH₄ conversion increased, but conversely there is a steep drop in CO₂ conversion. At steam to CH₄ ratio of 4:3, maximum CH₄ conversion (94%) was achieved. More steam in the feed facilitates WGS reaction producing more CO₂ and less of CO. In case of lower steam to CH₄ ratio, the rate of dry reforming is higher than steam reforming. By increasing H₂O/CH₄ ratio, yield of H₂ as well as H₂/CO ratio is increased. The H₂/CO values have a lot of significance for the synthesis of various chemicals. The CH₄:CO₂:H₂O ratio in proportion of 3:2:4 produces desired H₂/CO ratio of 2. This ratio is desirable for methanol, FT synthesis and many other applications. A plot depicting the influence of steam to carbon ratio on H₂/CO ratios is shown in Fig. 5.15. As may be seen from the plots, the H₂/Co ratio was less <1, when CH₄:CO₂:H₂O ratio was 3:2:1, while there is a gradual increase in H₂/CO ratio with increasing steam (H₂O) content from 1 to 4, finally reaching H₂/CO ratio of ~2, for the composition CH₄:CO₂:H₂O ratios in proportion of 3:2:4.

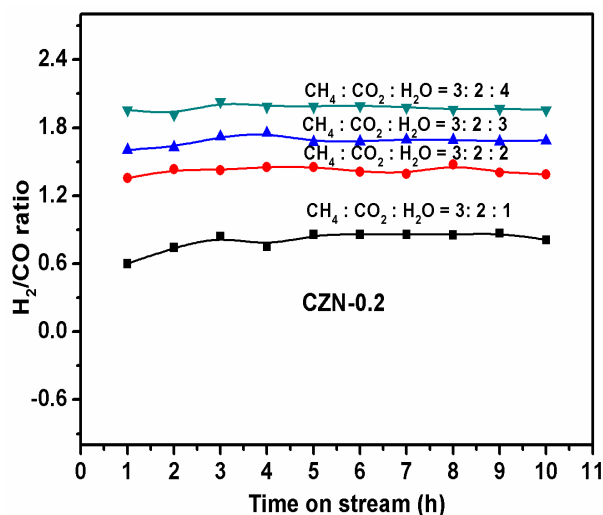
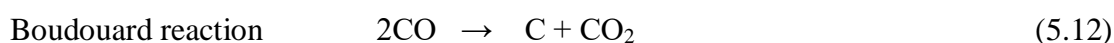
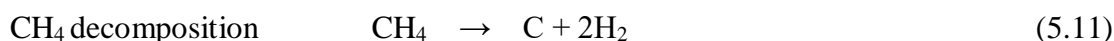


Fig. 5.15 Variation of H₂O/CH₄ ratio over the CaZr_{1-x}Ni_xO_{3-δ} for Bi-reforming reaction.

Reaction condition: GHSV = 19,200 h⁻¹, temperature = 800 °C and 1 atm.

5.5. Characterization of spent catalysts

During dry reforming reaction, some undesired reactions are responsible for the carbon (coke) formation, which may lead even to breakdown of the catalyst tablets, leading to pressure drop across the catalysts bed. This in turn can cause generation of hot spots, as a result of uneven flow distribution. [52] Two major reactions that are responsible for the carbon formation are;



Characterization of spent catalysts is expected to help to understand the carbon formation mechanism and types of carbon formed in relation to the nature of support. Hence, the spent catalysts were extensively characterized by XRD, TGA, TEM, XPS and Raman spectroscopy.

5.5.1. X-ray diffraction and Thermo gravimetric analysis of spent catalysts

Powder XRD of MZr_{0.8}Ni_{0.2}O_{3-δ} (M = Ca, Sr and Ba) catalysts that were used for 12 h of SRM reaction are given in Fig. 5.16A. The diffraction patterns show that the structure is retained under the reaction. However, spectra of SrZr_{0.8}Ni_{0.2}O_{3-δ} and BaZr_{0.8}Ni_{0.2}O_{3-δ} catalysts after reaction have an additional peak at 2θ = 26.4°, which is assigned to the graphitic carbon (JCPDS-41-1487). On the otherhand, only a small peak of negligible intensity was seen for CaZr_{0.8}Ni_{0.2}O_{3-δ} spent catalyst. Besides this

carbon peak, small peaks that belong to alkaline earth carbonates were also seen, particularly in Sr and Ba substituted catalysts. The intensity of the graphitic peak of BaZr_{0.8}Ni_{0.2}O_{3-δ} is relatively higher compared to SrZr_{0.8}Ni_{0.2}O_{3-δ} after 12 h of DRM reaction. In addition, presence of metallic Ni(111) was also noticed, crystallite size of which was estimated using Scherrer's equation. The crystallite sizes of metallic Ni in used catalysts were 13.4, 30.0 and 35.2 for catalysts CaZr_{0.8}Ni_{0.2}O_{3-δ}, SrZr_{0.8}Ni_{0.2}O_{3-δ} and BaZr_{0.8}Ni_{0.2}O_{3-δ} respectively.

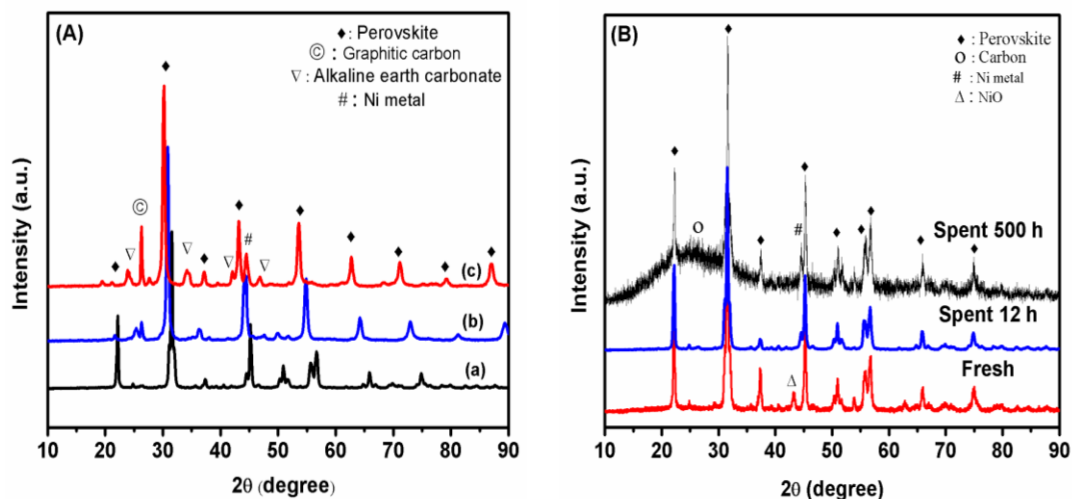


Fig. 5.16 Spent XRD of (A) MZr_{0.8}Ni_{0.2}O_{3-δ} (where M = (a) Ca, (b) Sr and (c) Ba) and (B) CaZr_{0.8}Ni_{0.2}O_{3-δ} catalysts before and after DRM reaction for different TOS

Figure 5.16B illustrates the XRD pattern of CaZr_{0.8}Ni_{0.2}O_{3-δ} catalyst prior to the reaction and after 12 h and 500 h of DRM reaction. No crystalline graphitic peak was observed even after 500 h of reaction, but a broad hump centered around 2θ = 26.4° was observed, which may be assigned to amorphous carbon. It appears that this amorphous carbon has hardly affected the activity of the catalyst, as CH₄ and CO₂ conversions remained same even after 500 h on stream. The metallic Ni crystallite size estimated after 500 h reaction was 15.2 nm, which was increased from 13.4 nm observed after 12 h of reaction. These results show that there is only small growth of Ni crystallite size, probably as a result of strong interaction between the metal and the support. These results clearly explain the reasons for high stability of CaZr_{0.8}Ni_{0.2}O_{3-δ} catalyst.

To further understand the extent of carbon formation after 12 h time on stream, all the three samples were investigated by TGA analysis. These experiments were carried out in presence of air and the carbon oxidized was calculated in terms of moles of carbon per gram of catalyst per hour. Results are given in Fig. 5.17, which illustrate that after 12 h of reaction, the average carbon accumulation increased per gram of catalyst while moving from CaZr_{0.8}Ni_{0.2}O_{3-δ} to BaZr_{0.8}Ni_{0.2}O_{3-δ} catalysts. This shows that alkaline earth cation substituted at the A site of perovskite catalyst plays significant role along with Ni particle size and oxygen defects in coke accumulation during the DRM reaction. Zhang et al. reported that the rate of coke accumulation depends on the Ni particle size. [53] On the other hand, there was negligible coke formation in CaZr_{0.8}Ni_{0.2}O_{3-δ} catalysts even after 500h of time on stream.

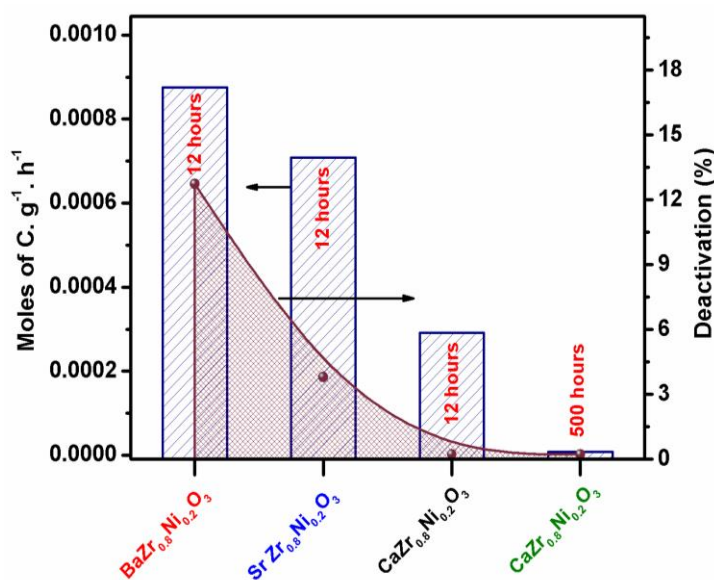


Fig. 5.17 Coke estimated (moles of C.g⁻¹.h⁻¹) after DRM using TGA analysis.

Ruckenstien and Wang et al. studied deactivation rate of Rh supported on various supports for dry reforming reaction. They found that catalysts are stable when there is a balance between coke/ carbon generation and its oxidative removal under DRM conditions. [54] In case of CaZr_{0.8}Ni_{0.2}O_{3-δ} catalyst, probably this balance is maintained as carbon formation and its removal as CO/CO₂ are in equilibrium. Hence, it has not shown any observable deactivation even after 500 h of reaction.

5.5.2. HRTEM of spent catalysts

The XRD results show the formation of coke mostly on SrZr_{0.8}Ni_{0.2}O_{3-δ} and BaZr_{0.8}Ni_{0.2}O_{3-δ} perovskites. The type of carbon formed on the spent catalysts was investigated by electron microscopy. The TEM micrographs expected to reveal presence of different types of carbon species formed on the three catalysts depending on the nature (basicity) of support, oxygen defects and Ni particle size (derived from CO chemisorption). Generally, three types of carbons can be seen, i.e., (i) amorphous carbon, (ii) graphitic carbon and (iii) multi walled carbon nanotubes (MWCNT). Carbon nanotubes can form through diffusion/elimination path way, which would result in the separation of active Ni species from the support. ^[55] On the otherhand, some pear shaped Ni particles placed at the tip of carbon nanotubes are expected to be still active for the reaction, while Ni particles that are incorporated into the carbon nanotubes may no longer participate in the reaction.

TEM micrographs of samples tested for 12 h reaction is shown in Fig. 5.18. The SrZr_{0.8}Ni_{0.2}O_{3-δ} and BaZr_{0.8}Ni_{0.2}O_{3-δ} catalysts show different kinds of surface carbons. These are amorphous carbon, filamentous carbon or carbon nanotubes with nickel at the tip and carbon nanotubes with embedded Ni particles inside

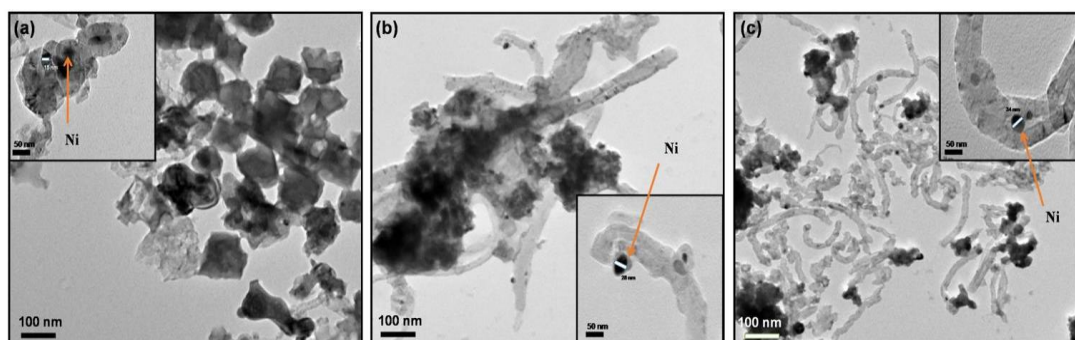


Fig. 5.18 TEM images of spent catalysts (a) CaZr_{0.8}Ni_{0.2}O_{3-δ}, (b) SrZr_{0.8}Ni_{0.2}O_{3-δ}, (c) BaZr_{0.8}Ni_{0.2}O_{3-δ}.

On the otherhand, on CaZr_{0.8}Ni_{0.2}O_{3-δ} catalyst, only amorphous carbon was seen, which may not cause any catalyst deactivation during the DRM reaction. Over SrZr_{0.8}Ni_{0.2}O_{3-δ} catalyst, formation of CNT along with Ni particles in the range of 25-30 nm were seen, which were separated from the perovskite phase. Whereas, in case of BaZr_{0.8}Ni_{0.2}O_{3-δ} catalyst, formation of CNT with embedded Ni particles (30-40 nm)

inside the tube were seen. These masked Ni particles can no longer be active for the DRM reaction.

5.5.3. XPS analysis

The XRD and TEM analysis reveal the formation of different kinds of carbon species like amorphous carbon, carbon nanotubes and graphitic carbon during the DRM reaction over the catalysts. However, these techniques are inadequate to identify carbonate and carbide formation on the active metal surface while, XPS is highly useful for this purpose. Figure 5.19A shows that the C1s spectra of all spent catalysts show a broad peak at 284.5 eV corresponding to the adsorbed carbon after exposure to ambient air or graphitic carbon. The intensity of this carbon peak (284.5eV) is very high for CaZr_{0.8}Ni_{0.2}O_{3-δ} and SrZr_{0.8}Ni_{0.2}O_{3-δ} perovskite catalysts. Whereas, in case of BaZr_{0.8}Ni_{0.2}O_{3-δ} and SrZr_{0.8}Ni_{0.2}O_{3-δ} spent catalysts, additional binding energy (BE) peak at 280 eV was seen. This is at lower position than the normal nickel carbide peak (283.9 eV), associated with the NiC_x species on the surface.^[56] These carbon species are formed on selective Ni faces of catalyst and are responsible for rapid deactivation of BaZr_{0.8}Ni_{0.2}O_{3-δ} and SrZr_{0.8}Ni_{0.2}O_{3-δ} catalysts. An additional higher binding energy peak is seen at 289.5 eV, which indicates the formation of oxidized carbon species on CaZr_{0.8}Ni_{0.2}O_{3-δ} and SrZr_{0.8}Ni_{0.2}O_{3-δ} perovskite catalysts.^[57]

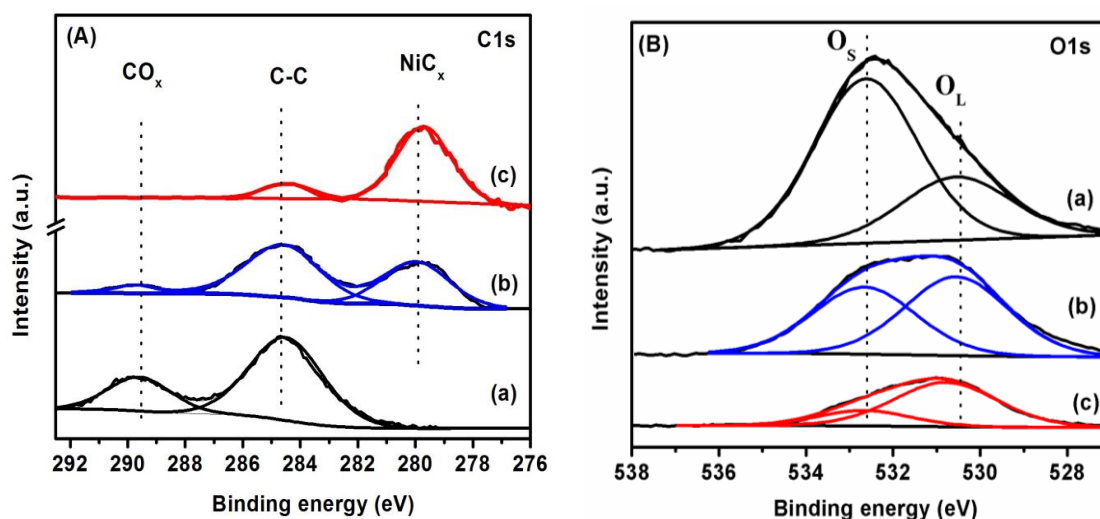


Fig. 5.19 (A) C1s XPS and (B) O1s XPS spectra of spent MZr_{0.8}Ni_{0.2}O_{3-δ} perovskites after 12 h of TOS study, where M= (a) Ca, (b) Sr and (c) Ba.

The above results show that the formation of different types of carbon species depends on the nature of substituted alkaline earth cation in the perovskite lattice, metal dispersion and oxygen defects. This is further confirmed through the analysis of O 1s spectra of all the catalysts after reaction. Two main peaks labelled as O_L and O_s with various intensities can be seen in Fig. 5.19B. The first peak at lower binding energy (530.4 eV) can be assigned to the O²⁻ ions which are part of perovskite lattice. The second peak at 532.5 eV corresponds to the surface oxygen containing species like carbonate and hydroxyl species. [58] The intensity of this peak is much higher for CaZr_{0.8}Ni_{0.2}O_{3-δ} catalyst compared to SrZr_{0.8}Ni_{0.2}O_{3-δ} or BaZr_{0.8}Ni_{0.2}O_{3-δ} perovskite catalysts. Table 5.3 provides information on binding energies of C1s and O1s and their assignments based on literature data. [59]

Table 5.3 C1s and O1s Binding energies of MZr_{0.8}Ni_{0.2}O_{3-δ} catalysts and their assignment.

Sample	C 1s B.E (eV)	Assignment	O 1s B.E (eV)	Assignment
CaZr _{0.8} Ni _{0.2} O _{3-δ}	284.5	Hydrocarbon	530.2	Lattice oxygen
	289.1	CO _x	532.5	Carbonate/ hydroxyl groups
SrZr _{0.8} Ni _{0.2} O _{3-δ}	280.0	Carbide	530.1	Lattice oxygen
	284.6	Hydrocarbon	532.4	Carbonate/ hydroxyl groups
	289.2	CO _x		
BaZr _{0.8} Ni _{0.2} O _{3-δ}	280.1	Carbide	530.3	Lattice oxygen
	284.5	Hydrocarbon	532.3	Carbonate/ hydroxyl groups

5.5.4. Raman analysis of spent catalysts

Raman spectroscopy is an effective tool to identify different types of carbon species present on the sample, i.e., carbon nanotubes, carbon films and synthetic diamond like carbon, after the DRM reaction. [60] There are many reports on various kinds of carbon species present on the catalyst surfaces. [61] Figure 5.20A shows first order transition Raman spectra of spent Ca, Sr and Ba substituted MZr_{0.8}Ni_{0.2}O_{3-δ} perovskite catalysts. The peaks were seen at 1330 and 1600 cm⁻¹ on all catalysts used for 12 h of DRM. These are assigned to D-band (1330 cm⁻¹) and G-band (1600 cm⁻¹). The band at 1330 cm⁻¹ corresponds to the disorder induced band and it is allowed only if the selection rule breaks down (k = 0), which is originating from structural

imperfections that exist in carbonaceous material. [62] This type of carbon is more reactive in reforming conditions. The G- band is attributed to stretching vibrations of sp² carbon in graphitic material and was designated as E_{2g} mode. This band intensity depends on crystal size of the carbon. The shoulder peak at 1610 cm⁻¹ (D'- band/ E_{2g}' mode) is an indication of disordered graphitic material. [63]

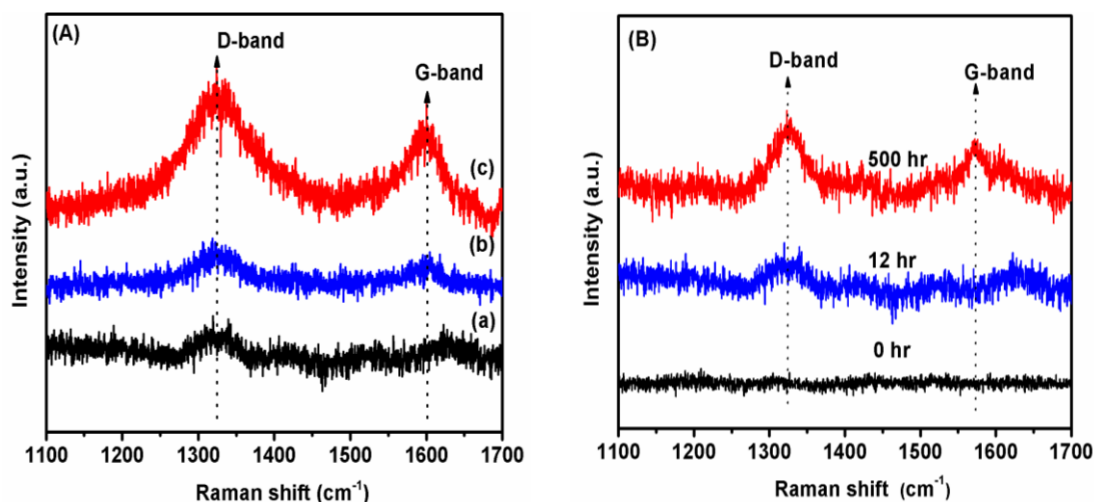


Fig. 5.20 Raman spectra of spent (A) $MZr_{0.8}Ni_{0.2}O_{3-\delta}$ perovskites after 12 h of TOS study, where M= (a) Ca, (b) Sr and (c) Ba ; (B) spent $CaZr_{0.8}Ni_{0.2}O_{3-\delta}$ after different hours of reaction.

The intensity ratios of D- and G-bands (I_D/I_G) provide information about index of the crystalline order of graphitic carbon. [64] In Fig. 5.20B, the intensities of D and G bands are compared for fresh $CaZr_{0.8}Ni_{0.2}O_{3-\delta}$ catalyst and catalysts used for reaction after 12 and 500 h of DRM reaction. It was observed that on increasing reaction time, only small increase in intensity of the disordered graphitic carbon was seen. The I_D/I_G values of all the spent catalyst samples were calculated. It was observed that I_D/I_G values decreased (Table 5.4) from $CaZr_{0.8}Ni_{0.2}O_{3-\delta}$ to $BaZr_{0.8}Ni_{0.2}O_{3-\delta}$ samples, with the Ba substituted sample showing very large graphitic carbon of 3.3 nm size just after 12 h of reaction. On the other hand, corresponding value for $CaZr_{0.8}Ni_{0.2}O_{3-\delta}$ catalyst was only 1.4 nm after 12 h of reaction, which has increased to 2.4 nm after 500 h DRM reaction. After 12 h of reaction, I_D/I_G ratios were 3.1, 2.1 and 1.3 for used Ca, Sr and Ba substituted perovskite catalysts respectively. Whereas, I_D/I_G of Ca perovskite catalyst after 500 h reaction was 1.86, giving graphitic carbon crystallite size of 2.4 nm.

Table 5.4 Crystallite size of graphitic carbon calculated using Raman spectra.

Catalysts	I _D /I _G	I _G /I _D	Crystallite size of graphitic carbon (nm) ^a
CaZr _{0.8} Ni _{0.2} O _{3-δ} - 12 h	3.14	0.32	1.4
SrZr _{0.8} Ni _{0.2} O _{3-δ} - 12 h	2.10	0.47	2.1
BaZr _{0.8} Ni _{0.2} O _{3-δ} - 12 h	1.32	0.75	3.3
CaZr _{0.8} Ni _{0.2} O _{3-δ} - 500 h	1.86	0.53	2.4

(^aEstimated from I_G/I_D using formula crystallite size (nm) = 4.4[I_G/I_D]).

The above results clearly show that crystalline order of graphitic carbon depends on the nature of substituted alkaline earth cation and Ni particle size. The crystallite size of graphitic carbon calculated based on a reported method has been summarized in Table 5.4. [65] Catalyst CaZr_{0.8}Ni_{0.2}O_{3-δ} shows very low crystallite size of graphitic carbon, which must be responsible for its high on-stream stability. Moreover, the smaller sized graphitic carbon can readily undergo oxidation or react with CO₂ (C + CO₂ → 2CO) leading to long catalyst life.

5.6. Conclusions

Perovskite oxides MZr_{1-x}Ni_xO_{3-δ} (M= Ca, Sr and Ba; x=0 and 0.2) were synthesized and evaluated as catalyst precursors in the dry reforming of methane. Changes in the lattice parameters, determined by XRD, confirmed that Ni is incorporated into MZrO₃ lattice. TPR of H₂ reveals that Ni in CaZr_{0.8}Ni_{0.2}O_{3-δ} perovskites was difficult to reduce as compared to corresponding Sr and Ba substituted samples. The results show that Ni reducibility, oxygen storage, Ni dispersion and surface area of catalyst play vital role in achieving good DRM activity and also helps in retaining the activity for long hours on stream. Among the catalysts, CaZr_{0.8}Ni_{0.2}O_{3-δ} seems to have all desirable characteristics, as it shows superior activity and sustains its activity even after 500 h. Transient pulse experiments suggest that redox property of the support is vital for the removal of carbon species formed during CH₄ decomposition and also in recovering the lattice oxygen through CO₂ activation. Infrared results revealed that adsorbed intermediates like formate and surface hydroxyl species are crucial in the minimization of carbon in dry reforming reaction. Additionally best catalyst was tested for steam reforming of simulated

biogas by changing the steam to carbon ratio, to yield syngas with variable H₂/CO ratio.

Characterization of spent catalysts, used in dry reforming reaction, show high growth of graphitic carbon on SrZr_{0.8}Ni_{0.2}O_{3-δ} and BaZr_{0.8}Ni_{0.2}O_{3-δ} catalysts, thus leading to their rapid deactivation. XPS analysis confirms the formation of NiC_x species on these catalysts, which must be partly responsible for their rapid deactivation, in addition to growth of Ni crystallites. This study clearly establishes that CaZr_{0.8}Ni_{0.2}O_{3-δ} is a highly active and durable catalyst for dry reforming of methane with immense potential for commercial exploitation.

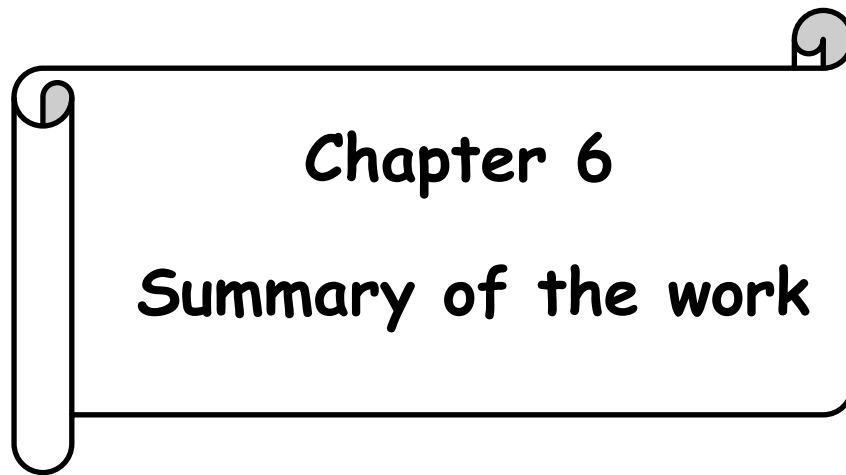
5.7. References

1. T.H Oh, *Renew. sust. energ rev.* 2010, **14**, 2697.
2. Z. L. Zhang and X. E. Verykios, *Catal. Lett.*, 1996, **38**, 175.
3. L. Kapokova, S. Pavlova, R. Bunina, G. Alikina, T. Krieger, A. Ishchenko, V. Rogov and V. Sadykov, *Catal. Today*, 2011, **164**, 227.
4. G. C. de Arauj, S. M. de Lima, J. M. Assaf, M. A. Pena, J. L. Garcia Fierro and M. d. C. Rangel, *Catal. Today*, 2008, **133**, 129.
5. Z. L. Zhang, V. A. Tsipouriari, A. M. Efstathiou and X. E. Verykios, *J. Catal.*, 1996, **158**, 51.
6. O. R. Inderwildi, S. J. Jenkins and D. A. King, *Angew. Chem., Int. Ed.*, 2008, **47**, 5253.
7. J. R. H. Ross, *Catal. Today*, 2005, **100**, 151.
8. C. Song, *Catal. Today*, 2006, **115**, 2.
9. H.Y. Wang, E. Ruckenstein, *Appl. Catal. A: Gen.*, 2000, **204**, 143.
10. S. Barama, C. D. Batiot, M. Capron, E. B. Richard, O. B. Mohammedi, *Catal. Today*, 2009, **141**, 385.
11. N. Sun, X. Wen, F. Wang, W. Peng, N. Zhao, F. Xiao, W. Wei, Y. Sun, J. Kang, *Appl. Surf. Sci.*, 2011, **257**, 9169.
12. S. Damyanova, B. Pawelec, K. Arishtirova, M.V. Martinez Huerta, J.L.G. Fierro, *Appl. Catal. B: Environ.*, 2009, **89**, 149.
13. J. Juan-Juan, M.C. Roman-Martinez, M.J. Illan-Gomez, *Appl. Catal. A: Gen.*, 2009, **355**, 27.
14. J.G. Zhang, H. Wang, A.K. Dalai, *J. Catal.*, 2007, **249**, 300.
15. M. Fan, A.Z. Abdullah, S. Bhatia, *Appl. Catal. B: Environ.*, 2010, **100**, 365.
16. P Ferreira-Aparicio, I. Rodríguez-Ramos, J.A. Anderson, A Guerrero-Ruiz, *Appl. Catal. A: Gen.* 2000, **202**, 183.
17. E. Rucksentein, Y.H. Hu, *Adv. Catal.*, 2004, **48**, 297.
18. S. Corthals, J. Van Nederkassel, J. Geboers, H. De Winne, J. Van Noyen, B. Moens, B. Sels, P. Jacobs, *Catal. Today*, 2008, **138**, 28.
19. M. Rezaei, S.M. Alavi, S. Sahebdehfar, P. Bai, X. Liu, Z.-F. Yan, *Appl. Catal. B: Environ.*, 2008, **77**, 346.
20. S. Damyanova, B. Pawelec, K. Arishtirova, M.V. Martinez Huerta, J.L.G. Fierro

- Appl. Catal. B: Environ.*, 2009, **89**, 149.
21. Y.-G. Chen, K. Tomishige, K. Yokoyama, K. Fujimoto, *Appl. Catal. A: Gen.*, 1997, **165**, 335.
22. V. Garcia, J. J. Fernandez, W. Ruiz, F. Mondragon, A. Moreno., *Catal. Commun.*, 2009, **11**, 240.
23. E. Pietri, A. Barrios, O. Gonzalez, M. Goldwasser, M. Perez Zurita, M. Cubeiro, J. Goldwasser, L. Leclercq, G. Leclercq, L. Gingembre, *Stud. Surf. Sci. Catal.*, 2001, **136**, 381.
24. T. Yamaguchi, *Catal. Today*, 1994, **20**, 199.
25. X. Li, J.S. Chang, M. Tian, S.E. Park, *Appl. Organometal. Chem.*, 2001, **15**, 109.
26. P. Kumar, Y. Sun, R.O. Idem, *Energy Fuel.*, 2007, **21**, 3113.
27. A. E. Pasto, *Condrate RE Advances in Raman Spectroscopy*, vol 1. Heyden & Son, London, 1973, 196.
28. K. Boobalan, A. Varun, R. Vijayaraghavan, K. Chidambaram, U. Kamachi Mudali, *Facile, Ceram. Int.* 2014, **40**, 5781.
29. M. Tarrida, H. Larguem, M. Madon, *Phys. Chem. Miner.* 2009, **36**, 403.
30. V.M. Orera, C. Pecharroman, J.I. Pena, R.I. Merino, C.J. Serna, *J. Phys. Condens. Matter* 1998, **10**, 7501.
31. C.H. Perry, D.J. MacCarthy, G. Rupprecht, *Phys. Rev.* 1965, **138**, 5, 1537–1538.
32. Ph. Colombar, C. Tran, O. Zaafrani, A. Slodczyk, *J. Raman Spectrosc.* 2013, **44**, 312.
33. A. Slodczyk, Ph. Colombar, S. Willemin, O. Lacroix, B. Sala, *J. Raman Spectrosc.* 2009, **40**, 513.
34. C. S. Bai, S. Soled, R. Kershaw, K. Dwight, A. Wold, *J. Solid State Chem.* 1992, **100**, 307.
35. S.M.A. Rodulfo-Baechler, W. Pernia, I. Aray, H. Figueroa, S. L. Gonzalez-Cortes, *Catal. Lett.* 2006, **112**, 231.
36. F. Rohr, S.D. Peter, E. Lox, M. Kogel, A. Sassi, L. Juste, C. Rigau, G. Belot, P. Gelin, M. Primet, *Appl. Catal. B* 2005, **56**, 201.
37. J. Rynkowski, P. Samulkiewicz, A.K. Ladavos, P.J. Pomonis, *Appl. Catal. A* 2004, **263**, 1.
38. A. Yan, M. Yang, Z. Hou, Y. Dong, M. Cheng, *J. Power Sources* 2008, **185**, 76.
39. C.M. Chan, R. Aris, W.H. Weinberg, *Appl. Surf. Sci.* 1978, **1**, 360.

40. K. Li, M. Haneda, M. Ozawa, *J. Mater. Sci.* 2013, **48**, 5733.
41. S. Pei, M.S. Kleefisch, T.P. Kobylinski, J. Faber, C.A. Udovich, V. Zhang-McCoy, B. Dabrowski, U. Balachandran, R.L. Mieville, R.B. Poeppel, *Catal. Lett.* 1995, **30**, 201.
42. G. S. Gallego, C. B. Dupeyrat, J. Barrault, E. Florez, F. Mondragon, *Appl. Catal. A: Gen.* 2008, **334**, 251.
43. J.D.A. Bellido, E.M. Assaf, *Appl. Catal. A: Gen.* 2009, **352**, 179.
44. P. Ferreira-Aparicio, C. Marquez-Alvarez, I. Rodríguez-Ramos, Y. Schuurman, A. Guerrero-Ruiz, C. Mirodatos, *J. Catal.* 1999, **184**, 202.
45. X. Yi-de, Y. Lin, G. Xie-Xian, *J. Nat. gas chemistry* 1999, **8**, 18.
46. M.M. Schubert, H.A. Gasteiger, R.J. Behm, *J. Catal.* 1997, **172**, 256.
47. J.H. Bitter, K. Seshan, J.A. Lercher, *J. Catal.* 1998, **176**, 93.
48. M. Ashrafi, T. Proll, C. Pfeifer, H. Hofbauer, *Energy Fuels* 2008, **22**, 4182.
49. J. R. Rostrup-Nielsen, J. Sehested, *Adv. Catal.* 2002, **47**, 65.
50. A. Effendi, K. Hellgardt, Z.-G. Zhang, T. Yoshida, *Fuel* 2005, **84**, 869.
51. A. M. D. Groote, G. F. Froment, *Appl. Catal., A* 1996, **138**, 245.
52. A. M. Gadalla, B. Bower, *Chem. Eng. Sci.* 1988, **43**, 3049.
53. Z. L. Zhang, X. E. Verykios, *Catal. Today* 1994, **21**, 589.
54. E. Ruckenstein, H. Y. Wang, *J. Catal.* 2002, **205**, 289.
55. C.Wang, N. Sun, N. Zhao, F. Xiao, W. Wei, J. Zhang, T. Zhao, Y. Sun, C. Sun, H. Liu, C.E. Snape, *Chem. Cat. Chem.* 2014, **6**, 640.
56. J.W. Shabaker, D.A. Simonetti, R.D. Cortright, J.A. Dumesic, *J. Catal.* 2005, **231**, 67.
57. J. L. Ewbank, L. Kovarik, C.C. Kevlin, C. Sievers, *Green Chem.* 2014, **16**, 885.
58. J. Requies, M.A. Cabrero, V.L. Barrio, M.B. Güemez, J.F. Cambra, P.L. Arias, F.J. Pérez-Alonso, M. Ojeda, M.A. Peña, J.L.G. Fierro, *Appl. Catal. A: Gen.* 2005, **289**, 214.
59. L. Guzzi, G. Stefler, O. Geszti, I. Sajo, Z. Paszti, A. Tompos, Z. Schay, *Appl. Catal. A: Gen.* 2010, **375**, 236.
60. C. Klinke, R. Kurt, J.M. Bonard, *J. Phys. Chem. B* 2002, **106**, 11191.
61. F. Tuinstra, J.L. J. Koeing, *Chem. Phys.* 1970, **53**, 1126.
62. A. Cuesta, P. Dhamelincourt, J. Laureyns, A. M. Alonso, J.M.D. Tascon, *Carbon* 1994, **32**, 1523.

63. R. Tsu, J. H. Gonzalez, I. C. Hernandez, *Solid State Commun.* 1978, **27**, 507.
64. T. Jawhari, A. Roid, J. Casado, *Carbon* 1995, **33**, 1561.



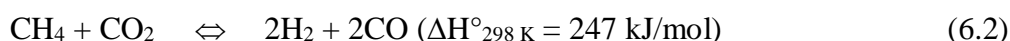
6.1. Summary and conclusions

Synthesis gas (syngas) is an important feedstock for methanol production, gas to liquid process (GTL), dimethyl ether (DME), H₂ for petroleum refining processes and as fuel for fuel cells. Syngas is mostly obtained through steam reforming of lower hydrocarbons, particularly natural gas. There is also a growing interest in the utilization of major greenhouse gases, viz., CH₄ and CO₂ for syngas production, through dry reforming of methane (DRM). But, DRM yields syngas with H₂/CO ratio close to '1', while methanol and DME processes need syngas with H₂/CO ratios in the range of 1.5 to 2. It is possible to realize required syngas composition by adding steam (bi-reforming) and O₂ + steam (tri reforming) to the input CH₄+CO₂ gas mixture. In these processes, steam to CH₄ (H₂O/C) and O/C ratios determines the H₂/CO ratio of syngas. Biogas contains CO₂ to the tune of 30-40%, in addition to CH₄ and other impurities. In addition to dry reforming, bi-reforming of methane (BRM) is an attractive route for syngas production as expensive CO₂ separation step can be avoided. Various reforming routes for syngas generation are described below:

Steam reforming of methane (SRM)



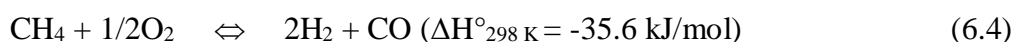
Dry reforming of methane (DRM)



When steam and dry reforming of methane are combined, it gives syngas with H₂/CO ratio close to 2.



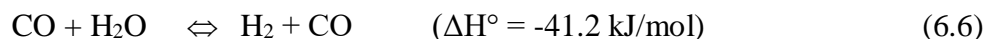
Oxidation of methane (POX or Combustion)



Tri-reforming of methane is a synergetic combination of endothermic steam reforming of methane (eq. 6.1), dry reforming of methane (eq. 6.2) and exothermic oxidation of methane (eq. 6.4 and 6.5). The tri-reforming concept was proposed as a new process route for the utilization of CO₂ in flue gas from fossil fuel based power plants without CO₂ separation to produce synthesis gas with variable H₂/CO ratios. This flexibility to produce syngas with variable H₂/CO ratios is useful in the synthesis of chemicals, particularly in oxo synthesis and long chain hydrocarbons by FT synthesis.

In addition to the above reactions, water gas shift (WGS), reverse water gas shift (RWGS) and carbon formation reactions (v, vi and vii) as described below are prevalent during reforming processes.

WGS and RWGS



Methane cracking



CO disproportionation



Boudouard reaction



The steam and dry reforming reactions are highly endothermic; hence need to be conducted at very high temperatures.

A major issue in syngas production is deactivation of the catalysts due to active metal sintering at high reaction temperatures and carbon deposition. Metal sintering can be avoided by promoting stronger metal to support interaction or by locking the active metal in a stable perovskite lattice, which can withstand red-ox atmosphere and high reaction temperatures. Hence, this work was aimed at preparing highly active and durable perovskite type oxide catalysts for syngas generation through steam reforming, dry reforming, bi-reforming and tri-reforming of methane. Nickel is a preferred metal in these catalysts, but it is highly prone to sintering and sulphur poisoning. Hence, this work also addresses this problem through incorporation of noble metals in perovskite lattice to carry out reforming of even sulfur containing methane gas.

Aim of this thesis is to prepare novel perovskite type oxide catalysts for steam, dry, bi- and tri-reforming of methane to generate syngas. For these processes, catalysts should be highly active and durable. Active metals in a perovskite-type structure are less prone to sintering. If the support has redox properties, it may help to oxidize the coke formed during reforming reactions. Further aim is to develop sulfur resistant catalysts, by doping noble metals such Rh into perovskite lattice and test their performance in steam reforming of simulated biogas. Hence, it was aimed at investigation of various perovskite compositions by using different physico-chemical characterization techniques and correlating the obtained results with their catalytic performance. To understand carbon formation and durability of these perovskite

catalysts, their performance has to be monitored for longer durations. Hence, the overall objective of this study is to unravel the factors influencing the catalytic activity and durability of transition metal doped perovskite catalysts in various reforming reactions.

The thesis is covered in six chapters, with three chapters dedicated to results & discussion sections. The description of each chapter is given below:

Chapter 1 gives a brief introduction to heterogeneous catalysis with an overview of global warming as a result of green house gas emissions to the atmosphere. This chapter also provides information on utilization of biogas, which is generated from bio-wastes, for production of syngas. It also discusses various syngas production technologies like steam, dry, bi- and tri- reforming reactions. Their thermodynamic possibilities at various temperatures, advantage and disadvantages are discussed. Desirable syngas production from dry reforming of methane (DRM), bi-reforming (BRM) and tri-reforming of methane (TRM) are more interesting to get feed stocks for chemical synthesis. The DRM is not only commercially attractive; it also has environmental significance as it utilizes CO₂, a green house gas. But, in case of DRM, the catalysts are prone to severe deactivation due to carbon formation and sintering of the active metal. Sintering can be prevented by anchoring the metal to the support through strong metal to support interaction and also by choosing a transition metal which is less prone to sintering. It also describes a variety of catalyst supports that are used in this study, such as perovskites, hydrotalcites and spinels. Finally, the objectives of the thesis are outlined briefly.

Chapter 2 describes the catalyst preparation methods and experimental methods used in characterization of catalyst materials. The catalysts prepared were Ni substituted LnAlO₃ (where Ln = La, Ce, Pr, Nd, Sm, Gd and Dy) perovskites using citrate gel method. In addition, noble metals like Ru and Rh were substituted in CeAlO₃ at Al site using citrate gel method. Besides these catalysts; Ni, Ru and Rh metal impregnated on CeAlO₃ were also prepared. Another family of novel perovskites, Ni substituted MZrO₃ (M = Ca, Sr and Ba) structures were prepared by citrate gel method. All these structured oxide catalysts were characterized using various physico-chemical techniques like XRD, N₂ sorption (BET), Thermal analysis TPR, TPD of CO₂/O₂, FTIR-DRIFT, Transient pulse experiments, Raman spectroscopy, ICP-OES, HRTEM, XPS etc. The results of these experiments helped

to understand the structural and textural properties of these materials which could be correlated with catalytic properties in reforming applications.

Chapter 3 describes the synthesis of $\text{LnAl}_{(1-x)}\text{Ni}_x\text{O}_3$ (Ln = La, Ce, Pr, Nd, Sm, Gd and Dy) perovskites and their characterization by various physico chemical techniques. Refinement of powder XRD and Raman analysis helped to establish substitution of lanthanides (La to Dy) in the perovskite lattice and the phase transition occurred from cubic to orthorhombic via rhombohedral phase. Among these catalysts $\text{CeAl}_{0.8}\text{Ni}_{0.2}\text{O}_3$, $\text{NdAl}_{0.8}\text{Ni}_{0.2}\text{O}_3$ and $\text{DyAl}_{0.8}\text{Ni}_{0.2}\text{O}_3$ were better in terms of Ni dispersion, higher labile oxygen and strong metal to support interaction as observed through CO chemisorption and temperature programmed techniques. These perovskite type oxides were tested for steam reforming of methane (SRM) and bi-reforming of simulated biogas. Their stability on stream and carbon formation were investigated. $\text{CeAl}_{0.8}\text{Ni}_{0.2}\text{O}_3$ shows superior activity as compared to other perovskites, hence this catalyst was tested for 500 h. The results clearly show that high metal dispersion, reducibility at appropriate temperature and active role of support through surface oxygen play important role in activity and stability of these catalysts.

Further, substituted Ni content in CeAlO_3 structure was varied and tested for SRM. The activity and stability of the substituted catalysts was compared with Ni impregnated CeAlO_3 catalyst. Impregnated catalyst shows lower activity and less stability as compared to substituted catalyst. The low activity and stability of the impregnated catalyst is attributed to weak metal to support interaction, resulting in the sintering of metal particles. Kinetic experiments were carried out over $\text{CeAl}_{0.8}\text{Ni}_{0.2}\text{O}_3$ catalysts following Wei and Iglesia mechanism, which states that the rate of reaction is proportional to CH_4 partial pressure and independent of the partial pressure of co-reactants (H_2O and CO_2). The activation energy obtained was 95 kJ/mol, which is in line with reported values.

Chapter 4 deals with the noble metal (Ru and Rh) substituted CeAlO_3 structures. These catalysts were tested for SRM and bi-reforming of methane (BRM), the later using a biogas composition. This chapter is divided in to two parts. The **first section** deals with substitution of Ru into CeAlO_3 prepared by citrate gel and impregnation methods and their characterization using various physico-chemical techniques. Refinement of XRD data reveals that all perovskites are in cubic phase. XPS and Raman analysis show that even after reduction part of Ru is located inside the perovskite lattice. Therefore, substituted Ru catalysts have greater interaction with

the support, compared to impregnated catalyst. These perovskite type oxides were tested for SRM by varying their Ru content. Optimum Ru content in perovskite structure enhanced the catalytic activity in steam reforming of methane. Moreover, it was proved that Ru substituted catalyst is better than Ru impregnated catalyst. Hence, kinetic experiments were carried out over $\text{CeAl}_{0.85}\text{Ru}_{0.15}\text{O}_3$ catalysts to get activation energy (75 kJ/mol) of methane reforming.

Since, Ru based catalysts are expensive, Ru promoted Ni substituted CeAlO_3 ($\text{CeAl}_{0.9-x}\text{Ru}_x\text{Ni}_{0.1}\text{O}_{3-\delta}$) was synthesized to test its activity and durability. Ru metal helps to improve reducibility of Ni in $\text{CeAl}_{1-x}\text{Ni}_x\text{O}_3$ catalyst thus leading to its better dispersion. This catalyst was tested for steam, bi- and tri-reforming methane reaction. This catalyst was highly durable when tested for 100 and 500 h respectively for bi- and tri-reforming reactions. Following the reaction carbon formation was estimated using TGA, which was only 5.1×10^{-5} and 1.5×10^{-5} mol of carbon $\text{g}^{-1}\text{h}^{-1}$ during bi- and tri-reforming reactions respectively. These results show that substitution of small amount of noble metal stabilizes the activity for longer duration.

In the **second section**, Rh substituted CeAlO_3 perovskites were investigated by varying Rh content to test them for SRM. These catalysts were prepared by the citrate gel method and characterized using various physico-chemical techniques. Rh incorporation into CeAlO_3 perovskite lattice was established by powder XRD and refinement studies. An optimum Rh content of about 2.3 wt% ($\text{CeAl}_{0.95}\text{Rh}_{0.05}\text{O}_3$) was found to give high CH_4 conversion. Optimized $\text{CeAl}_{0.95}\text{Rh}_{0.05}\text{O}_3$ catalyst was tested for its durability, as no deactivation was observed even after 50h on stream. Activity of these catalysts also did not get affected in presence of 11 ppm of H_2S in methane. Hence, this catalyst was tested for SRM of simulated biogas, by adding 11 ppm of H_2S to the feed. The catalyst showed stable activity even in presence of sulfur.

In **Chapter 5**, focus is mostly on the structure-basicity-performance relationship of $\text{MZr}_{1-x}\text{Ni}_x\text{O}_3$ perovskites (where M = Ca, Sr and Ba) in dry reforming of methane (DRM). These perovskite oxides were synthesized by citrate gel method. Following their characterization, they were evaluated in DRM. Refinement of XRD data revealed that substitution of Ca, Sr and Ba led to changes in perovskite phase from orthorhombic to cubic phase. Studies revealed that Ni on Ca perovskites has better reducibility and higher oxygen storage capacity at reaction temperature. Among the three alkaline earth substituted catalysts in dry reforming reaction, $\text{CaZr}_{0.8}\text{Ni}_{0.2}\text{O}_3$ shows superior activity in the temperature range of 600-800 °C. During 12 h of

reaction run, Sr and Ba substituted perovskites were deactivated due to coke formation on their catalyst surface. The Ca substituted catalyst was tested for its durability; it showed only little coke (8.1×10^{-6} moles of C. $\text{g}^{-1} \cdot \text{h}^{-1}$) after 500 h of reaction. These catalysts were also tested for steam reforming of simulated biogas by varying S/C ratio. They showed excellent performance with minimum carbon formation. The results clearly show that high metal dispersion, good reducibility and active role of the support through surface oxygen mobility play important roles in activity and stability of these Ca substituted perovskites.

6.2. Recommendations for future work

At present, there is a great focus world over on how to overcome green house gas affect emanating from CO₂ emissions. Utilization of this gas for syngas production through dry reforming, bi-reforming and tri-reforming of methane could be one option to overcome this problem. To accomplish and establish syngas production through these processes, highly active and durable catalysts are a must. Present work helped to unravel various aspects of these reactions and also established utility of various perovskite structures for syngas generation. This work need to be advanced further by scaling of these catalysts and test them more vigorously in pilot scale. In addition, bi-reforming is a useful process for reforming of biogas, which will bring down the cost of CO₂ separation. Based on our experience with various catalysts used for steam reforming and bi-reforming of simulated biogas, we suggest the following work for future studies.

1. Development of catalysts for steam reforming of biogas

Since, biogas is produced from many sources, its utilization is very important. However, in existing processes, CO₂ is separated and released to the atmosphere thus adding to GHG emissions. Hence, it will be prudent to use biogas without removal of CO₂ to get valuable syngas. This syngas in turn can be used to produce methanol or other fuels and chemicals. Since, this study helped to identify few good catalyst compositions; they may be scaled up and tested for reforming of real biogas. This study should also concentrate on affect of various impurities in biogas on the catalyst performance.

2. Developing sulfur tolerance reforming catalysts

During the reforming reaction, if the fuel has sulfur, NH_3 like poisoning compounds then the catalyst will not work for longer time. For example, biogas is produced from anaerobic degradation of plants and animal wastages. It has trace amount of sulfur along with CH_4 and CO_2 feed. During the reforming of biogas the active catalyst is poisoned by sulfur and the catalyst is deactivated. This process therefore requires a novel sulfur tolerant catalyst for reforming.

3. Bi- and Tri reforming process using monolith based catalysts

During the dry reforming reaction, if an oxidant like O_2 or H_2O is mixed with the feed in small quantities, the coke formed may be removed continuously without its accumulation on metal surface. In addition, the tri-reforming ($\text{CO}_2 + \text{CH}_4 + \text{O}_2 + \text{steam}$) and bi-reforming ($\text{CO}_2 + \text{CH}_4 + \text{steam}$) processes can also help to achieve the desired H_2/CO ratios. Hence, it is suggested to use the best catalysts of this study for scale up and apply them for tri- and bi-reforming studies. It is better to conduct these processes by wash coating these catalysts on metallic honeycomb monoliths that facilitate better control of contact time, heat transfer leading to suppression of coke as well as a gas with desired H_2/CO ratio.

List of publications

1. Tuning the dimensionality of layered $\text{Sr}_{n+1}\text{Ti}_{n-x}\text{Ni}_x\text{O}_{3n+1}$ perovskite structures for improved activity in syngas generation.

Srikanth Dama, Seema R Ghodke, Richa Bobade, Hanmant R Gurav, Satyanarayana Chilukuri, *J. Catal.* 360 (2018) 27-39.

2. Active and durable alkaline earth metal substituted perovskite catalysts for dry reforming of methane.

Srikanth Dama, Seema R Ghodke, Richa Bobade, Hanmant R Gurav, Satyanarayana Chilukuri, *Appl. Catal. B.* 224 (2018) 146-158.

3. Influence of preparation method on activity and stability of Ni catalysts supported on Gd doped ceria in dry reforming of methane.

Hanmant R Gurav, **Srikanth Dama**, Violet Samuel, Satyanarayana Chilukuri, *J. CO₂ Util.* 20 (2017) 357–367.

4. Correlation of Pt reducibility and surface oxygen with water gas shift reaction over Rare earth doped Pt/CeO₂ catalysts.

Richa Bobade, **Srikanth Dama**, Reji Nedumkandathil, Satyanarayana Chilukuri (Communicated to *Applied catalysis A*).

5. Structural characterization of Rare earth substituted Aluminate perovskites and their applications in steam reforming of methane and simulated biogas.

Srikanth Dama, Richa Bobade, Satyanarayana Chilukuri (to be communicated).

6. Effect of Ru concentration in $\text{CeAl}_{1-x}\text{Ru}_x\text{O}_3$ catalyst for steam, Bi and Tri reforming of methane reactions.

Srikanth Dama, Seema R Ghodke, Richa Bobade, Hanmant R Gurav, Satyanarayana Chilukuri (to be communicated).

7. Study and development of sulfur tolerance catalysts for catalytic steam reforming of methane and simulated biogas over Rh based perovskite catalysts.

Srikanth Dama, Richa Bobade, Hanmant R Gurav, Satyanarayana Chilukuri (Manuscript under preparation).

8. Mechanistic investigations of steam reforming of Ethanol over Ni substituted CeAlO₃ catalyst for fuel cell applications.

Srikanth Dama, Richa Bobade, Satyanarayana Chilukuri (Manuscript under preparation).

9. Comparative study of CO₂ hydrogenation reaction over Ru/Zeolite composite catalysts.

Srikanth Dama, Satyanarayana Chilukuri (manuscript under preparation).

Book chapter

1. Catalyst deactivation and regeneration, in “Industrial Catalytic Processes for Fine and Specialty Chemicals”, Elsevier, 2016.
Satyanarayana C.V.V , **Srikanth Dama**, Hanmant R. Gurav,

List of patents

1. Active and durable catalyst for synthesis gas generation,
C.V.V. Satyanarayana, **Srikanth Dama**, Hanmant R. Gurav.
2016-NF-0274 (Appl. No. 201611044559)
2. Improved perovskite catalysts for synthesis gas production with variable H₂/CO ratios.
C.V.V. Satyanarayana, Hanmant R. Gurav, **Srikanth Dama**.
2016-NF-0275 (Appl. No. 201713014438)